

AMPHETAMINE-INDUCED TOXICITY IN ASTROCYTES AND ITS  
IMPLICATIONS IN THE PATHOGENESIS OF  
PSYCHIATRIC DISORDERS

A DISSERTATION IN  
Pharmacology  
and  
Pharmaceutical Sciences

Presented to the faculty of the University  
of Missouri-Kansas City in partial fulfillment of  
the requirements for the degree

DOCTOR OF PHILOSOPHY

by

NITISH CHAUDHARI

Master of Pharmacy (Pharmacology & Toxicology), University of Mumbai, 2013  
Post Graduate Diploma (Patents Law), NALSAR University of Law, 2013  
Bachelor of Pharmacy, University of Pune, 2011

Kansas City, Missouri

2022

© 2022

NITISH CHAUDHARI

ALL RIGHTS RESERVED

AMPHETAMINE-INDUCED TOXICITY IN ASTROCYTES AND ITS  
IMPLICATIONS IN THE PATHOGENESIS OF  
PSYCHIATRIC DISORDERS

Nitish Chaudhari, Candidate for the Doctor of Philosophy Degree  
University of Missouri-Kansas City, 2022

ABSTRACT

Amphetamine-type stimulants (ATS), such as amphetamine (AMPH) and methamphetamine (METH), cause long-term toxic effects on the dopaminergic neurons in the brain leading to the development of several psychiatric disorders. The mechanisms underlying ATS neurotoxicity are unclear, but oxidative stress has been implicated. Most studies on ATS have focused on neurons. However, in recent years, the role of glial cells, particularly astrocytes, in ATS pathogenesis has received considerable focus. Yet, little work has been done to study gene expression changes in ATS-treated astrocytes as a part of the ATS neurotoxicity cascade. Therefore, these studies aimed to examine the contribution of gene expression in astrocytes to ATS toxicity and to identify novel gene targets for treating ATS-induced psychiatric disorders.

In the first chapter, we studied the effects of repeated METH exposure on astrocyte transcriptome using microarray. METH induced differential expression of 1,819 genes in astrocytes. Furthermore, METH significantly dysregulated biological pathways, molecular functions, cellular components, and transcriptional regulators involved in the cell cycle, DNA replication and repair, apoptosis, and phagocytosis. These results suggested that METH-induced gene expression changes play a critical role in METH-induced cell cycle arrest, defective DNA repair, and increased apoptosis.

In the second chapter, we investigated the effect of METH treatment on the expression of integrins in astrocytes and the involvement of integrins in METH-induced apoptosis. We found that METH significantly decreased the expression of 10 integrin subunits expressed in astrocytes and that integrin subunit  $\beta 1$  is involved in METH-induced apoptosis in astrocytes.

In the third chapter, we utilized a population-level study to determine the prevalence of psychiatric disorders in METH-abusing individuals using the Cerner Health Facts database. Our results showed a significantly higher prevalence of anxiety, depression, bipolar disorder, psychosis, and schizophrenia among METH-abusing individuals compared to the general population. We then identified common gene expression signatures by comparing gene expression changes from our microarray data and independent microarray datasets from patients with anxiety, depression, and schizophrenia retrieved from the gene expression omnibus (GEO) database.

In conclusion, we demonstrated that ATS-induced gene expression alterations are involved in developing neurotoxicity and psychiatric disorders in ATS-abusing users.

## APPROVAL PAGE

The faculty listed below, appointed by the Dean of School of Graduate Studies have examined the dissertation titled “Amphetamine-Induced Toxicity in Astrocytes and its Implications in the Pathogenesis of Psychiatric Disorders” presented by Nitish Chaudhari, candidate for the Doctor of Philosophy degree, and certify that in their opinion it is worthy of acceptance.

### Supervisory Committee

Jianping Wang, Ph.D., Committee Chair  
Division of Pharmacology and Pharmaceutical Sciences

Gerald Wyckoff, Ph.D.  
Division of Pharmacology and Pharmaceutical Sciences

Kun Cheng, Ph.D.  
Division of Pharmacology and Pharmaceutical Sciences

Peter Silverstein, Ph.D.  
Division of Pharmacology and Pharmaceutical Sciences

John Q. Wang, Ph.D.  
Department of Anesthesiology

Monica Gaddis, Ph.D.  
Department of Biomedical and Health Informatics

# CONTENTS

ABSTRACT .....	iii
TABLES .....	xi
ILLUSTRATIONS .....	xii
ABBREVIATIONS .....	xv
ACKNOWLEDGEMENTS .....	xvii
CHAPTER 1: GENERAL INTRODUCTION .....	1
1.1 Amphetamine-type Stimulants and Epidemiology of its Use .....	1
1.2 Clinical Presentation .....	4
1.3 Pathogenesis of METH Toxicity .....	6
1.3.1 Oxidative Stress and Mitochondrial Dysfunction .....	6
1.3.2 Excitotoxicity and Endoplasmic Reticulum (ER) Stress .....	10
1.3.3 Neuroinflammation .....	12
1.4 Integrins .....	15
1.4.1 Integrin Structure .....	15
1.4.2 Integrins in the CNS .....	17
1.4.3 Integrins, Cell Survival, and Anoikis .....	19
1.4.4 Integrins as Trophic Factors .....	20
1.5 Significance .....	23

## CHAPTER 2: TRANSCRIPTOME ANALYSIS OF METHAMPHETAMINE-TREATED

ASTROCYTES .....	25
2.1 Introduction .....	25
2.2 Materials and Methods .....	26
2.2.1 Materials .....	26
2.2.2 Cell Culture.....	27
2.2.3 Microarray .....	27
2.2.4 Quality Control.....	28
2.2.5 Normalization and Differential Gene Expression .....	31
2.2.6 Pathway Analysis .....	31
2.2.7 Gene Ontology Analysis.....	33
2.2.8 Upstream Regulatory Analysis.....	34
2.3 Results .....	38
2.3.1 Quality Control Assessments .....	38
2.3.2 Normalization and Differential Gene Expression .....	43
2.3.3 Pathway Analysis .....	54
2.3.3.4 Gene Ontology Analysis.....	91
2.3.3.5 Upstream Regulatory Analysis.....	95
2.4 Discussion.....	98

CHAPTER 3: EVALUATION OF THE EFFECT OF AMPHETAMINE ON THE  
EXPRESSION OF INTEGRINS AND CELL DEATH IN ASTROCYTES ..... 101

3.1 Introduction ..... 101

3.2 Materials and Methods ..... 102

3.2.1 Chemicals and Reagents ..... 102

3.2.2 Cell Culture ..... 103

3.3.3 Quantitative Real-Time Reverse Transcription Polymerase Chain Reaction (qRT-PCR)  
..... 104

3.3.4 Western Blot ..... 106

3.3.5 XTT Cell Viability Assay ..... 107

3.3.6 LDH Cytotoxicity Assay ..... 108

3.3.7 Caspase-3 Activity Assay ..... 109

3.3.8 *In vitro* Silencing Activity and Cell Death Analysis ..... 109

3.3.9 Statistical Analysis ..... 111

3.4 Results ..... 111

3.4.1 AMPH induces a dose- and time-dependent decrease in the mRNA expression of  
integrin  $\alpha$  subunits in astrocytes ..... 111

3.4.2 AMPH induces a dose- and time-dependent decrease in the mRNA expression of  
integrin  $\beta$  subunits in astrocytes ..... 118

3.4.3 AMPH induces a time-dependent decrease in the protein expression of integrin  
subunits in astrocytes ..... 124

3.4.4 AMPH induces cell death in primary human astrocytes .....	128
3.4.5 Caspase-3 is involved in AMPH-mediated apoptosis in astrocytes .....	130
3.4.6 Integrin subunits are involved in AMPH-mediated apoptosis in astrocytes .....	132
3.5 Discussion .....	135
<b>CHAPTER 4: PREVALENCE OF PSYCHIATRIC DISORDERS IN METH-ABUSING</b>	
<b>INDIVIDUALS AND IDENTIFICATION OF NOVEL GENE TARGETS IN METH-</b>	
<b>ASSOCIATED PSYCHIATRIC DISORDERS.....</b>	
	139
4.1 Introduction .....	139
4.2 Methods.....	141
4.1.1 Data Source.....	141
4.1.2 Study Population .....	141
4.1.4 GEO Analysis.....	142
4.3 Results .....	143
4.3.1 Demographic Characteristics.....	143
4.3.2 Prevalence of Psychiatric Disorders.....	145
4.3.3 GEO Analysis.....	145
4.4 Discussion .....	152
<b>CHAPTER 5: FUTURE DIRECTIONS.....</b>	<b>158</b>
<b>APPENDIX.....</b>	<b>160</b>
<b>REFERENCES .....</b>	<b>252</b>

VITA..... 297

## TABLES

Table 1. Average background, Raw Q, Percent Present, and 3'/5' GAPDH values of Control and METH samples.....	41
Table 2. Description of top 20 upregulated genes in METH-treated astrocytes.....	46
Table 3. Description of top 20 downregulated genes in METH-treated astrocytes.....	50
Table 4. Significantly affected pathways in METH-treated astrocytes .....	55
Table 5. Significantly enriched BP GO terms in METH-treated astrocytes.....	93
Table 6. Significantly enriched CC GO terms in METH-treated astrocytes .....	93
Table 7. Significantly enriched MF GO terms in METH-treated astrocytes.....	94
Table 8. Top 15 upstream regulators predicted as inhibited in METH-treated astrocytes .....	96
Table 9. Upstream regulators predicted as activated in METH-treated astrocytes.....	97
Table 10. List of primers and their annealing temperatures .....	105
Table 11: Cohort demographics.....	144
Table 12: Prevalence of psychiatric disorders in patients with a positive METH screen.....	145
Table 13: GEO Bipolar disorder microarray datasets used in the analysis.....	146
Table 14: GEO major depressive disorder microarray datasets used in the analysis .....	148
Table 14: GEO schizophrenia microarray datasets used in the analysis .....	150

ILLUSTRATIONS

Figure 1. Past Year METH Use among People Aged 12 or Older: 2015-2019..... 2

Figure 2. Methamphetamine injection, use disorder, receipt of substance use treatment and frequency of use, other substance use, and mental illness among adults  $\geq 18$  years old reporting past-year METH use in the United States, 2015–2018..... 3

Figure 3. Main molecular mechanisms involved in METH-induced toxicity. .... 7

Figure 4. Oxidative stress and mitochondrial dysfunction mechanisms involved in METH-induced neurotoxicity. .... 9

Figure 5. Excitotoxicity and ER stress mechanisms involved in METH-induced neurotoxicity. 11

Figure 6. Role of astrocytes and microglia in METH-induced neuroinflammation. .... 14

Figure 7. Integrin structures and domains and conformational changes. .... 16

Figure 8. Common pathways of anoikis induction after the loss of integrin-mediated adhesion. 22

Figure 9. Target genes consistent with the hypothesis considered. .... 37

Figure 10. Graphic for hypothesis HA..... 37

Figure 11. Microarray pictures of Control (A) and METH (B) samples..... 39

Figure 12. Density plot (A) and Boxplot (B) of array intensity distributions in Control and METH samples before normalization. .... 40

Figure 13. Signals values (log2) of (A) labeling controls (B) hybridization controls of Control and METH samples. .... 42

Figure 14. Principal component analysis (PCA) of Control and METH samples. .... 43

Figure 15. Density plot (A) and Boxplot (B) of array intensity distributions of Control and METH samples after normalization. ....	44
Figure 16. Volcano plot of gene expression in METH-treated astrocytes.....	45
Figure 17. Effect of METH on cell cycle pathway in astrocytes.....	59
Figure 18. Effect of METH on steroid biosynthesis pathway in astrocytes. ....	61
Figure 19. Effect of METH on DNA replication in astrocytes.....	64
Figure 20. Effect of METH on mismatch repair pathway in astrocytes. ....	66
Figure 21. Effect of METH on lysosome pathway in astrocytes.....	69
Figure 22. Effect of METH on apoptosis pathway in astrocytes.....	72
Figure 23. Effect of METH on p53 signaling pathway in astrocytes. ....	75
Figure 24. Effect of METH on base excision repair pathway in astrocytes. ....	78
Figure 25. Effect of METH on homologous recombination pathway in astrocytes. ....	81
Figure 26. Effect of METH on cellular senescence pathway in astrocytes. ....	83
Figure 28. Effect of METH on phagosome pathway in astrocytes.....	90
Figure 39. AMPH-mediated decrease in the expression of ITGA1 protein in astrocytes. ....	125
Figure 40. AMPH-mediated decrease in the expression of ITGA2 protein in astrocytes. ....	126
Figure 41. AMPH-mediated decrease in the expression of ITGB1 protein in astrocytes.....	127
Figure 42. AMPH-mediated induction of cell death in astrocytes.....	129
Figure 43. Involvement of caspase-3 in AMPH-mediated cell death. ....	131
Figure 44. Knockdown efficiency of ITGA1, ITGA2, and ITGB1 siRNAs in astrocytes. ....	132

Figure 45. Involvement of ITGA1, ITGA2, and ITGB1 in AMPH-induced cell death in astrocytes. .... 134

Figure 46. Co-expressed genes between BD microarray datasets from the GEO database and microarray dataset of METH-treated astrocytes. .... 147

Figure 47. Co-expressed genes between MDD microarray datasets from the GEO database and microarray dataset of METH-treated astrocytes. .... 149

Figure 48. Co-expressed genes between SCZ microarray datasets from the GEO database and microarray dataset of METH-treated astrocytes. .... 151

## ABBREVIATIONS

ADSS	Adenylosuccinate synthetase
AMPH	Amphetamine
ATS	Amphetamine-type stimulants
BD	Bipolar disorder
BP	Biological processes
CC	Cellular compartment
CDK	Cyclin-dependent kinase
CNS	Central nervous system
COL	Collagen
CTRL	Control
DA	Dopamine
DAT	Dopamine transporter
DEGs	Differentially expressed genes
DMEM	Dulbecco's Modified Eagle's medium
ECM	Extracellular matrix
ED	Emergency department
ER	Endoplasmic reticulum
FC	Fold change
FDR	False discovery rate
GAPDH	Glyceraldehyde-3-phosphate dehydrogenase
GR	Glucocorticoid receptor
GEO	Gene expression omnibus
GO	Gene ontology
GWAS	Genome-wide association studies
HA	Human astrocytes
HFA	Human fetal astrocytes
HPRT	Hypoxanthine phosphoribosyltransferase
ICD	International Classification of Diseases
iPG	iPathwayGuide
IRB	Institutional Review Board
ITG	Integrin
KEGG	Kyoto Encyclopedia of Genes and Genomes
LDH	Lactate dehydrogenase
MDD	Major depressive disorder
METH	Methamphetamine
MF	Molecular functions
MUD	Methamphetamine use disorder

NCBI	National Center for Biotechnology Information
NSDUH	National Survey on Drug use and Health
PBS	Phosphate-buffered saline
PCA	Principal component analysis
POL	Polymerase
QC	Quality control
qRT-PCR	Quantitative real-time reverse transcription polymerase chain reaction
ROS	Reactive oxygen species
SAC	Spindle assembly checkpoint
SCZ	Schizophrenia
SPON1	Spondin 1
STAT5B	Signal transducer and activator of transcription 5B
TAC	Transcriptome Analysis Console
VMAT2	Vesicle monoamine transporter 2
WB	Western blot

## ACKNOWLEDGEMENTS

Carrying out the requisite work and then writing this dissertation was, undoubtedly, the most arduous task I have undertaken. However, one of the joys of completing the dissertation is looking back at everyone who helped me throughout my Ph.D.

I want to begin by thanking my supervisors, Dr. Jianping Wang and Dr. Gerald Wyckoff, who have given me the opportunity and experience of completing my Ph.D. My dissertation would not be what it is without their insightful comments and discussions of all the chapters. Thank you so much for helping, supporting, and seeing me through to the end of my dissertation. I will never forget the many hours of conversation in your offices. You taught me so much about myself and the professional, scientific world. Thank you for supporting me and my career, giving me confidence in my work, and continuously looking out for my best interests.

I would like to express my most profound appreciation to my committee members, Dr. Kun Cheng, Dr. Peter Silverstein, Dr. John Q. Wang, and Dr. Monica Gaddis, for their continuous guidance and help during the meetings, seminars, and coursework, as well as during the time of critical thinking for the project. The advice from all of you has always been very valuable and helped me develop through these years as a graduate student. A special thanks to Dr. Monica Gaddis and Ms. Suman Sahil for providing me with patient data from the Cerner Health Facts database and helping me analyze it.

I would also like to express my sincere thanks to the whole staff of the Division of Pharmacology and Pharmaceutical Sciences, especially Ms. Sharon Self, Ms. Merima Delic, and Ms. Sarah Beach, for their help in all the administrative formalities right since the admission

process. I would also like to thank the Division of Pharmacology and Pharmaceutical Sciences for providing me with the funding and various scholarships throughout my Ph.D. journey.

I would like to extend my sincere thanks to fellow lab members Daniel, Leslie, Drinnan, and Lauren for helping me with my experiments and cheering me until the end. I am also grateful to my friends from the Division of Pharmacology and Pharmaceutical Sciences, Dr. Navid Ayon, Dr. Bhagyesh Sarode, Pratik, Nitish, Shivani, Mayank, Vidit, and Sherin for all their support throughout my Ph.D. years. Special thanks to my non-UMKC friends Saloni, Taylor, Sameer, Prajakta, Rachu, Deya, Nick, Shantanu, Pratik, Pranav, and Nikita, for believing in me and encouraging me until the very end of this rollercoaster journey.

To my family, particularly my parents, brother, and sister-in-law, thank you for your love, support, and unwavering belief in me. Without you, I would not be the person I am today. Writing words in this acknowledgment section will not suffice to express my love and gratitude for you. Time away from you is the hardest thing of all.

Above all, completing my dissertation would not have been possible without the unconditional love, constant support, and nurturing of my lovely wife, Vaishali. Thank you for keeping me sane over the last five years. Thank you for being my best friend. I owe you everything.

## DEDICATION

I would like to dedicate this dissertation to my family without whose constant support this dissertation was not possible.

## CHAPTER 1: GENERAL INTRODUCTION

### 1.1 Amphetamine-type Stimulants and Epidemiology of its Use

Amphetamine-type stimulants (ATS) are a class of synthetic stimulants that are chemical derivatives of the parent compound alpha-methylphenethylamine. Amphetamine (AMPH), methamphetamine (METH), ephedrine, pseudoephedrine, 3,4-methylenedioxymethamphetamine (MDMA), 3,4-methylenedioxyamphetamine (MDA), and 3,4-methylenedioxymethamphetamine (MDMA) are the common members of the ATS family. The unlawful street names for ATS include ice, meth, crystal, crank, bennies, and speed. In addition, prescription stimulants of the amphetamine class include dextroamphetamine and lisdexamfetamine [1].

Clinically, AMPH has been used to treat various illnesses, from asthma to attention deficit and hyperactivity disorder, and illegally, it is used for recreational purposes. The psychostimulant properties of ATS are due to chemical groups containing an unsubstituted phenyl ring, a methyl group at the alpha position, and the main amino group. Multiple changes on the phenyl ring of ATS provide a hallucinogenic effect in addition to the psychostimulant impact [2]. ATS are, therefore, notorious for their addictive nature and the prevalence of abuse.

METH remains the most abused ATS in the US. Based on nationally representative data from the National Survey on Drug Use and Health (NSDUH), the number of people 12 years or older reporting past-year use of METH in 2019 was 2.5 million, up from 1.4 million in 2016; the prevalence of past-year use increased from 0.5% in 2016 to 0.7% in 2019. Similarly, the number of people with past-year METH use disorder (MUD) increased from 684,000 or 0.3% in 2016 to 1.5 million or 0.4% in 2019 (Fig. 1). In addition, among individuals reporting past-year METH use, the number of reporting daily or near-daily use of METH increased by over 92%, from approximately 161,000 in 2016 to 310,000 in 2019 [3]. Notable trends included increased MUD

without injection by heterosexual men and women, gay/bisexual men, and lesbian/bisexual women, and non-Hispanic Whites, Blacks, Asians or Other Pacific Islanders, and Hispanics. Populations at increased risk for METH use have diversified rapidly, particularly among those with socioeconomic risk factors and more comorbidities. These changes in METH use patterns increase risks for overdose and other adverse outcomes [4].

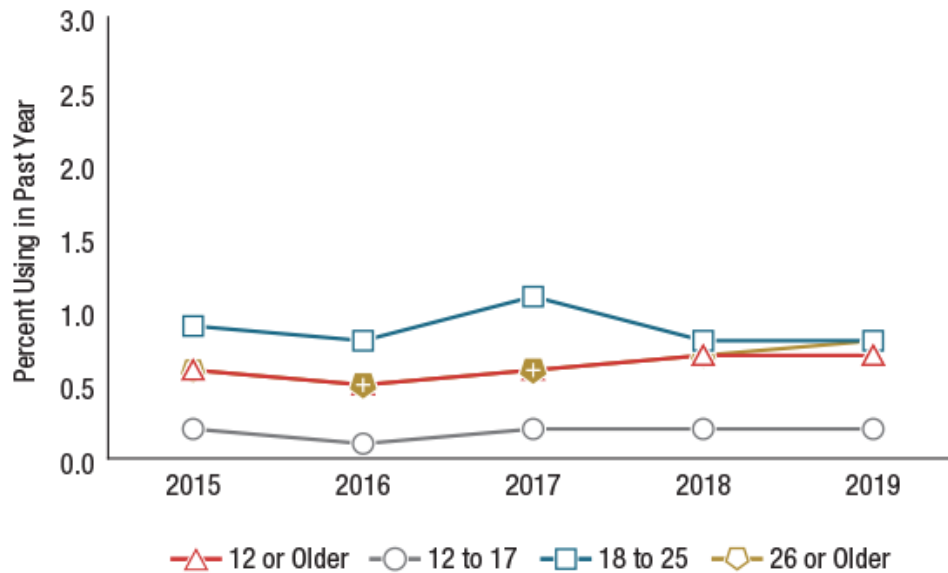


**Figure 1. Past Year METH Use among People Aged 12 or Older: 2015-2019** Source: National Surveys on Drug Use and Health, 2019. Adapted from Ref. [3].

According to NSDUH statistics, several other demographic and geographic characteristics have been related to METH usage. METH usage among adults was associated with male sex, age 26 or older, lower educational attainment, annual family income of < \$50,000, Medicaid-only or no health insurance, and residence in small metro and nonmetro counties [5]. In addition, METH usage increased among gay/lesbian and bisexual individuals and government aid recipients. Geographically, the West had the highest incidence of past-year METH usage among those aged 12 or older in 2019 (1.1%), followed by the Midwest (0.8%), South (0.7%), and Northeast (0.3%)

[3]. Co-occurring drug abuse and mental health issues are common among METH users. Adults who reported using METH in the previous year also reported using cannabis (68.7%), prescription opioid misuse (40.4%), cocaine (30.4%), prescription sedative or tranquilizer abuse (29.1%), prescription stimulant misuse (21.6%), and heroin usage (16.9%). In addition, respondents reported binge drinking (46.4%) and nicotine dependence (44.3%) in the previous month; 57.7 % had any mental disease during the last year, and 25.0% had a serious mental illness. In addition, among people who reported past-year METH use between 2015 and 2018, 52.9% fulfilled the diagnostic criteria for a past-year MUD, and 22.3% reported injecting METH in the last year (Fig. 2) [5].

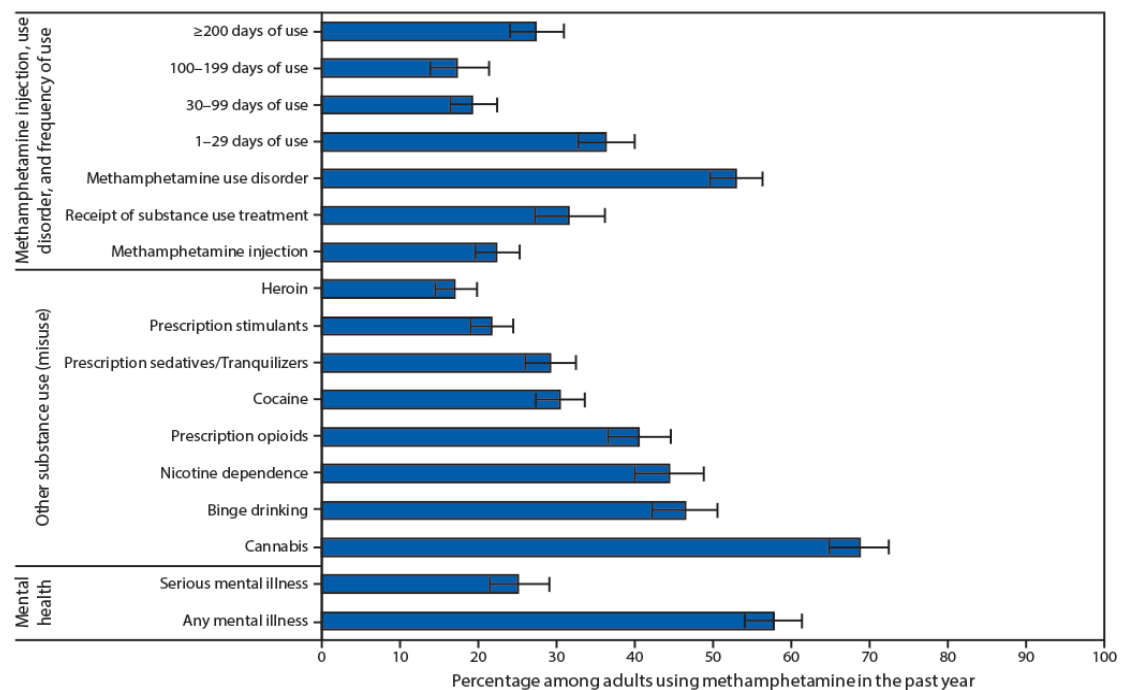


**Figure 2. Methamphetamine injection, use disorder, receipt of substance use treatment and frequency of use, other substance use, and mental illness among adults ≥ 18 years old reporting past-year METH use in the United States, 2015–2018. Adapted from Ref. [5].**

The prevalence of METH and MUD usage demonstrates the significance of preparing for the next drug abuse epidemic. However, whereas opioid use disorder may be treated

pharmacologically and behaviorally [6], treating MUD presents major obstacles [7]. Therefore, it is crucial to comprehend the three primary characteristics of MUD. First, the neurobiology of methamphetamine is more complex than the conventional understanding of it as a modulator of monoaminergic function. Second, the clinical presentation of substance use disorders is not confined to the symptoms associated with the condition but includes physical manifestations, most notably the cardiovascular and cerebrovascular systems. Third, pharmaceutical therapies aimed at regulating the monoaminergic pathways have mostly failed, necessitating the development of new pharmacologic strategies centered on novel therapeutic targets [7].

## **1.2 Clinical Presentation**

Acute effects of METH use include increased energy and alertness, less need for sleep, euphoria, enhanced libido, excessive talking, weight loss, sweating, clenched jaw muscles, grinding teeth, and lack of appetite [8]. METH use aggravates three types of symptoms: 1-suicidality, guilt, hostility, somatic concern, and self-neglect are examples of positive psychotic symptoms; 2-affective symptoms include depression, suicidality, guilt, hostility, somatic concern, and self-neglect; and 3-psychomotor symptoms include tension, excitement, distractibility, and motor hyperactivity [9].

The clinical picture might be complicated, and it can resemble various psychiatric diseases. The move from casual to obsessive METH use may be quick; some studies have found that it takes around 50 days from the initial drug use to the first drug craving, 60 days to regular use, and 85 days to compulsive use [10]. Although most METH-related psychoses are transient, lasting only a few hours to days, in some instances, psychotic episodes can continue up to 6 months and recur following drug withdrawal [11]. Psychotic symptoms are reported by 36.5% of METH users, regardless of age or sex, although this figure rises to 42.7% when lifetime symptoms are taken into

consideration [12]. Some have indicated that those who use crystal METH have a higher rate of self-reported mental illness than people who use other types of METH, which might be due to the purity of crystal METH and the self-selection of people who use it [13].

The mental comorbidity of the MUD is complicated since there is evidence for both preexisting variables and new factors that raise the risk of psychiatric disorders and new factors that increase the risk of psychiatric diseases [14]. Furthermore, because some people use METH as a coping mechanism, early life hardship, including emotional or sexual abuse, may raise the risk of MUD [15]. Additionally, MUD coexists with other mental illnesses, such as mood disorders (16%), psychotic disorders (13%), and anxiety disorders (7.0%) [16]. Early-life trauma and mental comorbidity have been linked to the age at which METH was first used and treatment effectiveness [17, 18].

Cardiovascular and cerebrovascular diseases are the most severe medical complications and leading causes of mortality related to MUD [19]. Hemorrhagic strokes related to METH use have been rising, particularly among young males [20]. METH use also causes vasoconstriction, pulmonary hypertension, atherosclerotic plaque development, cardiac arrhythmia, and cardiomyopathy [21]. METH-induced cardiomyopathy is characterized by left ventricular dilatation, poor left ventricular ejection fraction, and increased tissue markers of inflammation and fibrosis [22]. These patients commonly exhibit tachyarrhythmia, right axis deviation, left ventricular hypertrophy, a P pulmonale pattern, inferior Q waves, lateral T-wave inversion, and a prolonged QTc interval on electrocardiograms [23]. The symptoms preceding mortality due to the toxic effects of METH include collapse, trouble breathing, and overheating, which may be caused by abnormal heart enlargement [24]. METH was also found in 63% of opioid-related deaths [25]. It is critical to underline that the symptoms of dyspnea, angina, palpitations, cough, and hemoptysis

should encourage the doctor to closely follow the medical state of persons who come with acute METH intoxication to avoid mortality.

### **1.3 Pathogenesis of METH Toxicity**

METH has been conceptualized primarily as a releaser of dopamine, serotonin, noradrenaline, and adrenaline from nerve terminals in the central and peripheral nervous system, which occurs via several different mechanisms, including (1) redistributing catecholamines from synaptic vesicles to the cytosol, (2) reversing the plasma membrane transport of neurotransmitters, (3) blocking the activity of monoamine transporters, (4) decreasing the expression of dopamine (DA) transporters at the cell surface, (5) inhibiting monoamine oxidase activity, and (6) increasing the activity and expression of tyrosine hydroxylase, the critical enzyme for synthesizing DA [26]. However, there has been a significant increase in METH-associated neuronal targets during the last decade. Multiple molecular pathways are affected by METH, including oxidative stress, mitochondrial dysfunction, excitotoxicity, endoplasmic reticulum stress, and neuroinflammation [27] (Fig. 3).

#### **1.3.1 Oxidative Stress and Mitochondrial Dysfunction**

Oxidative stress is a crucial contributor to the cellular toxicity of METH. METH increases the oxidation of DA, resulting in the generation of reactive oxygen species (ROS) such as hydroxyl radicals ( $\text{OH}^-$ ), hydrogen peroxide ( $\text{H}_2\text{O}_2$ ), and superoxide anion ( $\text{O}^{2-}$ ) [28].

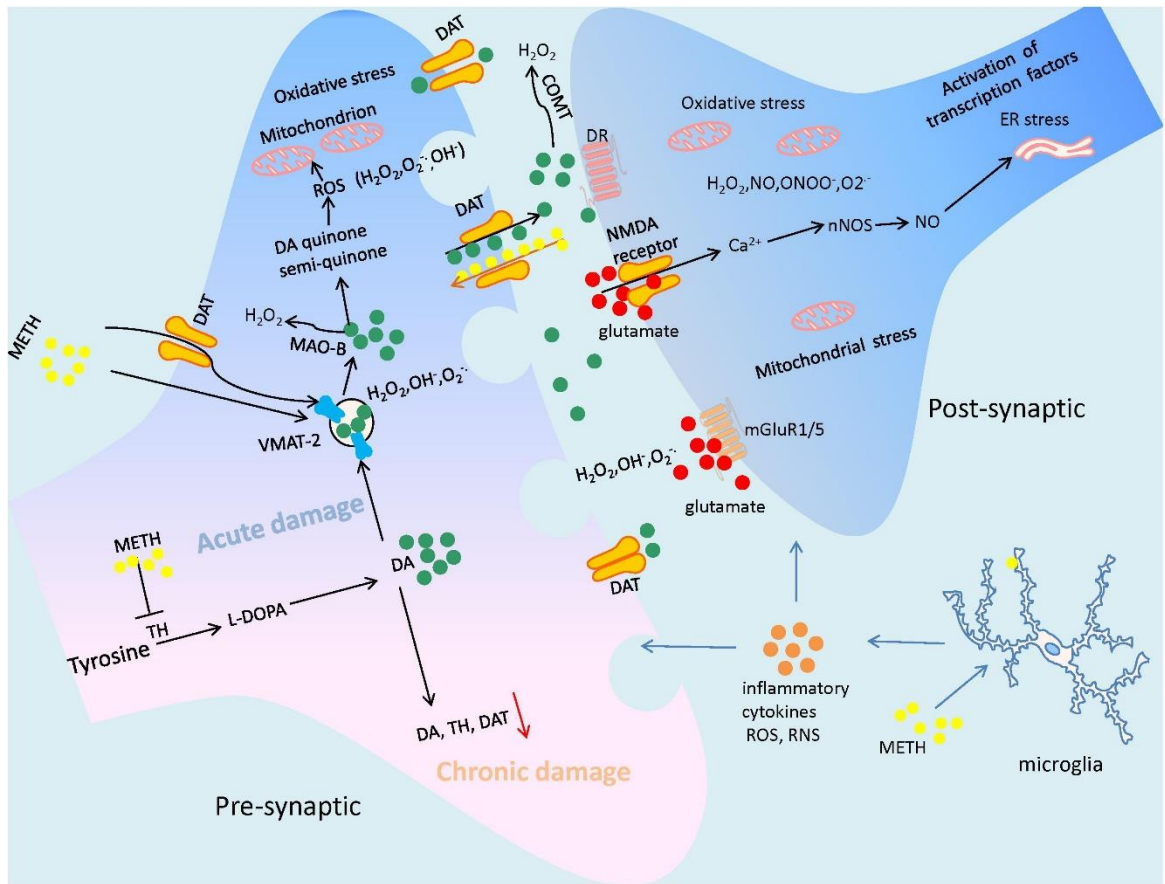


**Figure 3. Main molecular mechanisms involved in METH-induced toxicity.** Reprinted from Ref. [27] under the Creative Commons Attribution License (CC BY).

Because of its high lipid solubility, METH easily crosses the blood-brain barrier and enters the brain [29]. Due to its resemblance to DA, it then reaches dopaminergic terminals through the dopamine transporter (DAT) [30] and passive diffusion [26]. METH increases DA levels in the cytosol and synaptic cleft by affecting the function of vesicle monoamine transporter 2 (VMAT2) and encouraging DA release; this process may be the primary mechanism underpinning METH's neurotoxic action in the brain [31]. Excess DA is autoxidized to quinone or semi-quinone [32] in dopaminergic terminals and synaptic clefts, generating substantial quantities of H<sub>2</sub>O<sub>2</sub>, OH<sup>-</sup>, and O<sub>2</sub> [31]. Furthermore, H<sub>2</sub>O<sub>2</sub> is produced as a consequence of DA metabolism mediated by monoamine oxidase (MAO) or catechol-O-methyltransferase (COMT) [33]. When H<sub>2</sub>O<sub>2</sub> interacts with

transition metal ions, extremely toxic  $\text{OH}^\cdot$  is formed. Eventually, an excess of ROS triggers a series of oxidative stress processes, including lipid peroxidation and protease activation, which leads to cell death. Furthermore, by bypassing antioxidative enzymes, extremely toxic peroxynitrite ions ( $\text{ONOO}^-$ ) generated by  $\text{O}_2$  react with nitric oxide (NO) to destroy proteins, nucleic acids, and phospholipids in cells [33] (Fig. 3).

Mitochondria predominantly mediate METH-induced ROS generation in brain cells. Neuronal death and various neurodegenerative disorders have been linked to mitochondrial respiration defects [34]. Mitochondrial metabolic failure causes METH-induced dopaminergic neurotoxicity by inhibiting the Krebs cycle and electron transport chain (ETC) and promoting oxidative stress, resulting in an imbalance between oxidation and antioxidation in brain cells [30]. ROS and reactive nitrogen species (RNS) produced by DA oxidation directly block numerous critical enzymes, including complexes I, II, III, and IV of the ETC, resulting in mitochondrial malfunction, DNA structural damage, and genetic information loss [35-37]. As a result of electron leakage, METH inhibiting ETC components increases  $\text{O}_2$  generation. This positive feedback loop exacerbates mitochondrial energy metabolism disruption and neurotoxicity.

Dopaminergic toxicity caused by METH-induced mitochondrial damage has clinical implications since it leads to catastrophic neuropathological consequences in the brain due to subsequent caspase activation and apoptosis [38-40]. METH treatment has been shown to enhance pro-apoptotic proteins Bax, Bad, and Bid expression while decreasing anti-apoptotic proteins Bcl-2 and Bcl-xL expression [37, 41-43]. The Bcl-2/Bax ratio in mitochondrial fractions is reduced, which facilitates the release of cytochrome c (Cyt c) from mitochondria [44, 45]. Cyt c then becomes part of the apoptosome with apoptotic peptidase activating factor-1 (Apaf-1) and induces successive activation of the executioner caspases-3, -6, and -7 [40]. Several studies have now

shown that the apoptotic death caused by METH involves more than one molecule. Inhibition of protein kinase C delta (PKC $\delta$ ) or overexpression of a cleavage-resistant PKC $\delta$  mutant, for example, protects mesencephalic dopaminergic cell cultures against METH-induced death *in vitro* [46]. PKC $\delta$  inhibition may also help reverse METH-induced mitochondrial stress, apoptosis, and dopaminergic degeneration [39, 45, 47]. In PC12 cells and SH-SY5Y cells, a p53-upregulated modulator of apoptosis (PUMA) has also been involved in the mitochondrial apoptotic pathway generated by METH. PUMA interacts with Bax and Bcl-2 in mitochondrial membranes to promote Cyt c migration from mitochondria to the cytoplasm, resulting in caspase-3 and poly-ADP-ribose polymerase (PARP) activation, and apoptosis [48]. Furthermore, microinjection of anti-micro (mi)R143-dependent PUMA into the hippocampi of mice rescues METH-induced microglial death through apoptosis and autophagy regulation [49] (Fig. 4).

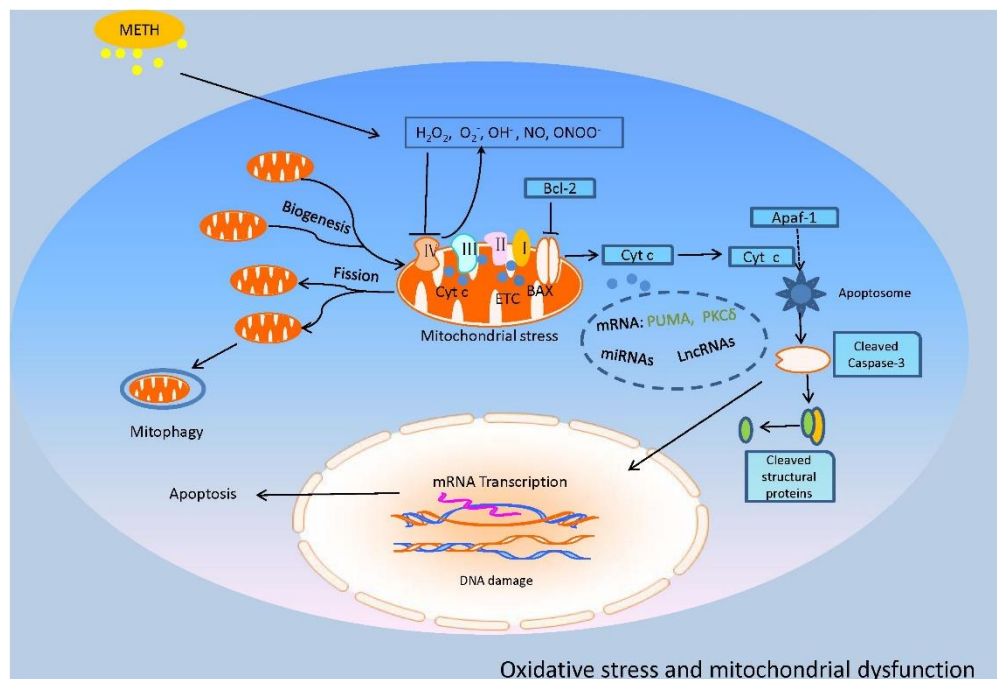


**Figure 4. Oxidative stress and mitochondrial dysfunction mechanisms involved in METH-induced neurotoxicity.** Reprinted from Ref. [27] under the Creative Commons Attribution License (CC BY).

### 1.3.2 Excitotoxicity and Endoplasmic Reticulum (ER) Stress

Glutamate (Glu), the principal excitatory neurotransmitter in the brain, has been demonstrated to have a significant role in METH-induced excitotoxicity. Glu over-activates several downstream signaling pathways, the majority of which include an increased Ca<sup>2+</sup> influx, resulting in a rise in intracellular Ca<sup>2+</sup> concentration [50]. Excess Glu stimulates N-methyl-D-aspartate (NMDARs) and metabotropic glutamate receptors (mGluRs) [51]. Activation of mGluRs causes phosphorylation of protein kinase C (PKC) and upregulation of NMDAR activity, resulting in an increase in Ca<sup>2+</sup> influx, which acts as a ubiquitous and pluripotent second messenger [52]. Excess intracellular Ca<sup>2+</sup> activates protein kinases, phosphatases, and nitric oxide synthase (NOS). The latter then stimulates NO generation [51], which induces ER stress, apoptotic pathway activation, and, finally, METH-induced neurotoxicity [53] (Fig. 5).

ER stress is characterized by the buildup of misfolded proteins and the activation of the unfolded protein response (UPR), which removes unfolded and misfolded proteins from the ER and restores ER equilibrium. Activating transcription factor-6 (ATF6), inositol requiring protein-1 (IRE1), and protein kinase RNA-like ER kinase (PERK) are three ER-resident transmembrane proteins that are activated by ER stress [54, 55]. To cope with proteotoxic stress, these three signaling pathways cause a decrease in protein synthesis and expression of certain genes [56]. IRE1, PERK, and ATF6 may stimulate pro-apoptotic signaling during prolonged ER stress by activating C/EBP homologous protein (CHOP), which then leads to the beginning of ER stress-mediated apoptosis via regulation of Bcl-2 family members [52]. Apoptosis is induced by ER stress through various mechanisms, including death receptor activation and involvement in the mitochondria-dependent cell death pathway [57]. In the rat striatum, neurotoxic dosages of METH have been found to stimulate the expression of many ER stress genes, including those encoding

the 78-kDa glucose-regulated protein (GRP-78), CHOP, and ATF4 [42, 58]. METH-induced ER stress has been linked to dopaminergic toxicity and the activation of the DA D1 receptor [42]. METH-induced apoptosis *in vitro* is mediated (at least in part) through an ER-dependent process that involves CHOP, spliced X-box binding protein 1 (XBP1), caspase-12, and caspase-3 [56]. Furthermore, high-dose METH enhances the expression of nuclear protein 1 (NUPR1), which promotes dopaminergic neuronal death and autophagy via the NUPR1/CHOP pathway [59] (Fig. 5).

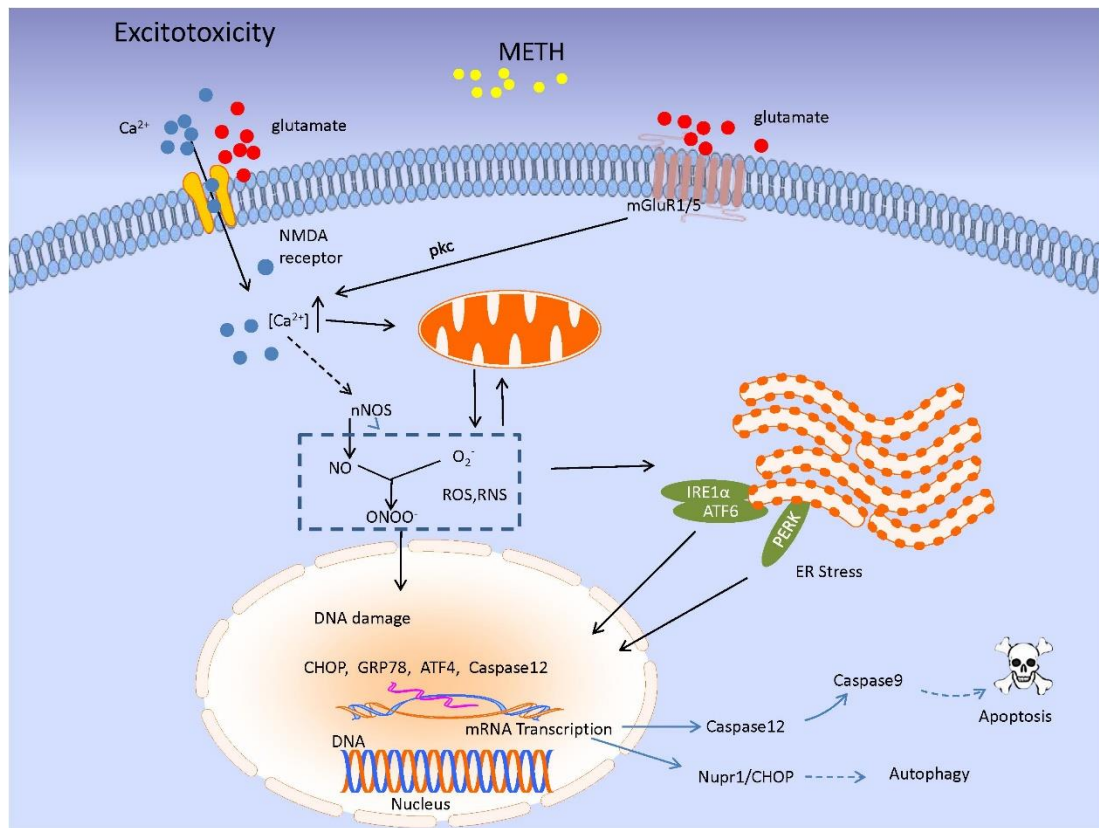


**Figure 5. Excitotoxicity and ER stress mechanisms involved in METH-induced neurotoxicity.** Reprinted from Ref. [27] under the Creative Commons Attribution License (CC BY).

### **1.3.3 Neuroinflammation**

#### ***1.3.3.1 Role of microglia***

METH-induced neuroinflammation is closely linked to glial activation, triggered quickly after METH injection in DA-innervated regions. The production of damage-associated molecular patterns (DAMPs) by neurons is thought to cause microglial activation after METH exposure [60]. It has been hypothesized that METH-induced microglial activation is controlled by DA-quinone (DAQ), a metabolite of DA, as it activates microglia in a dose- and time-dependent manner and because the reduction of DAQ production prevented (at least partially) microgliosis. Excessive DA released into the synaptic cleft may directly excite localized microglia and begin a hazardous signal cascade, demonstrating the critical function of DA in neuroinflammation [61]. Toll-like receptor 4 (TLR4) found on microglia is involved in the immune monitoring of pathogens, and foreign small molecules are thought to be the underlying mechanism of METH-induced microglial activation [61]. Microglia activation may also be mediated through the sigma-1 receptor and subsequent ROS production and activation of the mitogen-activated protein kinase (MAPK) and PI3K/Akt pathways [62]. Activated microglial cells release neurotrophic and cytotoxic mediators, including cytokines, which cause inflammation and neurotoxicity [49]. METH stimulates nuclear factor-kappa B (NF- $\kappa$ B), causing its translocation to the nucleus and enhancing the production of pro-inflammatory cytokines such as interleukin 6 (IL-6), interleukin 1 (IL-1), tumor necrosis factor (TNF), monocyte chemoattractant protein 1 (MCP-1), and cellular adhesion molecule (ICAM-1) [63-67] (Fig. 6)

#### ***1.3.3.2 Role of astrocytes***

Astrocytes are supportive cells present in the CNS that create intricate networks throughout the spinal cord, all brain regions, and neuronal layers [68]. Astrocytes and neurons are joined by

gap junctions and form lengthy processes with end-feet that engage in the control of blood flow, nutrition transport, and synaptic connection [69]. As a result of the peri-synaptic structure known as the "tripartite synapse," astrocytes exchange information with pre- and postsynaptic components, maintain proper homeostasis of ions and neurotransmitters, and participate in neuron modulatory signaling to modulate circuit activity [70]. Increasingly, it is acknowledged that astrocytes play a crucial role in gliotransmission [71]. Gliotransmission releases multiple transmitters at synapses via exocytosis, which is believed to regulate elements of brain metabolism. Astrocytes release gliotransmitters, such as ATP, Glu, and d-serine, which can result in signaling to neurons, increases, and reductions in neuronal excitability, regulation of synaptic transmission, and synaptic plasticity [72, 73]. Under pathological situations, the neuron–astrocyte regulation system is disturbed, resulting in aberrant activation of astrocytes and an increase in inflammatory processes, which disrupt specific communication between neurons and astrocytes, hence affecting synaptic activity and function.

As with microglia, astrocytes contribute to MUD [74]. METH treatment frequently results in the loss of TH-positive terminals and an increase in glial fibrillary acidic protein (GFAP)–containing astrocytes in the striatum [75, 76]. Initially, it was theorized that the loss of DA terminals would enhance the oxidation of DA and the formation of free radicals, resulting in astrogliosis [77]. However, it was later shown that upregulation of GFAP–containing astrocytes might occur without reduction of TH-positive terminals indicating that METH may have a direct effect on astrocytes [78] (Fig. 6). Indeed, acute exposure to METH causes oxidative stress in primary cortical astrocytes [79] and dramatic alterations in the transcriptional signature through the upregulation of MAP2K5, GPR65, and CXCL5 [80]. In addition, a recent study found that astrocyte-derived lipocalin-2 (LCN2) is predominantly expressed in the hippocampal following

METH exposure and can induce neuronal death both *in vitro* and *in vivo*, whereas inhibition of LCN2 can reduce METH-induced mitochondrion-related neuronal death in cultures of primary rat neuron and animal models [81]. Furthermore, METH-induced astrocyte senescence drives neuronal toxicity and contributes to the development of neurodegenerative diseases [82].

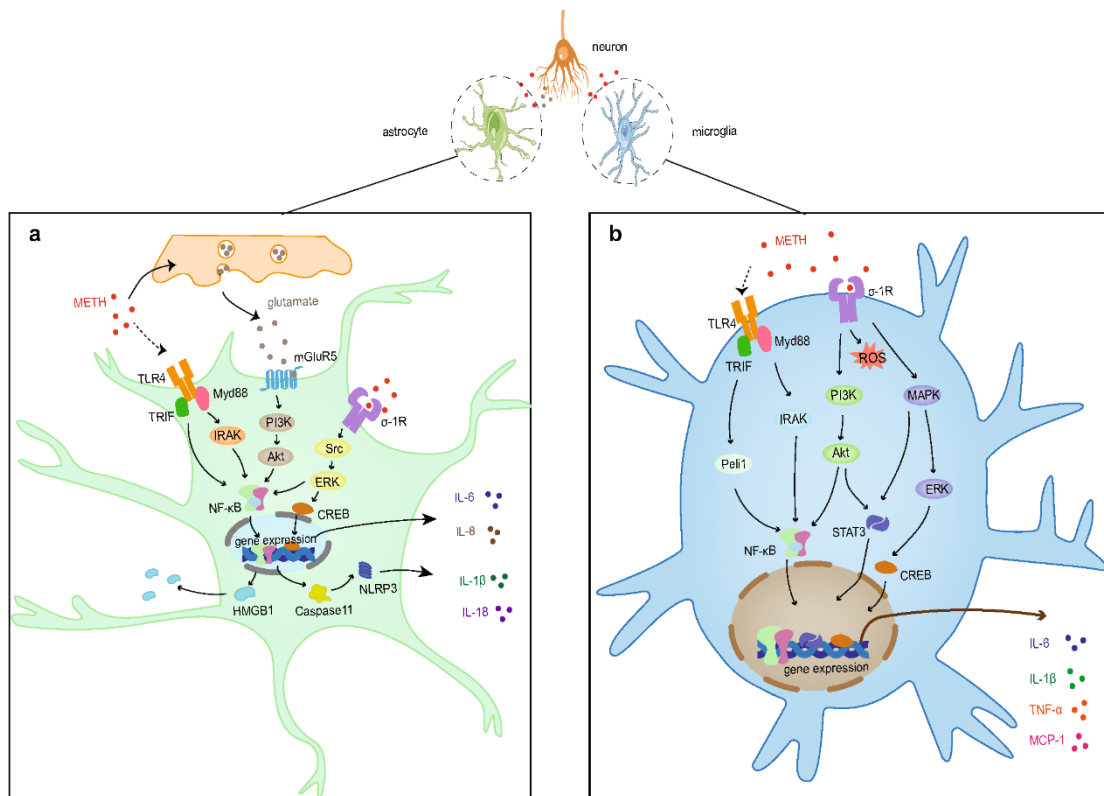


**Figure 6. Role of astrocytes and microglia in METH-induced neuroinflammation.** Reprinted from Ref. [67] with permission.

Significant astrocyte death occurs following reactive astrogliosis [83]. These dying astrocytes can then kill neighboring cells, implicating astrocyte apoptosis as a major hallmark of brain pathologies [84]. Astrocyte apoptosis can exacerbate neuronal death and CNS pathology as the exchange of neurotrophins between astrocytes and neurons through gap junctions is essential for neuronal survival. Indeed, compromised astrocyte function and survival have negatively impacted neurons in neurodegenerative diseases [85]. Therefore, it is of utmost importance to

better understand the mechanisms behind astrocyte death in MUD to develop potential new therapies.

## **1.4 Integrins**

Integrins are the most extensive family of cell-adhesion molecules, composed of non-covalently linked alpha ( $\alpha$ ) and beta ( $\beta$ ) subunits [23, 26, 28, 29]. The 18  $\alpha$  and 8  $\beta$  integrin subunits form at least 24 heterodimeric ( $\alpha/\beta$ ) receptors, each of which binds to its limited subset of extracellular matrix (ECM) and/or cell-surface ligands [85, 86]. These comprise structural ECM proteins like collagens, fibronectins, and laminins, as well as provisional ECM proteins like fibrin, vitronectin, tenascin, and osteopontin, which are deposited during tissue remodeling and thrombotic events. While integrins are found in almost every tissue, each integrin heterodimer's repertoire and ligand-binding activity is determined by the tissue and cell type that expresses it [87, 88]. No cell expresses all integrins. Instead, cells tend to express integrins compatible with the ECM ligands found in the microenvironment [89]. Notably, these variations in the expression of specific integrin heterodimers have been linked to the control of cell survival throughout tissue remodeling processes during development and diseases [90, 91]. The local ECM works as a trophic factor because the changing composition of the ECM determines which integrins may be ligated. Given the ECM's essential function, it is somewhat unsurprising that disruption of integrin contact with the ECM (i.e., ligand deprivation) impairs cell survival.

### **1.4.1 Integrin Structure**

Integrin  $\alpha$  and  $\beta$  subunits are type I transmembrane proteins with a large extracellular tract, one transmembrane segment, and a small cytoplasmic tail (except for the  $\beta_4$  subunit contains a long cytoplasmic tail) [92]. Together, the C-termini of the  $\alpha$  and  $\beta$  subunits form a globular ligand-binding headpiece. The leg segments link this headpiece to the plasma membrane. This intricate

multidomain structure is a distinguishing feature of integrins [93]. Activation of chemokine receptors and several growth factor receptors initiates an intracellular signaling cascade that finally impacts the cytoplasmic tails of integrins. The binding of signaling molecules (e.g., talin and kindlin) to the integrin cytoplasmic domains evokes the separation of the integrin cytoplasmic tails [94]. Dissociation of the  $\alpha$  and  $\beta$  subunit cytoplasmic tails is connected conformationally to the separation of the transmembrane domains from the membrane-proximal regions of the extracellular domains, generating a switchblade-like opening that results in an expanded conformation [95, 96]. During extension, the hybrid domain moves outward, an action connected to the piston-like downward movement of the C-terminal helix of domain I. The downward migration of the C-terminal  $\alpha$  helix of the  $\beta$ I domain induces the conversion of the MIDAS into an

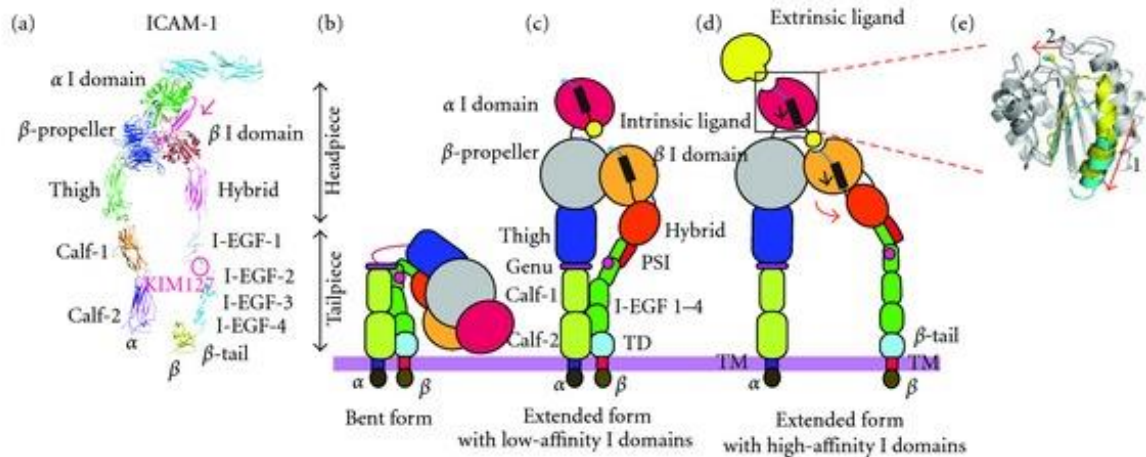


**Figure 7. Integrin structures and domains and conformational changes.** (a) Integrin extracellular segment model. (b)–(e) Global conformational changes between the bent (b), intermediate (c), and extended (d) conformations. Blowups (e) showing the structures of the high- and low-affinity conformations of the alpha I domain. A piston-like downward shift of the C-terminal helix (arrow 1) is allosterically linked to the conversion of the MIDAS to the high-affinity configuration (arrow 2). Superposition of the high- (blue) and closed low- (yellow) affinity I domain is shown. Regions undergoing significant conformational changes are shaded in color, whereas regions not undergoing such changes are shaded in gray. Reprinted from Ref. [93] under the Creative Commons Attribution License (CC BY).

open conformation, allowing it to bind to the C-terminal region of the  $\alpha$ I domain as an "internal" ligand [97]. This interdomain contact causes a downward shift of the C-terminal helix of the alpha I domain, so transforming it into a high-affinity conformation that binds to an "external" ligand (Fig. 7).

## **1.4.2 Integrins in the CNS**

### ***1.4.2.1 Neuronal Synapse Formation***

Integrins mediate neuron-to-neuron and astroglia-to-neuron interactions in the CNS [98, 99]. Integrins have been found to regulate synaptic plasticity at the neuron-to-neuron contact at synapses. Using integrin inhibiting Arg-Gly-Asp (RGD) peptides given to hippocampal slices, it has been demonstrated that integrin inhibition inhibits LTP [100, 101]. Integrins not only reinforce the physical contact between neurons at the synapse but also participate in the signaling that happens at the interface. The functions performed by synaptic integrins in the control of synaptic plasticity have been validated and substantiated by several studies employing integrin knockout mice [102-106].

Integrins are believed to play a crucial role in mediating astroglia-neurons connections at the tripartite synapse [99]. Thrombospondins, an ECM secreted by astrocytes to synapses, interact not only with the  $\alpha$ 2 $\delta$ 1-1 subunit of the voltage-dependent  $\text{Ca}^{2+}$  channel on neurons but also with the integrins on astrocytes and neurons. The first connection conveys a crucial signal for synaptic formation, whereas the second interaction may facilitate the attachment of glial cells to neurons [107]. It has been proven that neurons can generate synapses but not receive them unless they are in touch with astrocytes [108]. Integrin  $\alpha$ V $\beta$ 3 on astrocytes has been found to bind to the widely expressed glycoprotein Thy-1 on neurons [109]. When astrocytic integrins link to neuronal Thy-1, they release a signal that stimulates astrocytes. Upon attachment to astrocytic integrins, neuronal

Thy-1 receptors cluster and produce a signal inhibiting neurite development and retracting neuronal processes [110]. This bidirectional astrocyte-neuron communication via integrins may play a crucial role in axon restoration after neuronal injury. The  $\beta 1$  integrin on neurons enables their interface with local astrocytes, allowing the transfer of signals that trigger neuronal PKC activation, globally promoting excitatory synaptogenesis [111].

#### ***1.4.2.2 Glial Migration***

During astrocytosis, astrocytes become activated and concentrate at damage sites, producing inflammatory mediators such as ATP, cytokines, and chemokines [112]. Astrocytosis have both been involved in the etiology of several CNS pathologies [113]. As  $\beta 1$  integrins govern astrocyte migration,  $\beta 1$  integrins and matrix metalloprotease-2 (MMP-2) are colocalized at the leading edge of migratory astrocytes [114]. While matrix metalloprotease-2 (MMP-2) cleaves and degrades the network of ECM proteins, integrins promote cell migration, propelling tissues onward. In spinal cord injury, injured neurons release the chemokine MCP-1, which attracts and activates astrocytes [115].  $\beta 1$  integrins have also been linked to astrocyte migration to damage sites in the spinal cord [116]. Surprisingly, conditional deletion  $\beta 1$  integrin has been shown to cause partial reactive gliosis, thereby limiting the proliferation of astrocytes after brain injury [117]. Therefore, it seems that  $\beta 1$  integrin-mediated signaling in astrocytes is required to promote their acquisition of a mature, nonreactive state. However, more research is needed to understand the contribution of integrins in astrogliosis.

Schwann cells are a type of glial cells present in the peripheral nervous system. Schwann cells move to damaged neurons to facilitate tissue healing, especially remyelination in demyelinated nerves that have been damaged. Although integrins facilitate Schwann cell migration, astrocyte-produced aggrecan inhibits it [118]. Schwann cells create a laminin-

deposited, structured basal lamina when wrapping and myelinating neuronal axons, where  $\beta 1$  and  $\beta 4$  integrins interact with laminin. The Schwann cell-specific conditional deletion of  $\beta 1$  integrins impairs the development of normal axonal processes [119]. Schwann cell-specific  $\beta 4$  integrin deletion subsequently demonstrated that  $\alpha 6\beta 4$  integrin serves the primary role in axonal regeneration and subsequent myelination [120].

#### ***1.4.2.3 Hedgehog Pathway***

The glycoprotein Sonic hedgehog (Shh), a major ligand in the hedgehog signaling system, plays a crucial role in vertebrate organogenesis [121]. Shh has also been linked to neural development in vertebrates [122]. Shh controls integrin activity, hence dictating the adherence of neural epithelial cells [123]. Coordination of neural tube morphogenesis has been linked to Shh-regulated integrin activity in neural progenitor cells. Astrocytes are a major source of Shh secretion in the milieu of the BBB [124]. Shh produced by astrocytes binds to Hedgehog receptors expressed on BBB-endothelial cells throughout the embryonic phases of the neurovascular unit. This astrocytic communication to BBB endothelial cells via Shh promotes BBB development, preserving barrier function. Migration and adhesion of BBB-endothelial cells may include Shh-regulated integrin activity. In addition, in the adult stage, Shh secreted by astrocytes inhibits ICAM-1 expression in endothelial cells, hence dampening endothelial proinflammatory responses such as those observed in multiple sclerosis.

#### **1.4.3 Integrins, Cell Survival, and Anoikis**

Integrins, in their capacity as the primary cellular receptors for the ECM, help mediate cell anchoring to the ECM substrate and control cell shape [125]. The most severe instance of integrin 'ligand-deprivation' happens when a cell loses all contact with its substrate, leading to programmed cell death [126]. The name "anoikis" is used for programmed cell death caused by the lack of

substrate ECM interaction [127]. Direct stimulation with the cytokine Scatter Factor or indirect activation of growth factor receptor signaling pathways with oncogenes such as v-Src or ha-Ras reduces anoikis in certain cells. Anoikis is inhibited similarly by integrin-mediated attachment to RGD-containing ligands, but not by solubilized RGD peptides. Furthermore, substrate attachment without integrin engagement leads to programmed cell death, but integrin-mediated attachment restores cell viability [128]. Even though integrins lack intrinsic kinase activity, tyrosine kinase activity has been highlighted as an essential element in ECM-mediated survival. Nonetheless, integrin attachment to substrate ECM elicits signaling via related nonreceptor tyrosine kinases, such as members of the focal adhesion kinase (FAK, PYK2) and Src kinase families, thereby offering a mechanism for how integrins govern cell viability [129].

#### **1.4.4 Integrins as Trophic Factors**

Integrins influence cell survival in several other ways. The absence of a certain integrin (or integrins) can impede adhesion to a specific ECM substrate. Since each integrin heterodimer binds to a small selection of ECM ligands, attachment to any ECM component typically needs the expression of at least one kind of integrin heterodimer that is compatible with that ECM protein. For instance, integrins  $\alpha3\beta1$ ,  $\alpha6\beta1$ ,  $\alpha6\beta4$ , and  $\alpha7\beta1$  are the most prevalent laminin-binding integrins *in vivo*, and they are frequently detected on cells in contact with laminin. Three of these laminin-binding integrins may be found on epidermal epithelial cells close to (laminin-rich) basal lamina. These integrins are related to keratinocyte detachment from the lamina, differentiation, and cell death [91]. The repertoire of integrin heterodimers expressed on a cell is matched to the ligands present in its local surroundings.

Integrin ligation induces intracellular modifications needed for 'integrin-specific' signaling and cell survival. Cell spreading is a global phenomenon driven by integrin ligation in which a

spheroid cell flattens to expand its surface area with the substrate ECM. Spreading is based on Rho family GTPases signaling to the actin cytoskeleton, which induces the expansion of lamellipodia and pseudopodia [130]. This capacity to connect and spread ECM has a beneficial effect on the survival of cells in general. The canonical integrin-activated signaling pathway involves the activation of an apical nonreceptor tyrosine kinase such as FAK37 or an Src-family kinase [131, 132], which promotes the activation of small GTPases of the Ras and Rho families, resulting in the activation of MAPK (mitogen-activated proteins kinase) cascades [133] (Figure 8). In addition to direct impacts on cytosolic and cytoskeletal components, these signaling cascades govern transcription activities in the cell's nucleus and have major consequences on cell survival [134]. Several variables directly influencing cell resistance to apoptosis have been connected to integrin-mediated signaling, including cell cycle progression [87] and p53 activation [135], Bcl-2 family protein expression [136], death receptor and death ligand expression [137], and modulation of the PI3K/Akt/GSK axis [138]. In addition, these signaling events control the cellular synthesis of extracellular proteins, such as osteopontin [139], and intracellular adaptors, such as osteoprotegerin [140] and c-flip [137], which govern cell survival directly or indirectly.

Antagonism or downregulation of a variety of integrin subunits and heterodimers, including  $\alpha 2\beta 1$  [141],  $\alpha 4\beta 1$  [142],  $\alpha 5\beta 1$  [143],  $\alpha 6\beta 4$  [144],  $\alpha V\beta 3$  [145],  $\beta 1$  [146], and  $\beta 3$  [147], have been shown to induce apoptosis in different cells. Apoptosis, in these cases, usually happens because of the lack of the ability integrins to bind to ECM proteins and initiate downstream cell survival pathways such as PI3K/Akt and Ras/Raf/MEK pathways. Loss of ECM ligation to integrins results in disengagement of these cell survival signals with subsequent release of cytochrome C from mitochondria and activation of executioner caspases (caspase-3, -6, and -9), ultimately leading to anoikis [148] (Fig. 8).

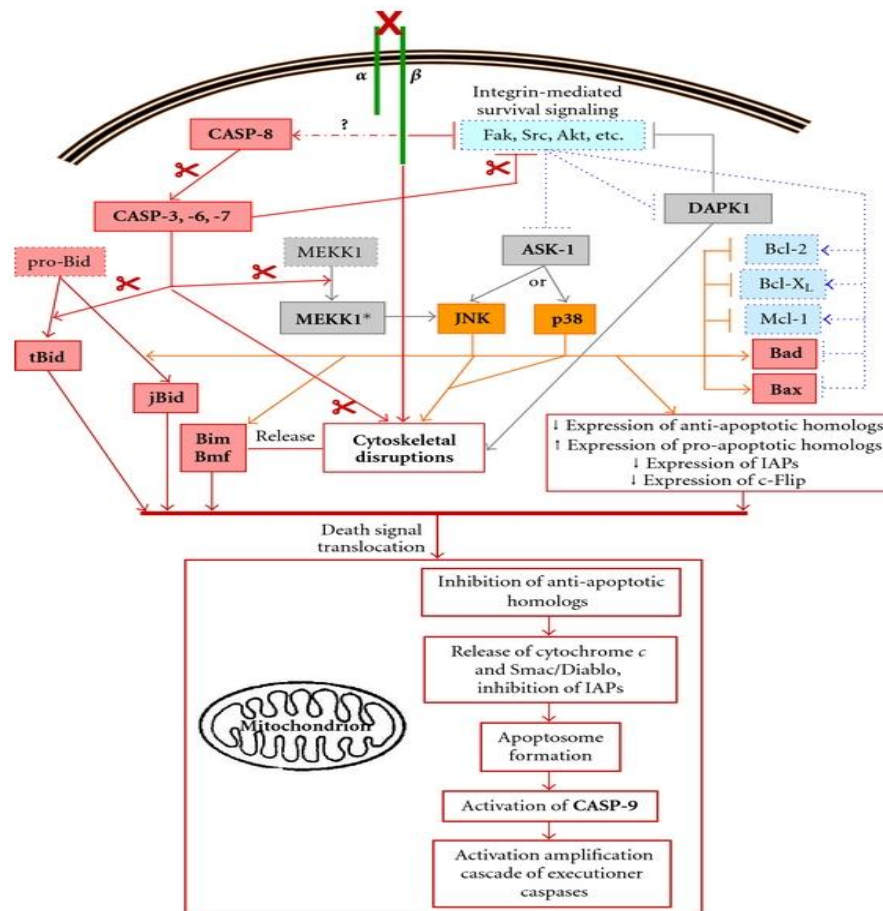


**Figure 8. Common pathways of anoikis induction after the loss of integrin-mediated adhesion.** Reprinted from Ref. [148] under the Creative Commons Attribution License (CC BY).

## 1.5 Significance

In the last several years, a significant amount of work has been performed to understand better the pathogenesis behind METH neurotoxicity and the development of associated psychiatric disorders. Nevertheless, significant gaps in research exist, particularly in our understanding of METH's effects on astrocytes and its contribution to the development of psychiatric disorders. The proposed study was, therefore, designed to understand how METH affects astrocyte physiology and causes toxicity. METH neurotoxicity is a multifaceted process, and our study attempted to investigate the alteration of the genetic signature of astrocytes, the expression of integrins, and integrin-mediated apoptosis. We also aimed to understand the prevalence of psychiatric disorders in the METH-abusing population and the identification of shared genes between METH-treated astrocytes and psychiatric disorders to discover potential targets. The present study was based on the central hypothesis that METH alters genetic signatures in astrocytes, decreases the expression of integrins, and causes apoptosis through the involvement of integrins. The long-term goal of the current study is to develop a therapeutic strategy to block METH-induced changes in astrocytes and integrin downregulation, which can tackle METH neurotoxicity and development of psychiatric disorders. The following specific aims were designed to elucidate our hypothesis:

1. To investigate the effects of repeated METH exposure on astrocyte transcriptome using microarray.
2. To explore the effect of AMPH on the expression levels of integrin subunits expressed on astrocytes and the contribution of expression changes in integrin subunits on astrocyte survival.

3. To examine the prevalence of psychiatric disorders in METH-abusing individuals using the Cerner Health Facts database and identify common gene expression patterns between METH-treated astrocytes and psychiatric disorders using microarray data.

The findings in the present study are of clinical importance as understanding altered gene expression in astrocytes can lead to the identification of potential novel gene targets for the treatment of METH-associated psychiatric disorders.

## CHAPTER 2: TRANSCRIPTOME ANALYSIS OF METHAMPHETAMINE-TREATED ASTROCYTES

### 2.1 Introduction

METH is a powerful stimulant drug of abuse. Current patterns of its use do not indicate that the problem is abating. The UN Office on Drugs and Crime reported recently that abuse of amphetamines, including designer drugs such as METH and MDMA, now exceeds that of cocaine and heroin on a global scale [149]. METH neurotoxicity has been under intense study for more than 20 years. Yet, much remains to be learned about how this dangerous drug causes damage to DA nerve endings. Leading theories of its neurotoxic mechanisms revolve around oxidative stress [28]. Drug-induced oxidative stress is an attractive construct that can account for many of the effects of METH on the DA nerve ending, such as inhibition of tyrosine hydroxylase activity and reductions in the DAT and the VMAT, and subsequent neuronal apoptosis. While the modulatory effects of METH on DA neurotransmission and its neurotoxicity in the CNS are well studied, its effects on modifying glial cell homeostasis, particularly astrocytes, to affect dopaminergic neurotoxicity have also attracted considerable attention in recent years.

Astrocytes are the most abundant population of cells within the CNS, and the structural diversity and functional complexity of cortical astrocytes is a distinguishing feature of the primate brain [150]. Astrocytes form a functionally connected network through a series of gap junctions and have several functions in maintaining the BBB and managing cerebral blood flow; regulating ion, water, and neurotransmitter homeostasis; and influencing synaptic transmission as a component of the tripartite synapse [151]. Astrocytes can respond to CNS injuries by adopting immune cell characteristics, and during healing, astrocytes undergo a range of genetic and functional alterations [113]. Recently, there has been a paradigm shift toward understanding the

critical involvement of astrocytes in the pathophysiology of neurodegeneration. Altered astrocyte physiology has also been linked with several neurodegenerative diseases such as AD, Huntington's disease, and aging brain [152]. Astrocytes also contribute to altered neuronal activity in several frontal cortex pathologies, such as ischemic stroke and epilepsy [153]. Moreover, astrocytes interact with neuronal cells to influence various biological activities that contribute to METH-induced neurotoxicity. Therefore, a greater understanding of how METH impacts astrocytes should provide new insights into molecular mechanisms of METH.

While studies have investigated the implications of acute METH treatment in astrocytes [80, 154], very few studies exist that detail the effect of repeated METH exposure on astrocytes. Therefore, we analyzed global changes in astrocyte transcriptome in the present study using microarray following repeated exposure to METH. These experiments represent a logical first step in assessing the role of astrocytes in METH-induced neurotoxicity and suggest that changes in the genetic signature of astrocytes could underlie METH neurotoxicity.

## **2.2 Materials and Methods**

### **2.2.1 Materials**

Dulbecco's Modified Eagle's medium (DMEM) (with L-Glutamine, 4.5g/L Glucose and Sodium Pyruvate), MEM nonessential amino acids (100X), sodium bicarbonate (7.5% solution), and gentamicin sulfate (50 mg/mL solution) were purchased from Corning Inc. (Corning, NY). Heat-inactivated fetal bovine serum (FBS) was purchased from R&D Systems, Inc. (Minneapolis, MN). Methamphetamine hydrochloride (METH) was purchased from Sigma-Aldrich (St. Louis, MO). RNeasy Mini Kit was purchased from QIAGEN Inc. (Germantown, MD).

### 2.2.2 Cell Culture

Human fetal astrocytes (HFA) were kindly provided by Dr. Anuja Ghorpade, University of North Texas (Denton, TX). Experimental use of HFA was approved by the UMKC Institutional Review Board (IRB) and Institutional Biosafety Committee (IBC). Cells were cultured in DMEM supplemented with 1% sodium bicarbonate, 1% nonessential amino acids, 10% (v/v) FBS, and 50 µg/ml of gentamicin sulfate. Cells were cultured in 75 or 150 cm<sup>2</sup> flasks in 15-25 ml complete DMEM and maintained in an incubator at 37° C and humidified air with 5% CO<sub>2</sub>. Cells were passaged after reaching confluency. The cells were incubated overnight to allow them to adhere and treated the following day.

### 2.2.3 Microarray

HFA (passage 3) were plated in a 75 cm<sup>2</sup> cell culture flask at a density of  $1.5 \times 10^6$  cells/flask and treated with 500 µM METH [dissolved in sterile 1X phosphate-buffered saline (PBS)] or 1X PBS (Control) once a day for three days. After three days, media was aspirated, and total RNA was isolated from the cells using the RNeasy Mini Kit. RNA purity and quantity were analyzed using NanoDrop™ ND-1000 Spectrophotometer (ThermoFisher Scientific, Waltham, MA). Quality control of RNA included A<sub>260</sub>/A<sub>280</sub> ratio of 1.7 to 2.3. Subsequent steps of target labeling, fragmentation, hybridization, and scanning were carried out at the Microarray Facility of the University of Kansas Medical Center (Kansas City, KS). Briefly, total RNA was spiked with diluted poly(A) RNA controls from the GeneChip Poly-A RNA Control Kit (ThermoFisher Scientific), and cDNA was synthesized by reverse transcription. Purified double-stranded (ds) cDNA was *in vitro* transcribed to generate biotin-labeled aRNA using GeneChip 3' IVT Plus Reagent Kit (ThermoFisher Scientific) and purified. Purified biotin-labeled aRNA was analyzed for purity and concentration using NanoDrop™ ND-1000 Spectrophotometer. Labeled aRNAs

were then fragmented by heating to obtain optimal assay sensitivity. The size of the fragmentation reaction products was assessed on an Agilent Bioanalyzer using RNA 6000 Nano Kit (Agilent Technologies, Inc., Santa Clara, CA). After confirming successful target preparation, cRNAs were hybridized to Affymetrix GeneChip HG-U133A2.0 arrays in a GeneChip Hybridization Oven 645 (ThermoFisher Scientific) overnight (16 h). Following hybridization, each array was washed and stained with streptavidin-phycoerythrin using a GeneChip Fluidics Station 450 (ThermoFisher Scientific) before being scanned using a GeneChip Scanner 3000 7G. (ThermoFisher Scientific). The GeneChip Command Console (AGCC) (v4.0) was used to generate probe cell intensity data (CEL files) which was then used to generate probe set summarization data (CHP files).

#### **2.2.4 Quality Control**

Quality control (QC) of the microarray data was performed using the *affy* package of Bioconductor, iPathwayGuide (iPG) (v2012) (Advaita Bioinformatics, Ann Arbor, MI), and Transcriptome Analysis Console (TAC) Software (v4.0.2.15) (ThermoFisher Scientific). Following QC parameters were assessed:

*2.2.4.1 Microarray pictures:* A general visual inspection of the spatial distribution of raw intensities on individual array chips was performed to check for inconsistencies.

*2.2.4.2 Density plots and Boxplots:* Relative distributions of each array's (raw, unnormalized) feature intensities were assessed by plotting  $\log_2$  intensities in density plots and boxplots. Normalization is generally required if differences in the shape or center of distribution are observed.

*2.2.4.3 Average Background and Noise (Q) Values:* Average background and noise (Q) values were assessed to account for slight variations in the digitized signal observed by the scanner

as it samples the array's surface. The average background and noise (RawQ) should remain consistent across the experiment and within  $\pm 3$  points of the median.

*2.2.4.4 Percent present:* The proportion of "Present" probe sets in relation to the total number of probe sets on the array was determined. Percent Present (% P) values vary according to various parameters, including cell/tissue type, biological or environmental stimulation, probe array type, and overall RNA quality. The % P values of replicate samples should be comparable. Extremely low % P values may indicate a low-quality sample.

*2.2.4.5 Internal Control Genes (Housekeeping Genes):* Internal control genes, or housekeeping genes, are gene transcripts that are constitutively expressed in most samples. These transcripts serve as internal controls, help monitor the quality of the starting sample (i.e., RNA), and are subject to any variability in the labeling of the sample and hybridization to the array. As housekeeping genes are relatively long, GeneChip contains separate probe sets targeting the 5' and 3' regions of their transcripts. The 3' and 5' signal intensity values were calculated for glyceraldehyde-3-phosphate dehydrogenase (GAPDH), and the 3'/5' ratio was used to measure the quality of the RNA hybridized to the array. The ratio of the signal values of 3' probe set to the 5' probe set should generally be around 1 for GAPDH.

*2.2.4.6 Labeling Controls (Poly-A Controls):* Poly-A RNA controls were used to monitor the entire target labeling process. Each eukaryotic GeneChip probe array includes probe sets from many *B. subtilis* genes not seen in eukaryotic samples, such as lys, phe, thr, and dap. The polyadenylated transcripts are premixed at staggered concentrations. The poly-A RNA controls were diluted and spiked directly into the sample RNA at the beginning of the labeling process, carried through the sample preparation, and evaluated their intensities. The Poly-A controls should have increasing signal values in the order of lys, phe, thr, dap.

2.2.4.7 *Spike controls (Eukaryotic Hybridization Controls)*: Additionally labeled cRNAs were added during the latter stages of the sample preparation protocol to evaluate sample hybridization efficiency on the arrays. BioB was added at a concentration of 1.5pM, corresponding to approximately three transcripts per cell, the lower limit of detection for the system. These transcripts (BioB, BioC, BioD, and CreX) are derived from *B. subtilis* and spiked into the solution before placing them on an array. The intensity of these transcripts is dependent on the hybridization/scanning steps. BioC, BioD, and CreX were spiked at increasing concentrations and should be called Present with increasing signal values.

2.2.4.8 *Principal Component Analysis (PCA)*: PCA was used to decrease the dimensionality of the data to simplify the visualization of patterns, including plate/batch effects. PCA transforms correlated variables into sets of uncorrelated linear combinations of these variables (referred to as principal components, PCs) that contain the most significant amount of information about the data. Geometrically, for the first PC, PCA determines the vector (referred to as the loading vector) along which the greatest variance in the data occurs in the space of the original variables. The scores are the vector projections of the data points. The second PC is determined in the same manner as the first PC, requiring that the second PC's loading vector is orthogonal to the first PC's loading vector (the scores are uncorrelated with those of the first PC). Subsequent PCs are located so that the  $m^{\text{th}}$  PC loading vector is orthogonal to all prior loading vectors. PCA presupposes that high variance has a significant structure, that the principal components are orthogonal, and that the principal components are linear [155].

### **2.2.5 Normalization and Differential Gene Expression**

The CEL files that passed QC were normalized using the GCRMA algorithm in iPG. The background adjustment in GCRMA consisted of three sequential steps: (1) optical background correction, (2) probe intensity adjustment through non-specific binding (NSB) utilizing affinity information and optical noise-adjusted MM intensities, and (3) probe intensity adjustment through gene-specific binding (GSB), where NSB-adjusted PM intensities are further corrected for the effect of PM probe affinities [156].

After normalization, differentially expressed genes (DEGs) were determined using iPG to assess transcriptome changes induced by METH treatment. The comparison was performed between Control and METH-treated samples using one-way ANOVA. DEG selection criteria was set to  $\log_2$  fold change of 0.6 (~ 1.5-fold change in linear scale),  $p$ -value  $< 0.05$ , and adjusted  $p$ -value [false discovery rate (FDR) or  $q$ -value]  $< 0.05$ .

### **2.2.6 Pathway Analysis**

The effect of METH treatment on biological pathways was analyzed with iPG, which evaluates pathways using the "Impact Analysis" approach [157-159]. Impact analysis uses two pieces of evidence: 1) the over-representation of DEGs in a specific pathway and 2) the perturbation of that pathway determined by propagating observed expression changes throughout the pathway topology. These factors are represented by two distinct probability values,  $pORA$ , and  $pAcc$ , which are then merged to provide a unique pathway-specific  $p$ -value. The underlying pathway topologies are derived from the Kyoto Encyclopedia of Genes and Genomes (KEGG) database (Release 100.0+/11-12, Nov 2021) [160].

The first probability,  $pORA$ , reflects the likelihood of getting more than or equal to the number of DEGs seen by random chance in a particular pathway [161]. Consider the following

scenario: there are  $N$  genes tested in the experiment, with  $M$  of them on the provided route.  $K$  out of  $M$  genes were determined to be differentially expressed based on the user-defined a priori selection of DEGs. Based on the hypergeometric distribution, the chance of finding precisely  $x$  DEGs on the given pathway is computed using the following formula:

$$(1) \quad P(X = x|N, M, K) = \frac{\binom{M}{x} \binom{N-M}{K-x}}{\binom{N}{K}}$$

Due to the discrete nature of the hypergeometric distribution, the probability of randomly detecting less than  $x$  genes on a given route may be computed by adding the odds of randomly observing 0, 1, 2, ...,  $x-1$  DEGs on the pathway:

$$(2) \quad p_u(x-1) = P(X = 1) + P(X = 2) + \dots + P(X = x-1) = \sum_{i=0}^{x-1} \frac{\binom{M}{i} \binom{N-M}{K-i}}{\binom{N}{K}}$$

iPG calculates the probability of randomly observing several DEGs on the given pathway that is greater than or equal to the number of DEGs obtained from data by computing the over-representation p-value:  $pORA = p_o(x) = 1 - p_u(x-1)$ :

$$(3) \quad p_u(x) = 1 - \sum_{i=0}^{x-1} \frac{\binom{M}{i} \binom{N-M}{K-i}}{\binom{N}{K}}$$

The second probability, pAcc, is determined using the total amount of accumulation detected in each pathway. A perturbation factor is calculated for each gene along the route using the following formula:

$$(4) \quad PF(g) = \alpha(g) \cdot \Delta E(g) + \sum_{u \in \mathcal{E}} \beta_{ug} \frac{PF(u)}{N_{ds}(u)}$$

In Equation 4,  $PF(g)$  denotes the perturbation factor for gene  $g$ ,  $\Delta E(g)$  is the signed normalized measured change in gene  $g$ 's expression, and  $\alpha(g)$  denotes an a priori weight depending

on the gene's type. The last term is the total of perturbation factors for all genes  $u$  that are immediately upstream of the target gene  $g$ , normalized by the number of downstream genes for each such gene  $N(u)$ . The value of measures the interaction intensity between the genes  $g$  and  $u$ . The sign of indicates the nature of the interaction: positive for activation-like signals and negative for inhibitory signals. Following that, iPG determines the accumulation at the gene level,  $Acc(g)$ , as the difference between the perturbation factor  $PF(g)$  and the observed log fold-change:

$$(5) \quad Acc(g_i) = PF(g_i) - \Delta E(g_i)$$

All perturbation accumulations are calculated concurrently by solving the system of linear equations formed by combining Equation 4 for all genes on a specific pathway. After computing all gene perturbation accumulations, iPG calculates the pathway's overall accumulation as the sum of all absolute accumulations of the genes in the pathway. The bootstrap analysis is used to determine the significance of attaining a total accumulation (pAcc) at least as large as obtained only by chance.

Fisher's method is used to integrate the two pieces of data, pORA, and pAcc, into an overall pathway score. The adjustments in the p-value for multiple comparisons is made using FDR and Bonferroni corrections.

### **2.2.7 Gene Ontology Analysis**

The Gene Ontology (GO) Consortium maintains a dynamic, regulated vocabulary for annotating genes that are based on three distinct ontologies: cellular components (CC), molecular functions (MF), and biological processes (BP) [162]. For each GO term, the number of DEGs annotated to the term was compared to the number of DEGs expected just by chance using the iPG and Gene Ontology Consortium database (2021-Nov 4 Release). iPG uses an over-representation approach to compute the statistical significance of observing at least the given number of DEGs.

The p-value was calculated using the hypergeometric distribution described for pORA in the pathway analysis section (see section 2.2.6) and corrected for multiple comparisons using FDR.

The conventional enrichment approach assumes that all GO keywords are independent. Each gene annotated to a GO keyword also has its ancestors annotated. As a result, the enrichment strategy counts each gene numerous times by propagating it up the GO hierarchy from the most particular phrase to the root of the ontology. This approach creates duplication into the study and classifies many generic and uninformative words as necessary. To circumvent this constraint, iPG provides two more complex pruning methods: *high specificity pruning* and *the smallest common denominator pruning*. The approach of *high specificity pruning* determines the most specific GO keywords linked with the collection of DEGs. Consider the branches BP1 = "induction of apoptosis by intracellular signals" and BP2 = "induction of apoptosis by extracellular signals," which are subsets of BP3 = "induction of apoptosis." If enough DEGs are related to BP1 and BP2, they will be classified as significant by high specificity pruning. The *smallest common denominator pruning* strategy determines the GO words that best encompass the collection of DEGs, sometimes merging the relevance of two or more terms into a single common parent. In the above example, this pruning strategy may indicate BP3 as important since it is the most precise biological term that encompasses all DEGs that contribute to the significance of BP1 and BP2.

### **2.2.8 Upstream Regulatory Analysis**

The expected upstream gene regulators were identified using the iPG. The analysis used experimental DEG enrichment data in conjunction with the Advaita Knowledge Base (AKB) (v2012) and STRING (v11.0) database. The prediction of upstream regulators is based on two types of information: i) the enrichment of differentially expressed genes from the experiment and ii) a network of regulatory interactions from the databases. The network is a directed graph in

which the nodes represent genes, and the edges represent regulatory interactions between two genes. A signed edge in this graph consists of a source gene, a target gene, and a sign to indicate the type of signal: activation (+) or inhibition (-). To create the network, the analysis selects only those edges observed in the literature with at least a medium confidence (evidence score greater than or equal to 400). The analysis considers two hypotheses:

HA - The upstream regulator is *activated* in the condition studied.

HI - The upstream regulator is *inhibited* in the condition studied.

The analysis divides the set of all the genes obtained from the NCBI Gene database or AKB into several subsets based on the measurements in the experiment and the definitions shown in Fig. and Fig. Let the sign of a measured DEG be the sign of the log fold change value: (+) for upregulated genes and (-) for downregulated genes. A gene is a target gene if it corresponds to a node in the network that has at least one incoming edge. A *consistent gene* is defined as a target DEG such that the sign of the gene is consistent both with the type of the signal and with the hypothesis considered. Formally, by definition, a target DEG  $g$  is consistent with Hypothesis HA if and only if an incoming edge  $e$  exists such that  $sign(g) = sign(e)$ . In other words, this describes the situation when the upstream regulator is predicted as activated, the signal is activation, and the target DEG is upregulated, or the signal is inhibition, and the target DEG is downregulated (see panel A in Fig. 9). A target DEG  $g$  is consistent with Hypothesis HI if and only if an incoming edge  $e$  exists such that  $sign(g) \neq sign(e)$ . This second case captures the situation in which the upstream regulator is inhibited, the signal is inhibition, and the target DEG is upregulated, or the signal is activation, and the target DEG is downregulated (see panel B in Fig. 9).

### 2.2.8.1 Upstream Regulators' Z-score

For both research hypotheses, the analysis computes a Z-score for each upstream regulator  $z(u)$  by iterating over the genes in DT ( $u$ ) and their incoming edges  $in(g)$ . The p-value corresponding to the z-score  $P_z$  is then calculated as the one-tailed area under the probability density function for a normal distribution,  $N(0,1)$ .

### 2.2.8.2 Upstream Regulators Predicted as Activated

Here, the research hypothesis considers the upstream regulator as activated is present. For each upstream regulator  $u$ , the number of consistent DE genes downstream of  $u$ ,  $DTA(u)$  is compared to the number of measured target genes expected to be both consistent and DEGs just by chance. iPG uses an over-representation approach to compute the statistical significance of observing at least the given number of consistent DEGs (Fig. 10). The p-values is computed using the hypergeometric distribution.

After computing a p-value for both types of evidence,  $P_z$  and  $P_{act}$ , these two probabilities are combined into one global probability value,  $P_G$  that is used to rank the upstream regulators and test the research hypothesis that the upstream regulators are predicted as activated or present in the condition studied. Since only a positive z-score indicates that the upstream regulator is predicted as activated or present, p-values are only combined for a positive z-score. Moreover, only  $P_z$  for significant z-scores ( $z \geq 2$ ) are combined to avoid introducing false positives. The analysis uses the standard Fisher's method to combine p-values into one test statistic

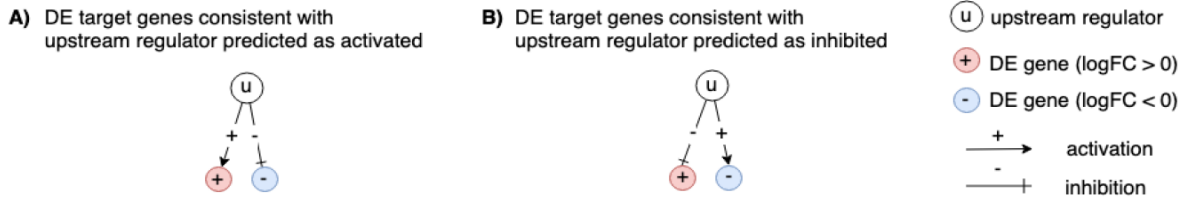


**Figure 9. Target genes consistent with the hypothesis considered.** In panel A, the signs of the DEGs match the signs of their respective incoming edges, increasing the likelihood that the upstream regulator  $u$  is activated. In panel B, the signs of the DEGs are opposite to the signs of their edges, increasing the likelihood that the upstream regulator  $u$  is inhibited.

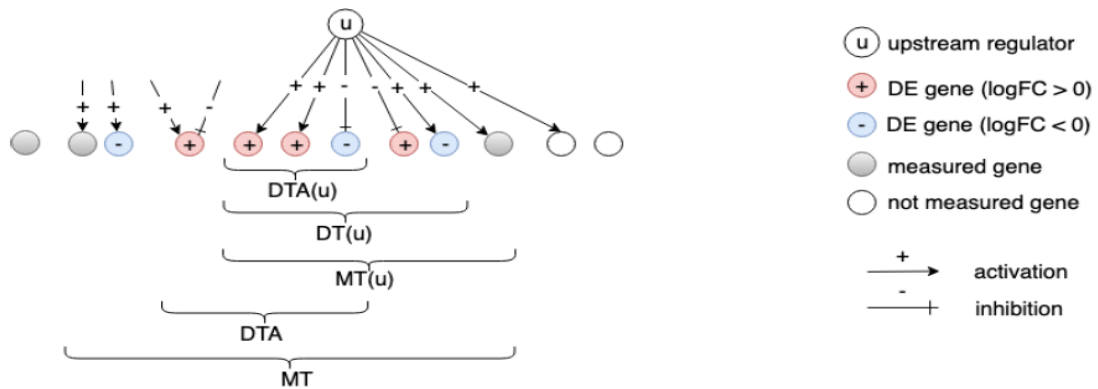


**Figure 10. Graphic for hypothesis HA.** The set of all genes includes the set of measured genes that are also targets in the network, or Measured Targets (MT). We define the subset of "DE Targets consistent with the first hypothesis that the upstream regulators are Activated", DTA. For a selected upstream regulator  $u$ , we have the set of "Measured Targets of  $u$ "  $MT(u)$ , "Differentially expressed Targets downstream of  $u$ "  $DT(u)$ , and the set of "DE targets consistent with the hypothesis HA that  $u$  is Activated"  $DTA(u)$ . The equivalent graphic for the hypothesis HI associated with DTI and DTI( $u$ ) is not shown.

### 2.2.8.3 Upstream Regulators Predicted as Inhibited

In parallel with upstream regulators predicted as activated,  $P_z$  and  $P_{inh}$  are used to predict inhibited upstream regulators. Here, the research hypothesis states that the upstream regulators are inhibited or absent in the conditions studied. For each upstream regulator  $u$ , the number of consistent DEGs downstream of  $u$ ,  $DTI(u)$  is compared to the number of measured target genes expected to be both consistent and DE just by chance. Using Fisher's method described above, the analysis combines  $P_z$  and  $P_{inh}$ , where  $P_z$  is considered only for significant negative z-scores ( $z \leq -2$ ).

## **2.3 Results**

### **2.3.1 Quality Control Assessments**

To elucidate the molecular mechanisms responsible for METH-mediated toxicity in astrocytes, whole-transcriptome analysis was performed using human fetal astrocytes treated with METH for 3 days. The RNA samples were analyzed using the HG-U133A 2.0 GeneChip Microarray. The array covers over 18,000 protein-coding transcripts from 14,500 Entrez genes, with a median of 22 probes per gene, thereby providing excellent genome-wide coverage. After scanning, the arrays were subjected to extensive QC checks before proceeding with the data analysis.

A thorough visual inspection after hybridization and scanning revealed no inconsistencies on individual arrays. No white specking, holes, smudges, areas of saturation, or uneven hybridization were observed (Fig.11). Next, we checked the intensity distributions of individual arrays by plotting a graph of the superimposed log intensity versus density plot for each sample and a boxplot showing the log intensity distribution. All samples displayed similar distributions in their intensities, as evident by the relative similarities in the distribution of the density graph (Fig. 12A) and the medians in the boxplot (Fig. 12B).

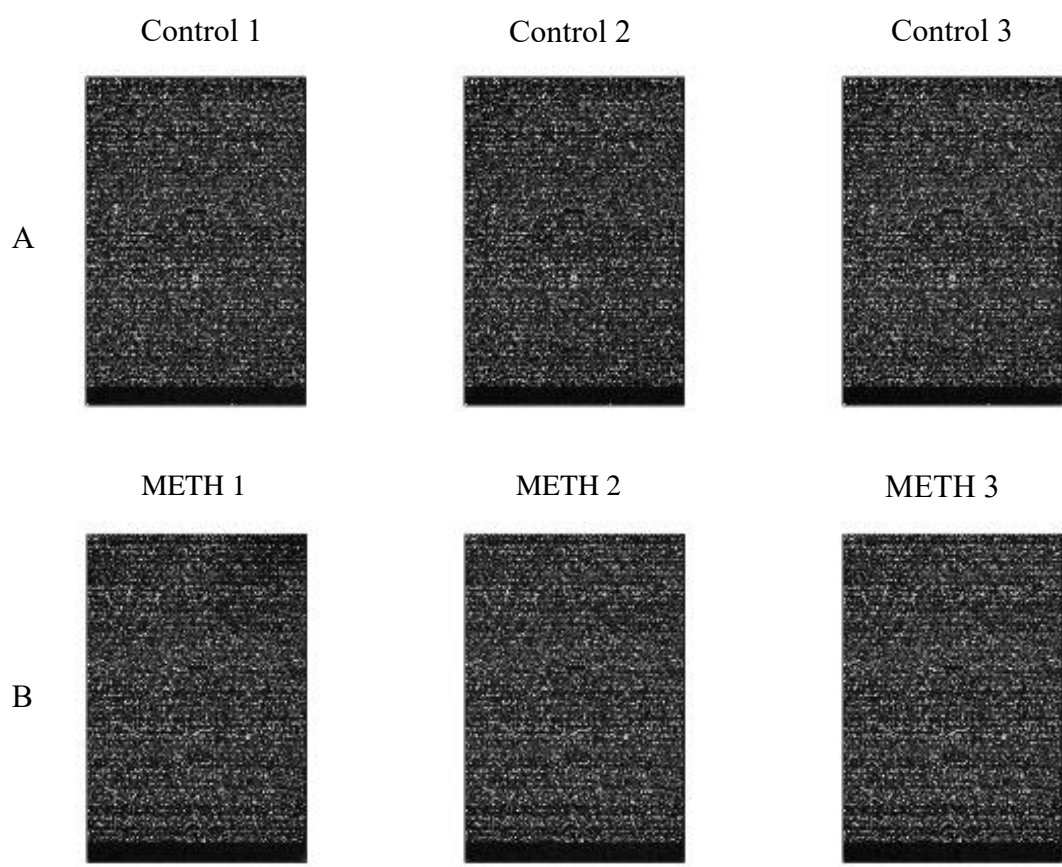


**Figure 11. Microarray pictures of Control (A) and METH (B) samples.**

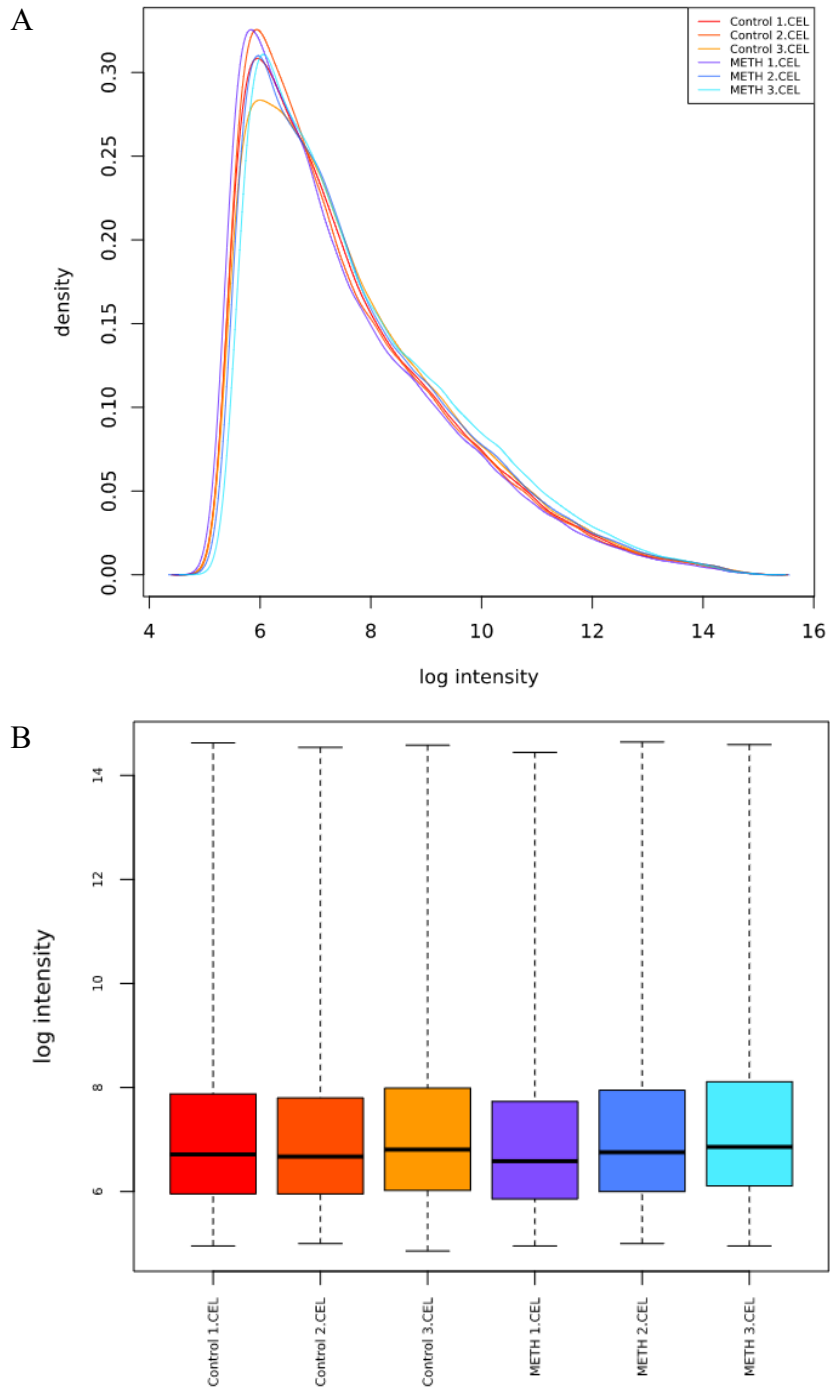


**Figure 12. Density plot (A) and Boxplot (B) of array intensity distributions in Control and METH samples before normalization.** The Control samples are displayed in blue gradient and METH samples are displayed using the red gradient. The arrays are represented by their CEL file names.

Average background and noise (Raw Q) values were consistent (within  $\pm 3$  points of the median) across all 6 arrays (Table 1). The 'mean' average background was  $38.56 \pm 0.23$  SD for Control samples and  $40.05 \pm 2.45$  SD for METH samples. The mean of Raw Q values was 1.25 for Control samples and  $1.33 \pm 0.12$  SD for METH samples. There were no significant differences in the average background (p-value = 0.36) and Raw Q values (p-value = 0.32) between the Control and METH groups indicating no pixel-to-pixel variation among the probe sets of all the arrays. Percent present values were also similar between all the samples, with no statistical difference between the control and METH groups (p-value = 0.26), confirming the hybridization of a uniform amount of cRNAs across all arrays. The 3'/5' ratio values of the internal control gene GAPDH (glyceraldehyde 5-phosphate dehydrogenase) were around 1 for all the samples indicating that no degradation of total RNA occurred during the microarray procedure and transcription of ds cDNA was efficient.

**Table 1. Average background, Raw Q, Percent Present, and 3'/5' GAPDH values of Control and METH samples**

Sample	Average Background	Raw Q	% Present	3' / 5' GAPDH
Control 1	<b>38.31</b>	<b>1.25</b>	<b>62.28</b>	<b>1</b>
Control 2	<b>38.76</b>	<b>1.25</b>	<b>62.92</b>	<b>1.12</b>
Control 3	<b>38.6</b>	<b>1.25</b>	<b>62.43</b>	<b>0.96</b>
METH 1	<b>37.73</b>	<b>1.2</b>	<b>62.61</b>	<b>1.12</b>
METH 2	<b>39.82</b>	<b>1.35</b>	<b>62.83</b>	<b>1.06</b>
METH 3	<b>41.62</b>	<b>1.45</b>	<b>63.72</b>	<b>1.19</b>

Premixed spikes derived from *B. subtilis* were added to the samples to monitor the labeling (Poly-A) and hybridization process. The final concentrations of the labeling controls relative to the total RNA population were 1:100,00 (lys), 1:50,000 (phe), 1:25,000 (thr), and 1:7,500 (dap). The hybridization controls were prepared in staggered concentrations with the final concentrations being 1.5 pM (BioB), 5 pM (BioC), 25 pM (BioC), and 100 pm (Cre). All labeling (Fig. 13A) and hybridization controls (Fig. 13B) were “Present” in all 6 samples with increasing signal values (lys<phe<thr<dap and BioB<BioC<BioD<Cre) reflective of their relative concentrations. These results indicated that efficient target labeling and hybridization occurred during the microarray procedure.

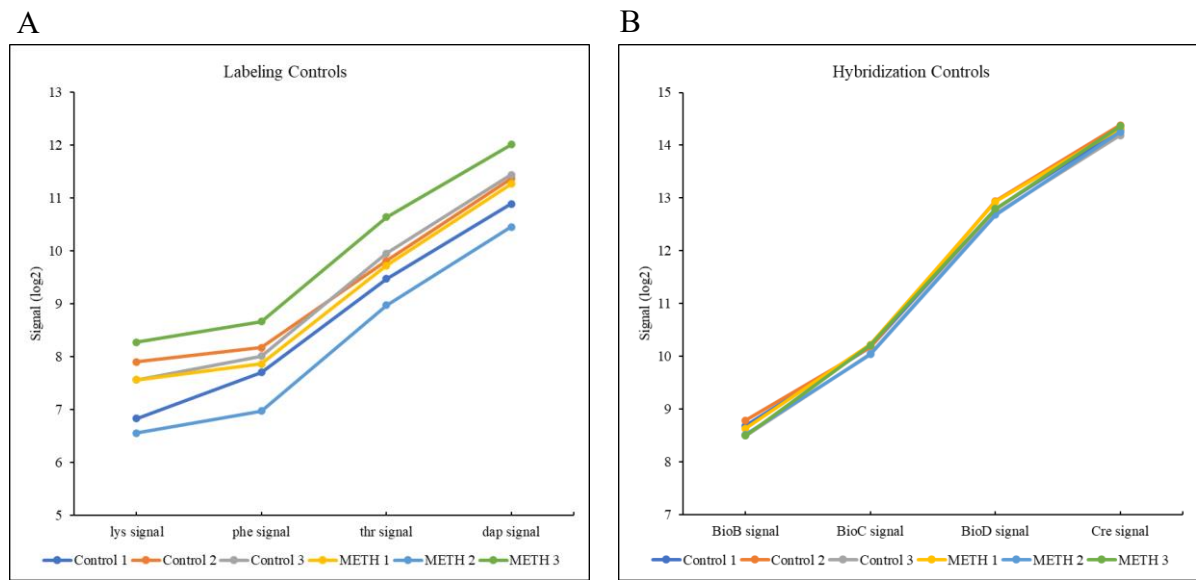


**Figure 13. Signals values (log2) of (A) labeling controls (B) hybridization controls of Control and METH samples. The color code distinguishes the 6 different samples.**

PCA mapping (Fig. 14) was performed on the Control (blue spheres) and METH (red spheres) samples. The principal components accounted for 94.3% of the variance in the datasets.

As expected, PCA revealed that the Control and METH samples form discrete groupings, demonstrating that both the groups have distinct global gene expression profiles.

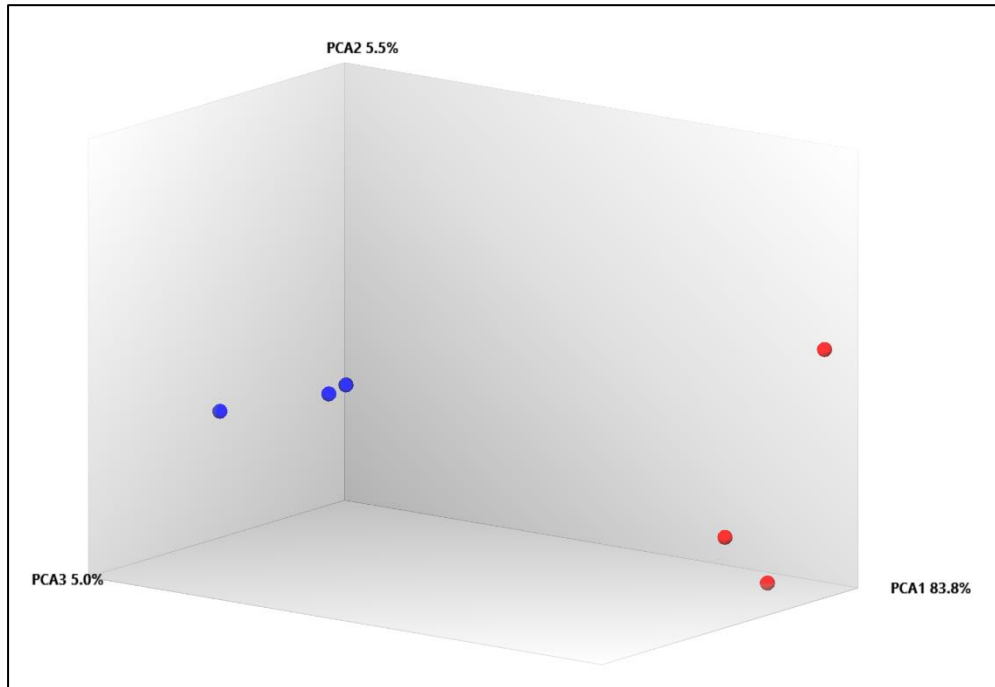


**Figure 14. Principal component analysis (PCA) of Control and METH samples.** PCA was performed on Control (blue spheres) and METH (red spheres) datasets and the resulting scores for the first three principal components are presented.

### 2.3.2 Normalization and Differential Gene Expression

As all samples successfully passed QC, they were subjected to normalization and differential gene expression. All sample CEL files were normalized in iPG using the GCRMA normalization method and presented as a density graph and boxplot. After normalization, the probe-intensity distribution of all samples was similar to one another (Fig. 15A). Accordingly, the quantile distribution and normalized median for all the arrays were the same (Fig. 15B).

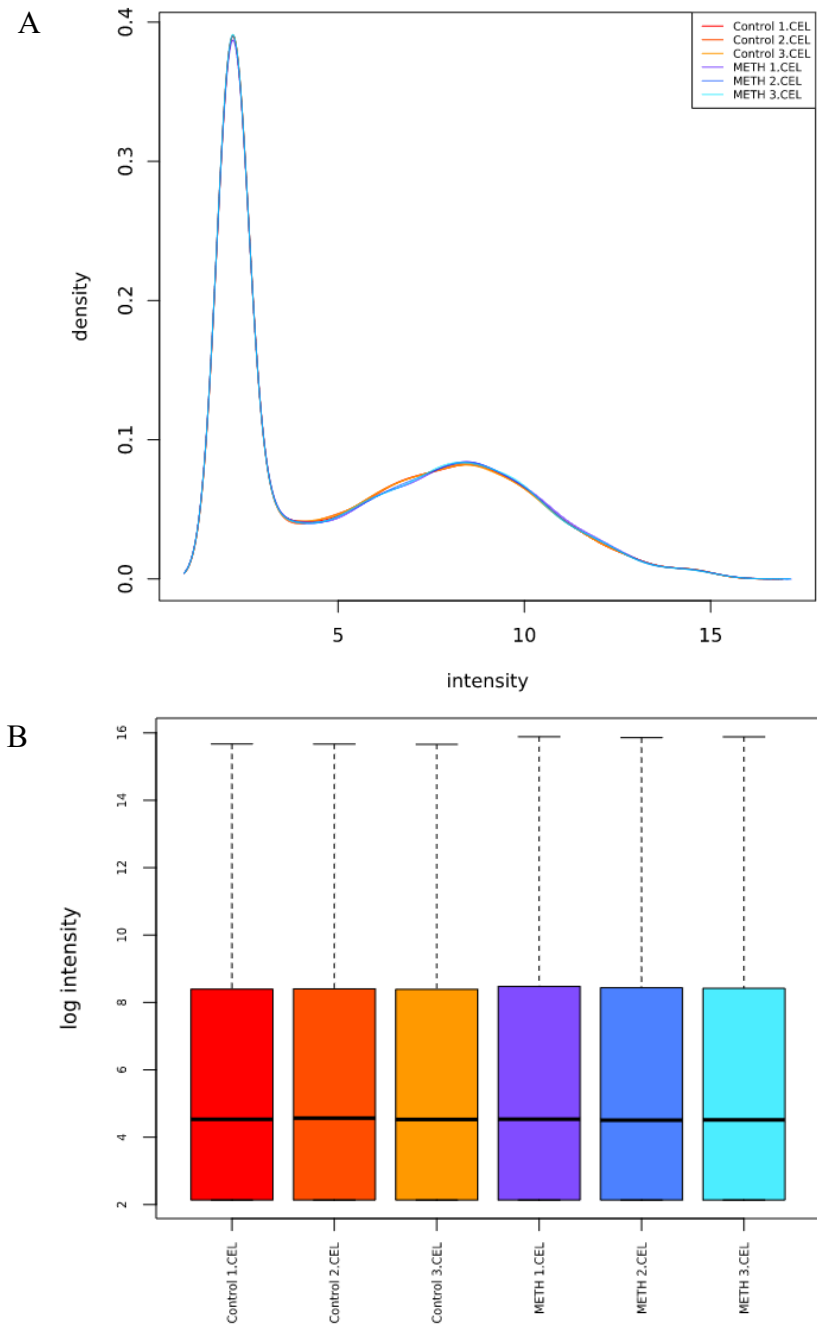


**Figure 15. Density plot (A) and Boxplot (B) of array intensity distributions of Control and METH samples after normalization.** The Control samples are displayed in blue gradient and METH samples are displayed using the red gradient. The arrays are represented by their CEL file names.

Of the 12,399 expressed genes in astrocytes, 1,819 DEGs were identified based on the set threshold of 0.05 for FDR p-value and log<sub>2</sub> fold change value of at least 0.6. The sign of the log<sub>2</sub> fold change was used to classify the DEGs into up- and downregulated groups, with 1,071 DEGs being upregulated and 748 downregulated in response to METH treatment (Fig. 16). Table 2 shows the top 20 upregulated genes with the highest upregulation of 5.71 for the gene DKK1 (dickkopf WNT signaling pathway inhibitor 1). Table 3 shows the top 20 downregulated genes with the highest downregulation of -8.49 for the gene RRM2 (ribonucleotide reductase regulatory subunit M2).

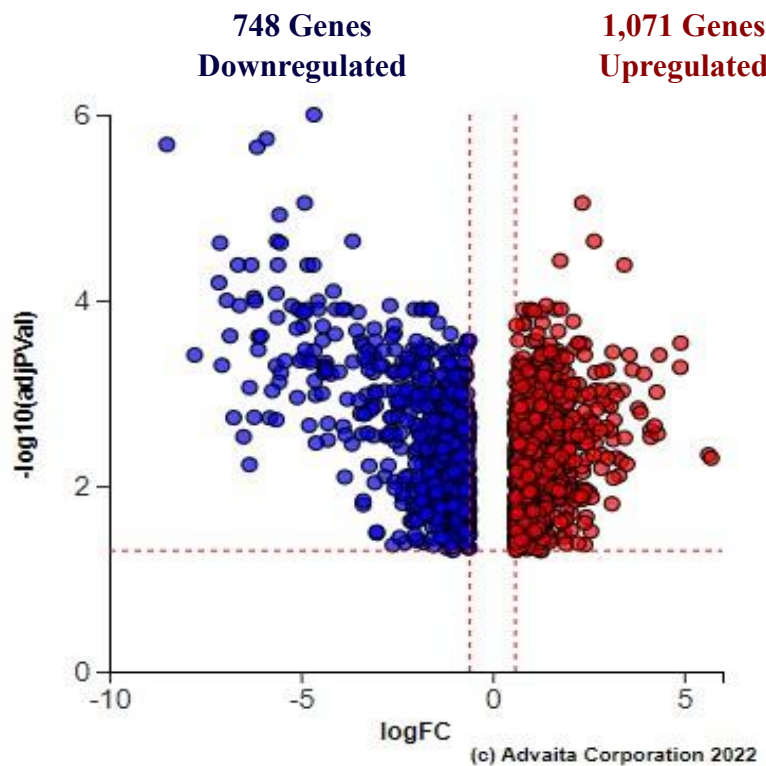


**Figure 16. Volcano plot of gene expression in METH-treated astrocytes.** Significantly differentially expressed genes (DEGs) (1819) are represented in terms of their measured significance of the change (y-axis) and expression change (x-axis). The dotted line represents the threshold used to select the DEGs: 0.05 adjusted p-value or 1.3  $-\log_{10}(\text{adjusted p-value})$  and  $\pm 1.6 \log_2\text{FC}$  for expression change. The upregulated genes (positive log fold change) are shown in red, while the down-regulated genes (negative log fold change) are shown in blue.

**Table 2. Description of top 20 upregulated genes in METH-treated astrocytes**

No.	Gene Symbol	Gene Name	Entrez ID	Log <sub>2</sub> Fold Change	FDR p-value	Function
1	DKK1	Dickkopf WNT signaling pathway inhibitor 1	22943	5.71	5.03E-03	Encodes a protein from the dickkopf family that binds to the LRP6 co-receptor and suppresses $\beta$ -catenin-dependent Wnt signaling. Involved in embryonic development. Expression is elevated in various human malignancies, and the encoded protein may increase proliferation, invasion, and growth in cancer cell lines.
2	GDF15	Growth differentiation factor 15	9518	5.64	4.63E-03	Encodes a secreted transforming growth factor- $\beta$ (TGF- $\beta$ ) superfamily protein ligand that binds to TGF- $\beta$ receptors, resulting in the recruitment and activation of SMAD family transcription factors. Plays a role in the stress response pathway of cells after cellular damage. Elevated protein levels are linked to tissue hypoxia, inflammation, acute injury, and oxidative stress.
3	GPNMB	glycoprotein nmb	10457	4.91	2.89E-04	Encodes a type I transmembrane glycoprotein. Expression is observed in low-metastatic human melanoma cell lines and xenografts but not in highly metastatic cell lines. May have a role in restraining growth and lowering the risk of metastatic spread.
4	PRKCB	protein kinase C beta	5579	4.90	5.29E-04	Encoded a protein that is a member of the PKC family. Involved in various physiological processes, including stimulation of B cells, induction of apoptosis, endothelial cell proliferation, and intestinal sugar absorption.

5	SCD	stearoyl-CoA desaturase	6319	4.36	3.89E-04	Encodes an enzyme that catalyzes a rate-limiting step in fatty acid biosynthesis, primarily the synthesis of oleic acid which is formed by desaturation of stearic acid. The ratio of stearic acid to oleic acid has been implicated in regulating cell growth and differentiation through effects on cell membrane fluidity and signal transduction.
6	COBL	cordon-bleu WH2 repeat protein	23242	4.31	2.75E-03	Encodes a protein with WH2 domains (WASP, Wiskott-Aldrich syndrome protein, homology domain-2) that interact with actin. The encoded actin regulator protein is required for the growth and assembly of brush-border microvilli that play a role in maintaining intestinal homeostasis.
7	CCN3	cellular communication network factor 3	4856	4.29	9.77E-04	Encodes a small, secreted cysteine-rich protein which is a member of the CCN family of regulatory proteins. Interacts with the extracellular matrix and plays an essential role in cardiovascular and skeletal development, fibrosis, and cancer development.
8	BHLHE41	basic helix-loop-helix family member e41	79365	4.23	2.26E-03	Encodes a basic helix-loop-helix protein expressed in various tissues. Interacts with ARNTL or competes for E-box binding sites in the promoter of PER1 and repress CLOCK/ARNTL's transactivation of PER1. Involved in the control of circadian rhythm and cell differentiation. Defects in this gene are associated with the short sleep phenotype.
9	FABP3	fatty acid binding protein 3	2170	4.13	3.00E-03	Participate in the uptake, intracellular metabolism and/or transport of long-chain fatty acids. Also responsible for the modulation of cell growth and proliferation. Candidate tumor suppressor gene for human breast cancer.
10	DHCR7	7-dehydrocholesterol reductase	1717	4.13	2.51E-03	Encodes an enzyme that removes catalyzes the conversion of 7-dehydrocholesterol to cholesterol. Mutations cause Smith-Lemli-Opitz syndrome (SLOS), which is characterized by metabolically characterized by reduced serum cholesterol levels and elevated serum 7-dehydrocholesterol levels and phenotypically characterized by cognitive disability, facial

						dysmorphism, syndactyly of second and third toes, and holoprosencephaly.
11	SFRP4	secreted frizzled related protein 4	6424	3.96	6.20E-04	Member of the SFRP family that contains a cysteine-rich domain homologous to the putative Wnt-binding site of Frizzled proteins. Act as soluble modulators of Wnt signaling. Expression in ventricular myocardium correlates with apoptosis-related gene expression.
12	PNPLA3	patatin like phospholipase domain containing 3	80339	3.86	1.62E-03	Encodes a triacylglycerol lipase that mediates triacylglycerol hydrolysis in adipocytes. The encoded protein, which appears to be membrane-bound, may be involved in balancing energy usage/storage in adipocytes.
13	GPX3	glutathione peroxidase 3	2878	3.81	1.46E-03	Encodes a protein belonging to the glutathione peroxidase family, members of which catalyze the reduction of organic hydroperoxides and hydrogen peroxide by glutathione and thereby protect cells against oxidative damage. Downregulation is observed in a wide spectrum of human malignancies, including thyroid cancer, hepatocellular carcinoma and chronic myeloid leukemia.
14	APOE	apolipoprotein E	348	3.65	5.62E-04	Encoded a major apoprotein of the chylomicron which then binds to a specific liver and peripheral cell receptor and is essential for the normal catabolism of triglyceride-rich lipoprotein constituents. Mutations result in familial dysbetalipoproteinemia, or type III hyperlipoproteinemia (HLP III).
15	HGF	hepatocyte growth factor	3082	3.57	3.89E-04	Encodes a protein that binds to the HGF receptor to regulate cell growth, cell motility and morphogenesis in numerous cell and tissue types. Also plays a role in angiogenesis, tumorigenesis, and tissue regeneration. Mutations are associated with nonsyndromic hearing loss.
16	JADE2	jade family PHD finger 2	23338	3.51	5.84E-03	Predicted to enable ubiquitin protein ligase activity. Involved in histone acetylation.

17	RBM47	RNA binding motif protein 47	54502	3.45	3.05E-03	Enables RNA binding activity. Predicted to act upstream of or within cytidine to uridine editing and hematopoietic progenitor cell differentiation.
18	ALOX5	arachidonate 5-lipoxygenase	240	3.44	4.16E-05	Encodes the enzyme 5-lipoxygenase which catalyzes two reactions in the formation of leukotrienes. Mutations lead to a diminished response to antileukotriene drugs used in the treatment of asthma and may also be associated with atherosclerosis and several cancers.
19	KCNJ4	potassium inwardly rectifying channel subfamily J member 4	3761	3.39	9.46E-04	Encodes a small-conductance inward rectifier potassium channel that is found in heart and brain The encoded protein has a small unitary conductance compared to other members of this protein family.
20	SPP1	secreted phosphoprotein 1	6696	3.36	5.35E-03	Encodes a protein that is involved in the attachment of osteoclasts to the mineralized bone matrix via the osteoclast vitronectin receptor. Also a cytokine that upregulates expression of IFN- $\gamma$ and IL-12.

**Table 3. Description of top 20 downregulated genes in METH-treated astrocytes**

No.	Gene Symbol	Gene Name	Entrez ID	Log <sub>2</sub> Fold Change	FDR p-value	Function
1	RRM2	Ribonucleotide reductase regulatory subunit M2	6241	-8.49	2.10E-06	Encodes the small subunit (R2) of ribonucleotide reductase, a heterodimeric enzyme that catalyzes the rate-limiting step in generating deoxyribonucleotides required for the S phase DNA synthesis.
2	PBK	PDZ binding kinase	55872	-7.77	3.89E-04	Encodes a serine/threonine-protein kinase that belongs to the dual specific mitogen-activated protein kinase kinase (MAPKK) family. The encoded protein is involved in activating lymphoid cells and the support of testicular activities, with possible participation in the spermatogenesis process. PBK overexpression has been linked to cancer.
3	DTL	Denticleless E3 ubiquitin protein ligase homolog	51514	-7.13	6.47E-05	Contributes to ubiquitin-protein transferase activity. Involved in several processes, including protein ubiquitination; regulation of G2/M transition of mitotic cell cycle; and translesion synthesis.
4	BIRC5	Baculoviral IAP repeat containing 5	332	-7.11	2.41E-05	Inhibitor of apoptosis (IAP), or programmed cell death, that is selectively overexpressed in common human cancers
5	PCLAF	PCNA clamp associated factor	9768	-7.06	5.02E-04	Enables chromatin binding activity. Involved in various functions, including the biosynthesis of cellular macromolecules; the centrosome cycle; and the reaction to UV.
6	ASPM	Assembly factor for spindle microtubules	259266	-6.93	1.00E-04	Required for regular mitotic spindle activity and regulation in embryonic neuroblasts. Mutations are associated with microcephaly primary type 5.

7	SHCBP1	SHC binding and spindle associated 1	79801	-6.85	2.42E-04	Predicted to enable SH2 domain binding activity. Predicted to be involved in fibroblast growth factor receptor signaling pathway and regulation of neural precursor cell proliferation.
8	TOP2A	DNA topoisomerase II alpha	7153	-6.75	1.84E-03	Encodes a DNA topoisomerase, a transcription enzyme that regulates and modifies the topologic states of DNA. Condenses chromosomes, separate chromatids, and relieves torsional stress caused by DNA transcription and replication. Serves as a target for several anticancer drugs, and a number of mutations in this gene have been linked to the development of treatment resistance. Decreased activity may also play a role in ataxia-telangiectasia.
9	BUB1B	BUB1 mitotic checkpoint serine/threonine kinase B	701	-6.64	4.16E-05	Encodes a kinase implicated in the operation of the spindle checkpoint. Localized to the kinetochore inhibits the anaphase-promoting complex/cyclosome (APC/C), delaying the initiation of anaphase and ensuring normal chromosomal segregation. Numerous types of cancer have been associated with impaired spindle checkpoint function.
10	DLGAP5	DLG associated protein 5	9787	-6.60	1.14E-04	Predicted to enable microtubule-binding activity. Predicted to be involved in several processes, including centrosome localization, kinetochore assembly, and mitotic spindle organization.
11	CENPU	Centromere protein U	79682	-6.49	2.96E-03	The centromere is a unique chromatin region that exists throughout the cell cycle and serves as a platform for the transitory assembly of the kinetochore during mitosis. CENPU is essential for the assembly of centromeres.
12	ACTC1	Actin alpha cardiac muscle 1	70	-6.34	5.92E-03	Encodes for alpha-actin, which is found in muscle tissues and is a major constituent of the contractile apparatus. Defects in this gene have been associated with idiopathic dilated cardiomyopathy (IDC) and familial hypertrophic cardiomyopathy

13	CCNB2	Cyclin B2	9133	-6.34	8.72E-04	It forms a complex with p34cdc2 and is an essential component of the cell cycle regulation mechanism. Binds to transforming growth factor beta RII as well, suggesting that cyclin B2/cdc2 may be important in transforming growth factor beta-mediated cell cycle regulation.
14	CDC20	Cell division cycle 20	991	-6.29	4.16E-05	Acts as a regulatory protein interacting with several other proteins at multiple points in the cell cycle. Required for two microtubule-dependent processes, nuclear movement prior to anaphase and chromosome separation.
15	NEK2	NIMA related kinase 2	4751	-6.22	9.34E-05	Encodes a serine/threonine-protein kinase that is involved in mitotic regulation. Centrosome-localized and undetectable during G1, but increases gradually during S phase, reaching maximum levels in late G2.
16	RAD51AP1	RAD51 associated protein 1	10635	-6.22	1.83E-03	Enables nucleic acid binding activity. Involved in DNA repair; cellular response to ionizing radiation; and positive regulation of DNA recombination.
17	KIF18B	Kinesin family member 18B	146909	-6.19	1.02E-04	Enables cytoskeletal motor activity and kinesin binding activity. Involved in microtubule depolymerization; mitotic cell cycle; and regulation of cell division. Located in cytosol; microtubule; and nuclear body.
18	KIF20A	Kinesin family member 20A	10112	-6.14	2.24E-06	Enables protein kinase binding activity. Involved in microtubule bundle formation; midbody abscission; and regulation of cytokinesis. Implicated in restrictive cardiomyopathy.
19	CEP55	Centrosomal protein 55	55165	-6.11	3.41E-04	Enables identical protein binding activity. Involved in cranial skeletal system development; establishment of protein localization; and midbody abscission. Implicated in multinucleated neurons, anhydramnios, renal dysplasia, cerebellar hypoplasia and hydranencephaly

---

20	ID1	Inhibitor of DNA binding 1, HLH protein	3397	-6.10	2.46E-04	Encodes a helix-loop-helix (HLH) protein that can form heterodimers with members of the basic HLH family of transcription factors. The encoded protein has no DNA binding activity and therefore can inhibit the DNA binding and transcriptional activation ability of basic HLH proteins with which it interacts. May play a role in cell growth, senescence, and differentiation.
----	-----	---	------	-------	----------	---

---

Upregulated genes were involved in apoptosis (BIRC5), cell cycle, and cell division (PBK, DTL, ASPM, SHCB1, BUB1B, DLGAP5, CCNB2, CDC20, NEK2, KIF18B, KIF20A, and CEL55), DNA binding (TOP2A and RAD51AP1), DNA repair (PCLAF), DNA replication (RRM2), muscle contraction (ACTC1), and transcriptional regulation (CENPU and ID1) (Table 2). Downregulated genes were involved in actin binding (COBL), apoptosis and transcriptional regulation (PRKCB), cell adhesion and proliferation (SPP1 and CCN3), cell motility (HGF), circadian rhythm (BHLEHE41), inflammation (GPNMB), ion transport (KCNJ4), leukotriene biosynthesis (ALOX5), lipid metabolism (SCD, FABP3, DHCR7, PNPLA3, and APOE), protein ubiquitination (JADE2), oxidative stress (GPX3), RNA binding (RBM47) stress response (GDF15), and Wnt signaling pathway (DKK1 and SFRP1) (Table 3). These results show that METH potently induces gene expression changes in astrocytes across several biological processes and molecular functions.

### **2.3.3 Pathway Analysis**

The signaling and metabolic pathways affected in METH-treated astrocytes were examined using iPG. Twelve pathways were significantly affected after FDR correction (Table 4). Significantly affected pathways after METH treatment included cell cycle, steroid biosynthesis, DNA replication, mismatch repair, lysosome, apoptosis, p53 signaling pathway, base excision repair, homologous recombination, cellular senescence, focal adhesion, and phagosome.

**Table 4. Significantly affected pathways in METH-treated astrocytes**

No.	Pathway	FDR p-value	-Log <sub>10</sub> FDR p-value	DEGs	All Genes	Upregulated DEGs		Downregulated DEGs	
						Count	Percentage	Count	Percentage
1	Cell Cycle	3.67E-06	5.43	46	114	6	13.0	40	87.0
2	Steroid Biosynthesis	3.80E-04	3.42	14	19	13	92.9	1	7.1
3	DNA Replication	3.80E-04	3.42	26	34	1	3.8	25	96.2
4	Mismatch Repair	3.80E-04	3.42	14	22	1	7.1	13	92.9
5	Lysosome	3.80E-04	3.42	43	111	42	97.7	1	2.3
6	Apoptosis	3.80E-04	3.42	39	128	27	69.2	12	30.8
7	p53 Signaling Pathway	4.76E-04	3.32	29	64	13	44.8	16	55.2
8	Base Excision Repair	1.31E-03	2.88	15	30	4	26.7	11	73.3
9	Homologous Recombination	1.82E-03	2.74	17	38	3	17.6	14	82.4
10	Cellular Senescence	2.10E-02	1.68	37	141	18	48.6	19	51.4
11	Focal Adhesion	2.59E-02	1.59	39	186	25	64.1	14	35.9
12	Phagosome	2.85E-02	1.55	35	132	28	80.0	7	20.0

### ***2.3.3.1 Cell Cycle***

Treatment with METH significantly (FDR p-value = 3.80E-04) affected cell cycle progression in astrocytes with the downregulation of 40 out of 46 DEGs (Fig. 17). Throughout the mitotic cell cycle development, DNA replication (S phase) and mitosis (M phase), separated by the G1 and G2 phases, occur regularly. Cyclin-dependent kinases (CDKs) are critical regulatory enzymes that modulate the activity of essential substrates to control cell development through distinct stages. The transcription factor E2F and its regulator RB (retinoblastoma susceptibility protein) are two of CDKs' downstream targets. CDKs must be activated and inactivated at exact times during the cell cycle to guarantee orderly cell division. CKIs such as p16Ink4a, p15Ink4b, p27Kip1, and p21Cip1 are involved in the negative control of CDK activity, providing a mechanism for the cell cycle to be negatively regulated. Three major checkpoints make up the cell cycle pathway. The G1 checkpoint is the first and controls whether a cell will divide. The G2 checkpoint decides whether the cell will proceed through mitosis. The G1 and G2 checkpoints can be affected by the presence or absence of specific growth hormones, DNA damage, or replicative senescence. Before cell division, the final checkpoint, spindle assembly checkpoint (SAC), ensures that the chromosomes are correctly aligned.

G1 cyclin-CDK complexes become active in response to a pro-mitotic extracellular signal, preparing the cell for the S phase by stimulating the production of transcription factors that, in turn, stimulate the expression of S cyclins and DNA replication enzymes. Cyclin D (CCND) is the first cyclin produced in the cells that enter the cell cycle in response to extracellular signals (e.g., growth factors) [163]. CCND then binds to existing CDK4/6, forming the active cyclin D-CDK4/6 complex, which mono-phosphorylates RB to pRB. The

'hyperphosphorylated' Rb activates E2F transcription factors leading to the transcription of several genes such as CCNE, CCNA, and DNA POL. CCNE then binds to CDK2 forming CCNE/CDK2 complex, which pushes the cell from G1 to the S phase [164]. METH treatment resulted in the downregulation of genes encoding CCND2, RB-like 1 protein (RBL1), CCNE1, CCNE2, and CDK2, disrupting G1/S transition. When DNA damage occurs, checkpoint kinase 1 (CHK1) phosphorylates the cell division cycle (CDC) 25, resulting in its proteasomal degradation [165]. This proteasomal degradation inhibits the formation of CDKs, arresting cells at multiple time points, including G1/S transition, S phase, and G2/M transition. CHK1 also mediates DNA repair mechanisms during the S phase by activating repair factors, including PCNA and others [166]. Treatment with METH significantly downregulated the genes encoding CHK1, CDC25A, CDC25C, and PCNA, signifying METH-induced cell cycle arrest and impairments in the DNA repair process in astrocytes.

Activation of DNA replication during the cell cycle occurs in two stages. In the first stage, sequential assembly of the origin replication complex (ORC), CDC6, and MCM2-MCM7 complex occurs onto the replication origin. This assembly occurs during the late M and G1 phases resulting in the origin becoming 'licensed' for DNA replication. In the second stage, licensed origins work at different times during the S phase to initiate a pair of replication forks. The second stage requires the action CDK and CDC7/DBF4 [167]. Another kinase, CDC45, is also required in conjunction with CDC7/DB4 to trigger the initiation of DNA replication [168]. CDC25C activates the CCNB/CDK1 complex at the end of the S phase, which progresses the cells into and out of the M phase [169]. In METH-treated astrocytes, significant decrease in the expression of ORC4, ORC6, CDC6, MCM2, -3, -4, -5, -6, and -7, CDC7/DBF4, CDC45, CCNB1, CCNB2, and CDK1 were observed. METH also

downregulated S-phase kinase-associated proteins 1 (SKP1) and 2 (SKP2), which regulate the cell cycle by promoting the degradation of CDK inhibitor 1B predominantly in the S, G2, and initial part of the M phase [170, 171]. Overall, these results suggest a strong inhibitory effect of METH on DNA replication in the S phase and the blockage of S/M transition in astrocytes. DNA replication in the S phase is followed by the G2 phase, during which rapid cell growth and protein synthesis occur in preparation for mitosis. Accumulation of proteins during the G2 phase activates CCB/CDK1. As the cell progresses through the G2 phase and reaches the G2/M transition, the CDC2/CCNB complex is activated, promoting entry into mitosis [172].

The process of mitosis is divided into stages: prophase, prometaphase, metaphase, anaphase, and telophase. During the mitosis phase, chromosomes are separated into two nuclei. During these phases, the already duplicated chromosomes condense and attach to spindle fibers that pull one copy of each chromosome to opposite sides of the cell resulting in two genetically identical daughter nuclei. The rest of the cells may then continue to divide by cytokinesis to produce two daughter cells [173]. The metaphase-to-anaphase transition of mitosis constitutes a spindle assembly checkpoint (SAC) that prevents the separation of the duplicated chromosomes (anaphase) until each chromosome is correctly attached to the spindle [174]. Only this attachment pattern ensures that each daughter cell receives one copy of the chromosome. METH treatment downregulated several genes encoding proteins involved in the SAC, including CDC20, Mitotic checkpoint serine/threonine-protein kinase BUB1, and mitotic arrest deficient 2 like 1 (MAD2L1). METH also decreased the expression of extra spindle pole bodies like 1 (ESPL1/Separase), PTTG1 Regulator Of Sister Chromatid Separation (PTTG1/Securin), and structural maintenance of chromosomes 1A (SMC1A), all

of which are important for regulating sister chromatid cohesion before the onset of anaphase [175].

Our results indicate that METH exposure results in the downregulation of several cell cycle regulatory proteins, leading to cell cycle arrest at key checkpoints such as G1/S, G2/M, and SAC.

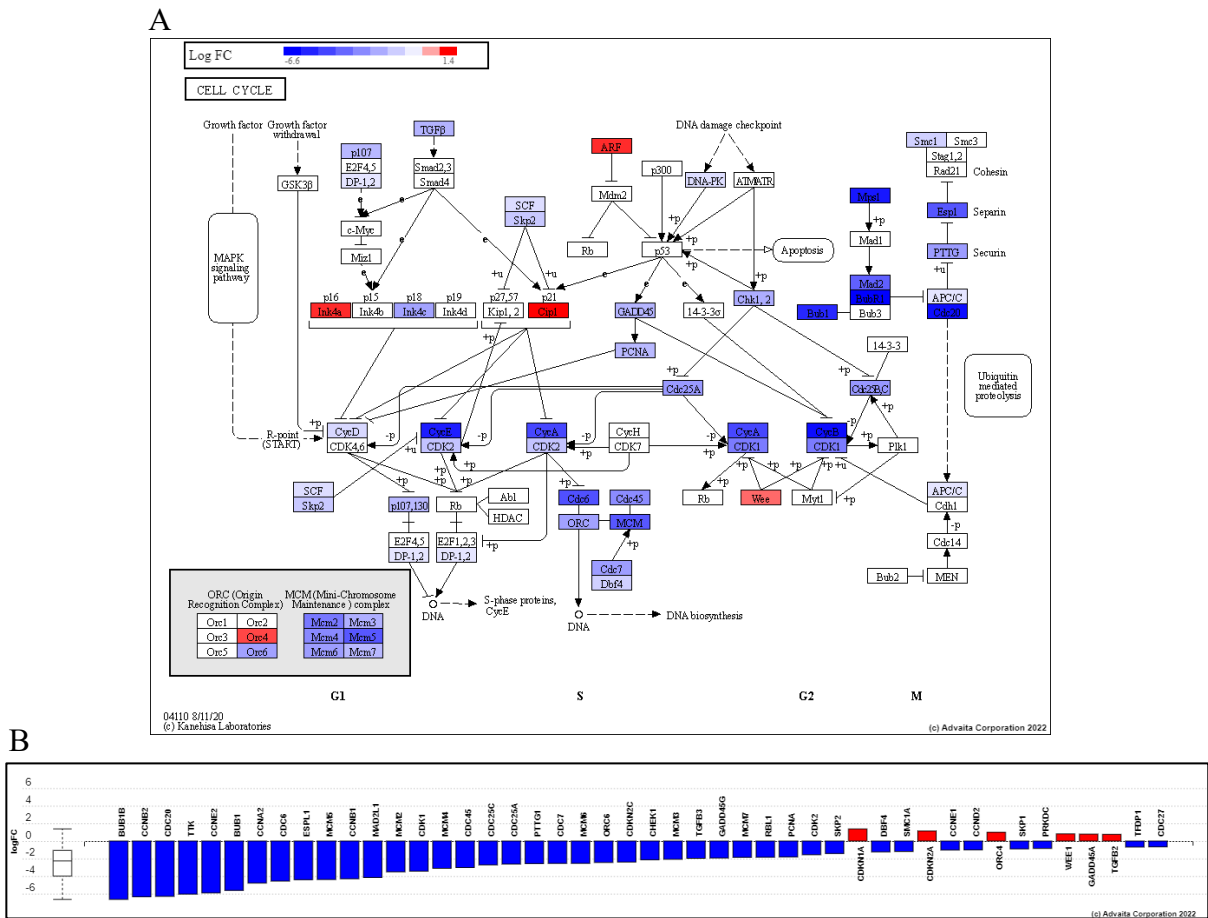


**Figure 17. Effect of METH on cell cycle pathway in astrocytes.** A. Graphical representation of DEGs in the pathway. Upregulated genes are shown in red. The figure was obtained with iPathwayGuide ([www.advaitabio.com](http://www.advaitabio.com)), using pathway data obtained from the KEGG resource (Pathway: hsa04110). B. Gene measured expression bar plot. All DEGs in the pathway are ranked based on their absolute value of log fold change. Upregulated genes are shown in red, downregulated genes are shown in blue. The box and whisker plot on the left summarizes the distribution of all the differentially expressed genes in this pathway. The box represents the 1st quartile, the median, and the 3rd quartile, while the outliers are represented by circles.

### **2.3.3.2 Steroid Biosynthesis**

The results showed that METH treatment significantly activated the steroid biosynthesis pathway (FDR p-value = 3.80E-04) in astrocytes with the significant ( $p < 0.05$ ) upregulation of 13 out of 14 DEGs in the pathway (Fig. 18). All upregulated DEGs encode enzymes involved in cholesterol biosynthesis, with DHCR7 (7-Dehydrocholesterol reductase) being the most upregulated gene. The DHCR7 gene encodes the critical enzyme delta-7-sterol reductase, which catalyzes the conversion of 7-dehydrocholesterol to cholesterol. Other essential upregulated genes include TM7SF2 [Delta (14)-Sterol Reductase] and DHCR24 (24-dehydrocholesterol reductase), which encode enzymes that catalyze the reduction of critical sterol intermediates during cholesterol biosynthesis. The remaining upregulated genes included NSDHL, LIPA, EBP, HSD17B7, SC5D, LSS, MSM01, SQLE, FDFT1, and SOAT1. One gene, LBR (lamin B receptor), was downregulated.

In the brain, astrocytes are the most active steroidogenic cells as they express the enzymes P450<sub>scc</sub>, P450<sub>c17</sub>, 3 $\beta$ HSD, 17 $\beta$ HSD, and P450<sub>arom</sub> needed for the synthesis of neurosteroids such as pregnenolone, progesterone, estradiol, and testosterone [176]. Astrocyte-derived neurosteroids serve several vital functions in the brain [177]. Furthermore, estradiol and progesterone have been shown to protect against METH-induced neurotoxicity [178, 179] and memory deficits [180]. Cholesterol serves as the starting substrate for the synthesis of these neurosteroids. However, METH has been shown to inhibit the activity of P450<sub>scc</sub>, 3 $\beta$ HSD, 17 $\beta$ HSD, and P450<sub>arom</sub> in granulosa cells [181]. Therefore, even though METH was shown to increase cholesterol biosynthesis in astrocytes in our data, it is likely that METH-induced



### **2.3.3.3 DNA Replication**

Treatment with METH significantly (FDR p-value = 3.80E-04) inhibited DNA replication in astrocytes with the downregulation of 25 out of 26 DEGs (Fig. 19). DNA Replication follows a multistep enzymatic pathway and requires a complex network of interacting proteins and enzymes. At the DNA replication fork, a DNA helicase precedes the DNA synthetic machinery. It unwinds the duplex parental DNA in cooperation with the single-stranded DNA binding protein (SSB) or replication protein A (RPA). On the leading strand, replication occurs continuously in a 5 to 3 direction, whereas on the lagging strand, DNA replication occurs discontinuously by synthesis and joining of short Okazaki fragments. In eukaryotes, three DNA polymerases ( $\alpha$ ,  $\delta$ , and  $\epsilon$ ) have been identified. DNA primase forms a permanent complex with DNA polymerase  $\alpha$ . Proliferating cell nuclear antigen (PCNA) and replication factor C (RFC) function as a clamp and a clamp loader. Flap endonuclease (FEN1) and RNase H1 remove the RNA from the Okazaki fragments, and DNA ligase I join the DNA.

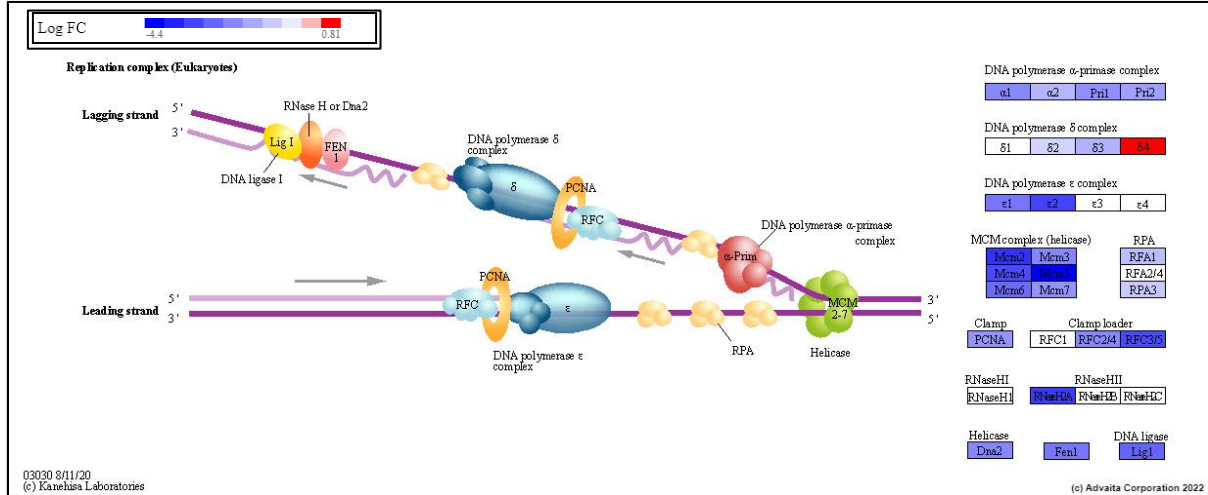
METH treatment decreased the expression of several genes that encode proteins involved in DNA replication initiation, elongation, and termination phases. The minichromosome maintenance (MCM) proteins – 2,3,4,5,6 and 7, required for all phases of DNA replication, were downregulated. MCM proteins are needed for DNA helicase activity, and inactivation of any of the six MCM proteins during the S phase prevents further progression of the replication fork [182]. METH also downregulated replication proteins A1 (RPA1) and A3 (RPA3), which prevents the single-stranded DNA from rewinding on itself or forming secondary structures keeping DNA unwound for DNA polymerases to replicate it [183]. However, METH treatment also downregulated DNA polymerase (POL) subunits  $\alpha$ ,  $\delta$ , and  $\epsilon$ , which are required to generate two copies of the parental genome after DNA helicase

has unwound the DNA duplex [184]. POL  $\alpha$  cannot continue DNA replication and must be replaced with another polymerase to continue DNA synthesis [185]. Therefore, DNA replication requires the coordinated action of all three DNA polymerases: POL  $\alpha$  for priming synthesis, POL  $\epsilon$  for leading-strand replication, and the POL  $\delta$ , constantly loaded, for generating Okazaki fragments during lagging-strand synthesis. Polymerase switching requires DNA clamp and clamp loaders [186]. In eukaryotic cells, PCNA acts as a DNA clamp to hold POL  $\delta$  to DNA to increase the processivity of leading strand synthesis [187]. PCNA is clamped to the DNA through RFC [188]. METH treatment significantly downregulated PCNA and RFC subunits 2,3,4 and 5.

METH treatment also decreased the expression of RNase H2 subunit A (RNASEH2A), FEN1, and DNA ligase 1 (LIG1), which are all involved in the elongation phase of DNA replication. RNase H recognizes the DNA: RNA hybrids formed using RNA primers and is responsible for removing them from the replicated strand, leaving behind a primer: template junction. POL  $\alpha$  identifies these sites and elongates the breaks left by primer removal. A small amount of the DNA segment immediately upstream of the RNA primer is also displaced, creating a flap structure. This flap is then cleaved by FEN1. At the replication fork, the gap in DNA after removing the flap is sealed by LIG1, which repairs the nicks left between the 3'-OH and 5'phosphate of the newly synthesized strand [189].

Inaccuracies in DNA replication can lead to the accumulation of mutations that disrupt several cellular and molecular processes such as cell cycle and mismatch repair and lead to cancer development [190]. Effects of METH on cell cycle dysregulation in astrocytes and other cell types have been well documented [191-193]. However, the significance of these changes in relevance to METH neurotoxicity remains an active area of investigation.

A



B

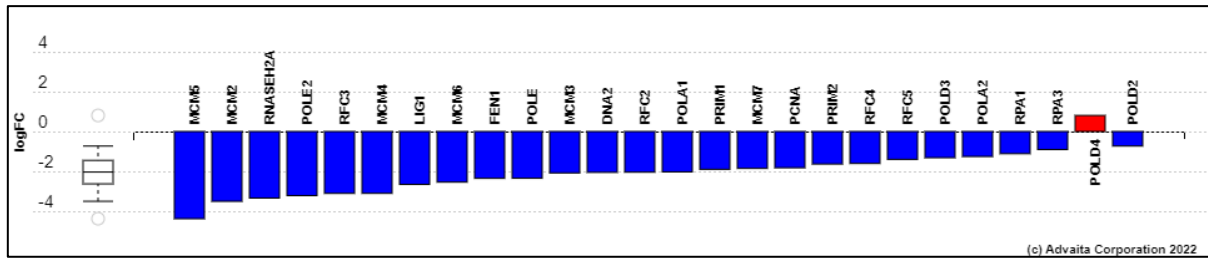


**Figure 19. Effect of METH on DNA replication in astrocytes.** A. Graphical representation of DEGs in the pathway. Upregulated genes are shown in red. The figure was obtained with iPathwayGuide ([www.advaitabio.com](http://www.advaitabio.com)), using pathway data obtained from the KEGG resource (Pathway: ko03030). B. Gene measured expression bar plot. All DEGs in the pathway are ranked based on their absolute value of log fold change. Upregulated genes are shown in red, downregulated genes are shown in blue. The box and whisker plot on the left summarizes the distribution of all the differentially expressed genes in this pathway. The box represents the 1st quartile, the median, and the 3rd quartile, while the outliers are represented by circles.

#### **2.3.3.4 Mismatch Repair**

METH significantly (FDR p-value = 3.80E-04) inhibited DNA mismatch repair (MMR) in astrocytes (Fig. 20). MMR is a highly conserved biological pathway that is important for genomic integrity. MMR corrects DNA mismatches produced during DNA replication, preventing mutations in dividing cells from becoming permanent. The damage is corrected by recognizing the mismatch's deformity, distinguishing the template and non-template strands, and excising and replacing the incorrectly integrated base with the correct nucleotide [194].

The MMR pathway begins with binding a MutS homodimer to the mismatch. The combined action of MutS, MutL, MutH and ATP then locates and cleaves a hemimethylated dGATC site 5' or 3' to the mismatch. MutH's strand-specific nick at hemimethylated dGATC is a starting point for removing the mispaired base. Helicase II (UvrD) loads at the nick and unwinds the duplex from the nick to the mismatch [195], yielding ssDNA that is quickly bound by ssDNA-binding protein (SSB) protected from nuclease assault [196]. ExoI or ExoX (3'5' exonuclease), or ExoVII or RecJ (5'3' exonuclease), excises the nicked strand from the nicked site (the dGATC site) up to and somewhat past the mismatch, depending on the position of the strand break relative to the mismatch. DNA polymerase III, SSB, and DNA ligase repair the single-stranded gap by resynthesizing DNA and ligating it [197]. All essential MMR proteins, including MutS homolog 2 (MSH2), MutL homolog 1 (MHL1), exonuclease 1 (EXO1), DNA POL  $\delta$  – 2 (POLD2), 3 (POLD3), and 4 (POLD4); and DNA ligase 1 (LIG1), were significantly downregulated by METH. METH similarly downregulated other MMR proteins such as PCNA, RPA, and RFC; the roles of these proteins in DNA replication are discussed in section 2.3.3.3.

Failure to recognize and fix mismatches results in microsatellite instability (MSI) and an increased spontaneous mutation rate (mutator phenotype). Inactivation of MMR in human cells is associated with hereditary and sporadic human cancers [198]. For example, the downregulation of MMR genes MLH1 and MLH3 and 11 additional DNA repair genes is associated with both low-grade and high-grade astrocytomas [199]. Therefore, METH-induced MMR defects in astrocytes may contribute to cancer development.

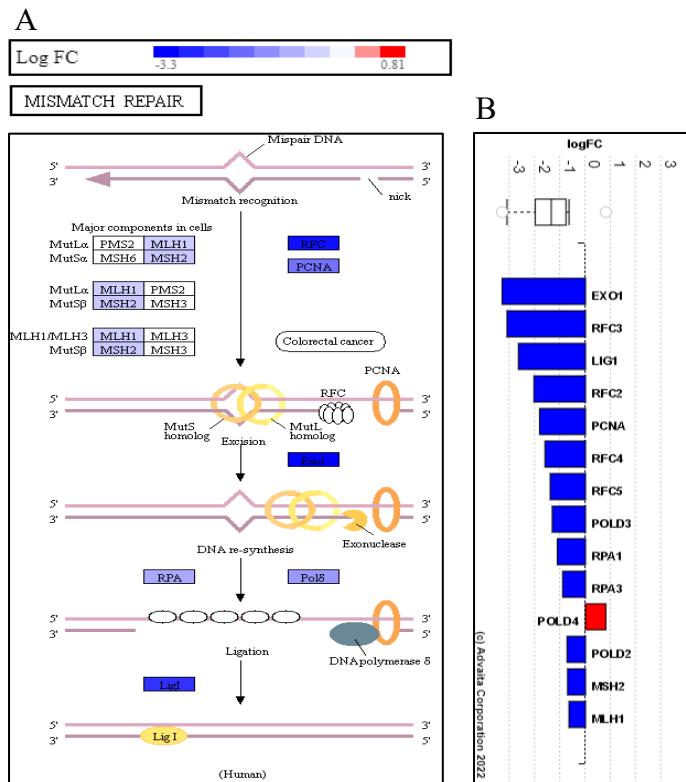


**Figure 20. Effect of METH on mismatch repair pathway in astrocytes.** A. Graphical representation of DEGs in the pathway. Upregulated genes are shown in red. The figure was obtained with iPathwayGuide ([www.advaitabio.com](http://www.advaitabio.com)), using pathway data obtained from the KEGG resource (Pathway: hsa03430). B. Gene measured expression bar plot. All DEGs in the pathway are ranked based on their absolute value of log fold change. Upregulated genes are shown in red, downregulated genes are shown in blue. The box and whisker plot on the left summarizes the distribution of all the differentially expressed genes in this pathway. The box represents the 1st quartile, the median, and the 3rd quartile, while the outliers are represented by circles.

### 2.3.3.5 *Lysosome*

The lysosomal pathway was the second most significantly (FDR p-value = 3.80E-04) activated pathway in METH-treated astrocytes (Fig. 21A). Lysosomes are membrane-delimited organelles in animal cells serving as the cell's main digestive compartment to which all sorts of macromolecules are delivered for degradation. They contain more than 40 hydrolases in an acidic environment (pH of about 5). After synthesis in the endoplasmic reticulum, lysosomal enzymes are decorated with mannose-6-phosphate residues, recognized by mannose-6-phosphate receptors in the trans-Golgi network. They are packaged into clathrin-coated vesicles and are transported to late endosomes. The lysosomes acquire substances for digestion via a series of processes, including endocytosis, phagocytosis, and autophagy.

METH treatment significantly upregulated genes encoding lysosomal enzymes and membrane proteins in astrocytes (Fig. 21B). Among 43 DEGs, 42 were upregulated, and only one was downregulated in response to METH treatment. Some of the critical upregulated genes included the genes encoding lysosomal proteases: cathepsins C (CTSC), D (CTSD), A (CTSA), and F (CTSF); glycosidases: neuraminidase 1 (NEU1), hexosaminidase alpha (HEXA), and beta (HEXB), N-acetyl-alpha-glucosaminidase (NAGLU) and mannosidase beta (MANB); lipases: lipase (LIPA); sphingomyelinase; ceramidase; and others. METH treatment also significantly upregulated several genes encoding lysosomal membrane proteins, including lysosomal associated membrane protein 1 (LAMP1), NPC intracellular cholesterol transporter 1 (NPC1) and 2 (NPC2), cystinosin (CTNS), sialin, mannose-6-phosphate receptor (M6PR), and ATPase H<sup>+</sup> Transporting V0 Subunits B (ATP6V0B), D1 (ATP6V0D1), and A1 (ATP6V0A1).

Owing to its weak base properties, METH destabilizes intracellular pH in acidic organelles such as lysosomes leading to the osmotic swelling and vacuolization of lysosomal membranes. As a result, lysosomal contents are released in the cytosol [200, 201]. Concurrent with earlier findings, our data showed that METH increases LAMP1, LAMP2, and cathepsin D levels in astrocytes [200, 202-204]. In addition, METH also increased the levels of cathepsin C, A, and F and several other lysosomal enzymes and proteins. Glia-derived cathepsins have been observed to promote neuroinflammation by activating the NLRP3 inflammasome and causing the release of pro-inflammatory cytokines such as CCL2, CXCL2, IL-1 $\beta$ , IL-6, and TNF- $\alpha$  [205-208]. Cytosolic cathepsins also initiate apoptosis by degrading antiapoptotic proteins such as BCL-2, BCL-XL, and MCL-1 and by activating caspases [209]. Upregulation of NEU1 has also been associated with apoptosis, inflammatory processes, and necrosis [210-212]. In addition, the collapse of lysosomal function and increased lysosomal membrane permeabilization can also impair cytoprotective autophagy and lead to cell death [213]. Accordingly, evidence supports the role of increased cytosolic lysosomal enzymes in several neurodegenerative and metabolic inflammatory diseases such as Alzheimer's disease and other age-related neurodegenerative diseases, type 2 diabetes, atherosclerosis, and chronic kidney diseases [214-218].

Our results indicate that METH leads to lysosomal membrane disruption, releasing lysosomal enzymes in the cytosol, leading to increased apoptosis and neuroinflammation.

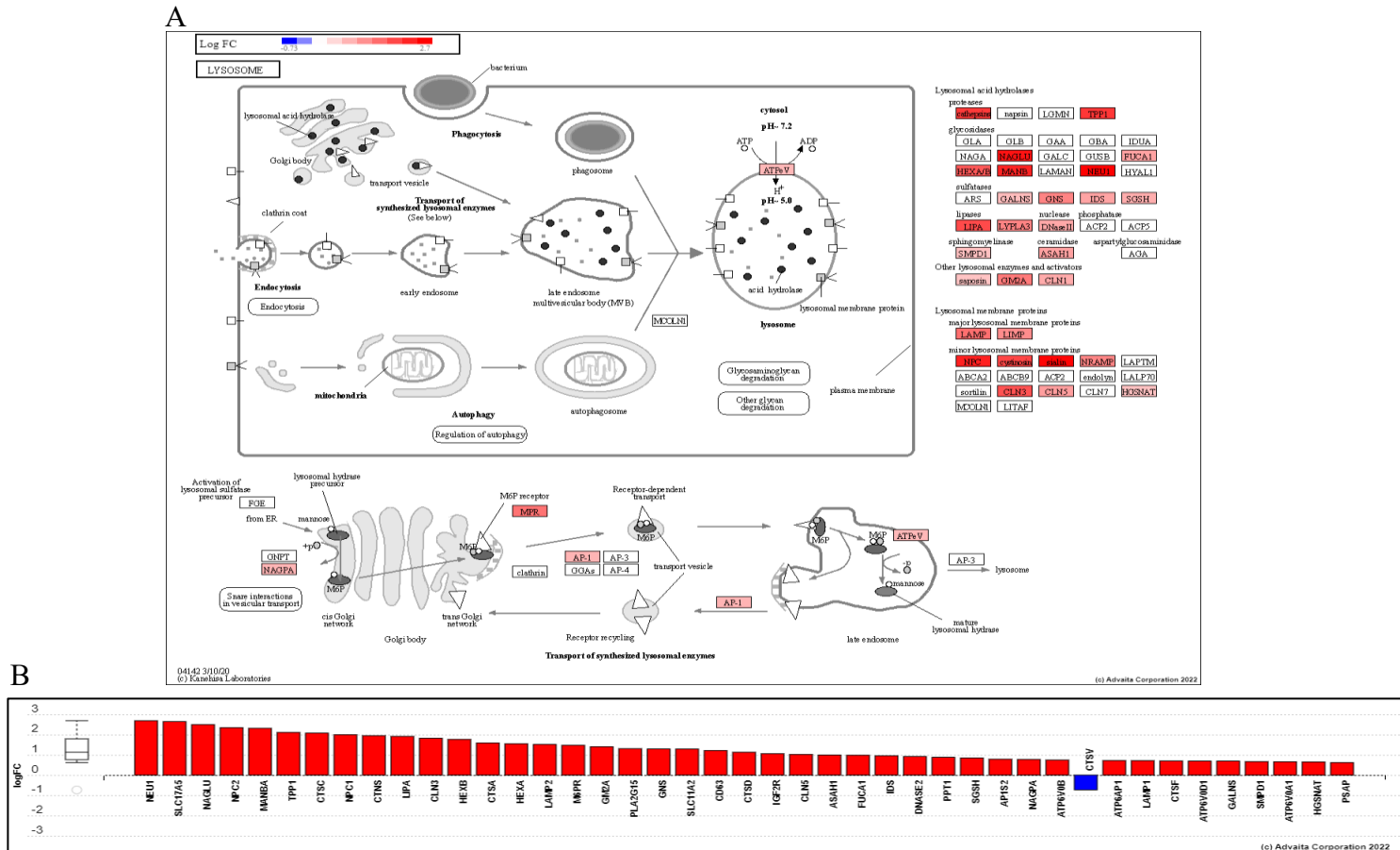


**Figure 21. Effect of METH on lysosome pathway in astrocytes.** A. Graphical representation of DEGs in the pathway. Upregulated genes are shown in red. The figure was obtained with iPathwayGuide ([www.advaitabio.com](http://www.advaitabio.com)), using pathway data obtained from the KEGG resource (Pathway: map04142). B. Gene measured expression bar plot. All DEGs in the pathway are ranked based on their absolute value of log fold change. Upregulated genes are shown in red, downregulated genes are shown in blue. The box and whisker plot on the left summarizes the distribution of all the differentially expressed genes in this pathway. The box represents the 1st quartile, the median, and the 3rd quartile, while the outliers are represented by circles.

### ***2.3.3.6 Apoptosis***

The treatment with METH significantly (FDR p-value = 3.80E-04) activated proapoptotic cascade in astrocytes (Fig. 22). Apoptosis is a genetically programmed cell death that involves the activation of caspases. Numerous interrelated pathways influence apoptosis. The 'extrinsic' pathway involves stimulation of members of the tumor necrosis factor (TNF) receptor subfamily, such as TNFR1, CD95/Fas, or TRAILR (death receptors), located at the cell surface, by their specific ligands, such as TNF- $\alpha$ , FasL or TRAIL, respectively. The 'intrinsic' pathway is activated mainly by non-receptor stimuli, such as DNA damage, ER stress, metabolic stress, UV radiation, or growth-factor deprivation. The central event in the intrinsic pathway is the mitochondrial outer membrane permeabilization (MOMP), leading to cytochrome c. These two pathways converge at the level of effector caspases, such as caspase-3 and caspase-7. The balance between the proapoptotic and antiapoptotic signals determines whether cells will undergo apoptosis, survive, or proliferate.

Treatment with METH resulted in the upregulation of several members of the extrinsic or death receptor pathway of apoptosis, including TRADD (TNFRSF1A associated via death domain), FAS (Fas cell surface death receptor), TNFRSF10B (TNF receptor superfamily member 10b), and caspase-8. TRADD and FAS are death receptors that bind to TRAIL (TNF-related apoptosis-inducing ligand) and Fas-L (Fas ligand), respectively [219]. Upon activation, TRADD recruits MAP3K5 (mitogen-activated protein kinase 5) and activates p38 MAPK/JNK pathways [220]. Activation of JNK results in the cleavage of BID (BH3 interacting domain death agonist) to jBID, which then disrupts the mitochondrial membrane and releases cytochrome c that activates the sequential cleavage of caspase-9, poly ADP-ribose polymerase (PARP), and caspase-3 to promote apoptotic cell death [221]. METH upregulated MAP3K5,

MAP2K2, JUN (Jun proto-oncogene, AP-1 transcription factor subunit), and FOS (Fos proto-oncogene, AP-1 transcription factor subunit). Surprisingly, METH downregulated BID and PARP1 and -2 but upregulated PARP4 and caspase-9. However, there was an upregulation of the proapoptotic genes BAD (BCL2 associated agonist of cell death) and BAX (BCL2 associated X, apoptosis regulator). In addition to jBID, elevated levels of BAX can also disrupt mitochondria through MOMP, releasing cytochrome C in the cytosol, which can activate caspase-9 [222]. BAX-induced MOMP releases HTRA2 (HtrA Serine Peptidase 2) and AIFM1 (apoptosis-inducing factor mitochondria associated 1) in the cytosol. HTRA2 activates caspases by neutralizing the inhibitors of apoptosis (IAP) [223], whereas AIFM1 translocates to the nucleus, where it causes DNA fragmentation [224]. Indeed, HTRA2 and AIFM1 were upregulated, and an IAP, BIRC2 (Baculoviral IAP Repeat Containing 2), were downregulated in response to METH treatment in astrocytes. JNK-mediated activation of HRK (harakiri, BCL2 interacting protein) was also observed in our data. HRK promotes apoptosis by neutralizing the antiapoptotic genes BCL-2 and BCL-XL [225].

METH treatment also upregulated several members of the ER stress pathway, including PERK (proline-rich receptor-like protein kinase), ATF4 (activating transcription factor 4), and CHOP (C/EBP homologous protein). These genes are sequentially activated following the unfolded protein response (UPR). Although PERK and ATF4 can activate apoptotic signals during prolonged ER stress, CHOP primarily relays the proapoptotic signals by neutralizing antiapoptotic genes BCL-2 and BCL-XL and causing MOMP, which then leads to the activation of the caspases [54]. In addition to the molecules directly involved in extrinsic and intrinsic apoptosis pathways, METH treatment upregulated several proapoptotic genes such as cathepsins (CTS) C, D, and F, DFFA (DNA fragmentation factor subunit alpha), GADD45A

(growth arrest and DNA damage-inducible alpha), and PTPN13 (protein tyrosine phosphatase non-receptor type 13). METH treatment also downregulated several antiapoptotic genes, including lamin (LMN) B1 and B2, and TUBA1B (tubulin alpha-1B chain)

Results from our data corroborated the well-documented apoptotic effects of METH. However, the roles of several uniquely affected genes from our results, such as HTRA2, BIRC1, HRK2, and PTPN13 in METH-induced apoptosis, require further investigation.

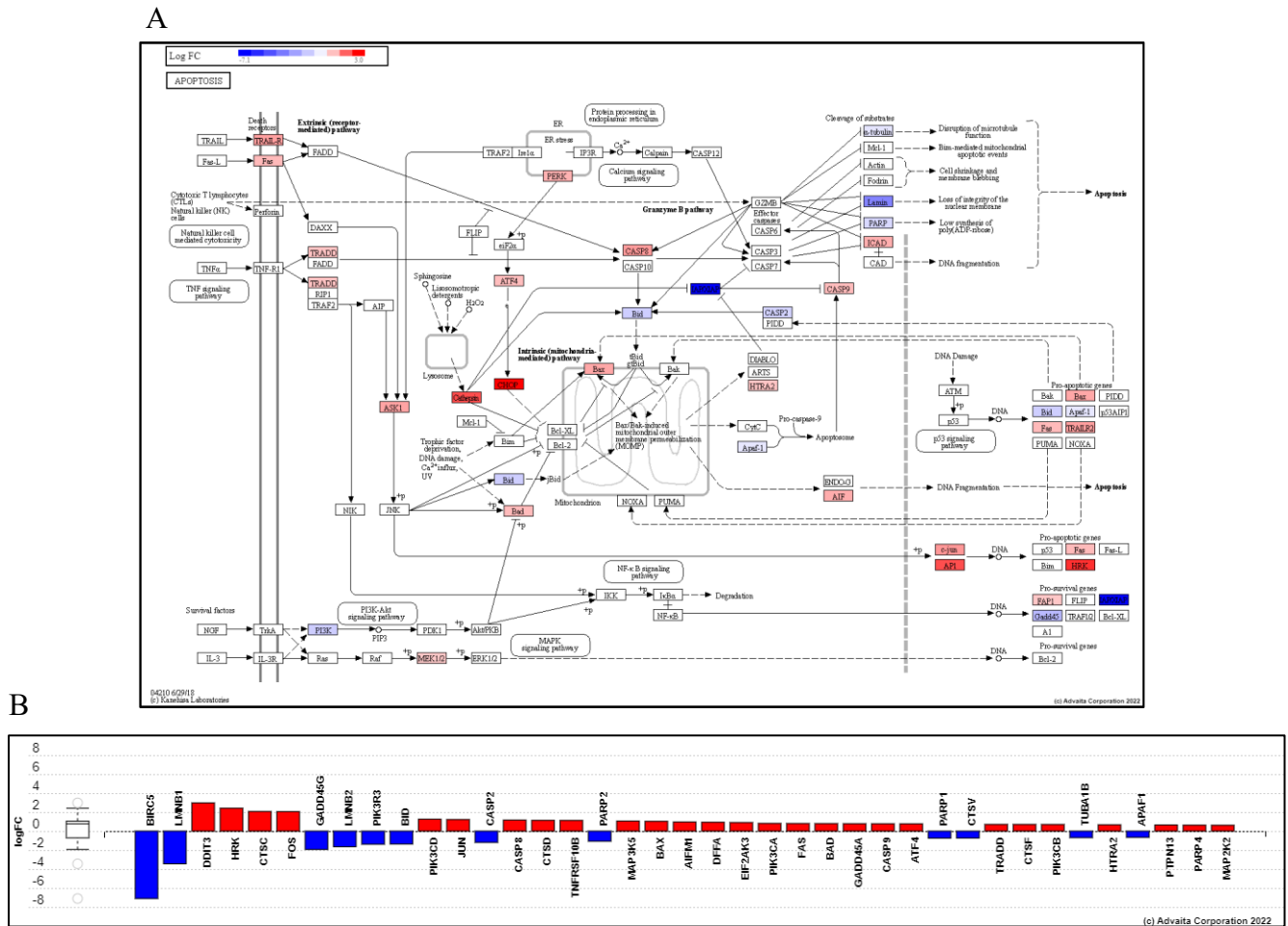


**Figure 22. Effect of METH on apoptosis pathway in astrocytes.** A. Graphical representation of DEGs in the pathway. Upregulated genes are shown in red. The figure was obtained with iPathwayGuide ([www.advaitabio.com](http://www.advaitabio.com)), using pathway data obtained from the KEGG resource (pathway #04210). B. Gene measured expression bar plot. All DEGs in the pathway are ranked based on their absolute value of log fold change. Upregulated genes are shown in red, downregulated genes are shown in blue. The box and whisker plot on the left summarizes the distribution of all the differentially expressed genes in this pathway. The box represents the 1st quartile, the median and the 3rd quartile, while the outliers are represented by circles.

### ***2.3.3.7 p53 Signaling Pathway***

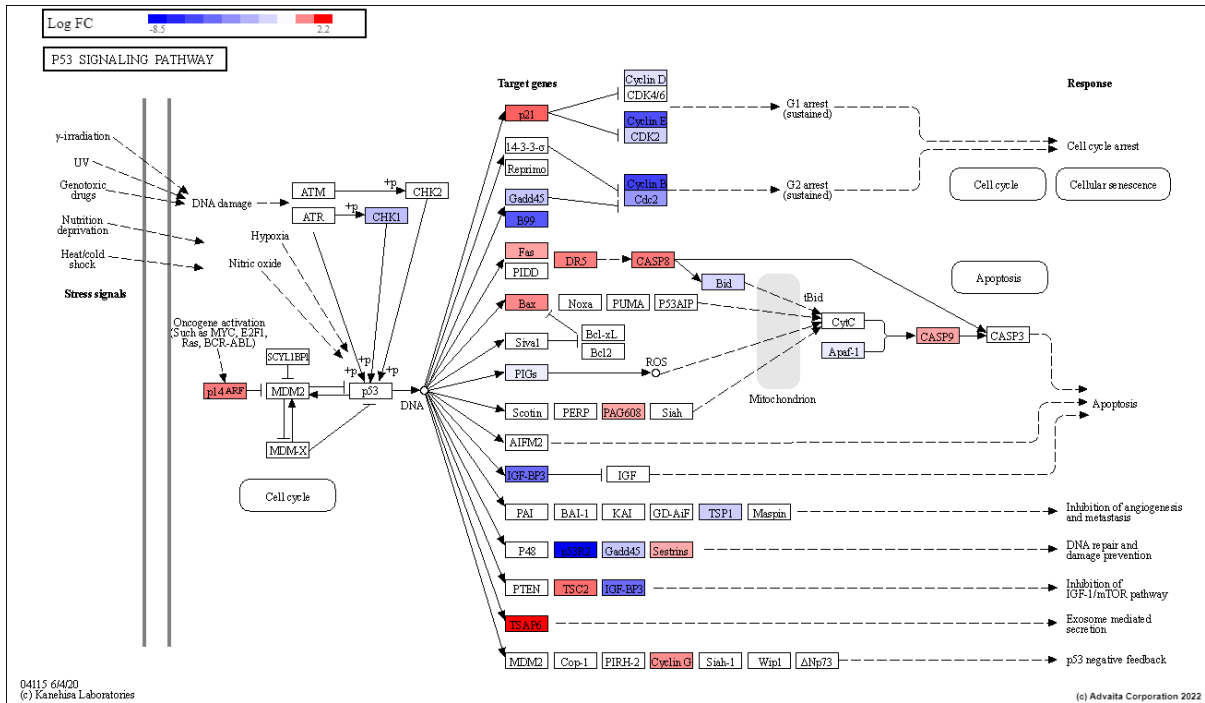
The p53 signaling pathway comprises a network of genes and their products designed to respond to a wide range of intrinsic and extrinsic stress signals affecting cellular homeostatic systems such as DNA replication, chromosomal segregation, and cell division [226]. Post-translational alterations activate the p53 protein in a specific way in response to a stress signal, resulting in cell cycle arrest, cellular senescence, or cellular death [227]. Several internal or external pressures that would cause a loss of fidelity in DNA replication, genome stability, cell cycle progression, or faithful chromosomal segregation are accommodated, or the clone of cells with these faults can be eradicated from the body.

METH significantly (FDR p-value = 4.76E-04) inhibited the p53 signaling pathway with the downregulation of 16 DEGs and upregulation of 13 DEGs (Fig. 23). Stress signals, including DNA damage, activate the p53 protein. METH causes significant DNA damage and impairs astrocyte DNA repair mechanisms, as explained in sections 2.3.3.2.3 and 2.3.3.2.4. METH treatment led to decreased expression of p14ARF (ARF tumor suppressor) or CDKN2A (cyclin-dependent kinase inhibitor 2A). p14ARF inhibits MDM2 and promotes p53 and p51 resulting in the activation of cyclin-CDK complexes and cell cycle progression through the G1-S checkpoint. METH also downregulated TP53I3 (tumor protein p53 inducible protein 3). Downstream of p53, METH affected expression levels of genes involved in cell cycle regulation, apoptosis, and DNA repair. METH downregulated several genes involved in cell cycle regulation (discussed in detail in section 2.3.3.1), including CCNB2, CCNE2, GTSE1 (G2 and S-phase expressed 1), CCNB1, CDK1, GADD45G, CDK2, CCNE1, and CCND2. Pro-apoptotic genes such as Caspase-9, FAS, BAX, TNFRSF100B, and Caspase-8

were upregulated (discussed in section 2.3.3.6). Ribonucleotide reductase regulatory subunit M2 (RRM2), a gene involved in DNA repair, was also downregulated.

Our results indicate that METH treatment significantly inhibits the p53 signaling pathway in astrocytes. Deficient p53 signaling can contribute significantly to the METH's neurotoxicity by triggering dysregulation of diverse downstream cellular processes such as cell cycle arrest, increased apoptosis, and DNA damage among others.

A



B

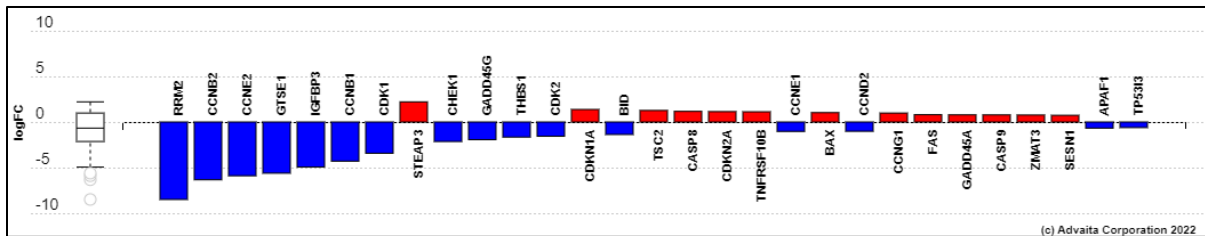


**Figure 23. Effect of METH on p53 signaling pathway in astrocytes.** A. Graphical representation of DEGs in the pathway. Upregulated genes are shown in red. The figure was obtained with iPathwayGuide ([www.advaitabio.com](http://www.advaitabio.com)), using pathway data obtained from the KEGG resource (Pathway: hsa04115). B. Gene measured expression bar plot. All DEGs in the pathway are ranked based on their absolute value of log fold change. Upregulated genes are shown in red, downregulated genes are shown in blue. The box and whisker plot on the left summarizes the distribution of all the differentially expressed genes in this pathway. The box represents the 1st quartile, the median, and the 3rd quartile, while the outliers are represented by circles.

### ***2.3.3.8 Base Excision Repair***

Base excision repair (BER) is the primary DNA damage repair pathway for removing minor base lesions caused by oxidation and alkylation [228]. BER is often characterized as DNA repair initiated by lesion-specific DNA glycosylases and finished by one of two sub-pathways: short-patch BER, in which only one nucleotide is replaced, or long-patch BER, in which 2-13 nucleotides are replaced. Each sub-pathway of BER relies on the formation of protein complexes that assemble at the DNA lesion site and promote coordinated repair. This mechanism of the complex building appears to boost the selectivity and efficiency of the BER pathway, hence enabling genomic integrity maintenance by limiting the buildup of highly toxic repair intermediates [229]

A DNA glycosylase identifies a damaged base as the initial step in BER. After recognizing the broken base, the appropriate DNA glycosylase cleaves an N-glycosidic link, eliminating the damaged base and generating an apurinic or apyrimidinic site (AP site). The DNA backbone is broken by a DNA AP endonuclease or a DNA AP lyase, a characteristic of certain glycosylases. AP endonuclease activity generates a single-stranded DNA nick 5' to the AP site, in contrast to DNA AP lyase activity, which generates a nick 3' to the AP site. The freshly formed nick is digested by the AP endonuclease, forming a single nucleotide gap in the DNA. Notably, the generated gap comprises a 3'- hydroxyl and a 5'-phosphate, substrates suitable for the subsequent enzyme activities in BER. A DNA polymerase inserts the proper nucleotide into the gap. By closing the nick, DNA ligase completes the repair process and restores the helix's integrity [230].

All 15 DEGs involved in BER in astrocytes were downregulated after METH treatment. Downregulated DNA glycosylases included nei like DNA glycosylase 3 (NEIL3),

N-methylpurine DNA glycosylase (MPG), and single-strand-selective monofunctional uracil-DNA glycosylase 1 (SMUG1). Flap endonuclease 1 (FEN1), which removes the 5' flap generated during long patch BER, was also downregulated. Other downregulated enzymes included poly(ADP-ribose) polymerase – 1 (PARP1), PARP2, and PART4; DNA POL –  $\epsilon$ ,  $\epsilon$ 2,  $\delta$ 2,  $\delta$ 3, and  $\delta$ 4; and LIG1. Decreased expression of PCNA, the processivity factor of POL  $\epsilon$ , was also observed. Scaffolding protein XRCC1 (X-ray repair cross-complementing 1), which coordinates short-patch BER, was also downregulated.

Our findings indicate that METH suppresses the BER pathway in astrocytes, hence increasing oxidative DNA damage. Neurodegenerative diseases, such as Alzheimer's, have been associated with a decrease in BER [231]. Patients with amyotrophic lateral sclerosis and Parkinson's disease also demonstrate higher levels of oxidative lesions and ssDNA breaks [232, 233]. These data suggest the potential that BER abnormalities contribute to METH-induced neurotoxicity.

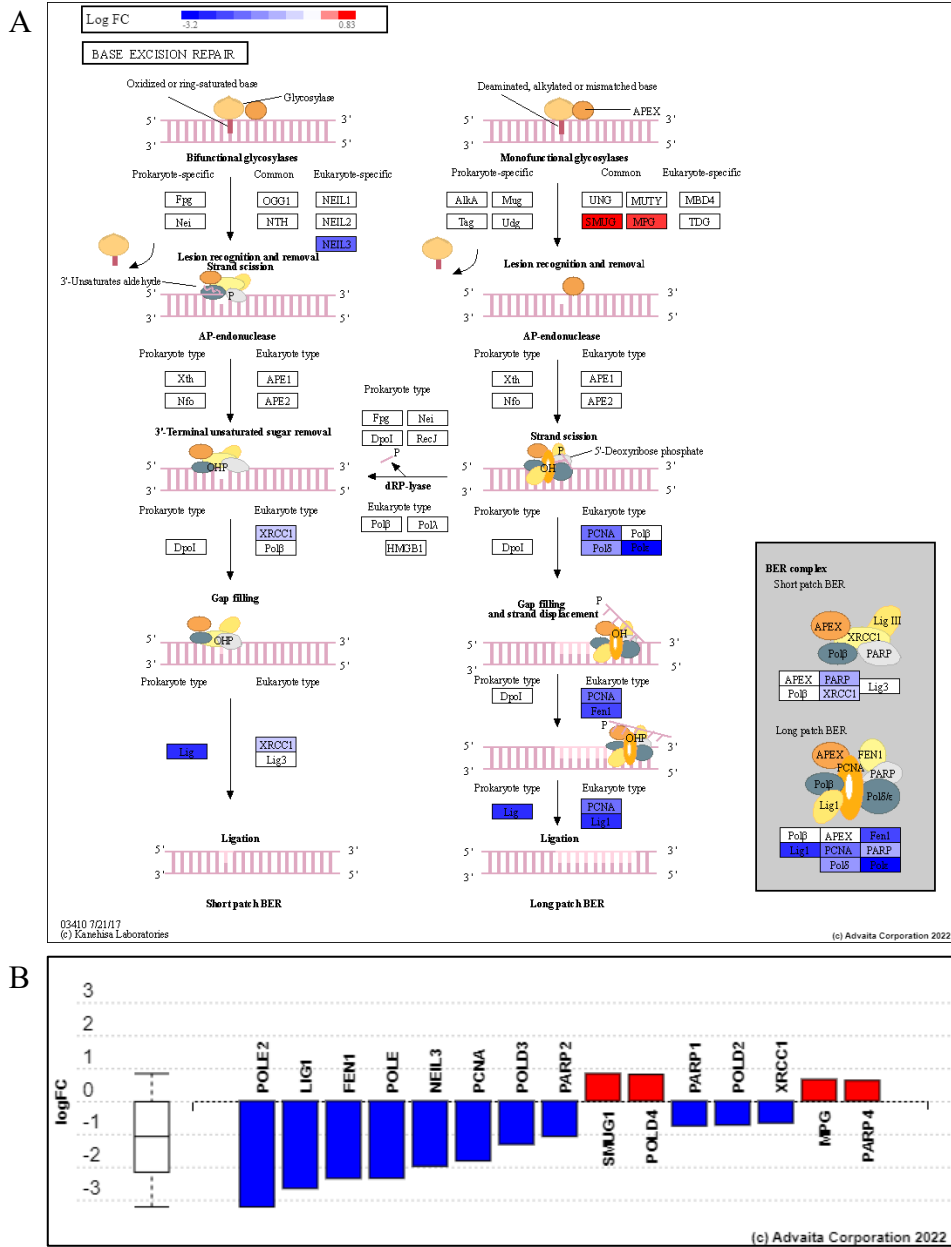


**Figure 24. Effect of METH on base excision repair pathway in astrocytes.**

A. Graphical representation of DEGs in the pathway. Upregulated genes are shown in red. The figure was obtained with iPathwayGuide ([www.advaitabio.com](http://www.advaitabio.com)), using pathway data obtained from the KEGG resource (Pathway: hsa03410). B. Gene measured expression bar plot. All DEGs in the pathway are ranked based on their absolute value of log fold change. Upregulated genes are shown in red, downregulated genes are shown in blue. The box and whisker plot on the left summarizes the distribution of all the differentially expressed genes in this pathway. The box represents the 1st quartile, the median, and the 3rd quartile, while the outliers are represented by circles.

### ***2.3.3.9 Homologous Recombination***

Homologous recombination (HR) is a DNA repair mechanism that plays a vital role in genomic stability by repairing damaged chromosomes that contain DNA double-strand breaks (DSBs) and other types of damage. Two primary models of HR-mediated repair of DSBs are the DSB repair (DSBR) pathway and the synthesis-dependent strand annealing (SDSA) pathway. Both pathways share similar initial steps [234]. After a DSB occurs, the MRN complex (consisting of MRE11, RAD50, and Nibrin) binds to DNA on either side of the break. Next, sections of DNA around the 5' ends of the break are cut away in a process called resection [235]. The replication protein A (RPA) protein, which has a high affinity for single-stranded DNA, binds the 3' overhangs [236]. The RAD51 protein subsequently creates a nucleic acid and protein filament on the single strand of DNA coated with RPA with the aid of many other proteins that mediate the process. In the strand invasion step that follows, an overhanging 3' end of the broken DNA molecule then "invades" a similar or identical DNA molecule that is not broken, forming a displacement loop (D-loop). After strand invasion, a DNA polymerase extends the end of the invading 3' strand by synthesizing new DNA. This changes the D-loop to a cross-shaped structure known as a Holliday junction. Following this, more DNA synthesis occurs on the invading strand (i.e., one of the original 3' overhangs), effectively restoring the strand on the homologous chromosome that was displaced during strand invasion [234].

METH significantly (FDR p-value = 1.82E-03) inhibited HR in astrocytes with the downregulation of 14 out of 17 DEGs (Fig. 25). Expression of genes encoding the proteins of MRN complex, MRE11 (MRE11 homolog, double-strand break repair nuclease), and Nibrin were decreased. As mentioned earlier, the MRN complex plays a vital role in initiating DNA end resection before repair by HR [235]. Downregulation of RPA1, RPA3, and RAD51 was

also observed after METH treatment. RAD54B, which interacts with RAD51 and binds dsDNA [237], was also downregulated. Furthermore, METH also reduced the expression of BRCA1 and BRCA2. The localization of RAD51 to the DSB requires the formation of the BRCA1-PALB2-BRCA2 complex [238]. In addition, BRCA2 binds the single-stranded (ss) DNA and directly interacts with RAD51 to stimulate and maintain strand invasion [239]. METH treatment also downregulated the expression of BRCA1-associated RING domain protein 1 (BARD1) and BRCA1-interacting protein 1 (BRIP1). BARD1/BRCA1 interaction is essential to rapidly relocate BRCA1 and RAD51 proteins to the DSBs [240]. The expression of BLM RecQ-like helicase (BLM) was decreased in response to METH treatment. BLM contributes to the resection of DNA DSBs to generate a single-stranded intermediate that is bound by RPA and RAD51 [241]. Topoisomerase II $\beta$ -binding protein 1 (TOPBP1), known to contribute to DNA repair and be involved in HR [242], was also downregulated after METH treatment. Lastly, METH also downregulated POL  $\delta$  – 2,3, and 4.

Our results demonstrate that METH significantly inhibits HR in astrocytes. In earlier studies, METH has been demonstrated to cause DNA damage in various CNS and non-CNS cells [243-245]. The inability of cells to effectively repair DSBs can result in increased cytotoxicity, cell death, and, potentially, cancer development.

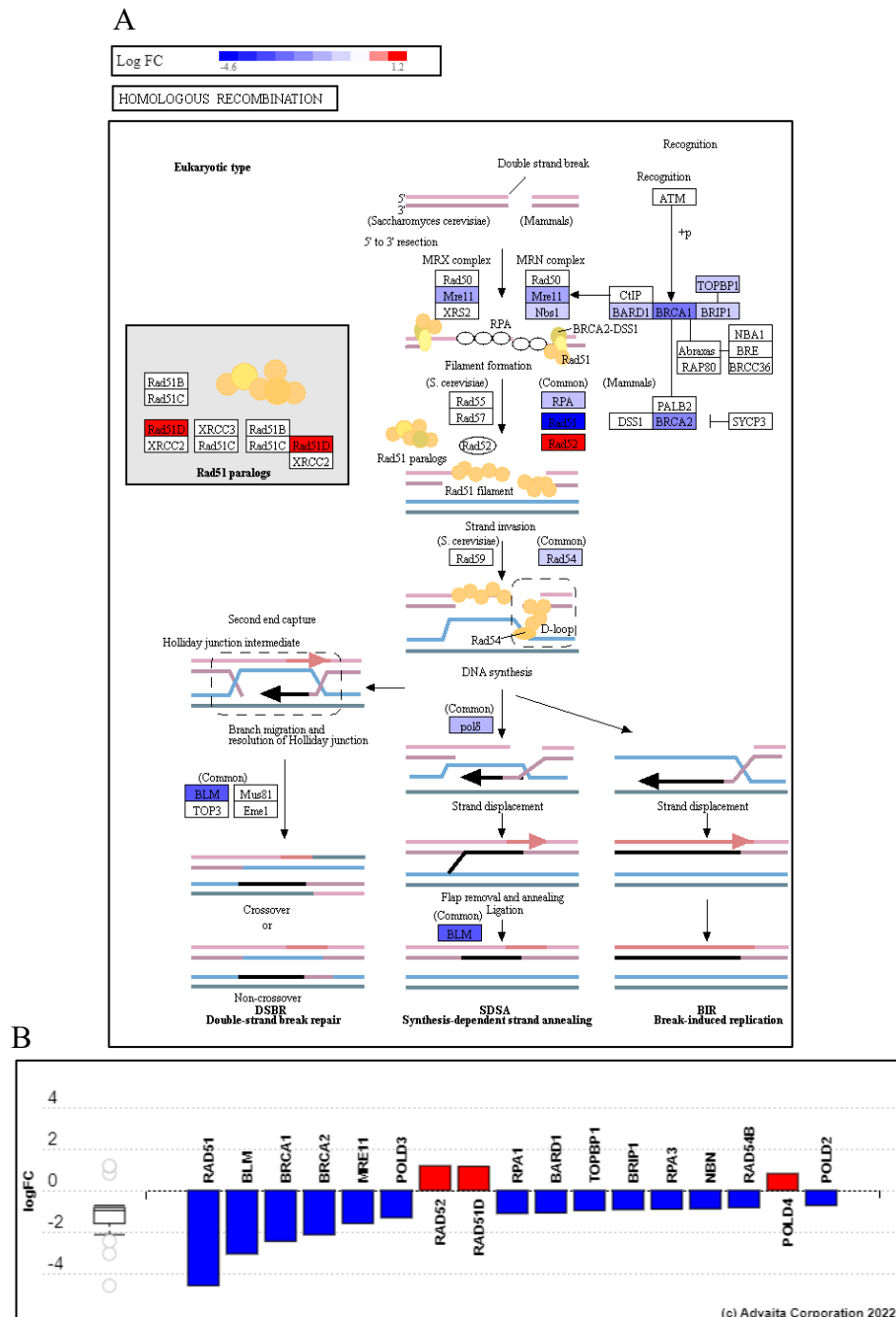


**Figure 25. Effect of METH on homologous recombination pathway in astrocytes.** A. Graphical representation of DEGs in the pathway. Upregulated genes are shown in red. The figure was obtained with iPathwayGuide ([www.advaitabio.com](http://www.advaitabio.com)), using pathway data obtained from the KEGG resource (Pathway: ko03440). B. Gene measured expression bar plot. All DEGs in the pathway are ranked based on their absolute value of log fold change. Upregulated genes are shown in red, downregulated genes are shown in blue. The box and whisker plot on the left summarizes the distribution of all the differentially expressed genes in this pathway. The box represents the 1st quartile, the median, and the 3rd quartile, while the outliers are represented by circles.

### 2.3.3.10 Cellular Senescence

Cellular senescence is an irreversible cellular arrest caused by various events, including telomere shortening, oncogene activation, irradiation, DNA damage, and oxidative stress. As part of the senescence-associated secretory phenotype (SASP), it is characterized by an expanded, flattened shape, senescence-associated beta-galactosidase (SA-b-gal) activity, and the production of inflammatory cytokines, growth factors, and matrix metalloproteinases (SASP). Many biological processes, including aging, neuroprotection, and tumor suppression, are functionally related to cellular senescence [246].

Senescence is generally caused by the activation of one or both p53/p21<sup>WAF1/CIP1</sup> and p16<sup>INK4A</sup>/pRB tumor suppressor pathways [247]. Because p53 and pRB are major transcriptional regulators, they primarily sustain the senescence state by generating extensive changes in gene expression; p21<sup>WAF1/CIP1</sup> acts downstream of p53, whereas p16<sup>INK4A</sup> acts upstream of pRB. They are cyclin-dependent kinase inhibitors (CDKIs) that function as negative regulators of cell cycle progression and are essential components of each pathway [248]. METH significantly decreased the expression of p21<sup>WAF1/CIP1</sup> and p16<sup>INK4A</sup>. Several upstream effectors of p21<sup>WAF1/CIP1</sup> and p16<sup>INK4A</sup> were also upregulated, including HLA (human leukocyte antigen), TSC2 (TSC complex subunit 2), and p62/SQSTM1 (sequestosome 1). A number of genes implicated in cell cycle control downstream of p21<sup>WAF1/CIP1</sup> and p16<sup>INK4A</sup>, were downregulated, indicating cell cycle arrest. These genes included several cyclins and CDKs (explained in detail in section 2.3.3.1). TGF $\beta$  and insulin like growth factor binding protein 3 (IGFBP3), both implicated in the SASP, were likewise downregulated in response to METH treatment (Fig. 26).

Our results showed that METH induces cellular senescence in astrocytes by causing cell cycle arrest. Senescent cells are hypothesized to have a role in developing age-related diseases such as Alzheimer's disease, ALS, and type 2 diabetes [249]. Neurodegeneration is also known to be aided by senescent astrocytes and microglia [250]. As a result, cellular senescence may play a role in METH-induced astrocyte neurotoxicity.

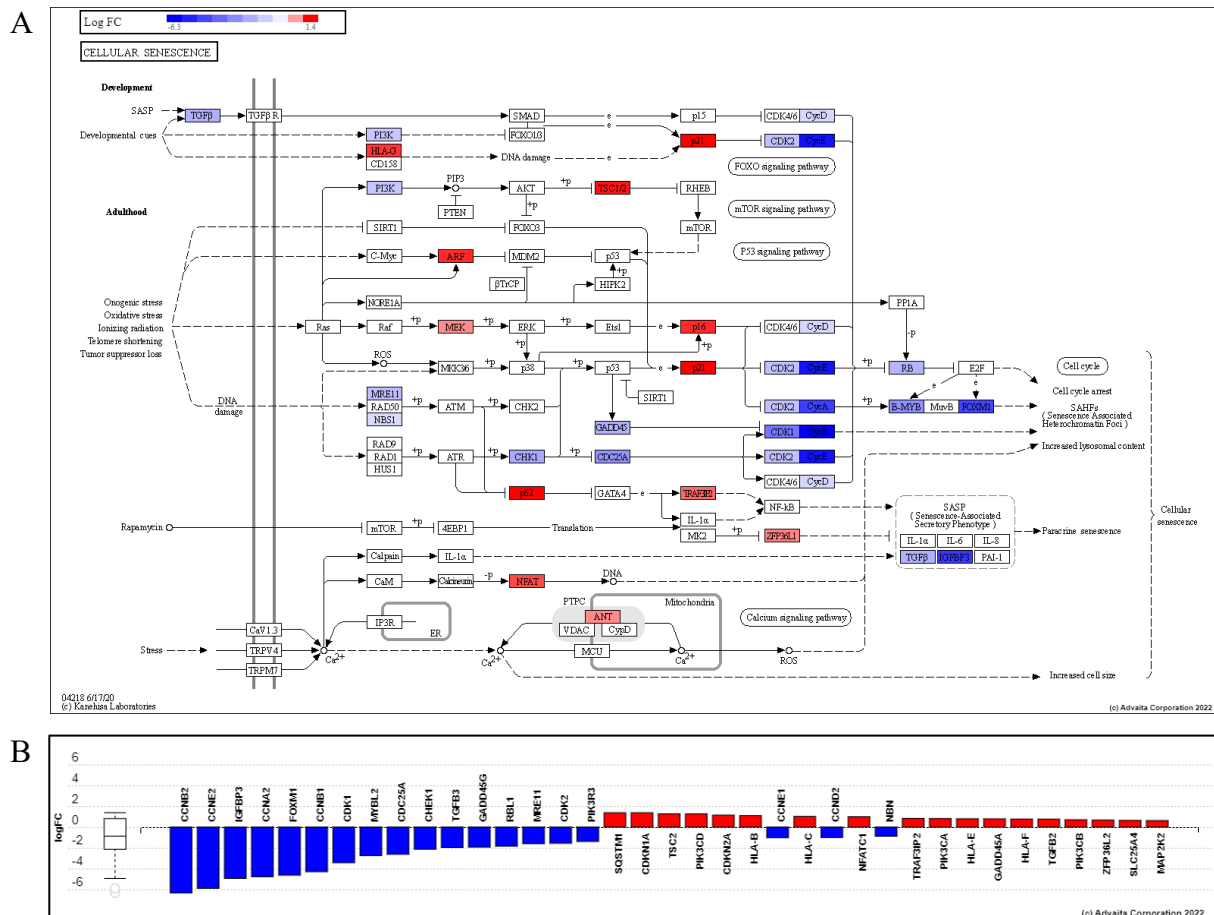


**Figure 26. Effect of METH on cellular senescence pathway in astrocytes.** A. Graphical representation of DEGs in the pathway. Upregulated genes are shown in red. The figure was obtained with iPathwayGuide ([www.advaitabio.com](http://www.advaitabio.com)), using pathway data obtained from the KEGG resource (Pathway: hsa04218). B. Gene measured expression bar plot. All DEGs in the pathway are ranked based on their absolute value of log fold change. Upregulated genes are shown in red, downregulated genes are shown in blue. The box and whisker plot on the left summarizes the distribution of all the differentially expressed genes in this pathway. The box represents the 1st quartile, the median, and the 3rd quartile, while the outliers are represented by circles.

### ***2.3.3.11 Focal Adhesion***

Cell-matrix adhesions are required to function correctly in numerous biological processes, including cell motility, proliferation, differentiation, gene control, and cell survival. At the cell-ECM interface, specialized structures called focal adhesions are generated, in which bundles of actin filaments are tethered to transmembrane integrin family receptors via a multi-molecular complex of junctional plaque proteins. While some members of focal adhesions operate structurally as a link between membrane receptors and the actin cytoskeleton, others act as signaling molecules, including numerous protein kinases and phosphatases, their substrates, and other adaptor proteins. Integrin signaling is dependent on the FAK and Src proteins' non-receptor tyrosine kinase activity and their adaptor protein roles to activate downstream signaling processes. These signaling cascades culminate in actin cytoskeleton remodeling, which is required for cell shape, motility, and gene expression changes. Similar morphological changes and gene expression regulation are started by growth factor binding to their respective receptors, highlighting the extensive interaction between adhesion- and growth factor-mediated signaling.

Treatment with METH significantly (FDR p-value = 0.026) activated the focal adhesion pathway in astrocytes. METH treatment resulted in the downregulation of 14 DEGs and upregulation of 25 DEGs in the focal adhesion pathway (Fig. 27). METH treatment significantly downregulated the genes encoding several ECM proteins, including various collagen (COL) subtypes such as COL1A1, COL9A2, COL9A3, COL1A2, and COL4A6; fibronectin 1 (FN1), and thrombospondin 1 (TSP1). Evidence shows that METH's effect on collagen and fibronectin is cell/tissue-dependent. For example, METH mediates MMP-9-induced degradation of COL1A1 in wounds impairing the wound healing process [251],

whereas METH increases collagen deposition in heart muscles contributing to the development of cardiomyopathy [252, 253]. In astrocytes, collagen induces TSP1 expression [254]. TSP1 is an astrocyte-derived neurogenic factor promoting neurite outgrowth and survival, neuronal migration, and synaptogenesis [255, 256]. TSP1 levels decrease in the human brain with Alzheimer's disease and astrocytes treated with amyloid  $\beta$  proteins [257]. As METH also causes astrogliosis, METH-induced decrease in collagen can lead to reduced expression of TSP-1 in astrocytes. Furthermore, collagen-binding integrin (ITG)  $\alpha 1\beta 1$  is required for collagen-induced TSP-1 expression in astrocytes [254]. In our data, integrin  $\alpha 1$  (ITGA1) was downregulated in response to METH treatment. Although we did not observe any change in integrin  $\beta 1$  (ITGB1) expression, METH has been shown to downregulate integrin  $\beta 1$  in the brain cortex [258]. ITGB1 deletion from astrocytes has also been shown to cause partial reactive gliosis [117]. Our results suggest that METH-induced downregulation of collagen and integrin  $\alpha 1\beta 1$  can decrease TSP1 expression, worsening METH-induced astrogliosis and synaptic alterations.

Treatment with METH resulted in the upregulation of ITGA3, ITGA6, ITGAV, ITGB4, and ITGB5 in astrocytes. Even though METH treatment induced upregulation in integrin subunits, a decrease in the expression of their ligands (collagen and fibronectin) can prevent integrin activation and downstream signaling events. Interestingly, in a previous report, METH administration led to the downregulation of all aforementioned integrin subunits [258]. These conflicting results might stem from the differences in the model (*in vitro* and microarray vs. *in vivo*), the dose used, and the treatment regimen employed. Nevertheless, the effect of METH on integrins requires further studies. There was an upregulation of several growth factors, including platelet-derived growth factor C (PDGFC), vascular endothelial

growth factor B (VEGFB), and hepatocyte growth factor (HGF). Accordingly, METH-treatment upregulated several molecules downstream of ECM/integrin and growth factor-derived signaling such as the catalytic subunits of PI3K family members PI3KCA, -CB, and -CD; protein kinase C  $\beta$  (PRKCB), Rac family small GTPase 3 (Rac3), SHC adaptor protein 2 (SHC2) and 3 (SHC3), and p21 (RAC1) activated kinase 2 (PAK2)

Overall, our results indicate that METH treatment activates the focal adhesion pathway in astrocytes. However, some changes observed in our data, particularly ECM proteins and integrins, conflict with the literature reports. Therefore, a more thorough investigation into the effects of METH on ECM proteins, integrins, and downstream signaling is required.

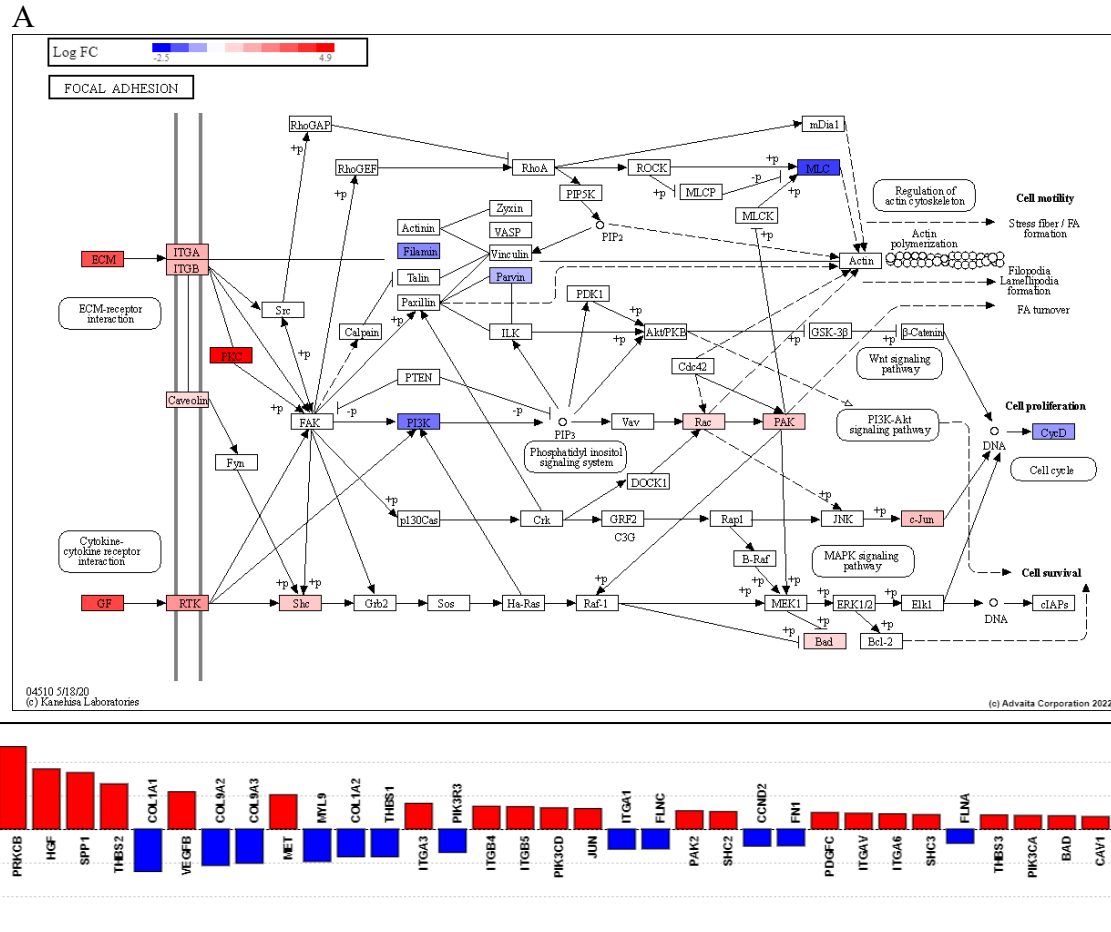


**Figure 27. Effect of METH on focal adhesion pathway in astrocytes.** A. Graphical representation of DEGs in the pathway. Upregulated genes are shown in red. The figure was obtained with iPathwayGuide ([www.advaitabio.com](http://www.advaitabio.com)), using pathway data obtained from the KEGG resource (Pathway: hsa04510). B. Gene measured expression bar plot. All DEGs in the pathway are ranked based on their absolute value of log fold change. Upregulated genes are shown in red, downregulated genes are shown in blue. The box and whisker plot on the left summarizes the distribution of all the differentially expressed genes in this pathway. The box represents the 1st quartile, the median and the 3rd quartile, while the outliers are represented by circles.

### ***2.3.3.12 Phagosome***

Treatment with METH significantly (FDR p-value = 0.029) activated the phagocytic pathway in astrocytes (Fig. 28). Phagocytosis is when a cell takes in relatively big particles and is an essential mechanism in tissue remodeling, inflammation, and infection defense. A phagosome is generated when specialized receptors on the phagocyte surface recognize ligands on the particle surface. Because early phagosomes cannot remove foreign particles, phagosomes gain the essential proteins for maturation through fusion and fission events with endocytic organelles (early or sorting endosomes, late endosomes, and lysosomes) after the development of nascent phagosomes. This is referred to as phagosome maturation. The early, middle, and late phagosomes and the phagolysosome are phases of phagosome development. Early phagosomes are gradually acidified during maturation to create a degradative environment for the destruction of foreign particles and the delivery of various proteins, such as Ras-associated binding GTPase (RAB GTPase), vacuolar ATPase (V-ATPase), acid hydrolases, acidic proteases, and MHC class II molecules. Finally, phagosomes and lysosomes combine to form phagolysosomes, which have an acidic and oxidizing environment and may break down their contents using a variety of hydrolytic enzymes.

METH treatment significantly upregulated transferrin receptor (TNFR) and RAB7A, which are the markers of early [259] and late phagosomes [260], respectively. RAB7A is essential for the fusion between late-stage phagosomes and lysosomes and, consequently, for the function of phagocytes in both pathogen and apoptotic cell clearance [261, 262]. Upregulation in the lysosomal markers, lysosomal-associated membrane protein 1 (LAMP1) and – 2 (LAMP2), and mannose-6-phosphate receptor (M6PR) were also observed.

Furthermore, METH treatment also upregulated syntaxin 7 (STX7), localized to late phagosomes and critical for phagosome-lysosome fusion to form phagolysosomes [263].

Due to the transfer of significant numbers of protons (H<sup>+</sup>) to the lumen of phagosomes via the enhanced buildup of V-ATPase on phagosomal membranes, phagolysosomes contain a very acidic compartment (pH as low as 4.5). V-ATPases are multisubunit complexes composed of two rotary domains. Hydrolysis of ATP in the V1 domain results in the movement of a central rotary complex, which results in H<sup>+</sup> translocation through the integral V0 domain [264]. METH upregulated several V-ATPase subunits of V1 and V0 domains, such as V1E1, V1F, V1C1, V0A1, V0B, V0D1, and V0E1. METH also upregulated genes encoding several subunits of MHC class I (subunits B, C, E, and F) and class II (DM $\alpha$ , DP $\alpha$ 1, DP $\beta$ , and DR $\beta$ 4) molecules, which are presented on the surface of cells after phagocytosis to stimulate antigen-specific T cells.

Microglia in the CNS has been regarded as the only major phagocytes that mediate the elimination of synapses, apoptotic cells, neural debris, and pathogenic proteins [265, 266]. However, it has been demonstrated lately that astrocytes possess a considerable phagocytic ability and contribute to removing synapses and neuronal debris. [267, 268]. The phagocytic activity of astrocytes is increased in neuroinflammatory conditions such as Alzheimer's disease (AD) [269], brain ischemia [270], and motor neuron disease [271]. Glial cell phagocytosis may play beneficial or deleterious roles in the brain when dysregulated. The phagocytic capacity of astrocytes may be necessary for clearing unnecessary synapses, synaptic debris, and extracellular protein aggregates, thus maintaining brain homeostasis and preventing aberrant immune responses [268]. However, hyperactivation of phagocytic pathways can induce damage to live synapses during AD [272] and neurons during stroke [273], respectively.

Results from our data indicate that METH increases the phagocytic activity of astrocytes. As METH induces astrogliosis and causes severe neuroinflammation, further studies are necessary to understand the effect of increased phagocytosis (potentially due to neuroinflammation) on METH's neurotoxicity.

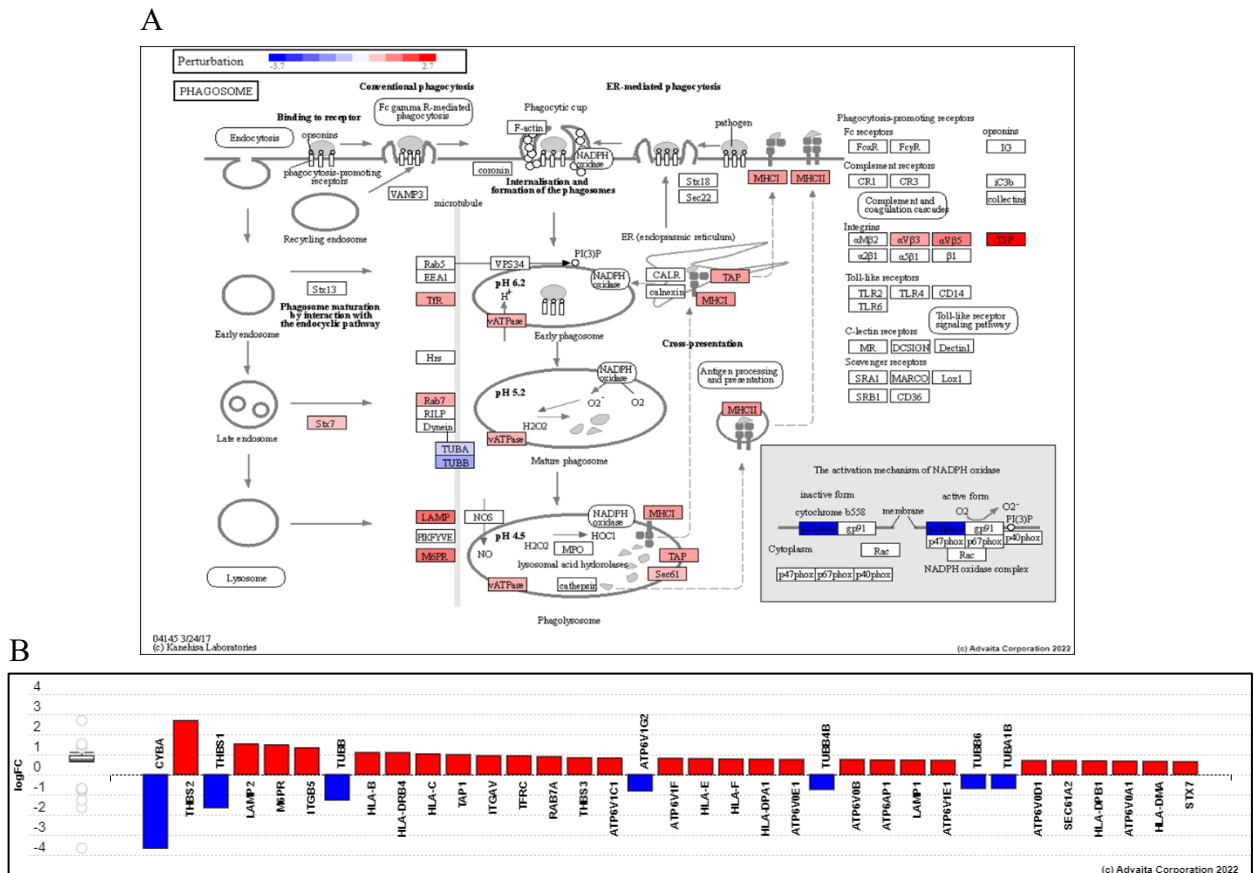


**Figure 28. Effect of METH on phagosome pathway in astrocytes.** A. Graphical representation of DEGs in the pathway. Upregulated genes are shown in red. The figure was obtained with iPathwayGuide ([www.advaitabio.com](http://www.advaitabio.com)), using pathway data obtained from the KEGG resource (Pathway: ko04145). B. Gene measured expression bar plot. All DEGs in the pathway are ranked based on their absolute value of log fold change. Upregulated genes are shown in red, downregulated genes are shown in blue. The box and whisker plot on the left summarizes the distribution of all the differentially expressed genes in this pathway. The box represents the 1st quartile, the median, and the 3rd quartile, while the outliers are represented by circles.

#### **2.3.3.4 Gene Ontology Analysis**

The DEGs were used to identify significantly enriched GO terms in METH-treated astrocytes. The GO terms were used to describe the highest-ranked biological processes (BP), cellular compartment (CC), and molecular function (MF). For each GO term, the number of DEGs annotated to the term was compared to the number of DEGs expected just by chance. Elimination pruning p-value correction was used to iteratively eliminate the genes mapped to a significant GO term from more general GO terms.

Sixteen BP GO terms, 23 CC GO terms, and 7 MF GO terms were found to be significantly enriched after Elim pruning and iterative merging procedure. BP GO terms (Table 5) were mostly related to DNA replication (6 GO terms), cell cycle (3 GO terms), action potential (1 GO term), cell differentiation (1 GO term), and steroid biosynthesis (1 GO term). CC GO terms (Table 6) were primarily associated with the nucleus (10 GO terms), followed by cytoplasm (7 GO terms), lysosome (3 GO terms), and extracellular space (2 GO terms). MF GO terms (Table 7) were associated with DNA replication (5 GO terms) and protein binding (2 GO terms). The GO enrichment analysis demonstrates that METH-treated astrocytes have altered cell cycle and DNA replication.

No.	GO ID	Biological Processes (BP) GO Term Name	Category	# DEGs	p-value (elim)	-Log10 p-value
1	<b>51301</b>	<b>Cell division</b>	<b>Cell cycle</b>	<b>143</b>	<b>2.52E-11</b>	<b>10.60</b>
2	<b>32201</b>	<b>Telomere maintenance via semi-conservative replication</b>	<b>DNA replication</b>	<b>18</b>	<b>3.78E-06</b>	<b>5.42</b>
3	<b>6271</b>	<b>DNA strand elongation involved in DNA replication</b>	<b>DNA replication</b>	<b>16</b>	<b>3.19E-05</b>	<b>4.50</b>
4	<b>0006270</b>	<b>DNA replication initiation</b>	<b>DNA replication</b>	<b>23</b>	<b>3.78E-05</b>	<b>4.42</b>
5	<b>0045540</b>	<b>Regulation of cholesterol biosynthetic process</b>	<b>Steroid biosynthesis</b>	<b>22</b>	<b>6.85E-05</b>	<b>4.16</b>
6	<b>0000727</b>	<b>Double-strand break repair via break-induced replication</b>	<b>DNA repair</b>	<b>10</b>	<b>9.90E-05</b>	<b>4.00</b>
7	<b>0006297</b>	<b>Nucleotide-excision repair, DNA gap filling</b>	<b>DNA repair</b>	<b>14</b>	<b>8.93E-04</b>	<b>3.05</b>
8	<b>0006268</b>	<b>DNA unwinding involved in DNA replication</b>	<b>DNA replication</b>	<b>11</b>	<b>8.93E-04</b>	<b>3.05</b>
9	<b>0000082</b>	<b>G1/S transition of mitotic cell cycle</b>	<b>Cell cycle</b>	<b>73</b>	<b>3.91E-03</b>	<b>2.41</b>
10	<b>0000724</b>	<b>Double-strand break repair via homologous recombination</b>	<b>DNA repair</b>	<b>43</b>	<b>4.33E-03</b>	<b>2.36</b>
11	<b>0019227</b>	<b>Neuronal action potential propagation</b>	<b>Action potential</b>	<b>7</b>	<b>1.19E-02</b>	<b>1.92</b>
12	<b>0000729</b>	<b>DNA double-strand break processing</b>	<b>DNA repair</b>	<b>11</b>	<b>1.85E-02</b>	<b>1.73</b>
13	<b>0000079</b>	<b>Regulation of cyclin-dependent protein serine/threonine kinase activity</b>	<b>Cell cycle</b>	<b>27</b>	<b>4.26E-02</b>	<b>1.37</b>
14	<b>0045669</b>	<b>Positive regulation of osteoblast differentiation</b>	<b>Cell differentiation</b>	<b>20</b>	<b>4.59E-02</b>	<b>1.34</b>
15	<b>0006267</b>	<b>Pre-replicative complex assembly involved in nuclear cell cycle DNA replication</b>	<b>DNA replication</b>	<b>6</b>	<b>4.59E-02</b>	<b>1.34</b>

16	1900264	Positive regulation of DNA-directed DNA polymerase activity	DNA replication	6	4.59E-02	1.34
----	---------	---	-----------------	---	----------	------

**Table 5. Significantly enriched BP GO terms in METH-treated astrocytes**

**Table 6. Significantly enriched CC GO terms in METH-treated astrocytes**

No.	GO ID	Cellular Compartment (CC) GO Term Name	Location	# DEGs	FDR p-value (elim)	-Log10 p- value
1	0005765	Lysosomal membrane	Lysosome	74	1.05E-03	2.98
2	0043202	Lysosomal lumen	Lysosome	30	1.05E-03	2.98
3	0005813	Centrosome	Cytoplasm	104	1.17E-03	2.93
4	0031390	Ctf18 RFC-like complex	Nucleus	6	2.81E-03	2.55
5	0031298	Replication fork protection complex	Nucleus	7	2.81E-03	2.55
6	1990023	Mitotic spindle midzone	Cytoplasm	8	5.46E-03	2.26
7	0030496	Midbody	Cytoplasm	40	6.01E-03	2.22
8	0000777	Condensed chromosome kinetochore	Nucleus	34	7.74E-03	2.11
9	0005658	Alpha DNA polymerase: primase complex	Nucleus	5	1.01E-02	1.99
10	0000781	Chromosome, telomeric region	Nucleus	39	1.28E-02	1.89
11	0005811	Lipid droplet	Cytoplasm	23	1.28E-02	1.89
12	0005737	Cytoplasm	Cytoplasm	1375	1.62E-02	1.79
13	0005730	Nucleolus	Nucleus	146	1.62E-02	1.79
14	0005829	Cytosol	Cytoplasm	672	1.95E-02	1.71
15	0072687	Meiotic spindle	Nucleus	6	1.95E-02	1.71
16	0042470	Melanosome	Cytoplasm	31	2.34E-02	1.63
17	0005654	Nucleoplasm	Nucleus	528	3.51E-02	1.46
18	0000799	Nuclear condensin complex	Nucleus	4	3.51E-02	1.46
19	0030175	Filopodium	Extracellular space	26	3.51E-02	1.46

20	<b>0005871</b>	<b>Kinesin complex</b>	<b>Cytoplasm and nucleus</b>	<b>14</b>	<b>3.51E-02</b>	<b>1.46</b>
21	<b>0042555</b>	<b>MCM complex</b>	<b>Nucleus</b>	<b>6</b>	<b>3.62E-02</b>	<b>1.44</b>
22	<b>0031902</b>	<b>Late endosome membrane</b>	<b>Lysosome</b>	<b>28</b>	<b>3.99E-02</b>	<b>1.40</b>
23	<b>0070062</b>	<b>Extracellular exosome</b>	<b>Extracellular space</b>	<b>306</b>	<b>4.27E-02</b>	<b>1.37</b>

No.	GO ID	Molecular Functions (MF) GO Term Name	# DEGs	FDR p-value (elim)	-Log10 p-value
1	<b>0017116</b>	<b>single-stranded DNA helicase activity</b>	<b>12</b>	<b>2.01E-05</b>	<b>4.70</b>
2	<b>0042802</b>	<b>identical protein binding</b>	<b>295</b>	<b>1.02E-03</b>	<b>2.99</b>
3	<b>0003688</b>	<b>DNA replication origin binding</b>	<b>13</b>	<b>1.02E-03</b>	<b>2.99</b>
4	<b>0043138</b>	<b>3'-5' DNA helicase activity</b>	<b>10</b>	<b>1.09E-02</b>	<b>1.96</b>
5	<b>0003697</b>	<b>single-stranded DNA binding</b>	<b>31</b>	<b>1.53E-02</b>	<b>1.81</b>
6	<b>0003689</b>	<b>DNA clamp loader activity</b>	<b>6</b>	<b>2.63E-02</b>	<b>1.58</b>
7	<b>0019901</b>	<b>protein kinase binding</b>	<b>114</b>	<b>9.38E-02</b>	<b>1.03</b>

**Table 7. Significantly enriched MF GO terms in METH-treated astrocytes**

### 2.3.3.5 Upstream Regulatory Analysis

To identify upstream transcription regulators that can potentially explain the experimental DEGs, iPG's predicted upstream regulators analysis was performed. This analysis classified the upstream regulators as activated (present) or inhibited (absent). For example, upstream regulators that are predicted to be downregulated in METH samples relative to Controls were classified as inhibited, and vice versa for activated regulators.

One hundred and seventy-nine upstream regulators were predicted as significantly (FDR p-value < 0.05) inhibited, and 13 upstream regulators were predicted as significantly activated in METH-treated astrocytes. Table 8 lists the top 15 significantly inhibited upstream regulators, and table 9 lists activated regulators. For each upstream regulator  $u$ , the table shows the number of DE targets supporting the hypothesis that the regulator is inhibited  $DTI(u)$  (Table 8) or activated  $DTA(u)$  (Table 9) and the total number of DEGs downstream of  $u$   $DT(u)$ . Inhibited transcriptional regulators are associated with the transcriptional control of cell division, intracellular transport, and cell migration. In contrast, activated regulators are involved in the transcriptional regulation of genes in sterol biosynthesis, chromatin binding, cell cycle, RNA splicing, nerve growth, and innate immunity.

Taken together, upstream regulatory analysis demonstrates that several transcriptional regulators involved in critical cellular functions are robustly dysregulated in METH-treated astrocytes.

**Table 8. Top 15 upstream regulators predicted as inhibited in METH-treated astrocytes**

No.	Upstream regulators predicted as inhibited		DTI(u)	DT(u)	p-value	z-score
	Symbol	Name				
1	RANGAP1	Ran GTPase activating protein 1	33	34	1.52E-14	-5.49
2	PPP2CB	Protein phosphatase 2 catalytic subunit beta	32	33	1.52E-14	-5.40
3	RANBP2	RAN binding protein 2	43	45	1.52E-14	-6.11
4	PPP2R5A	Protein phosphatase 2 regulatory subunit B'alpha	31	31	1.52E-14	-5.57
5	NUP43	Nucleoporin 43	41	43	1.52E-14	-5.95
6	INCENP	Nnner centromere protein	31	32	1.52E-14	-5.30
7	PAFAH1B1	Platelet activating factor acetylhydrolase 1b regulatory subunit 1	31	32	1.52E-14	-5.30
8	PPP2R1B	Protein phosphatase 2 scaffold subunit Abeta	31	32	1.52E-14	-5.30
9	PPP2R5B	Protein phosphatase 2 regulatory subunit B'beta	31	32	1.52E-14	-5.30
10	PPP2R5C	Protein phosphatase 2 regulatory subunit B'gamma	31	32	1.52E-14	-5.30
11	CLIP1	CAP-Gly domain containing linker protein 1	31	32	1.52E-14	-5.30
12	MAD1L1	Mitotic arrest deficient 1 like 1	31	32	1.52E-14	-5.30
13	ZW10	ZW10 kinetochore protein	31	32	1.52E-14	-5.30
14	NUDC	Nuclear distribution C, dynein complex regulator	31	32	1.52E-14	-5.30
15	CLASP1	Cytoplasmic linker associated protein 1	31	32	1.52E-14	-5.30

**Table 9. Upstream regulators predicted as activated in METH-treated astrocytes**

No.	Upstream regulators predicted as activated		DTA(u)	DT(u)	p-value	z-score
	Symbol	Name				
1	NFYB	Nuclear transcription factor Y subunit beta	11	11	1.32E-07	3.32
2	NFYC	Nuclear transcription factor Y subunit gamma	10	10	7.27E-07	3.16
3	SREBF2	Sterol regulatory element binding transcription factor 2	12	12	2.12E-06	3.46
4	RBL2	RB transcriptional corepressor like 2	9	9	3.91E-06	3.00
5	NFYA	Nuclear transcription factor Y subunit alpha	10	11	4.24E-06	2.71
6	E2F5	E2F transcription factor 5	7	7	7.19E-05	2.65
7	E2F4	E2F transcription factor 4	8	8	7.19E-05	2.83
8	SRSF10	Serine and arginine rich splicing factor 10	17	18	9.14E-05	3.77
9	RCHY1	Ring finger and CHY zinc finger domain containing 1	7	7	4.54E-03	2.65
10	BDNF	Brain derived neurotrophic factor	13	13	8.69E-03	3.61
11	IRF9	Interferon regulatory factor 9	11	12	2.00E-02	2.89
12	STAT2	Signal transducer and activator of transcription 2	11	11	4.12E-02	3.32
13	ISL1	ISL LIM homeobox 1	5	5	4.91E-02	2.24

## 2.4 Discussion

METH is a strong psychostimulant that produces significant neurotoxicity with repeated use. Although several mechanisms, such as oxidative stress, excitotoxicity, and neuroinflammation, are proposed as crucial drivers of METH's neurotoxicity, molecular underpinnings for these mechanisms are yet to be fully elucidated. Astrocytes outnumber neurons in the human brain and play critical roles in various functions within the CNS, including the trophic and metabolic support of neurons [274]. Any changes in astrocyte physiology can have significant implications on neuronal and CNS homeostasis. Limited studies examining the effect of METH on astrocytes exist in the literature. Therefore, the purpose of the present study was to perform a detailed characterization of METH-induced transcriptome changes in astrocytes.

METH abuse has many clinical manifestations, but here we focused primarily on the effects of a 3-day, once-daily exposure to METH. Our dose of 500  $\mu\text{M}$  is comparable to the casual abuse of METH that results in plasma concentrations in the mid  $\mu\text{M}$  with up to ten times accumulation in brain tissue [275-277]. Our transcriptome-wide microarray demonstrated significant alterations in the expression profile of various genes in the astrocytes, as seen by the large number of genes differentially regulated by repeated treatments of METH. Our present study shows that once-daily treatment for 3 days drastically changes the gene expression profile in astrocytes, with 1,819 DEGs (748 downregulated and 1,071 upregulated genes) by greater than 1.5-fold. These DEGs are critically associated with METH-induced re-programming of astrocytes and can serve as putative biomarkers for the development of neurotoxicity.

Pathway analysis of the DEGs revealed 12 biological pathways to be significantly (FDR  $p\text{-value} < 0.05$ ) affected in METH-treated astrocytes. Several essential genes, including cyclins and CDKs, which are involved in the regulation of the cell cycle at critical checkpoints such as

G1/S, G2/M, and SAC, were downregulated after METH treatment indicating the induction of cell cycle arrest in astrocytes. Treatment with METH also significantly inhibited DNA replication in astrocytes which takes place in the S phase of the cell cycle. METH upregulated genes that kickstart the p53 signaling pathway and cellular senescence, further contributing to the cell cycle arrest. Damage and errors are difficult to repair once cell cycle arrest occurs over the course of cell division. Moreover, METH significantly inhibited 3 main pathways of DNA repair in astrocytes – mismatch repair, BER, and homologous recombination. During various cell cycle phases, several DNA repair mechanisms are active, allowing the cells to repair DNA damage. These repair activities are crucial for maintaining the genomic integrity of cells [278]. When the damaged DNA persists, apoptosis, regulatory response to DNA damage, is triggered to eliminate cells with substantial genomic instability [279]. Indeed, METH significantly induced apoptosis in astrocytes. In addition to the pathways, METH significantly enriched several molecular functions and cellular components involved in the cell cycle, DNA replication, and repair. The combinatorial failure of cell cycle regulation, DNA replication, and DNA repair mechanisms resulting in cell cycle arrest and apoptosis can significantly contribute to METH's neurotoxicity.

There is increasing evidence that astrocyte activation and dysfunction have an active role in the pathogenesis of several neurodegenerative disorders [280, 281]. The concept that glial cells can contribute to disease severity and accelerate its progression is perhaps most advanced in ALS and Parkinson's disease. However, it is becoming apparent that this principle also extends to several substance use disorders [282]. While astrocytosis is the primary hallmark of substance abuse toxicity and neurodegenerative diseases, significant astrocyte death has been observed to follow astrocytosis [83]. These dying astrocytes can then kill neighboring cells, including neurons and microglia [84]. Therefore, although not necessarily instigators of neurodegeneration, both a

loss of their normal supportive function and a gain of toxic functions (e.g., reactive astrocytosis) are thought to underlie neuronal death in neurodegenerative diseases [152]. In recent years, substantial efforts have been devoted to the development of neuroprotective therapies. However, almost all the neuroprotective agents have failed to demonstrate efficacy in clinical trials [283, 284]. Although many factors have been identified that likely contribute to the failure in clinical translation of these neurocentric therapies, it is possible that saving neurons alone is not sufficient to benefit the neurotoxic brain.

Given their essential role in neuroprotection, astrocytes may be worthy therapeutic targets in the development of restorative therapies to treat METH neurotoxicity. Thus, to develop successful clinically relevant neuroprotective and neurorestorative strategies, additional research efforts on METH's effect on astrocytes are needed, in addition to the current neurocentric strategies.

## CHAPTER 3: EVALUATION OF THE EFFECT OF AMPHETAMINE ON THE EXPRESSION OF INTEGRINS AND CELL DEATH IN ASTROCYTES

### 3.1 Introduction

Integrins are transmembrane heterodimeric glycoprotein cell surface receptors consisting of non-covalently linked  $\alpha$  and  $\beta$  subunits. At least 24 distinct heterodimers are known to form by a combination of 18  $\alpha$ -subunits and 8  $\beta$ -subunits. Each integrin heterodimer consists of a large extracellular domain, a single membrane-spanning transmembrane domain, and a short intracellular cytoplasmic domain [85]. Integrins bind to various ECM proteins through the extracellular domain and generate an intracellular signal. Conversely, their functions can also be regulated by signals generated from within the cell. Integrins link the ECM to the intracellular cytoskeletal network and multiple signaling pathways that regulate cellular behaviors such as adhesion, proliferation, survival, shape, polarity, motility, gene expression, and differentiation [85].

Integrins are widely distributed in the brain, playing crucial roles in axon and dendrite outgrowth [285, 286], neuroblast migration [287, 288], synapse formation [289, 290], and synaptic plasticity [102-106]. Astrocytes, the most important supporting cells in the CNS, express integrin  $\alpha$ 1,  $\alpha$ 2,  $\alpha$ 3,  $\alpha$ 5,  $\alpha$ V,  $\beta$ 1,  $\beta$ 3,  $\beta$ 5,  $\beta$ 6, and  $\beta$ 8 subunits [98]. Integrin subunits expressed on astrocytes are known to play critical roles in various functions such as survival, synapse formation, metabolic support to neurons, transmitter uptake, and release [92, 290]. Astrocyte and neuronal functions vary during development and disease, as does integrin expression [291]. Altered integrin expression has been observed in several neurological and psychiatric disorders, making them attractive targets for pharmacological manipulations [292, 293].

Previous studies have shown that the downregulation of integrin subunits is associated with the induction of cell death in a wide variety of cells, including astrocytes [141-147, 294]. Apoptosis, in these cases, usually happens because of the lack of the ability of integrins to bind to ECM proteins and initiate downstream cell survival cascades such as PI3K/Akt and Ras/Raf/MEK pathways [148]. As neurons depend on astrocytes for nutritional support and other critical functions, any changes in astrocyte survival can negatively impact neuronal survival and contribute to neurotoxic effects.

AMPH, a highly addictive ATS affecting mainly monoamine neurotransmitter systems, causes apoptosis via several mechanisms such as oxidative stress, ER stress, and excitotoxicity [27]. METH has been shown to cause downregulation of integrins subunits in rat cortex [258]. However, whether METH-induced integrin downregulation is related to functional outcomes, such as cell death, is unknown. Therefore, the present study was undertaken to understand the effect of AMPH on the expression of integrin subunits in astrocytes and its potential contribution to cell death. This study addresses an important gap in our knowledge in view of the possible role of integrins in METH-induced toxic effects in astrocytes.

## **3.2 Materials and Methods**

### **3.2.1 Chemicals and Reagents**

Dulbecco's Modified Eagle's medium (DMEM) (with L-Glutamine, 4.5g/L Glucose, and Sodium Pyruvate), MEM nonessential amino acids (100X), sodium bicarbonate (7.5% solution), and gentamicin sulfate (50 mg/mL solution) were purchased from Corning Inc. (Corning, NY). Heat-inactivated fetal bovine serum (FBS) was purchased from R&D Systems, Inc. (Minneapolis, MN). Amphetamine hemisulfate (AMPH) was purchased from Sigma-Aldrich (St. Louis, MO). RNeasy Mini Kit was purchased from QIAGEN Inc. (Germantown, MD). Anti-Integrin  $\alpha 1$

antibody (#ab243032) was purchased from AbCam (Waltham, MA). Anti-Integrin  $\alpha$ 2 antibody (#sc-74466) was purchased from Santa Cruz Biotechnology, Inc (Dallas, TX). Antibodies against integrin  $\beta$ 1 (#4706), caspase-3 (#9662), cleaved caspase-3 (#9661), and GAPDH (#5174) were obtained Cell Signaling Opti-MEM™ I Reduced Serum Medium, and Lipofectamine™ 3000 Transfection Reagent were purchased from Thermo Fisher Scientific (Waltham, MA). siRNAs against integrins  $\alpha$ 1 (#sc-43125),  $\alpha$ 2 (#sc-29371), and  $\beta$ 1 (#sc-35674) and control siRNA (#sc-37007) were obtained from Santa Cruz Biotechnology, Inc (Dallas, TX)

### **3.2.2 Cell Culture**

All cell culture experiments were conducted using primary adult human astrocytes (HA) isolated from post-mortem cortical tissues of four adult donors. HA from donors 1 and 2 were obtained from Neuromics (Edina, MN), and HA from donors 3 and 4 were obtained from Cell Applications, Inc. (San Diego, CA). Experimental use of HA was approved by the UMKC Institutional Review Board and Institutional Biosafety Committee. Cells were cultured in Dulbecco's Modified Eagle's medium (DMEM) supplemented with 1% sodium bicarbonate, 1% non-essential amino acids, 10% (v/v) fetal bovine serum, and 50  $\mu$ g/ml of Gentamicin sulfate. Serum-free media was used for experiments when necessary. Cells were cultured in 75 or 150 cm<sup>2</sup> flasks in 15-25 ml complete DMEM and maintained in an incubator at 37°C and humidified air with 5% CO<sub>2</sub>. Cells were passaged after reaching confluency. All experiments were performed with cells between 2 - 10 passages. The cells were incubated overnight to allow them to adhere and treated the following day.

### 3.3.3 Quantitative Real-Time Reverse Transcription Polymerase Chain Reaction (qRT-PCR)

qRT-PCR primers for integrin subunits  $\alpha 1$  (ITGA1),  $\alpha 2$  (ITGA2),  $\alpha 3$  (ITGA3),  $\alpha 5$  (ITGA5),  $\alpha V$  (ITGAV),  $\beta 1$  (ITGB1),  $\beta 3$  (ITGB3),  $\beta 5$  (ITGB5),  $\beta 6$  (ITGB6), and  $\beta 8$  (ITGB8) were designed and ordered using Integrated DNA Technologies (Coralville, IA) PrimerQuest™ tool (Primer sequences shown in Table 10). The annealing temperature for a given integrin primer pair was first determined by performing melt curve analysis followed by agarose gel electrophoresis. After determining the correct annealing temperature for integrin primers, the effect of AMPH on the mRNA expression of integrin subunits was assessed. Briefly, astrocytes were plated in 6-well culture plates at  $0.5 \times 10^6$  cells/well (for time points up to 12 h) and  $0.25 \times 10^6$  cells/well (for 24, 36, and 48 h time points). Cells were then treated with 25, 50, 100, 200, 500, and 1000  $\mu\text{M}$  AMPH (dissolved in 1X PBS) once for 1, 3, 6, 12, 24, 36, and 48 hrs. At indicated time points, media was aspirated, and total RNA was extracted from the cells using an RNA isolation kit from IBI Scientific (Dubuque, IA). RNA purity and quantity were analyzed using NanoDrop™ ND-1000 Spectrophotometer. RNA (100  $\mu\text{g}$ ) from each sample was used for qRT-PCR using iTaq™ Universal SYBR® Green One-Step Kit (Bio-Rad Laboratories, Hercules, CA) on CFX Connect™ Real-Time System (Bio-Rad Laboratories, Hercules, CA). qRT-PCR consisted of reverse transcription, denaturation, annealing, and extension steps. Annealing temperatures for the primers are shown in Table 10. After qRT-PCR, the relative fold expression of the genes was calculated using the  $2^{-\Delta\Delta\text{Ct}}$  method. Hypoxanthine phosphoribosyltransferase (HPRT) was used as the internal control.

**Table 10. List of primers and their annealing temperatures**

No.	Gene	Primer sequence	Annealing Temperature (°C for 30 sec)
1	ITGA1	Fwd: 5'-GTA GTT GAC AAC ACA AAA CAA ACA A-3' Rev: 5'-GCT TCA TTC CAA CAA AAT TTT ATT T-3'	55.5
2	ITGA2	Fwd: 5'-GGA ACG GGA CTT TCG CAT-3' Rev: 5'-TGA TGA GAA AGC CGA AGT ACC-3'	53.6
3	ITGA3	Fwd: 5'-AAG GGA CCT TCA GGT GCA-3' Rev: 5'-ATG GTA AAT CAC CGG CTA CA-3'	54.6
4	ITGA5	Fwd: 5'-TGC AGT GTG AGG CTG TGT ACA-3' Rev: 5'-AGA GCG TCA GGT GGC CAC-3'	57.5
5	ITGAV	Fwd: 5'-ATA GGG TGA CTT GTG TTT TTA GG-3' Rev: 5'-GGA CCT TAG CAA TCA TGT CTT T-3'	55.2
6	ITGB1	Fwd: 5'-GTA ACC AAC CGT AGC AAA GGA-3' Rev: 5'-TCC CCT GAT CTT AAT CGC AAA AC-3'	54.2
7	ITGB3	Fwd: 5'-CCG TGA CGA GAT TGA GTC A-3' Rev: 5'-TTC TAG TGG AAA GTC CAT CCT-3'	55.8
8	ITGB5	Fwd: 5'-GGA GCC AGA GTG TGG AAA CA-3' Rev: 5'-GAG GGA GTT TGC AAA GTT TC-3'	57.1
9	ITGB6	Fwd: 5'-GAG GAC TAC CCG GTG GAT TTG-3' Rev: 5'-TCC TTT ATT GTG TTG AGG TCG TC-3'	53.5
10	ITGB8	Fwd: 5'-ACC AGG AGA AGT GTC TAT CCA G-3' Rev: 5'-TCC CGT GAC TTT CGT CTT GG-3'	58.7
11	HPRT	Fwd: 5'-GCT TTC CTT GGT CAG GCA GTA-3' Rev: 5'-CCA ACA CTT CGT GGC GTC CTT T-3'	55

### 3.3.4 Western Blot

Astrocytes were plated in 6-well plates at  $0.25 \times 10^6$  cells/well and treated with 500  $\mu$ M AMPH once for 24, 36, and 48 h. For experiments involving integrin subunits  $\alpha 1$ ,  $\alpha 2$ , and  $\beta 1$ , cells were seeded into 6-well plates precoated with collagen type I. At indicated time points, whole-cell lysates were prepared by lysing cells with RIPA buffer containing Halt™ Protease and Phosphatase Inhibitor Single-Use Cocktail (100  $\mu$ L/10 mL RIPA Buffer). Protein concentration was measured using Pierce™ BCA Protein Assay Kit and Benchmark Plus™ Microplate Spectrophotometer (Bio-Rad Laboratories, Hercules, CA). Twenty to 40  $\mu$ g protein samples were loaded on 12% polyacrylamide gel and electrophoresed at 90 V for 150 min using a Mini-PROTEAN Tetra Cell System (Bio-Rad Laboratories, Hercules, CA). Proteins were then transferred to polyvinylidene difluoride (PVDF) membranes at 25V for 35 min using Trans-Blot Turbo Transfer System (Bio-Rad Laboratories, Hercules, CA). Membranes were blocked in 5% nonfat dry milk in 1X PBS containing 0.1% Tween® 20 (PBST) for 1 h followed by overnight incubation with primary antibody diluted 1:1500 in PBST. Membranes were washed and incubated in species-specific secondary antibodies (1:2000) for 2 h.

The blots were visualized using Immobilon™ Western Chemiluminescent HRP Substrate (Millipore Corporation, Billerica, MA) on a FluorChem E Gel Documentation System (ProteinSimple, Inc., San Hose, CA). After probing for ITGA1, blots were stripped and re-probed for ITGA2 and ITGB1. Similarly, after probing for caspase-3 and cleaved caspase-3, blots were re-probed for the loading control, glyceraldehyde 3-phosphate dehydrogenase (GAPDH). Stripping was performed immediately after exposure of the membrane to film, care being taken to ensure that the membrane did not dry out. The membranes were stripped by incubating in Restore™ PLUS Western Blot Stripping Buffer

(ThermoFisher Scientific, Waltham, MA), followed by washing with 1X PBS , and blocking in 5% nonfat dry milk in 1X PBST. Quantification was done using spot densitometry with AlphaView Software (ProteinSimple, Inc., San Hose, CA). As blot was stripped and re-probed with different antibodies, same loading controls (GAPDH) were used to normalize expression values of ITGA1, ITGA2, ITGB1 from AMPH-treated astrocytes from all donors, and caspase-3 and cleaved caspase-3 from AMPH-treated astrocytes from donors 1 and 2. Separate loading controls were used to normalize expression values for caspase-3 and cleaved caspase-3 from donor 3.

### **3.3.5 XTT Cell Viability Assay**

XTT Cell Viability Assay Kit (Biotium, Inc., Fremont, CA) was used to determine cell viability based on the ability of mitochondrial enzymes in metabolically active astrocytes to reduce the yellow tetrazolium derivative 2,3-Bis-[2-methoxy-4-nitro-5-sulfohenyl]-2H-tetrazolium-5-carboxanilide (XTT) to form water-soluble, orange-colored formazan product. Briefly, astrocytes were plated in 96-well plates at a density of 10,000 cells/well (100  $\mu$ L total volume/well) and treated with either sterile 1X PBS (Control) or 500  $\mu$ M AMPH (Test) for 24 and 48 h. Activated XTT solution was prepared immediately before use by mixing 25  $\mu$ L activation reagent with 5 mL XTT solution. After the incubation period, 50  $\mu$ L activated XTT solution was added to each well, and the plates were incubated for 6 h at 37°C. The absorbance (A) was measured at 450 nm at a background of 650 nm using a Benchmark Plus™ Microplate Spectrophotometer. Corrected absorbance values ( $A_{450} - A_{650}$ ) of six replicates were used to calculate % viability using the formula:  $(\text{Corrected } A_{\text{Test}} / \text{Corrected } A_{\text{Control}}) \times 100$ .

### 3.3.6 LDH Cytotoxicity Assay

Lactate dehydrogenase (LDH) is a cytosolic enzyme that is released in the cell culture media after plasma membrane damage. The extracellular LDH in the media can be quantified by a coupled enzymatic reaction in which LDH catalyzes the conversion of lactate to pyruvate via NAD<sup>+</sup> reduction to NADH. Oxidation of NADH by diaphorase leads to the reduction of a tetrazolium salt to a red formazan product that is measured spectrophotometrically. The level of formazan formation is directly proportional to the amount of LDH released into the medium, indicating cytotoxicity [295]. Invitrogen™ CyQUANT™ LDH Cytotoxicity Assay Kit (ThermoFisher Scientific, Waltham, MA) was used to measure the cytotoxic effect of AMPH on astrocytes. Briefly, astrocytes were plated in 96-well plates at a density of 8,000 cells/well (100 μL total volume/well) and allowed to grow to adequate confluency. One day before incubation, complete DMEM was replaced with 100 μL serum-free DMEM, and the plate was incubated overnight at 37°C and humidified air with 5% CO<sub>2</sub>. The next day, in compound-treated LDH activity wells, media was replaced with 100 μL serum-free DMEM containing 500 μM AMPH. In the spontaneous LDH activity wells, media was replaced with 90 μL serum-free DMEM and 10 μL sterile distilled water. In the maximum LDH activity wells, 10 μL media was aspirated, and 10 μL of 10X lysis buffer (positive control) was added. The plate was then incubated for 24 or 48 h at 37°C and humidified air with 5% CO<sub>2</sub>. After the incubation period, 50 μL of each sample medium was transferred to a new 96-well plate, and 50 μL of the reaction mixture was added to each well. The plate was incubated in the dark at 25°C for 30 min, and 50 μL of the stop solution was added to each well. The absorbance was measured at 490 nm at a background of 690 nm using a Benchmark Plus™ Microplate Spectrophotometer. Corrected absorbance values ( $A_{490}-A_{690}$ ) of three replicates were used to calculate %

cytotoxicity using the formula:  $[(LDH_C - LDH_S) / (LDH_M - LDH_S)] \times 100\%$ , where LDH<sub>C</sub>, LDH<sub>S</sub>, and LDH<sub>M</sub> represent the compound-treated, spontaneous, and maximum LDH activity, respectively.

### **3.3.7 Caspase-3 Activity Assay**

Caspase-3/ CPP32 colorimetric assay kit (BioVision inc., Mountain View, CA) was used to determine caspase-3 activation in AMPH-treated astrocytes. The assay is based on spectrophotometric detection of the chromophore p-nitroaniline (pNA) after cleavage from the labeled substrate DEVD-pNA. Briefly, astrocytes were plated in 6-well plates at a density of  $0.5 \times 10^6$  cells/well, allowed to adhere overnight, and treated with either sterile 1X PBS or 500  $\mu$ M AMPH for 24 and 48 h. After the treatment, cells were detached from the plate, resuspended in 50  $\mu$ L of chilled cell lysis buffer, and incubated on ice for 10 min. Cells were then centrifuged for 1 min at 10,000 g, and supernatant (cytosolic extract) was transferred to a fresh tube. Protein concentration in the cytosolic extract was measured using Pierce™ BCA Protein Assay Kit, and 200  $\mu$ g protein was diluted in 50  $\mu$ L lysis buffer. Each sample was mixed with 50  $\mu$ L of 2X Reaction Buffer (containing 10 mM DTT) and 5  $\mu$ L of the 4 mM DEVD-pNA substrate (200  $\mu$ M final concentration) and incubated at 37°C for 2 h. Absorbance was measured at 405 nm using a Benchmark Plus™ Microplate Spectrophotometer.

### **3.3.8 *In vitro* Silencing Activity and Cell Death Analysis**

The contribution of integrins to AMPH-induced apoptosis was investigated by silencing the expression of ITGA1, ITGA2, and ITGB1 and performing LDH cytotoxicity and caspase-3 activity assays. First, the ability of siRNAs to silence the expression of integrin  $\alpha$ 1,  $\alpha$ 2, and  $\beta$ 1 subunits in astrocytes was assessed. Briefly,  $0.5 \times 10^6$  cells were seeded in a 6-well plate pre-coated with collagen in serum-free DMEM and allowed to adhere overnight. The

next day, culture media was removed, cells were washed twice with 1X PBS, and fresh serum-free DMEM was added to the wells. Transfection medium (Opti-MEM™ I Reduced-Serum Medium) and siRNA were added to a 2 mL tube to prepare solution A (siRNA duplex solution). Subsequently, transfection medium and transfection reagent (Lipofectamine 3000™) was added to another 2 mL tube to prepare solution B (dilute transfection reagent). Solution A was mixed in equal amounts with solution B and incubated for 30 min at room temperature. The culture medium was removed from the 12-well plate, 100 µl/well of the mixed solution was added to each well along with 900 µL of transfection medium to achieve 50 nM final siRNA concentration. A scrambled siRNA was used as a negative control. After transfection for 24 h, total RNA was isolated using an RNA isolation kit from IBI Scientific (Dubuque, IA). RNA purity and quantity were analyzed using NanoDrop™ ND-1000 Spectrophotometer. RNA (100 µg) from each sample was used to check mRNA expression levels of ITGA1, ITGA2, and ITGB1 with qRT-PCR using iTaq™ Universal SYBR® Green One-Step Kit (Bio-Rad Laboratories, Hercules, CA) on CFX Connect™ Real-Time System (Bio-Rad Laboratories, Hercules, CA) as described in section 3.3.3.

To check the effect of ITGA1, ITGA2, and ITGB1 silencing on apoptosis in astrocytes, cells were transfected with integrin siRNAs as described above. After 24 hours of transfection, the transfection media was replaced with complete DMEM, and the cells were incubated at 37°C for 8 h. After 8 h, cells were trypsinized and re-seeded at a density of 10,000 cells/well in 96-well plate for XTT cell viability assay. Cells were then treated with 500 µM AMPH for 24 and 48 h, XTT assay was performed, as described in section 3.3.5.

### 3.3.9 Statistical Analysis

Statistical analyses were performed using Microsoft Excel and GraphPad Prism (v8.0) (GraphPad Software, San Diego, CA). Data were represented as mean  $\pm$  standard deviation (SD) or mean  $\pm$  95% confidence interval (CI). Results were based on at least 3 separate experiments from each donor astrocyte unless otherwise specified. The comparisons between the Control/Scrambled control groups and treatment groups were performed using one-way ANOVA followed by Dunnett's multiple comparison test. p-value  $<$  0.05 was considered significant.

## 3.4 Results

### 3.4.1 AMPH induces a dose- and time-dependent decrease in the mRNA expression of integrin $\alpha$ subunits in astrocytes

Astrocytes were treated with 25, 50, 100, 200, 500, and 1000  $\mu$ M AMPH for 1, 3, 6, 12, 24, 36, and 48 h. At indicated time points, cells were harvested, total RNA was extracted, and mRNA expression levels of integrin  $\alpha$  subunits expressed on astrocytes were measured using qRT-PCR. A significant dose- and time-dependent decrease in the expression of ITGA1 (Fig. 29), ITGA2 (Fig. 30), ITGA3 (Fig. 31), ITGA5 (Fig. 32), and ITGAV (Fig. 33) was observed post AMPH treatment.

Except for the 25  $\mu$ M dose, the mRNA expression levels of all integrin  $\alpha$  subunits analyzed significantly decreased as soon as 1 h post-AMPH treatment and continued to decline till 12 or 24 h gradually. Previous studies have shown that the ability of amphetamines to cause toxicity is dependent on the cell-type. For example, in macrophages, 25  $\mu$ M METH reduces wound healing and facilitates host-mediated collagen degradation by increased expression and production of MMP-2. Furthermore, the same dose induces *Staphylococcus aureus* biofilm

formation and leads to detrimental effects on the functions of human and murine phagocytic cells, enhancing susceptibility to *S. aureus* infection [251]. Treatment of neurons with 25  $\mu$ M METH reduces glucose uptake in neurons. On the other hand, 25  $\mu$ M METH has been shown to cause no changes in glucose uptake or cell survival in astrocytes. Our results also showed no change in the mRNA expression level of integrin  $\alpha$  subunits in astrocytes treated with 25  $\mu$ M AMPH suggesting that 25  $\mu$ M might not be sufficient to elicit a toxic response.

Except for 25  $\mu$ M dose, a peak decrease in the mRNA expression was observed at 12 h for ITGA5 and 24 h for ITGA1, ITGA2, ITGA3, and ITGAV irrespective of the dose used. mRNA expression levels gradually increased until 48 h after the peak decrease. In a previous study, METH has been shown to downregulate the expression of ITGA3, ITGA4, ITGA5, ITGA6, and ITGA7 in rat brain cortex. In this study, researchers also observed a pattern of decreased mRNA expression till 12 h and the expression levels normalized by 24 h [258]. The observed decrease in the mRNA expression of in integrin  $\alpha$  subunits till 12 h and normalization of the expression by 48 h in our study seems to follow the general kinetics of mRNA stability. Nevertheless, it should be noted that the long-term abuse of amphetamines might produce a sustained decrease in the expression of integrin  $\alpha$  subunits in astrocytes.

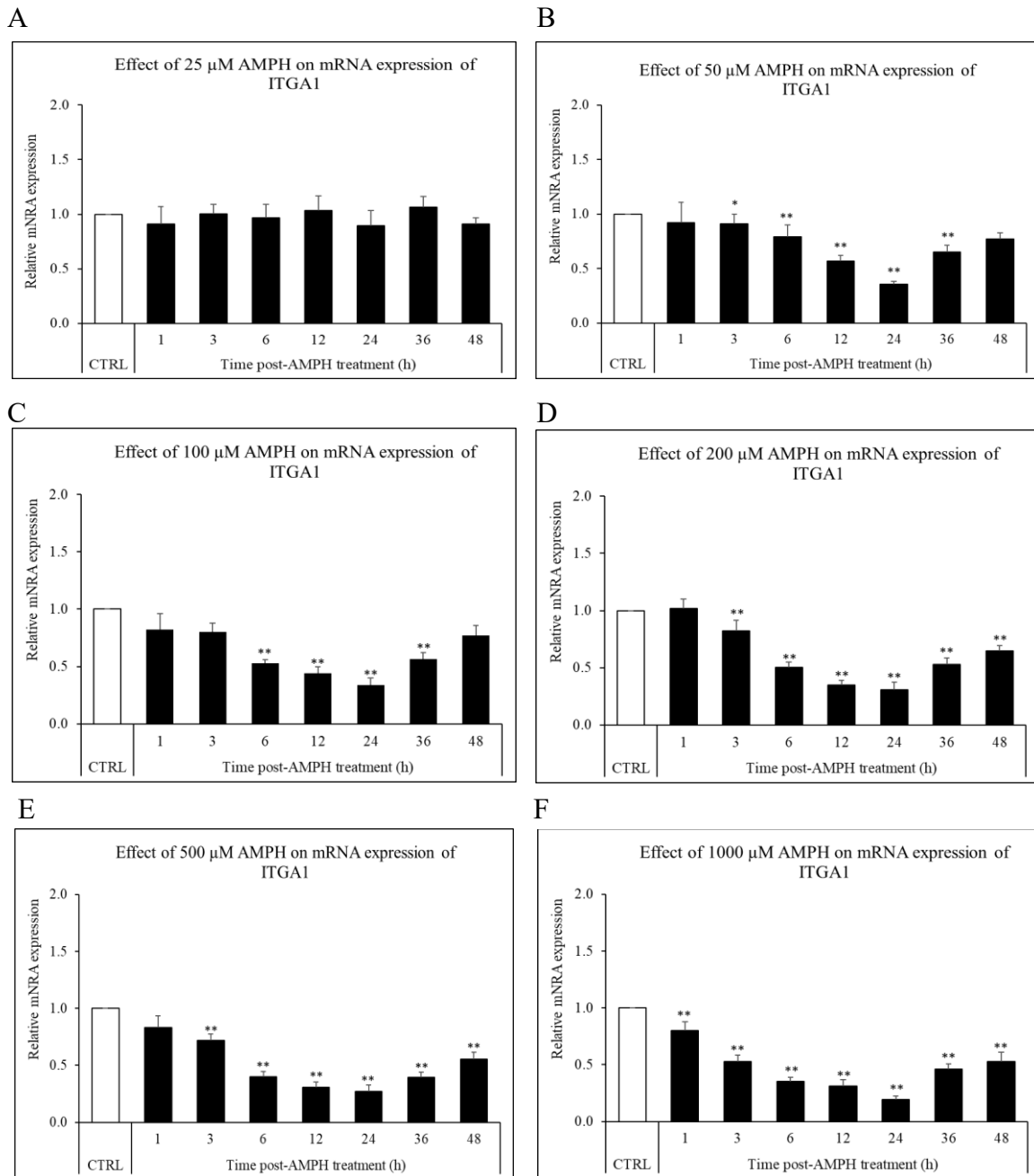


**Figure 29. AMPH-mediated decrease in the mRNA expression of ITGA1 in astrocytes.** Astrocytes were treated with 25 (A), 50 (B), 100 (C), 200 (D), 500 (E), and 1000  $\mu\text{M}$  (F) AMPH for 1, 3, 6, 12, 24, 36, and 48 h. At indicated time points, total RNA was extracted and mRNA expression levels of ITGA1 were measured using qRT-PCR. White bars represent the CTRL (Control), and black bars represent AMPH-treated samples. Each time point had corresponding CTRL samples. For simplification, only one CTRL sample is shown. The mRNA levels are presented as fold differences between the CTRL and AMPH-treated samples. Each panel represents the mean  $\pm$  SD of expression data from 3 donors with each experiment done in triplicates. The statistical significance was calculated using one-way ANOVA followed by Dunnett's multiple comparison test. \* and \*\* denote p-value of  $\leq 0.05$  and  $\leq 0.01$ , respectively.

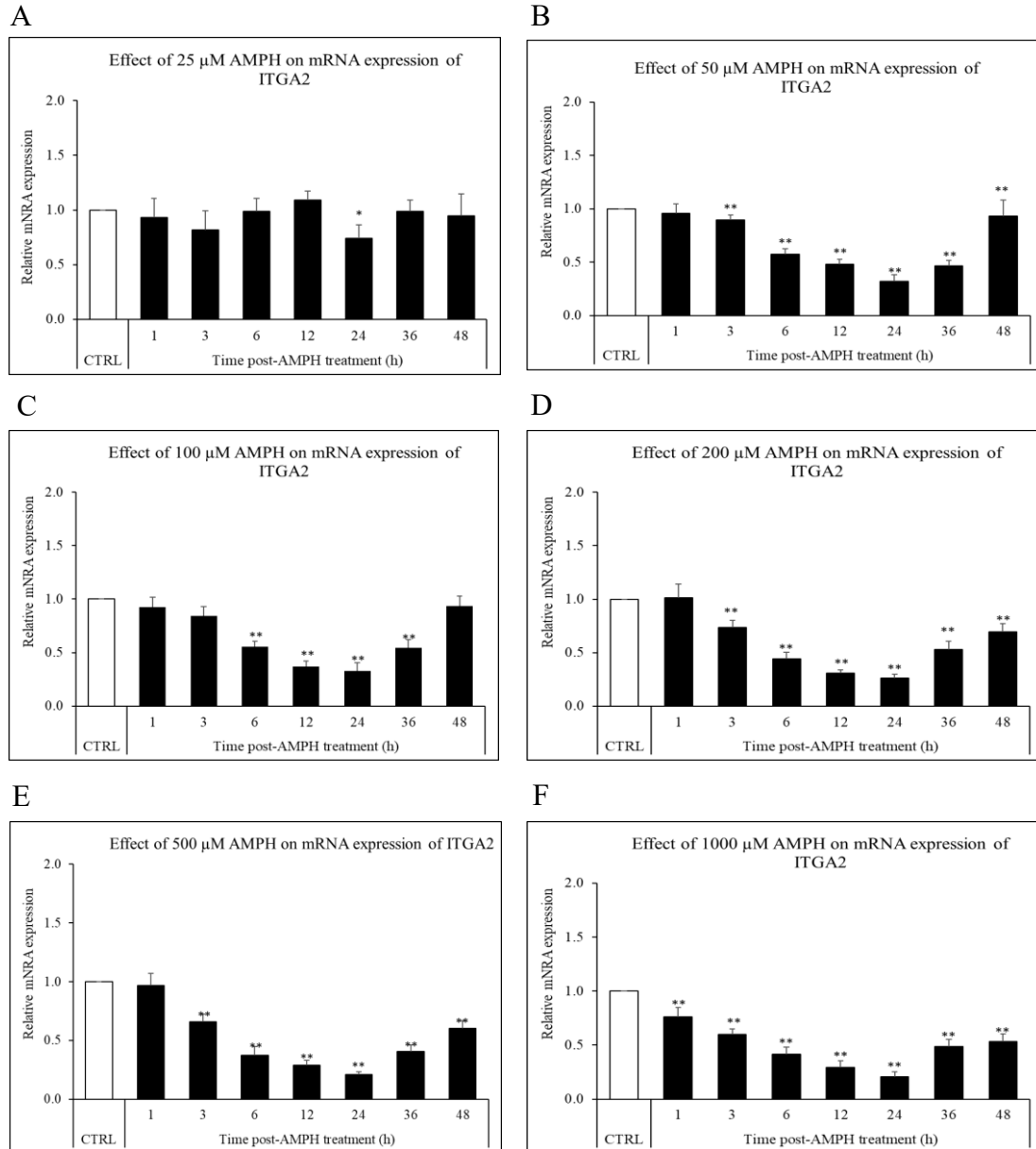


**Figure 30. AMPH-mediated decrease in the mRNA expression of ITGA2 in astrocytes.** Astrocytes were treated with 25 (A), 50 (B), 100 (C), 200 (D), 500 (E), and 1000  $\mu\text{M}$  (F) AMPH for 1, 3, 6, 12, 24, 36, and 48 h. At indicated time points, total RNA was extracted and mRNA expression levels of ITGA2 were measured using qRT-PCR. White bars represent the CTRL (Control), and black bars represent AMPH-treated samples. Each time point had corresponding CTRL samples. For simplification, only one CTRL sample is shown. The mRNA levels are presented as fold differences between the CTRL and AMPH-treated samples. Each panel represents the mean  $\pm$  SD of expression data from 3 donors with each experiment done in triplicates. The statistical significance was calculated using one-way ANOVA followed by Dunnett's multiple comparison test. \* and \*\* denote p-value of  $\leq 0.05$  and  $\leq 0.01$ , respectively.

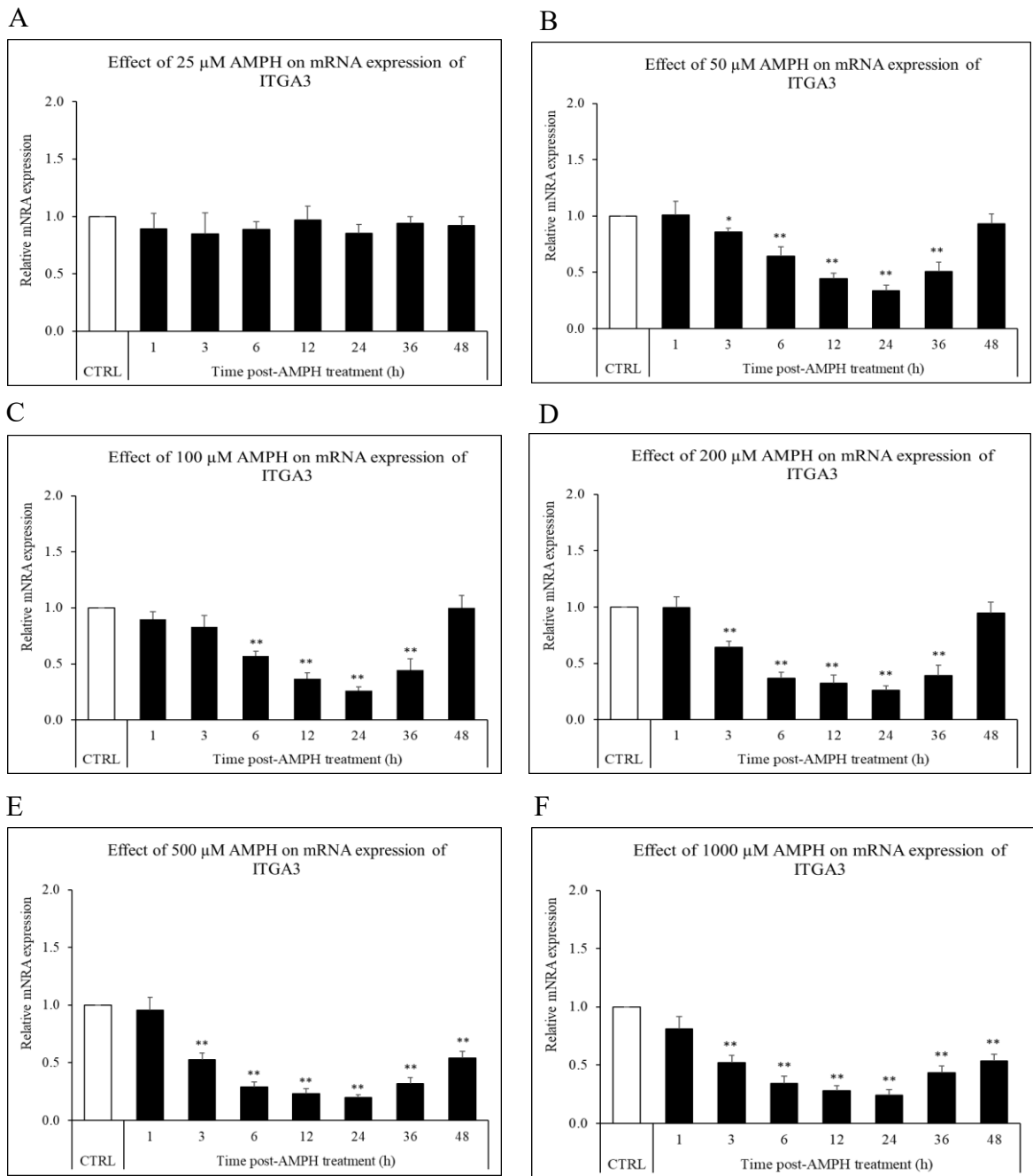


**Figure 31. AMPH-mediated decrease in the mRNA expression of ITGA3 in astrocytes.** Astrocytes were treated with 25 (A), 50 (B), 100 (C), 200 (D), 500 (E), and 1000  $\mu\text{M}$  (F) AMPH for 1, 3, 6, 12, 24, 36, and 48 h. At indicated time points, total RNA was extracted and mRNA expression levels of ITGA3 were measured using qRT-PCR. White bars represent the CTRL (Control), and black bars represent AMPH-treated samples. Each time point had corresponding CTRL samples. For simplification, only one CTRL sample is shown. The mRNA levels are presented as fold differences between the CTRL and AMPH-treated samples. Each panel represents the mean  $\pm$  SD of expression data from 3 donors with each experiment done in triplicates. The statistical significance was calculated using one-way ANOVA followed by Dunnett's multiple comparison test. \* and \*\* denote p-value of  $\leq 0.05$  and  $\leq 0.01$ , respectively.

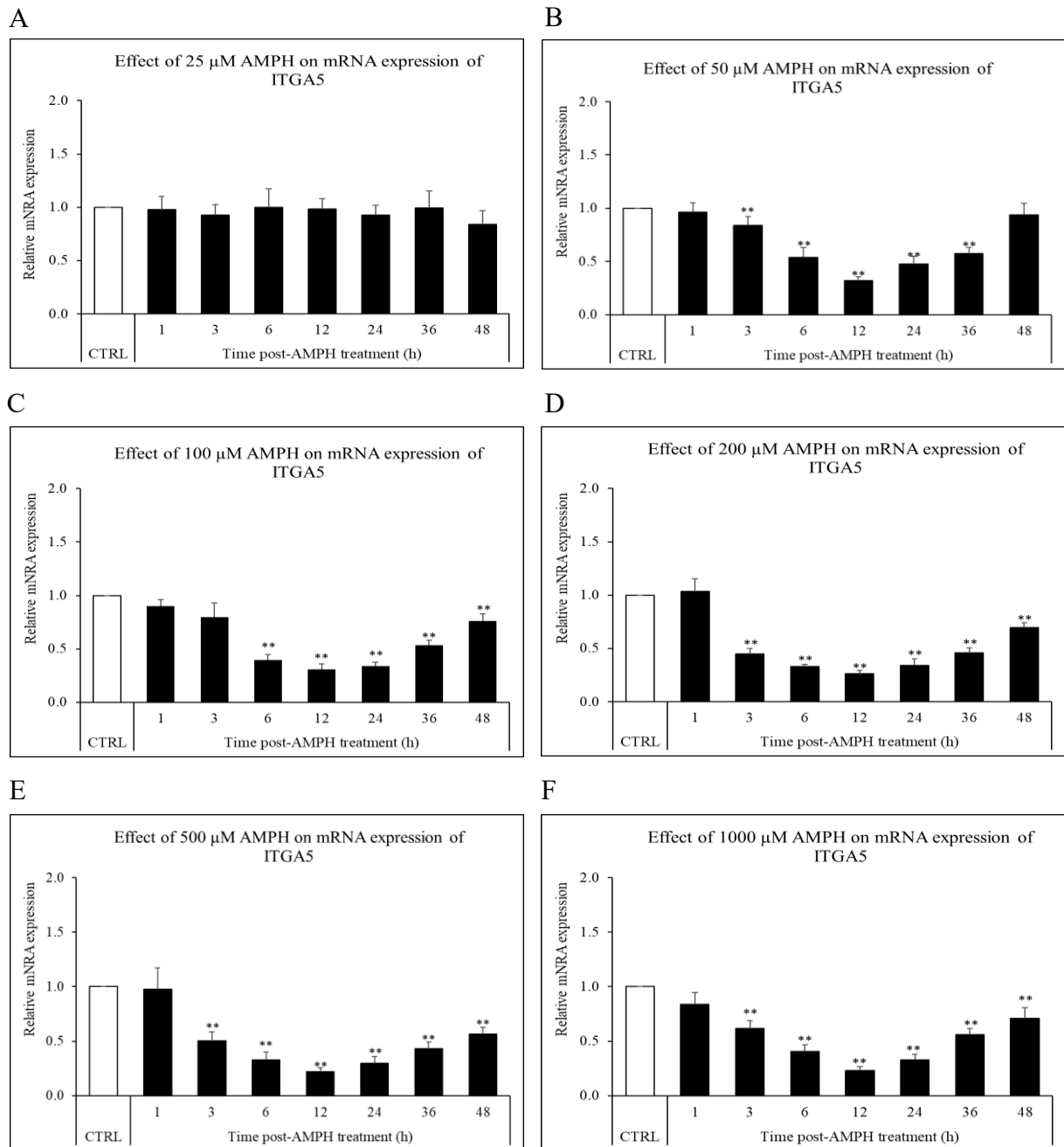


**Figure 32. AMPH-mediated decrease in the mRNA expression of ITGA5 in astrocytes.** Astrocytes were treated with 25 (A), 50 (B), 100 (C), 200 (D), 500 (E), and 1000  $\mu\text{M}$  (F) AMPH for 1, 3, 6, 12, 24, 36, and 48 h. At indicated time points, total RNA was extracted and mRNA expression levels of ITGA5 were measured using qRT-PCR. White bars represent the CTRL (Control), and black bars represent AMPH-treated samples. Each time point had corresponding CTRL samples. For simplification, only one CTRL sample is shown. The mRNA levels are presented as fold differences between the CTRL and AMPH-treated samples. Each panel represents the mean  $\pm$  SD of expression data from 3 donors with each experiment done in triplicates. The statistical significance was calculated using one-way ANOVA followed by Dunnett's multiple comparison test. \* and \*\* denote p-value of  $\leq 0.05$  and  $\leq 0.01$ , respectively.

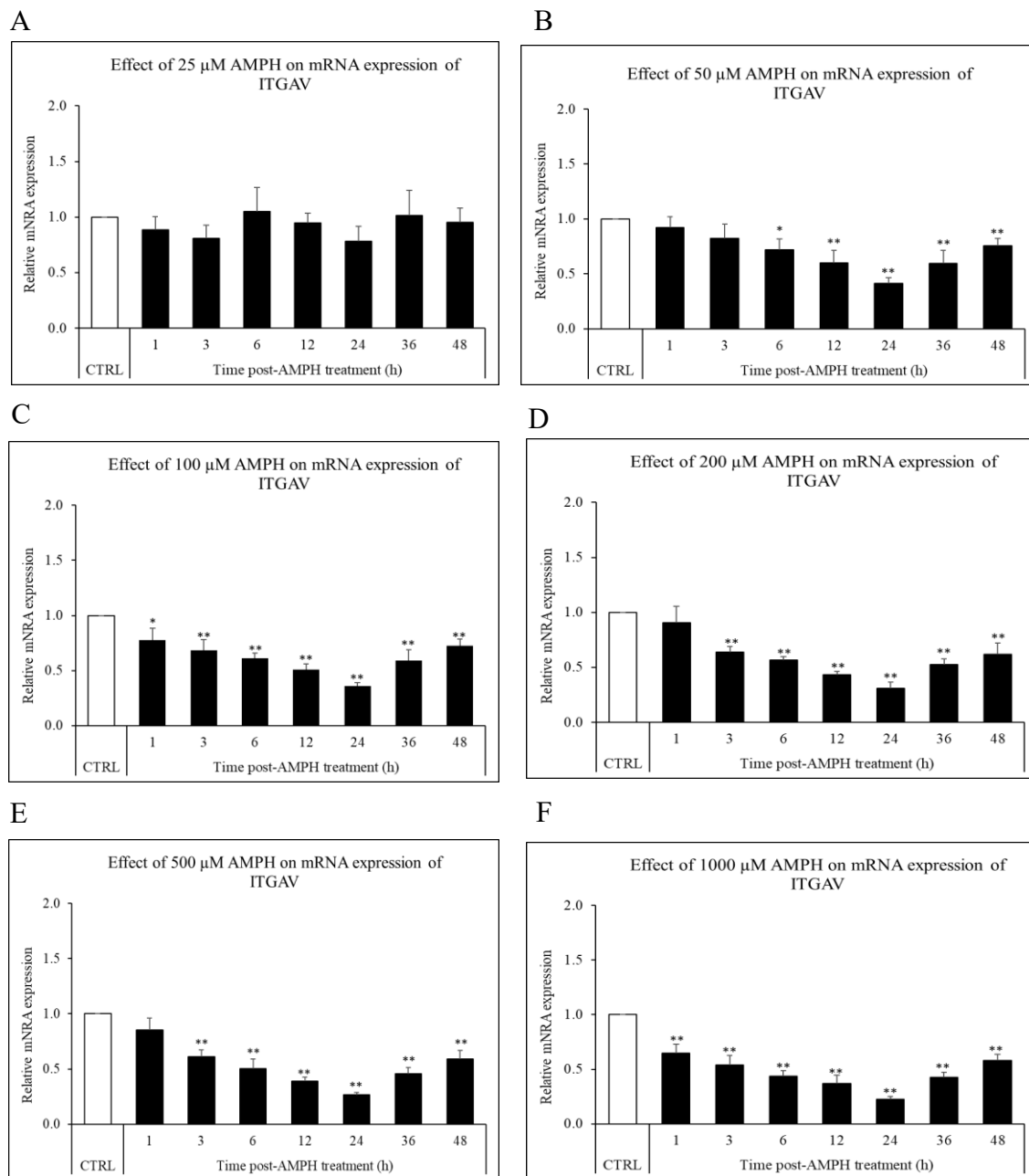


**Figure 33. AMPH-mediated decrease in the mRNA expression of ITGAV in astrocytes.** Astrocytes were treated with 25 (A), 50 (B), 100 (C), 200 (D), 500 (E), and 1000  $\mu\text{M}$  (F) AMPH for 1, 3, 6, 12, 24, 36, and 48 h. At indicated time points, total RNA was extracted and mRNA expression levels of ITGAV were measured using qRT-PCR. White bars represent the CTRL (Control), and black bars represent AMPH-treated samples. Each time point had corresponding CTRL samples. For simplification, only one CTRL sample is shown. The mRNA levels are presented as fold differences between the CTRL and AMPH-treated samples. Each panel represents the mean  $\pm$  SD of expression data from 3 donors with each experiment done in triplicates. The statistical significance was calculated using one-way ANOVA followed by Dunnett's multiple comparison test. \* and \*\* denote p-value of  $\leq 0.05$  and  $\leq 0.01$ , respectively.

### **3.4.2 AMPH induces a dose- and time-dependent decrease in the mRNA expression of integrin $\beta$ subunits in astrocytes**

Similar to the effect on  $\alpha$  integrin subunits, we also observed an AMPH-mediated dose- and time-dependent decrease in the expression of integrin  $\beta$  subunits ITGB1 (Fig. 34), ITGB3 (Fig. 35), ITGB5 (Fig. 36), ITGB6 (Fig. 37), and ITGB8 (Fig. 38) in astrocytes. Similar to integrin  $\alpha$  subunits, 25  $\mu$ M dose did not produce a decrease in the mRNA expression level of integrin  $\beta$  subunits in astrocytes. Except for the 25  $\mu$ M dose, the mRNA expression levels of integrin  $\beta$  subunits decreased significantly as soon as 1 h post-AMPH treatment and continued to gradually decline till 12 or 24 h. Irrespective of the dose used, a peak decrease in the mRNA expression was observed at 12 h for ITGB6 and ITGB8, and 24 h for ITGB1, ITGB3, and ITGB5. mRNA expression levels gradually increased until 48 h after the peak decrease.

Our results corroborate previous studies in which METH has been shown to downregulate ITGB1, ITGB5, and ITGB7 in rat brain cortex [258], wherein the mRNA expression of ITGB1 and ITGB7 continued to decrease 24 h after the treatment. METH has also shown to decrease integrin  $\beta$  subunit expression in addicted individuals [296]. Our study is, however, the first report to detail the dose- and time-dependent decrease in the expression of integrin  $\beta$  subunits in astrocytes. Long-term abuse of amphetamines can cause a sustained decrease in the mRNA expression levels of integrin  $\beta$  subunits, potentially exacerbating neurotoxicity.

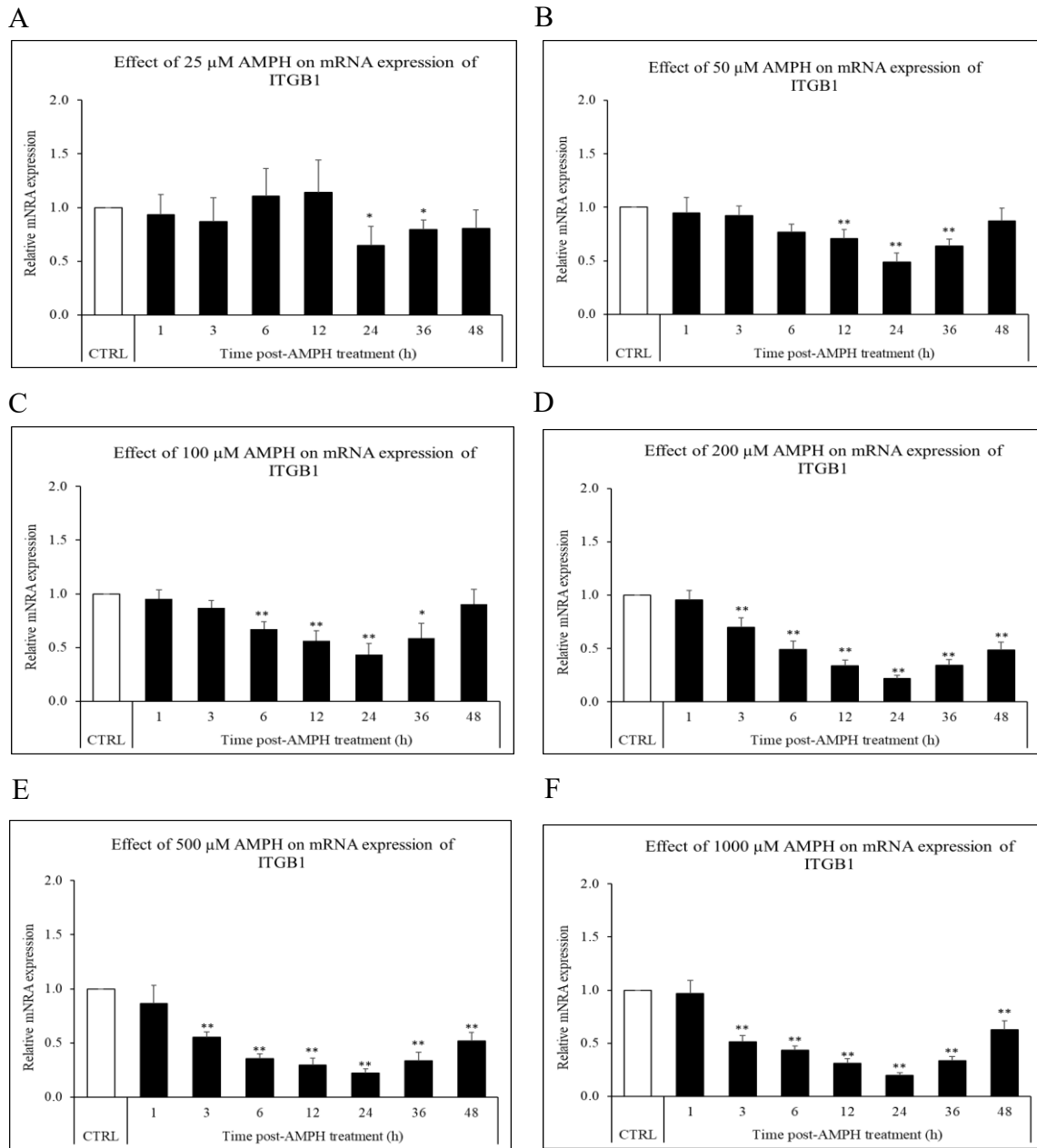


**Figure 34. AMPH-mediated decrease in the mRNA expression of ITGB1 in astrocytes.** Astrocytes were treated with 25 (A), 50 (B), 100 (C), 200 (D), 500 (E), and 1000 μM (F) AMPH for 1, 3, 6, 12, 24, 36, and 48 h. At indicated time points, total RNA was extracted and mRNA expression levels of ITGB1 were measured using qRT-PCR. White bars represent the CTRL (Control), and black bars represent AMPH-treated samples. Each time point had corresponding CTRL samples. For simplification, only one CTRL sample is shown. The mRNA levels are presented as fold differences between the CTRL and AMPH-treated samples. Each panel represents the mean ± SD of expression data from 3 donors with each experiment done in triplicates. The statistical significance was calculated using one-way ANOVA followed by Dunnett's multiple comparison test. \* and \*\* denote p-value of ≤ 0.05 and ≤ 0.01, respectively.

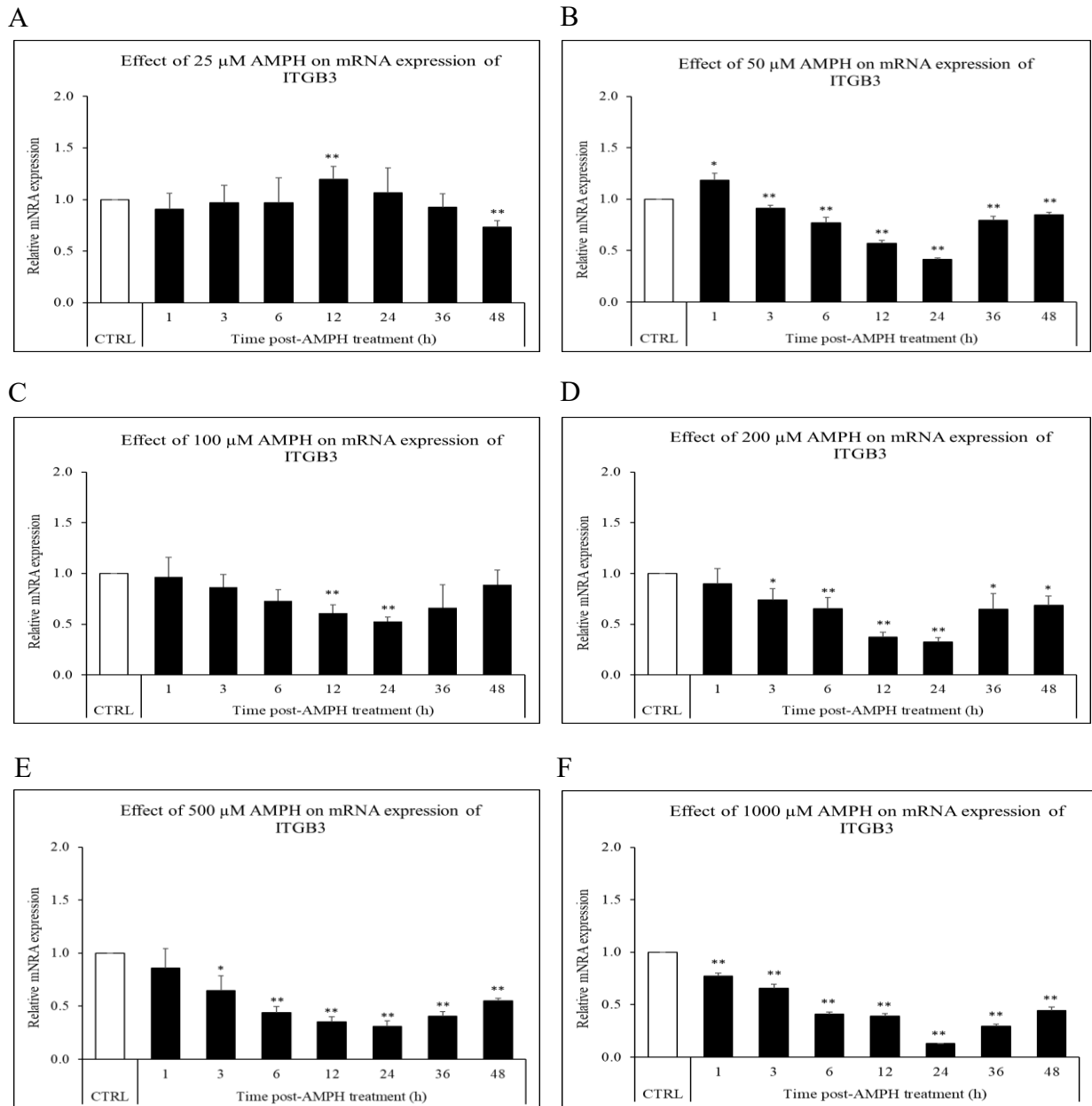


**Figure 35. AMPH-mediated decrease in the mRNA expression of ITGB3 in astrocytes.** Astrocytes were treated with 25 (A), 50 (B), 100 (C), 200 (D), 500 (E), and 1000 μM (F) AMPH for 1, 3, 6, 12, 24, 36, and 48 h. At indicated time points, total RNA was extracted and mRNA expression levels of ITGB3 were measured using qRT-PCR. White bars represent the CTRL (Control), and black bars represent AMPH-treated samples. Each time point had corresponding CTRL samples. For simplification, only one CTRL sample is shown. The mRNA levels are presented as fold differences between the CTRL and AMPH-treated samples. Each panel represents the mean ± SD of expression data from 3 donors with each experiment done in triplicates. The statistical significance was calculated using one-way ANOVA followed by Dunnett's multiple comparison test. \* and \*\* denote p-value of ≤ 0.05 and ≤ 0.01, respectively.

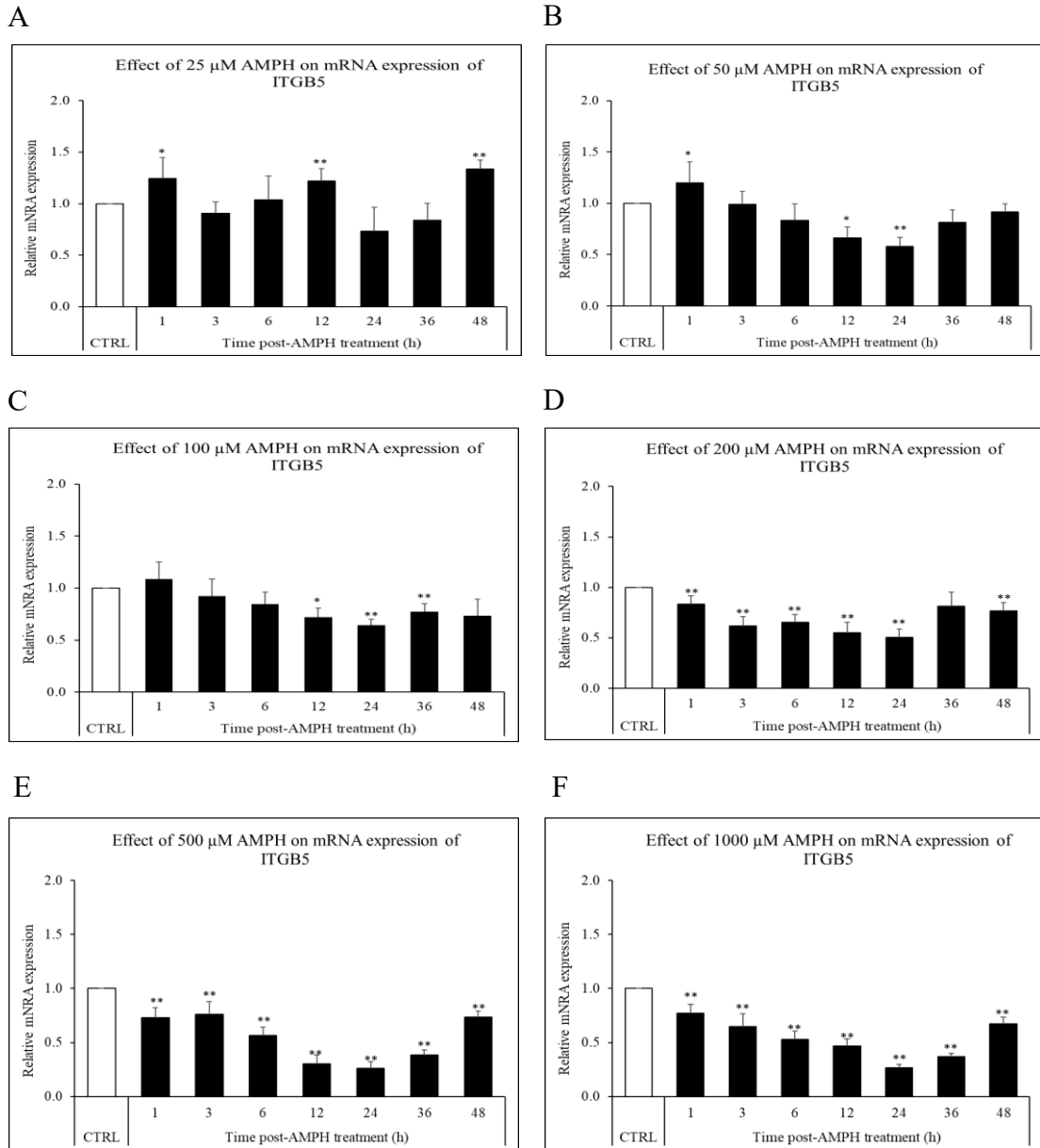


**Figure 36. AMPH-mediated decrease in the mRNA expression of ITGB5 in astrocytes.** Astrocytes were treated with 25 (A), 50 (B), 100 (C), 200 (D), 500 (E), and 1000 μM (F) AMPH for 1, 3, 6, 12, 24, 36, and 48 h. At indicated time points, total RNA was extracted and mRNA expression levels of ITGB5 were measured using qRT-PCR. White bars represent the CTRL (Control), and black bars represent AMPH-treated samples. Each time point had corresponding CTRL samples. For simplification, only one CTRL sample is shown. The mRNA levels are presented as fold differences between the CTRL and AMPH-treated samples. Each panel represents the mean ± SD of expression data from 3 donors with each experiment done in triplicates. The statistical significance was calculated using one-way ANOVA followed by Dunnett's multiple comparison test. \* and \*\* denote p-value of ≤ 0.05 and ≤ 0.01, respectively.

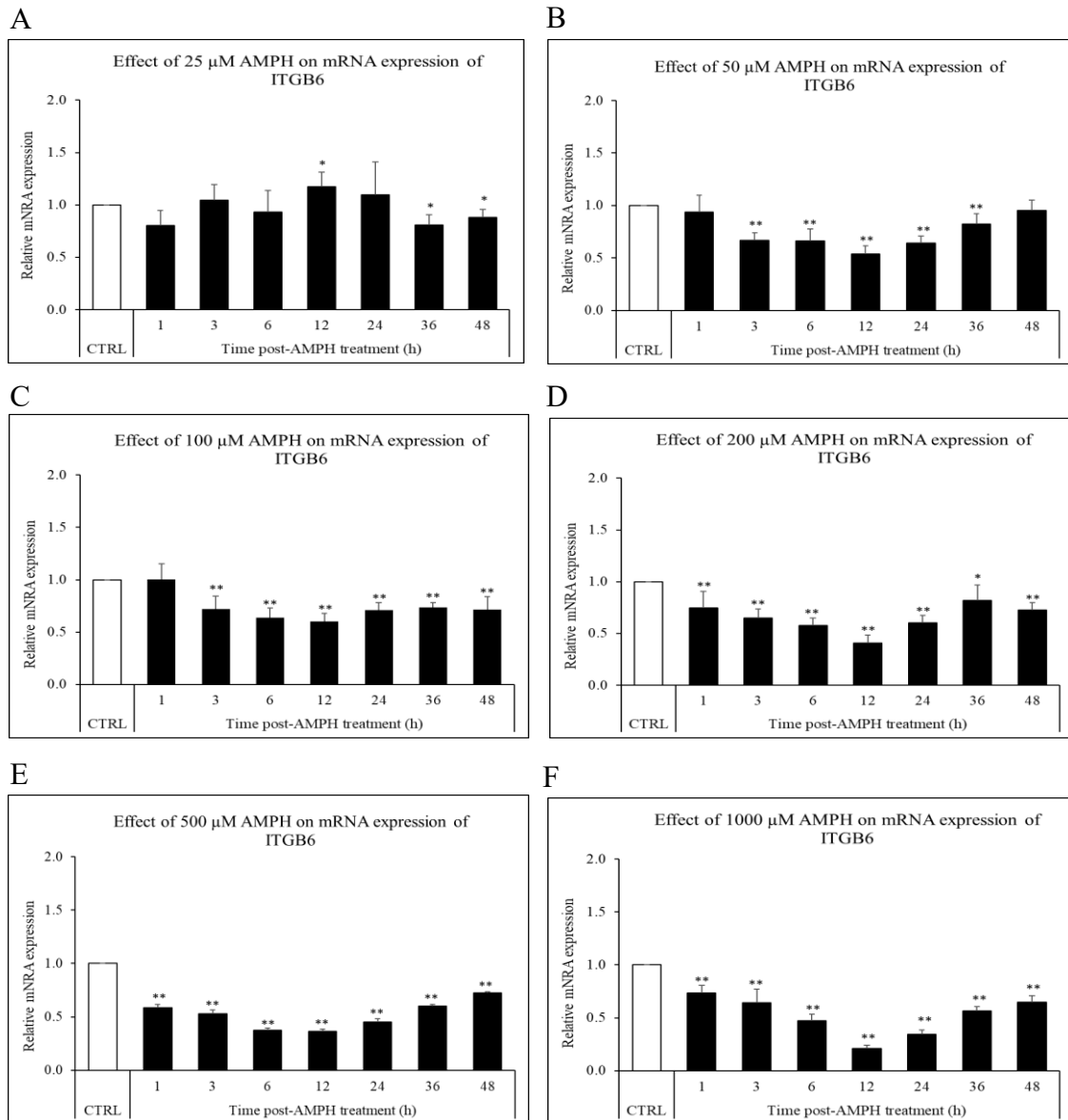


**Figure 37. AMPH-mediated decrease in the mRNA expression of ITGB6 in astrocytes.** Astrocytes were treated with 25 (A), 50 (B), 100 (C), 200 (D), 500 (E), and 1000  $\mu$ M (F) AMPH for 1, 3, 6, 12, 24, 36, and 48 h. At indicated time points, total RNA was extracted and mRNA expression levels of ITGB6 were measured using qRT-PCR. White bars represent the CTRL (Control), and black bars represent AMPH-treated samples. Each time point had corresponding CTRL samples. For simplification, only one CTRL sample is shown. The mRNA levels are presented as fold differences between the CTRL and AMPH-treated samples. Each panel represents the mean  $\pm$  SD of expression data from 3 donors with each experiment done in triplicates. The statistical significance was calculated using one-way ANOVA followed by Dunnett's multiple comparison test. \* and \*\* denote p-value of  $\leq 0.05$  and  $\leq 0.01$ , respectively.

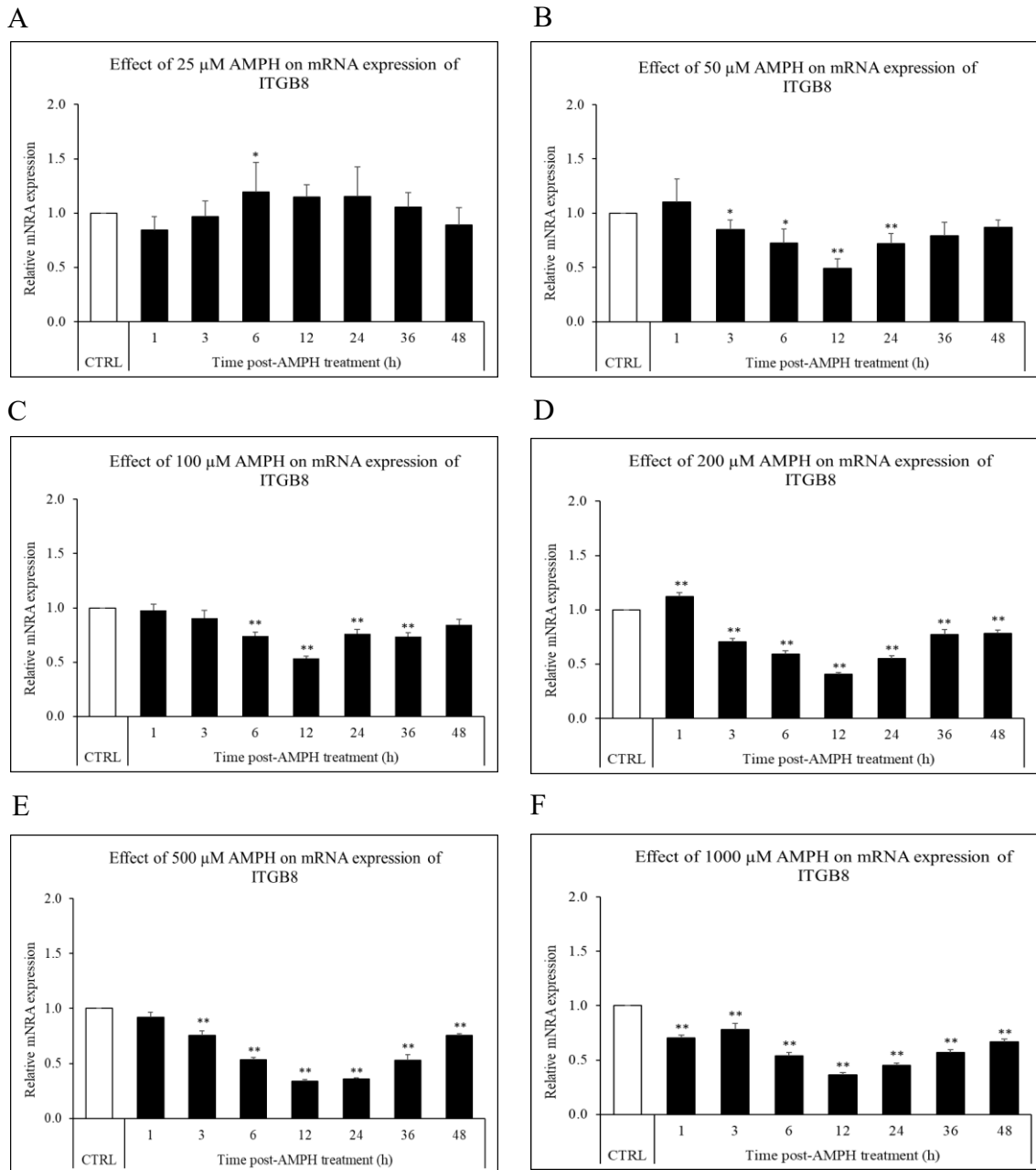


**Figure 38. AMPH-mediated decrease in the mRNA expression of ITGB8 in astrocytes.** Astrocytes were treated with 25 (A), 50 (B), 100 (C), 200 (D), 500 (E), and 1000  $\mu\text{M}$  (F) AMPH for 1, 3, 6, 12, 24, 36, and 48 h. At indicated time points, total RNA was extracted and mRNA expression levels of ITGB6 were measured using qRT-PCR. White bars represent the CTRL (Control), and black bars represent AMPH-treated samples. Each time point had corresponding CTRL samples. For simplification, only one CTRL sample is shown. The mRNA levels are presented as fold differences between the CTRL and AMPH-treated samples. Each panel represents the mean  $\pm$  SD of expression data from 3 donors with each experiment done in triplicates. The statistical significance was calculated using one-way ANOVA followed by Dunnett's multiple comparison test. \* and \*\* denote p-value of  $\leq 0.05$  and  $\leq 0.01$ , respectively.

### **3.4.3 AMPH induces a time-dependent decrease in the protein expression of integrin subunits in astrocytes**

After demonstrating that AMPH decreases mRNA expression of integrin subunits in astrocytes, we determined the effect of AMPH on the protein expression of ITGA1, ITGA2, and ITGB1 subunits in astrocytes. We selected ITGA1, ITGA2, and ITGB1 subunits as the astrocytic expression of these subunits have shown to decrease in brain pathologies [297]. We selected 500  $\mu\text{M}$  dose as it has been demonstrated to result in plasma concentrations in the mid  $\mu\text{M}$  with up to ten times accumulation in brain tissue, which is consistent with the casual abuse of AMPH [275-277].

To check the changes in protein expression levels of ITGA1, ITGA2, and ITGB1 in astrocytes, HA were treated with 500  $\mu\text{M}$  AMPH for 24, 36, and 48 h, whole-cell lysates were prepared, and western blot was performed. Among all donors, the expression level of ITGA1 at 24 post-AMPH treatment displayed a non-significant increase (1.13, 95% CI: 0.91 – 1.35) compared to the control, but the levels decreased significantly ( $p < 0.01$ ) at 36 h (0.65, 95% CI: 0.53 – 0.76) and 48 h post-treatment (0.52, 95% CI: 0.25 – 0.78) compared to the control (Fig. 39).

Compared to the control, the expression of ITGA2 did not change significantly ( $p$ -value = 0.25) at 24 h post-AMPH. The expression of ITGA2 at 36 h (0.68, 95% CI: 0.47 – 0.88) and 48 h (0.43, 95% CI: 0.30 – 0.56) post-AMPH decreased significantly compared to the control (Fig. 40). Similarly, the levels of ITGB1 did not decrease significantly ( $p$ -value = 0.13) at 24 h compared to the control but showed a significant decrease at 36 h (0.64, 95% CI: 0.50 – 0.79) and 48 h (0.64, 95% CI: 0.50 – 0.79) post-AMPH treatment. However, there was no significant difference ( $p$ -value: 0.99) between its expression levels of ITGB1 at 36 h and 48 h (Fig. 41).

Peak decrease in the expression levels of ITGA1, ITGA2, and ITGB1 was observed at 48 h among all donors.

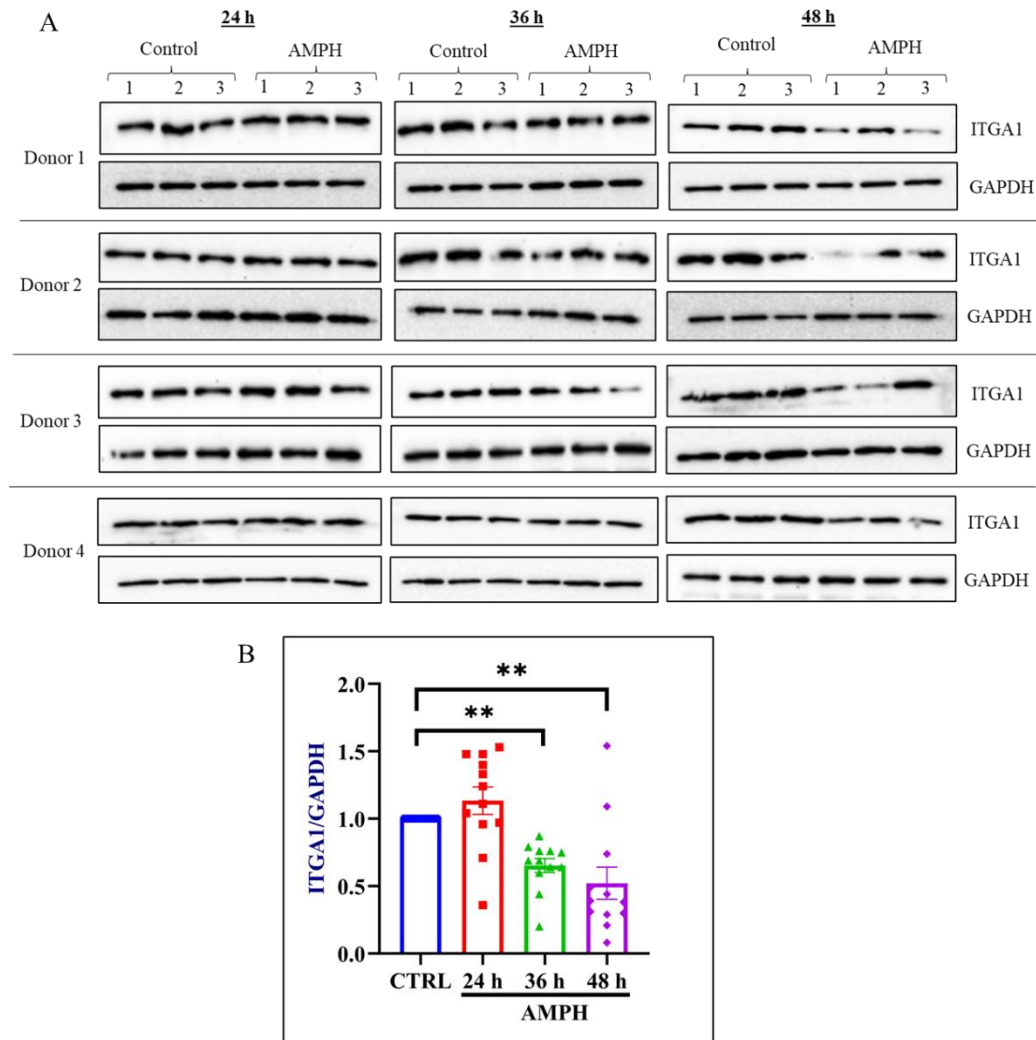


**Figure 39. AMPH-mediated decrease in the expression of ITGA1 protein in astrocytes.** A. Astrocytes were treated with 500  $\mu$ m AMPH for 24, 36, and 48 h. At indicated time points, whole-cell lysates were prepared from the cells and the expression level of ITGA1 was measured using western blot. A representative blot image with 3 Control and 3 AMPH for each time point and for each donor is shown. The expression levels of ITGA1 (130 kDa) were normalized to the housekeeping gene (GAPDH, 37 kDa) at respective time points. B. The bars, shown in the chart, show normalized values of the band intensities for ITGA1 over GAPDH. The bar chart represents the combined mean  $\pm$  95% CI of 3 independent experiments from the 3 donors. The statistical significance was calculated using one-way ANOVA followed by Dunnett's multiple comparison test. \*\* denote p-value of  $\leq 0.01$ .

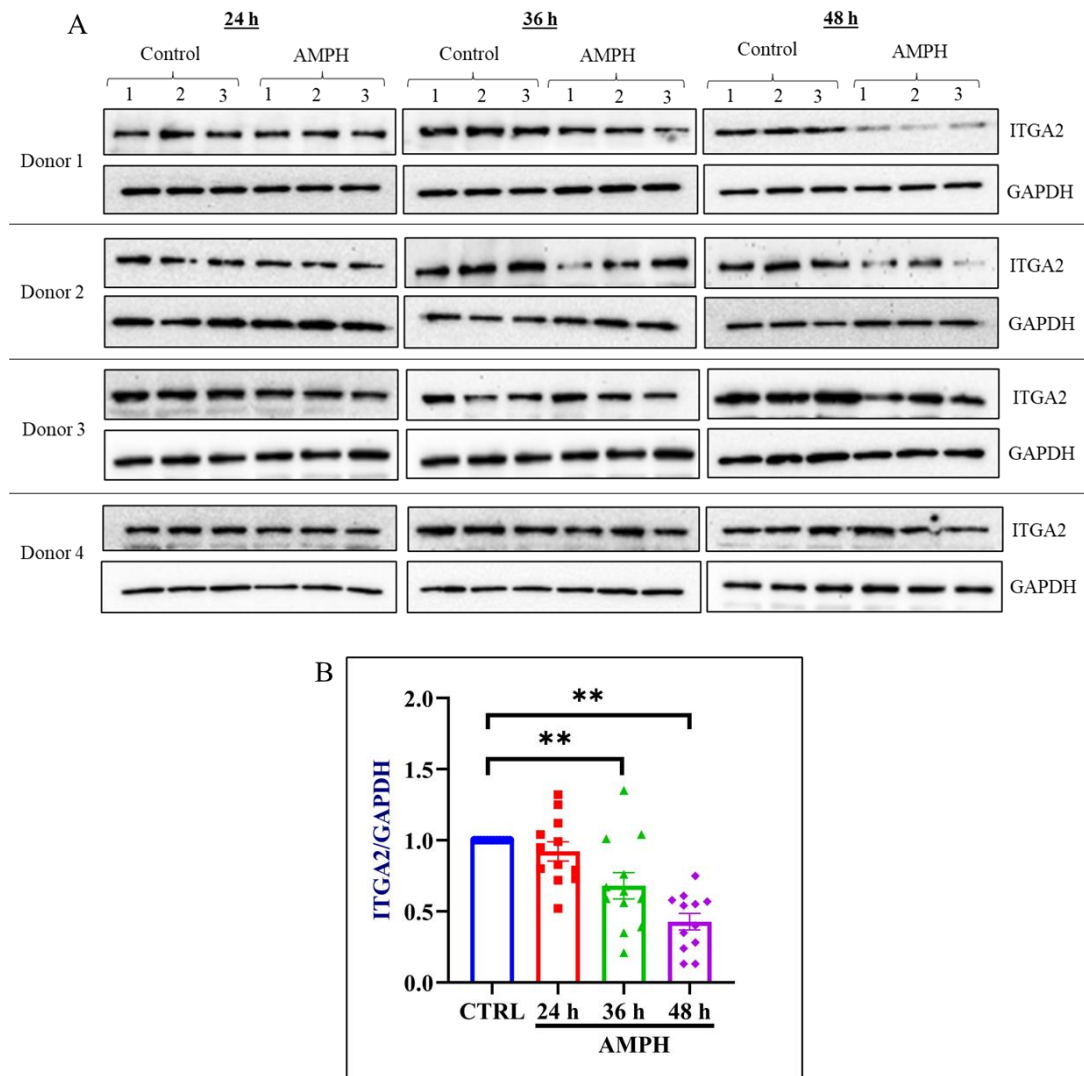


**Figure 40. AMPH-mediated decrease in the expression of ITGA2 protein in astrocytes.** A. Astrocytes were treated with 500  $\mu$ m AMPH for 24, 36, and 48 h. At indicated time points, whole-cell lysates were prepared from the cells and the expression level of ITGA2 was measured using western blot. A representative blot image with 3 Control and 3 AMPH samples for each time point and for each donor is shown. The expression levels of ITGA2 (150 kDa) were normalized to the housekeeping gene (GAPDH, 37 kDa) at respective time points. B. The bars, shown in the chart, show normalized values of the band intensities for ITGA1 over GAPDH. The bar chart represents the combined mean  $\pm$  95% CI of 3 independent experiments from the 3 donors. The statistical significance was calculated using one-way ANOVA followed by Dunnett's multiple comparison test. \*\* denote p-value of  $\leq$  0.01.

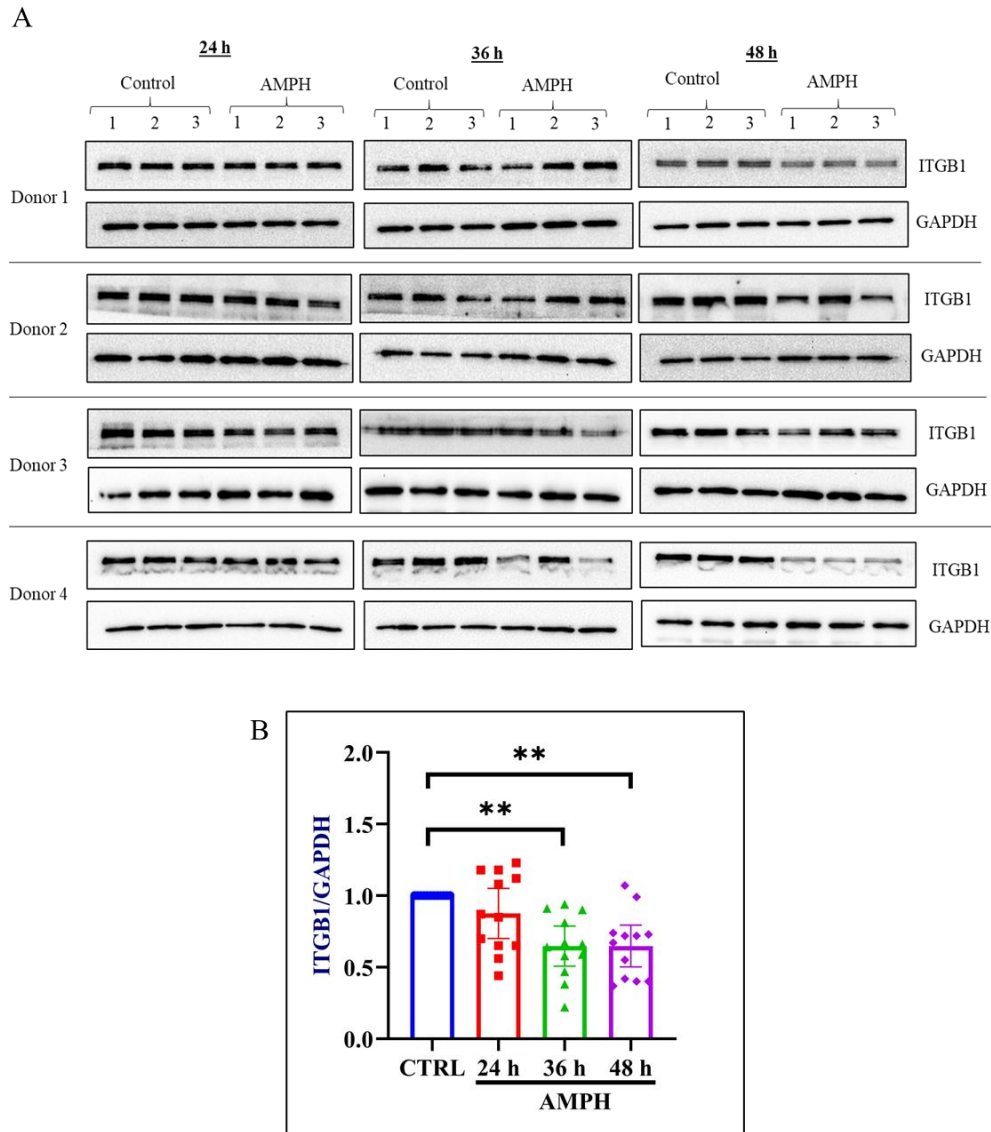


**Figure 41. AMPH-mediated decrease in the expression of ITGB1 protein in astrocytes.** A. Astrocytes were treated with 500  $\mu$ m AMPH for 24, 36, and 48 h. At indicated time points, whole-cell lysates were prepared from the cells and the expression level of ITGB1 was measured using western blot. A representative blot image with 3 Control and 3 AMPH for each time point and for each donor is shown. The expression levels of ITGB1 (138 kDa) were normalized to the housekeeping gene (GAPDH, 37 kDa) at respective time points. B. The bars, shown in the chart, show normalized values of the band intensities for ITGA1 over GAPDH. The bar chart represents the combined mean  $\pm$  95% CI of 3 independent experiments from the 3 donors. The statistical significance was calculated using one-way ANOVA followed by Dunnett's multiple comparison test. \*\* denote p-value of  $\leq$  0.01.

#### **3.4.4 AMPH induces cell death in primary human astrocytes**

AMPH and other ATS are known to induce cell death in various cells, but the data on the AMPH on astrocyte viability is limited [141-147]. Compromised astrocyte survival can negatively impact neuronal function, resulting in neuronal death and worsening AMPH toxicity. Therefore, to understand how AMPH affects astrocyte viability, we treated astrocytes with 500  $\mu\text{M}$  for 24 and 48 h and measured cell viability using XTT and LDH cytotoxicity assays. AMPH significantly ( $p < 0.001$ ) decreased astrocyte viability at 24 h ( $64.40 \pm 2\%$  decrease) and 48 h ( $44.21 \pm 3.6\%$  decrease) as compared to the respective controls (Fig 42A). Similarly, AMPH induced significant LDH release in a time-dependent manner. As shown in Fig. 42B, in AMPH treated cells, % LDH release was 45.57% as compared to control at 24 h and 71.09% as compared to control at 48 h.

Our results corroborate with a previous study wherein authors showed 50% decrease in astrocyte survival with a 24-h treatment with 500  $\mu\text{M}$  METH. Interestingly, METH concentrations of 5–200  $\mu\text{M}$  had no significant effect on cell toxicity. Overall, our results indicate that treatment with AMPH, particularly at the physiologically relevant concentration of 500  $\mu\text{M}$ , can significantly compromise astrocyte viability and induces cytotoxicity.

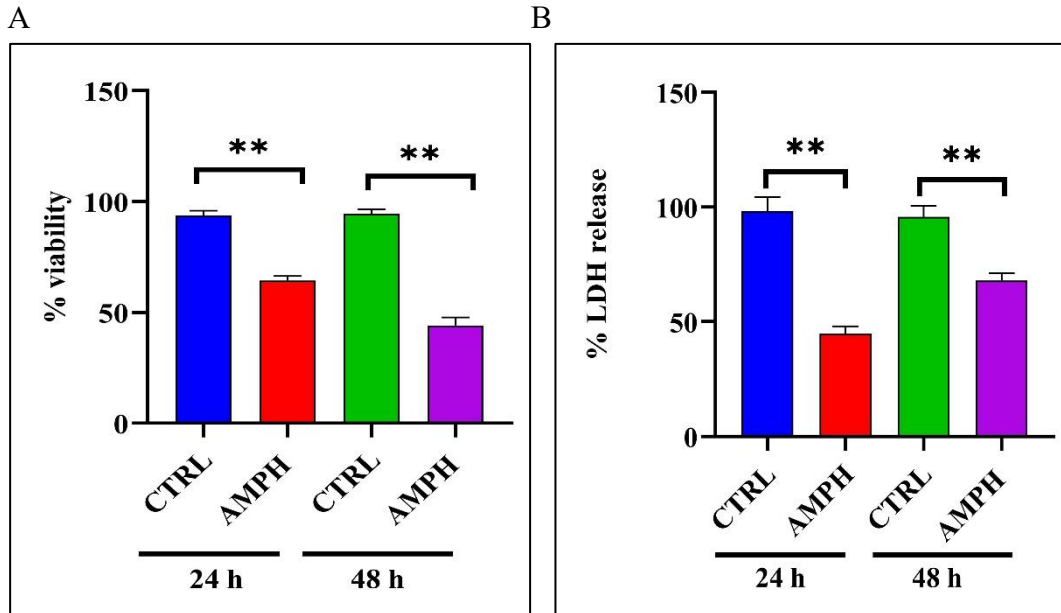


**Figure 42. AMPH-mediated induction of cell death in astrocytes.** A. Astrocyte viability was determined by XTT assay. The bars, shown in the chart, show the % viability of astrocytes treated with 500  $\mu$ M for 24 and 48 h. B. Cell damage was assessed with LDH assay. The bars, shown in the chart, show the % LDH release in astrocytes treated with 500  $\mu$ M for 24 and 48 h. The data is presented as mean  $\pm$  SD of 3 independent experiments from the 3 donors. The statistical significance was calculated using one-way ANOVA followed by Dunnett's multiple comparison test. \*\* denote p-value of  $\leq 0.01$ .

### **3.4.5 Caspase-3 is involved in AMPH-mediated apoptosis in astrocytes**

Caspase-3 is an executioner caspase involved in the final step of apoptosis. Activation of caspase-3 requires proteolytic processing of its inactive zymogen into activated p19 and p17 fragments. Caspase-3 activity can also serve to act as a reliable marker of neurotoxicity [298]. Therefore, we examined the effect of AMPH caspase-3 protein expression and activity in astrocytes.

To check changes in the expression levels of caspase-3 protein, we treated astrocytes with 500  $\mu$ M AMPH for 24, 26, and 48 h, and measured the expression levels of caspase-3 and cleaved caspase-3 proteins using western blot. Among all donors, the expression level of caspase-3 did not show any change at 24 and 36 h, the levels increased significantly ( $p$ -value $<0.01$ ) at 48 h (1.75, 95% CI: 1.42 – 2.06) compared to the control (Fig 43A and 43B). The expression levels of cleaved caspase-3 did not change at 24 h but increased significantly ( $p<0.01$ ) at 36 h (1.45, 95% CI: 1.20 – 1.76) and 48 h (2.17, 95% CI: 1.68 – 2.66) compared to the control (Fig. 43A and 43C). In addition, astrocytes treated with 500  $\mu$ M AMPH also showed significantly higher caspase-3 cleavage activity at 24 h and 48 h (Fig. 43D). These finding clearly suggest the involvement of caspase-3 in AMPH-mediated cell death in astrocytes.

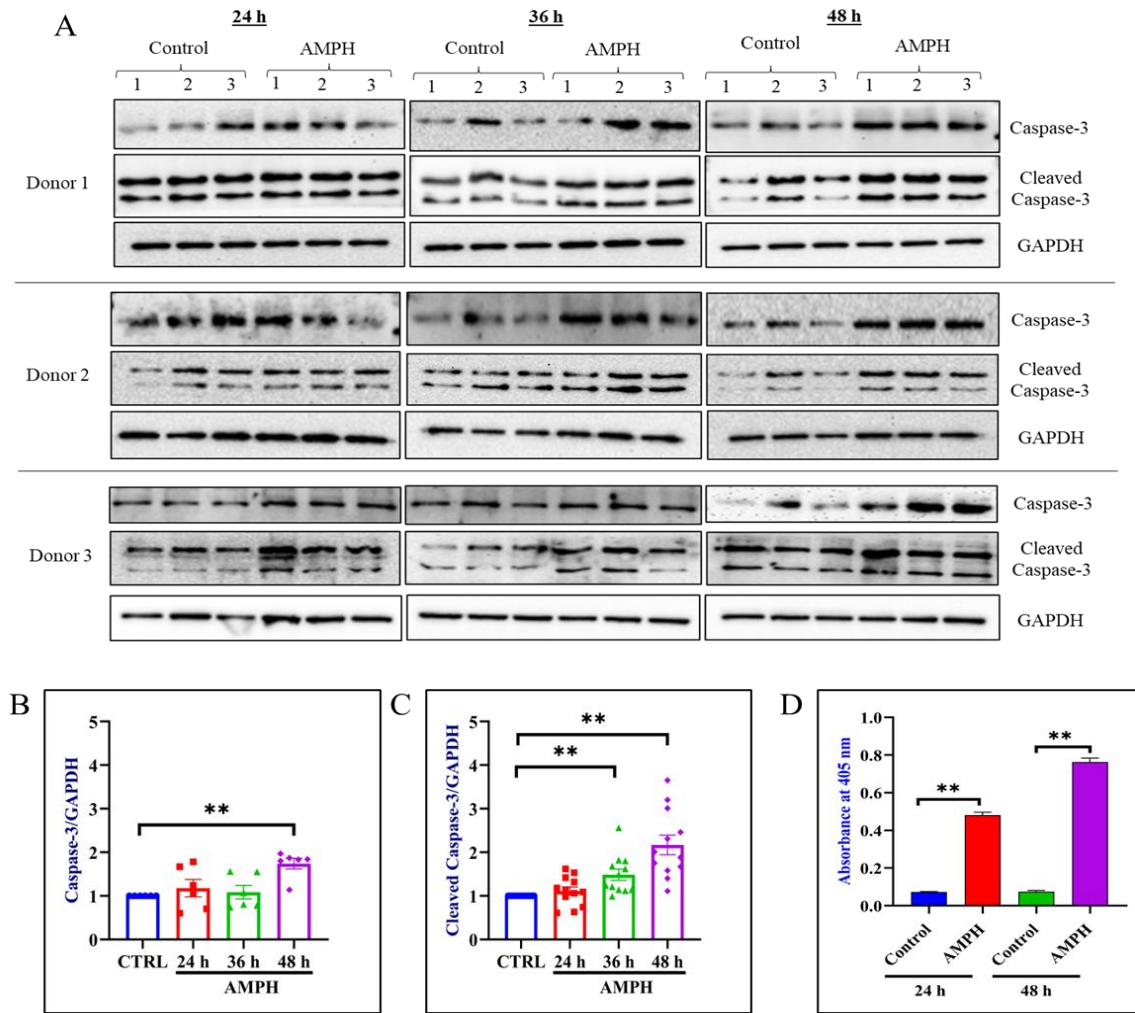


**Figure 43. Involvement of caspase-3 in AMPH-mediated cell death.** A. Astrocytes were treated with 500  $\mu$ M AMPH for 24, 36, and 48 h. At indicated time points, whole-cell lysates were prepared from the cells and the expression level of caspase-3 and cleaved caspase-3 were measured using western blot. A representative blot image with 3 Control and 3 AMPH for each time point and for each donor is shown. The expression levels of caspase-3 (35 kDa) and cleaved caspase-3 (17 and 15 kDa) were normalized to the housekeeping gene (GAPDH, 37 kDa) at respective time points. B and C. The bars, shown in the chart, show normalized values of the band intensities for caspase-3 and cleaved caspase-3 over GAPDH, respectively. The bar chart represents the combined mean  $\pm$  95% CI of 3 independent experiments from the 3 donors. The statistical significance was calculated using the student's t-test and \*\* denotes a p-value of  $\leq 0.01$ . D. Caspase-3 activity was measured after treating astrocytes with 500  $\mu$ M AMPH for 24 and 48 h using a colorimetric assay. The bars, shown in the chart, represent absorbance at 405 after caspase-3 mediated cleavage of the substrate. The bar chart represents the combined mean  $\pm$  95% CI (panels B and C) and mean  $\pm$  SD of 3 independent experiments from the 3 donors. The statistical significance was calculated using one-way ANOVA followed by Dunnett's multiple comparison test. \*\* denote p-value of  $\leq 0.01$ .

### 3.4.6 Integrin subunits are involved in AMPH-mediated apoptosis in astrocytes

Downregulation or antagonism of integrin subunits have been shown to cause apoptosis in several cell types. However, no information is available on astrocytes. Therefore, we checked whether AMPH-mediated downregulation of ITGA1, ITGA2, and ITGB1 subunits is involved in cell death in astrocytes. We first used siRNA to silence the expression of ITGA1, ITGA2, and ITGB1. Cells were treated with 50 nM siRNAs against ITGA1, ITGA2, and ITGB1 for 24 h. After 24 h, total RNA was extracted, and knockdown efficiency as assessed with qRT-PCR. As compared to the Scrambled control (SCR), mRNA expression ITGA1 ( $55.80 \pm 1.55\%$ ), ITGA2 ( $51.81 \pm 0.5\%$ ), and ITGB1 ( $59.95 \pm 1.03\%$ ) were significantly decreased ( $p$ -value  $< 0.01$ ) indicating that there was efficient knockdown of the mRNA (Fig. 44).

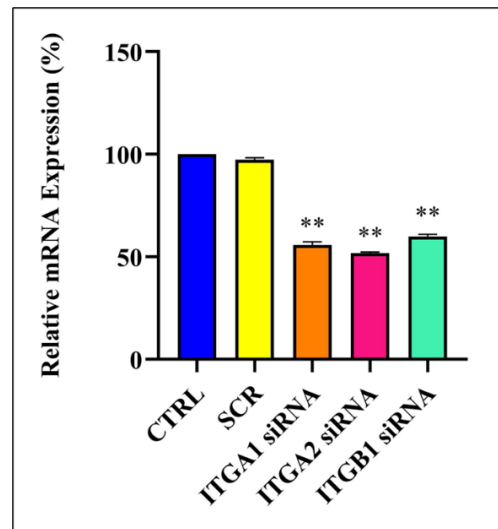


**Figure 44. Knockdown efficiency of ITGA1, ITGA2, and ITGB1 siRNAs in astrocytes.** Astrocytes were treated with 50 nm siRNA against ITGA1, ITGA2, and ITGB1 for 24 h, total RNA was extracted, and the relative mRNA expression of ITGA1, ITGA2, and ITGB1 was measured using qRT-PCR. Scrambled siRNA (SCR) was used as a negative control. Data from 3 donors are represented as mean  $\pm$  SE with each donor experiment done in triplicates. The bar chart represents the combined mean  $\pm$  SD of 3 independent experiments from the 3 donors. The statistical significance was calculated using one-way ANOVA followed by Dunnett's multiple comparison test. \*\* denote  $p$ -value of  $\leq 0.01$ .

Next, we wanted to check whether integrin downregulation is associated with AMPH-induced cell death. We treated astrocytes with ITGA1, ITGA2, and ITGB1 siRNAs for 24 h, cells were re-seeded, and XTT cell viability assay was performed. ITGA1 silencing and AMPH produced significantly ( $p < 0.01$ ) reduced cell viability at 24 h (Fig. 45A) and 48 h (Fig. 45B) compared to SCR and CTRL, respectively. Treating cells with ITGA1 siRNA and AMPH significantly decreased cell viability at 24 h (Fig. 45A) and 48 h (Fig. 45B) compared to SCR and AMPH, indicating the involvement of ITGA1 in AMPH-induced cell death in astrocytes.

ITGA2 silencing and AMPH also significantly ( $p < 0.01$ ) reduced cell viability at 24 h (Fig. 45C) and 48 h (Fig. 45D) compared to SCR and CTRL, respectively. However, treating cells with ITGA2 siRNA and AMPH significantly decreased cell viability at 24 h (Fig. 45C) and 48 h (Fig. 45D) compared to only SCR, but not AMPH. These results suggest that ITGA2 downregulation is not involved in AMPH-mediated cell death in astrocytes.

ITGB1 silencing and AMPH also significantly ( $p < 0.01$ ) reduced cell viability at 24 h (Fig. 45E) and 48 h (Fig. 45F) compared to SCR and CTRL, respectively. Furthermore, treating cells with ITGB1 siRNA and AMPH significantly decreased cell viability at 24 h (Fig. 45E) and 48 h (Fig. 45F) compared to only SCR and AMPH. These results suggest that ITGB1 downregulation is involved in AMPH-mediated cell death in astrocytes.

Taken together, these results suggest that downregulation of integrin  $\alpha 1\beta 1$ , but not integrin  $\alpha 2$ , is involved in AMPH-mediated cell death in primary human astrocytes.

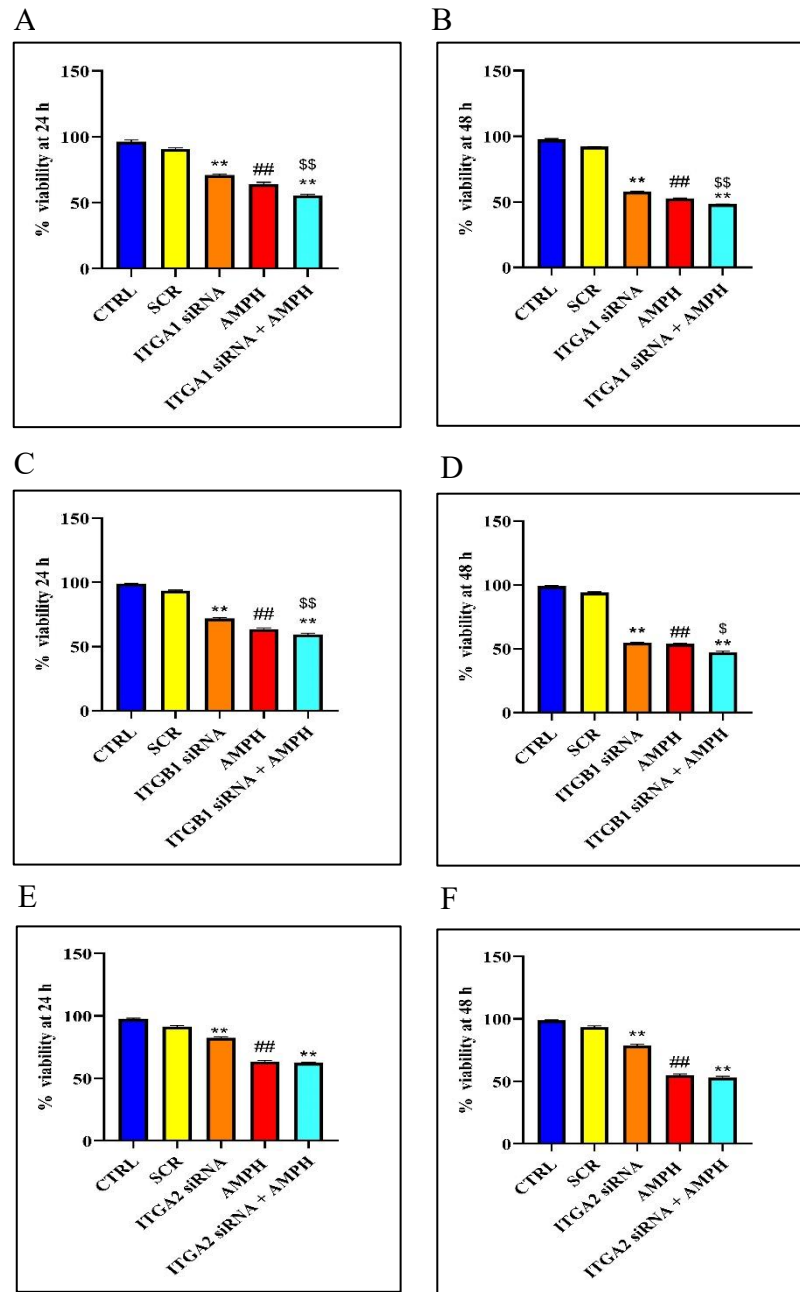


**Figure 45. Involvement of ITGA1, ITGA2, and ITGB1 in AMPH-induced cell death in astrocytes.** Astrocytes were treated with 50 nm siRNA against ITGA1, ITGA2, and ITGB1 for 24 h, cells were re-seeded, and XTT cell viability assay was performed. A and B represent the effect of ITGA1 siRNA on cell viability at 24 and 48 h, respectively. C and D represent the effect of ITGA2 siRNA on cell viability at 24 and 48 h, respectively. E and F represent the effect of ITGB1 siRNA on cell viability at 24 and 48 h, respectively. The data is presented as mean  $\pm$  SE of 3 independent experiments from the 3 donors. The statistical significance was calculated using one-way ANOVA followed by Dunnett's multiple comparison test. \*\* denote p-value of  $\leq 0.01$ .and \*\* denotes a p-value of  $\leq 0.01$  when compared to SCR, ## denotes the p-value of  $\leq 0.01$ , when compared to CTRL, \$ denotes a p-value of  $\leq 0.05$  and \$\$ denotes a p-value of  $\leq 0.01$  when compared to AMPH.

### 3.5 Discussion

Integrins are the cell adhesion receptors that mediate cell survival in response to the cues from the surrounding ECM [85]. These extracellular cues are transmitted into the cells through the direct or indirect interactions of integrins with a diverse array of cytosolic mediators, including protein and lipid kinases, adaptor proteins, and other modulatory proteins [299-301]. Antagonism or downregulation of integrin receptors causes cell death in a variety of cells [141, 143-146]. This “integrin-mediated cell death” occurs due to the lack of the ability of integrins to ligate with ECM proteins and initiate downstream cell survival signals. AMPH has been shown to cause the downregulation of a few integrin subunits in the brain cortex of rats [258]. AMPH has also been shown to cause cleavage of an ECM protein, intercellular adhesion molecule-1 (ICAM-1), further impacting the ability of integrins to attach to ECM [302]. However, no information exists in the literature about the effect of AMPH on the expression of integrins in CNS cells, particularly astrocytes, the most important supportive cells in the brain. Furthermore, whether METH-mediated integrin expression change causes any effects on astrocyte survival is also not known. Therefore, we sought to determine the effect of AMPH on the expression of integrin subunits on astrocytes and whether the effect of AMPH-mediated changes in integrin expression on cell death in astrocytes.

First, we investigated the effect of 6 different doses (50, 100, 200, 500, and 1000  $\mu$ M) of AMPH on the mRNA expression of five  $\alpha$  and five  $\beta$  integrin subunits at 7 timepoints (1, 3, 6, 12, 24, 36, and 48 h) using astrocytes isolated from 4 different post-mortem brain cortices (i.e., 4 donors). AMPH produced a dose- and time-dependent decrease in the mRNA expression levels of all integrin subunits from all donors. Peak mRNA decrease was observed either at 12 h or 24 h, and the expression gradually normalized by 48 h. Based on the mRNA

expression data, we further sought to determine the effect of 500  $\mu$ M AMPH on the protein expression of integrin  $\alpha$ 1,  $\alpha$ 2, and  $\beta$ 1 subunits post 24, 36, and 48 h treatment. We selected integrin  $\alpha$ 1,  $\alpha$ 2, and  $\beta$ 1 subunits because the expression levels of these integrins have been shown to decrease in neurodegenerative diseases. Indeed, AMPH significantly decreased the expression of integrin  $\alpha$ 1,  $\alpha$ 2, and  $\beta$ 1 proteins in all donors. Integrin  $\alpha$  and  $\beta$  subunits are synthesized at different rates in the endoplasmic reticulum and are dimerized before leaving the Golgi apparatus. Only functional dimers are transported to the plasma membrane, whereas isolated chains rapidly degrade [303]. Our finding of decreased expression of integrin subunits, as shown by both qRT-PCR and western blotting, suggests an action of AMPH on integrin expression rather than targeting. A decrease in the expression of integrins can significantly reduce their ability to ligate to ECM and initiate downstream signaling events of cell survival. Furthermore, deletion of integrin  $\beta$ 1 has also been shown to cause partial reactive gliosis, a hallmark feature of astrocytes [117]. Therefore, unligated integrins can significantly affect cellular physiology and contribute to the development of disease states.

Astrocytes isolated from parts of the brain impacted by the toxic effects of AMPH appear to be more susceptible to its effects than other equivalent cell populations [79, 304]. One of the main mechanisms of AMPH neurotoxicity is neuroinflammation, which is partly caused by persistent astrocyte activation called astrogliosis [305]. Astrogliosis has been shown to be followed by cell death, and these dying astrocytes can then kill neighboring cells, implicating astrocyte apoptosis as a major hallmark of brain pathologies [83, 84]. Astrocyte apoptosis can exacerbate neuronal death and CNS pathology as the exchange of neurotrophins between astrocytes and neurons through gap junctions is essential for neuronal survival [306]. Indeed, compromised astrocyte function and survival have negatively impacted neurons in

various brain pathologies [307-309]. The effect of AMPH on neuronal survival has been characterized by several researchers [310-312]. However, reports investigating the effect of AMPH on astrocyte survival and the involved mechanisms are limited [313, 314]. Therefore, we checked the effect of 500  $\mu$ M AMPH on astrocyte survival using XTT cell viability and LDH cytotoxicity assay. AMPH significantly induced cytotoxicity and cell death in astrocytes post-24 and 48 h treatment. AMPH-induced cell death in astrocytes was associated with the activation of caspase-3, indicating that AMPH-induced cell death is apoptotic rather than necrotic.

A substantial body of research suggests that diminished cell adhesion leads to altered signals from the cell surface to the nucleus. Studies have shown that cell survival depends on adherence to matrix proteins such as collagen type I via an integrin  $\beta$ 1-dependent mechanism [315]. The binding of the  $\beta$ 1 integrin family to ECM components results in the clustering of integrins and recruitment of a wide variety of molecules, leading to the formation of focal adhesions [87]. These link the ECM to the actin cytoskeleton and offer a structural underpinning for cell survival [316, 317]. Having demonstrated that AMPH causes significant downregulation of integrin subunits on astrocytes, we utilized siRNAs to check whether decreased expression of integrins  $\alpha$ 1,  $\alpha$ 2, and  $\beta$ 1 is involved in AMPH-induced cell death in astrocytes. Interestingly, silencing the expressions of  $\alpha$ 1,  $\alpha$ 2, and  $\beta$ 1 decreased astrocytic survival; however, only integrin  $\alpha$ 1 and  $\beta$ 1 were demonstrated to mediate AMPH-induced cell death. Integrin  $\alpha$ 1 $\beta$ 1 is a major collagen receptor and also mediates collagen synthesis [318]. The binding of collagen to integrin  $\alpha$ 1 $\beta$ 1 activates downstream cell survival signals. Downregulation of integrin  $\alpha$ 1 $\beta$ 1 disrupts these integrin-matrix interactions triggering a form of apoptosis called anoikis [89]. Prior studies have shown that loss of expression or active

conformation of integrins on astrocytes accompanies structural alterations in the surrounding microenvironment [319]. Therefore, astrocyte apoptosis resulting from AMPH-induced integrin  $\alpha 1\beta 1$  downregulation can compromise neuronal functions and survival, leading to the exacerbation of neurotoxicity.

In summary, in this study, we demonstrated that AMPH decreases the expression of integrin subunits on astrocytes and the decreased expression of integrin  $\alpha 1\beta 1$  is associated with the induction of cell death in astrocytes. We suggest that perturbation of cell-matrix adhesion may be a potential mechanism by which AMPH induces apoptosis in astrocytes. Our results may have important implications for understanding new cellular mechanisms involved in AMPH neurotoxicity.

## CHAPTER 4: PREVALENCE OF PSYCHIATRIC DISORDERS IN METH-ABUSING INDIVIDUALS AND IDENTIFICATION OF NOVEL GENE TARGETS IN METH-ASSOCIATED PSYCHIATRIC DISORDERS

### 4.1 Introduction

In recent years, METH use has become a serious global health concern, with an estimated 34 million users worldwide in 2020. In the US, 2.5 million people aged 12 and older reported using METH in 2021, while 1.5 million had MUD. Increases in purity and a shift in preference from the powdered form to the crystalline form contribute to the escalation of METH-related adverse effects. Additionally, METH-related emergency department (ED) visits, hospitalizations, and health care costs are rising. In the US, the age-adjusted rates of drug overdose deaths involving METH nearly quadrupled between 2012 and 2018. Prior research indicates that most METH users are white, male, between the ages of 25 and 40, use other recreational drugs and alcohol, and seek substance abuse treatment less frequently than other substance users.

Regular METH usage is associated with numerous psychiatric symptoms, including psychosis, anxiety, and depression [9, 16, 320]. METH has a more significant dependence potential than other psychostimulants and is more likely to cause psychiatric symptoms than other illicit substances [321, 322]. Approximately 18% of METH-related ED visits are due to psychiatric symptoms, necessitating psychiatric and therapeutic interventions [323]. Psychiatric symptoms can result in significant morbidity and may affect the response to treatment MUD [322, 324, 325]. In addition, psychiatric comorbidities among METH users are associated with increased resource consumption and demand for mental health care [326]. Nonetheless, patients with access to continuous mental health treatment that addressed METH-

related symptoms and co-occurring disorders had better substance addiction outcomes than those without [327].

No commercially available pharmacotherapy has been found to be broadly effective for treating MUD [328]. Likewise, there is no evidence that treatments can alleviate the psychological distress or symptoms associated with METH use [329-331]. The current clinical approaches advise treating METH-related psychiatric symptoms in accordance with guidelines for similar disorders that are not drug-induced. Psychological therapy is the primary treatment of choice for MUD, and it effectively reduces METH use [332]. Less is known, however, about the effects of these treatments on psychiatric symptoms and which psychological approaches are successful in lowering both METH usage and psychiatric symptoms [333, 334]. As a result, treating METH-associated psychiatric disorders is challenging for the multidisciplinary drug help facilities, first-aid providers, and hospital staff.

Health Facts captures and stores de-identified, longitudinal electronic health records (EHRs) of millions of patients and facilitates a unique opportunity to study more patient variables at once. Thus, understanding the prevalence of co-occurring psychiatric disorders may be an essential first step in planning additional mental health services required in treating MUD. Therefore, we applied a population-level approach using the Cerner Health Facts database to characterize the psychiatric comorbidities associated with METH use. We then identified common gene expression patterns by comparing DEGs from our microarray data METH-treated astrocytes and DEGs from validated microarray datasets of psychiatric disorders uploaded to the Gene Omnibus Expression (GEO) database of the National Center for Biotechnology Information (NCBI).

## **4.2 Methods**

### **4.1.1 Data Source**

We performed a retrospective, longitudinal study based on prospectively collected inpatient data from US hospitals from 2010 – 2018, obtained from an extensive, HIPAA-compliant EHR database, Health Facts (Cerner Corporation, Kansas City, MO). Health Facts database includes information from 863 US healthcare facilities representing over 69 million individual patients (at the time of data extraction), including visit-specific procedures, laboratory results, and healthcare charges. Health Facts is made available through a collaboration between the UMKC, Truman Medical Center, and Cerner Corporation. Institutional Review Board (IRB) exemption for this study was granted by UMKC School of Medicine IRB as a non-human subjects research.

### **4.1.2 Study Population**

Study cohort inclusion criteria were adults ( $\geq 18$  years) with an International Classification of Diseases, Ninth Revision (ICD-9) code V70.4 or Tenth Revision (ICD-10) codes Z02.83 and R78.9 specifying a positive METH screen. Patients with a diagnosis indicating positive drug screen other than METH, as well as children ( $< 18$  years) and elderly adults ( $> 100$  years), were excluded. Demographic data (e.g., age, gender, and race) and concomitant diagnosis codes of the patients included in the study were gathered. The diagnosis codes were used to identify the prevalence of psychiatric comorbidities associated with METH use. Data processing was performed to ensure the quality of the data. Patients with incomplete demographic information were excluded from the analysis.

#### **4.4.3 Prevalence of Psychiatric Disorders**

Data of patients with a positive METH screen were retrieved from Health Facts. Each patient visit to the ED was associated with a unique encounter ID and an associated ICD-9 diagnosis code and description. Next, the data was cleaned up by deleting duplicate or repeat diagnosis codes associated with one unique ED visit by a patient. Frequencies of diagnosis codes belonging to psychiatric disorders were then determined. The final percentage of psychiatric disorders were then calculated by using the formula: (Parent frequency/Patient count) x 100.

#### **4.1.4 GEO Analysis**

Gene Expression Omnibus (GEO) analysis was performed to identify common DEGs from our microarray dataset of METH-treated astrocytes (see chapter 1) and publicly available microarray datasets from bipolar disorder (BD), schizophrenia (SCZ), and major depressive disorder (MDD) patients. The GEO database of the National Center for Biotechnology Information (<https://www.ncbi.nlm.nih.gov/geo/>) was used to obtain microarray datasets belonging to psychiatric disorders using the following inclusion criteria:

1. Specimens had a clinical diagnosis of psychiatric disorder.
2. Healthy specimens were used as controls in the microarray studies.
3. Expression profiling was done by microarray, and the raw data had the CEL format.
4. Gene array was performed using the GPL570 platform (HG\_U133\_Plus\_2 / Affymetrix Human Genome U133 Plus 2.0 Array) or the GPL96 platform (HG\_U133 / Affymetrix Human Genome U133 Array)

By following the inclusion criteria, GEO datasets were downloaded by using the search terms “Bipolar Disorder/Schizophrenia/Major Depressive Disorder” (MeSH Terms), “*Homo sapiens*” (Organism), “CEL” (Supplementary Data), and “Expression profiling by the array (DataSet Type). DEGs were then identified from the GEO datasets. Each dataset was cleaned by removing duplicated genes and genes lacking expression values. Venn diagram analyses of the top 500 DEGs from each dataset and DEGs from METH-treated astrocytes were then performed to visualize and identify overlapping genes.

### **4.3 Results**

#### **4.3.1 Demographic Characteristics**

A total of 5,414 patients with a positive METH screen were identified with Cerner Health Facts database. Patients were 52.3% male, 47.7% female with a mean age of  $36.8 \pm 12.4$  years, median age of 35 years, and age range of 18 to 90 years. Among all patients, 63.6% were Caucasians, 24.3% were Native Americans, 1.7% were African Americans, 1.6% were Hispanics, 0.6% had Biracial, 0.4% were Asians, 0.1% were Pacific Islanders, and 5.6% did not provide race information. The patient population consisted of 58.7% single patients, 17.5% were married, 11% were divorced, 3.4% were legally separated, 2.1% were widowed, 0.9% had life partners, and no information was available for 6.4% of patients. Majority of the patients (73.6%) were located in an urban geographic area (Table 11).

**Table 11: Cohort demographics**

Demographic characteristics	n (%) n = 5,414
<b>Sex</b>	
Male	<b>2,830 (47.7)</b>
Female	<b>2,584 (52.3)</b>
<b>Age (years)</b>	
Mean $\pm$ SD	<b>36.8 <math>\pm</math> 12.4</b>
Median	<b>35</b>
Age range	<b>18 - 90</b>
<b>Race</b>	
Asian	<b>22 (0.4)</b>
African American	<b>93 (1.7)</b>
Biracial	<b>30 (0.6)</b>
Caucasian	<b>3,445 (63.6)</b>
Hispanic	<b>87 (1.6)</b>
Native American	<b>1,313 (24.3)</b>
Pacific Islander	<b>56 (0.1)</b>
Unknown	<b>302 (5.6)</b>
<b>Marital Status</b>	
Divorced	<b>595 (11)</b>
Legally separated	<b>184 (3.4)</b>
Life partner	<b>47 (0.9)</b>
Married	<b>950 (17.5)</b>
Single	<b>3,176 (58.7)</b>
Unknown	<b>348 (6.4)</b>
Widowed	<b>114 (2.1)</b>
<b>Geographic area</b>	
Rural	<b>1,430 (26.4)</b>
Urban	<b>3,984 (73.6)</b>

### 4.3.2 Prevalence of Psychiatric Disorders

A total of 8,714 frequencies belonging to 469 unique diagnosis codes were identified from the retrieved data. The prevalence of psychiatric disorders was anxiety (6.8%), bipolar disorder (3.7%), dissociative or somatoform disorders (2.2%), schizophrenia (2%), major depressive disorder (1.8%), dysthymic disorder (1.1%), adjustment reaction (0.9%), panic disorders (0.7%), personality disorders (0.7%), and episodic mood disorders (0.5%) (Table 12).

**Table 12: Prevalence of psychiatric disorders in patients with a positive METH screen**

No.	Psychiatric disorder	Diagnosis code frequency	Percentage (%)
1	Anxiety	595	6.8
2	Bipolar disorder	322	3.7
3	Dissociative and somatoform disorders	190	2.2
4	Schizophrenia	175	2
5	Major depressive disorder	154	1.8
6	Dysthymic disorder	98	1.1
7	Adjustment reaction	77	0.9
8	Panic disorder	64	0.7
9	Personality disorder	57	0.7
10	Episodic mood disorders	46	0.5

### 4.3.3 GEO Analysis

#### 4.3.3.1 Bipolar Disorder

Using the GEO database, we identified 5 microarray datasets prepared from RNA extracted from human postmortem brain tissue from adult subjects with BD and healthy controls. The mRNA for these microarray studies were isolated from prefrontal cortex, orbitofrontal cortex, parietal cortex, striatum, and hippocampus. The microarray datasets comprised samples from 156 BD patients and 165 controls (Table 13).

**Table 13: GEO Bipolar disorder microarray datasets used in the analysis**

No.	Data Source	Number of samples		Brain Region	Platform	References
		Cases	Controls			
1	GSE5389	10	11	Orbitofrontal cortex	Affy HG-U133A	[335]
2	GSE12654	11	15	Prefrontal cortex	Affy HG-U133A	[336]
3	GSE35978	50	50	Parietal cortex	Affy HG-U133A	[337]
		17	19	Prefrontal cortex		
4	GSE53987	18	18	Striatum	Affy HG-U133A_Plus2	[338]
		18	18	Hippocampus		
5	GSE12649	32	34	Prefrontal cortex	Affy HG-U133A	[339]
Total		156	165			

After retrieving the microarray datasets from the GEO database, DEGs each microarray dataset was carefully analyzed to removing duplicated genes and genes lacking expression values. Top 500 DEGs from all BD datasets were then overlapped with 1,924 DEGs from our microarray dataset of METH-treated astrocytes in a Venn diagram to identify common genes. Only one gene, ADSS (adenylosuccinate synthetase), was found to be common between the BD GEO datasets and our dataset of METH-treated astrocytes (Fig. 46). ADSS is an important enzyme involved in the purine ribonucleotide biosynthesis and has been shown to upregulate in BD patients [340]. Indeed, ADSS was also upregulated in all GEO datasets. ADSS was also upregulated in our microarray dataset of METH-treated astrocytes by 33.82 folds.

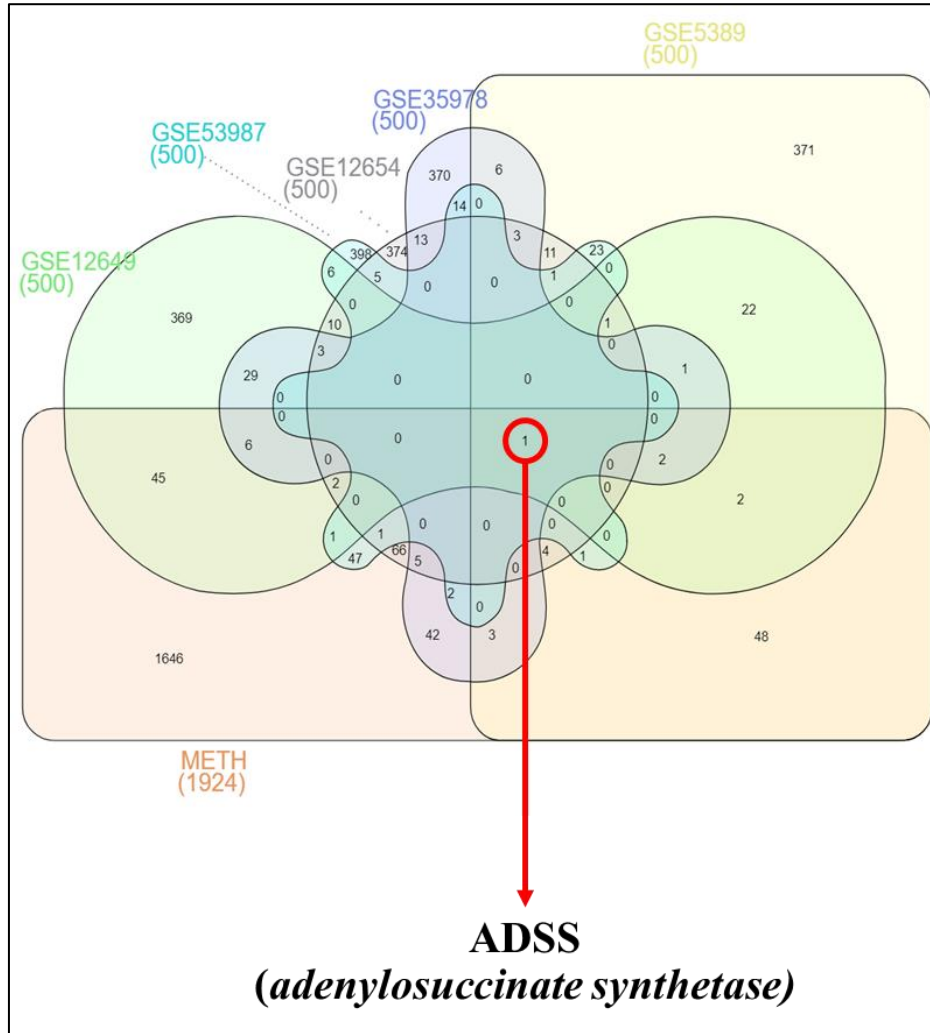


**Figure 46. Co-expressed genes between BD microarray datasets from the GEO database and microarray dataset of METH-treated astrocytes.** The top 500 DEGs from GEO BD datasets and 1,924 DEGs from METH microarray datasets were overlapped in a Venn diagram to identify shared gene expression patterns. Different shapes in the diagram represent different datasets.

### 4.3.3.2 Major Depressive Disorder

Using the GEO database, we identified 3 microarray datasets prepared from RNA extracted from human postmortem brain tissue from adult subjects with MDD and healthy controls. The mRNA for these microarray studies were isolated from prefrontal cortex. The microarray datasets comprised samples from 80 MDD patients and 86 controls (Table 14).

**Table 14: GEO major depressive disorder microarray datasets used in the analysis**

No.	Data Source	Number of samples		Brain Region	Platform	References
		Cases	Controls			
1	GSE53987	17	21	Prefrontal cortex	Affy HG-U133A_Plus2	[338]
2	GSE12654	50	50	Prefrontal cortex	Affy HG-U133A_Plus2	[336]
3	GSE54567	13	15	Prefrontal cortex	Affy HG-U133A_Plus2	[341]
Total		80	86			

After retrieving the microarray datasets from the GEO database, DEGs each microarray dataset was carefully analyzed to removing duplicated genes and genes lacking expression values. Top 500 DEGs from all MDD datasets were then overlapped with 1,924 DEGs from our microarray dataset of METH-treated astrocytes in a Venn diagram to identify common genes. Only one gene, STAT5B (Signal transducer and activator of transcription 5B), was found to be common between all MDD GEO datasets and our dataset of METH-treated astrocytes (Fig. 47). STAT5B is a transcription factor involved in diverse biological processes. It has been shown to regulate learning, memory formation, neuroplasticity, and behavior [342]. STAT5B was downregulated in all GEO MDD datasets and our METH microarray dataset (by 8.05 folds)

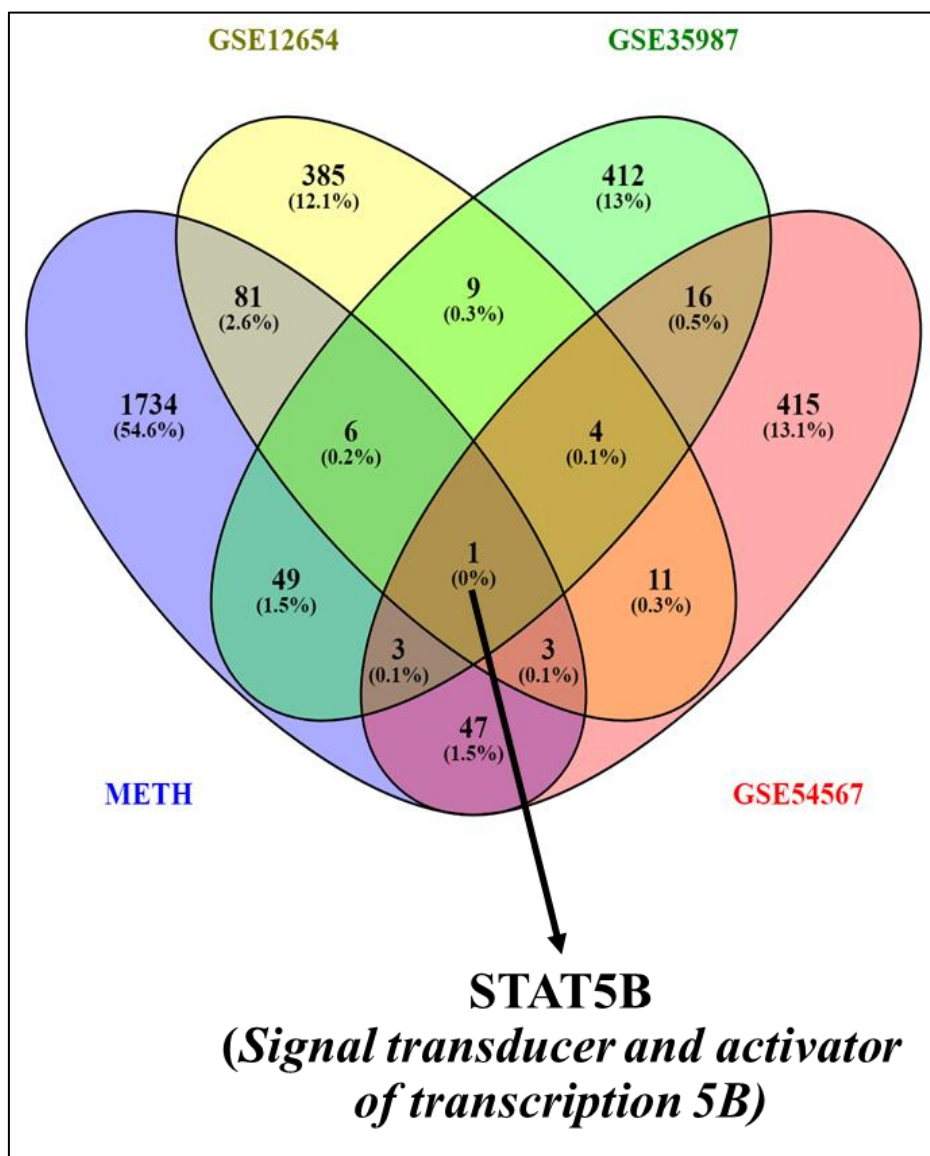


**Figure 47. Co-expressed genes between MDD microarray datasets from the GEO database and microarray dataset of METH-treated astrocytes.** The top 500 DEGs from GEO BD datasets and 1,924 DEGs from METH microarray datasets were overlapped in a Venn diagram to identify shared gene expression patterns. Different colors in the diagram represent different datasets.

### 4.3.3.2 Schizophrenia

Using the GEO database, we identified 5 microarray datasets prepared from RNA extracted from human postmortem brain tissue from adult subjects with SCZ and healthy controls. The mRNA for these microarray studies were isolated from prefrontal cortex. The microarray datasets comprised samples from 176 MDD patients and 185 controls (Table 14).

**Table 14: GEO schizophrenia microarray datasets used in the analysis**

No.	Data Source	Number of samples		Brain Region	Platform	References
		Cases	Controls			
1	GSE12654	13	15	Prefrontal cortex	Affy HG-U133A	[336]
2	GSE35978	50	51	Parietal cortex	Affy HG-U133A	[337]
3	GSE12649	35	35	Prefrontal cortex	Affy HG-U133A	[339]
4	GSE53987	15	19	Prefrontal cortex	Affy HG-U133A_Plus2	[338]
		18	18	Striatum		
		15	18	Hippocampus		
5	GSE21138	30	29	Prefrontal cortex	Affy HG-U133A_Plus2	[343]
Total		176	185			

After retrieving the microarray datasets from the GEO database, DEGs each microarray dataset was carefully analyzed to removing duplicated genes and genes lacking expression values. Top 500 DEGs from all MDD datasets were then overlapped with 1,924 DEGs from our microarray dataset of METH-treated astrocytes in a Venn diagram to identify common genes. Only one gene, SPON1 (Spondin 1), was found to be commonly expressed between all MDD GEO datasets and our dataset of METH-treated astrocytes (Fig. 48). SPON1 is an extracellular matrix protein involved in the growth of axons during embryonic development [344], differentiation of neural cells [345], and the promotion of axonal regeneration post-

injury [346]. SPON1 has been shown to be downregulated in SCZ patients [347]. Indeed, SPON1 was also downregulated in all GEO datasets and METH microarray dataset ( $\log_2FC$ : -4.213).

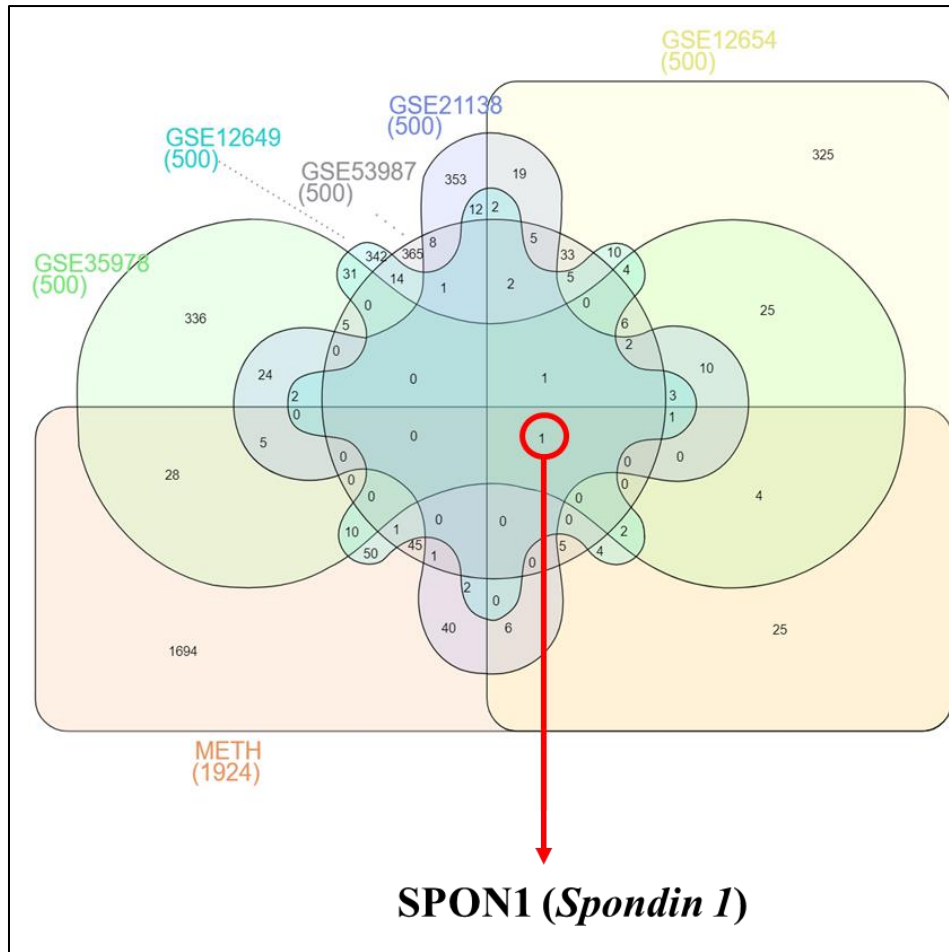


**Figure 48. Co-expressed genes between SCZ microarray datasets from the GEO database and microarray dataset of METH-treated astrocytes.** The top 500 DEGs from GEO BD datasets and 1,924 DEGs from METH microarray datasets were overlapped in a Venn diagram to identify shared gene expression patterns. Different shapes in the diagram represent different datasets.

#### 4.4 Discussion

Psychiatric disorders associated with METH use can result in significant morbidity among users. According to published studies, a considerable number of METH-dependent individuals exhibit symptoms severe enough to warrant psychiatric hospitalization, and many have attempted suicide in their lives [322]. Although a substantial amount of research has been devoted to documenting psychiatric comorbidity in cocaine users and the broader drug-using community [348-350], limited information is available on METH-dependent populations [14, 16, 351]. When co-occurring psychiatric problems are present, the response to treatment for substance use disorders may be negatively impacted [352]. According to published studies, patients who had access to ongoing mental health therapy had better substance abuse outcomes than those who did not [327]. Consequently, identifying and describing co-occurring illnesses is a crucial initial step in the treatment of co-occurring psychiatric problems in METH use. Knowledge of the frequency of co-occurring disorders may result in enhanced diagnostic efficacy and precision. This information may help inform clinical and programmatic planning for extra mental health treatments that may be necessary for the treatment of MUD. Accordingly, we analyzed data from Cerner Health Facts to examine the prevalence of psychiatric disorders in patients hospitalized for MUD.

The demographic characteristics showed that a typical METH-user with a psychiatric comorbidity is young, Caucasian, single, and living in urban area. The overall prevalence of anxiety (6.8%), MDD (1.8%), dysthymic disorders (1.1%), adjustment disorders (0.9%), panic disorders (0.7%), and episodic mood disorders (0.5%) in METH-using individuals was notably lower than the reported estimates for US populations (20-30% for anxiety, 8.4% for MDD, 3% for dysthymic disorders, 12% for adjustment disorders, 3.7% for panic disorders, and 9.7% for

episodic mood disorders) [3, 353-356] . However, the prevalence of bipolar disorder (3.7%), dissociative and somatoform disorders (2.2%), and schizophrenia (2%) were notably higher in METH-using individuals than reported US estimates (2.8% for bipolar disorder, 1.1-1.5% for dissociative and somatoform disorders, and 1% for schizophrenia) [357].

There are several limitations to the study. First, the full patient history was not available. Thus, we were unable to distinguish individuals with newly diagnosed psychiatric disorders, from individuals with existing psychiatric disorders. Second, the diagnosis codes used for billing may not include all subtypes of a psychiatric disorder such as anxiety. Consequently, this study likely underestimates the prevalence of psychiatric disorders in METH-using individuals. Third, there was a lack of data on age-matched controls who did not test positive for METH. Future studies performed using Cerner Health Facts or any other EHRs should address these gaps in data to accurately determine the prevalence of psychiatric disorders. While this data has noted limitations, the size of the Cerner Health Facts Database is extremely large, with over 69 million encounters captured during the study period. This allows the analysis of more patient variables and stratification of data according to patient variables is possible

We also analyzed GEO microarray datasets of bipolar disorder, major depressive disorder, and schizophrenia, and compared them with our microarray dataset of METH-treated astrocytes to find shared genes. The hypothesis driving this work is that genetic predispositions lead to the development of psychiatric disorders with long-term METH use. Identifying genes associated with psychiatric disorders and those affected by METH use may thus yield a set of candidate genes for predisposition of psychiatric comorbidities. While our analysis showed a set of genes in common between different GEO datasets or between individual GEO datasets

across each disorder and METH dataset, a much smaller set of genes were common across all of the analyzed datasets for each disorder and METH dataset. Only one significant overlapping gene was noted for each disorder.

For Bipolar Disorder (BD), the shared gene identified between the GEO BD datasets and the METH dataset was ADSS. ADSS is an enzyme that plays an essential role in purine biosynthesis. ADSS has been found to be downregulated in BD patients [340]. Interestingly, ADSS has been found to code to chromosomal locus, 1cen-q12, previously linked to SCZ by meta-analysis [340, 358, 359]. Genetically, ADSS gene resides in the susceptibility loci and the blood-derived RNA of ADSS was among the 8 genes with putatively differential diagnostic power for SCZ [360]. An extensive genetic overlap exists between BD and SCZ. Therefore, it is very likely that the same risk loci might be shared between BD and SCZ [361, 362]. Although our results clearly suggest the involvement of ADSS downregulation in BD onset in METH abusers, more studies, especially the examination of single nucleotide polymorphisms (SNPs), are required to further support ADSS as a susceptibility gene for BD.

For MDD, the STAT5B gene was found to be shared between MDD GEO and METH datasets. STAT5B is a transcription factor, and its activation is mediated by signals that originate from cytokine receptors, most notably interleukin-2 receptors (IL-2R). It is involved in diverse biological processes, such as T-cell receptor signaling, apoptosis, adult mammary gland development, and sexual dimorphism of liver gene expression. STAT5B also interacts with glucocorticoid receptor (GR) and is vital for postnatal growth [363]. Furthermore, several STAT5-recruiting cytokines are involved in memory formation, neuroplasticity, behavior, and other cognitive aspects [364]. In patients with MDD, DEGs enriched in STAT5-mediated IL-2 signaling have been observed [365]. Moreover, decreased expression of STAT5B has been

observed in mouse models of post-traumatic stress disorder (PTSD) [366] as well as in patients with PTSD [367, 368]. There is evidence for a shared heritable influence on PTSD and MDD [369]. An analysis of the genome-wide association studies (GWAS) by the Psychiatric GWAS Consortium has reported SNP with significant heritability for European-American females and found evidence for overlapping genetic risk between PTSD and MDD [370, 371]. Another GWAS comparison analysis between PTSD and MDD identified the UBA7 gene with a high probability of a shared causal expression quantitative trait loci (eQTL) variant [372]. UBA7 encodes an E1 ubiquitin-activating enzyme involved in STAT1-mediated interferon- $\alpha$  regulation of hippocampus neurogenesis and apoptosis [373]. The UBA7 eQTL shares genetic effects with PTSD and MDD GWAS variants, suggesting a potential pleiotropic mechanism at this locus [372]. The majority of these findings represent SNPs and eQTLs from a PTSD enriched dataset that colocalize with MDD GWAS variants. This demonstrates not only the phenotypic comorbidity between PTSD and MDD but identifies genes and genomic regions of possible pleiotropy.

Our results and the published analysis of shared PTSD and MDD GWAS studies identified STAT5B as a potential gene target. As mentioned earlier, STAT5 forms a complex with GR [363]. Dysregulation of hypothalamic-pituitary-adrenocortical (HPA) axis activity is a significant neuroendocrine abnormality in MDD, resulting in elevated plasma levels of corticotropin and cortisol [374, 375]. The function of the HPA axis interrelates with glucocorticoid (GC) signaling, which is disrupted in MDD [376, 377]. Moreover, a reduction in the GR mRNA and its activity has been observed in the hippocampus and forebrain of MDD patients [376]. Therefore, downregulation of STAT5B can cause MDD by disrupting GR-

mediated transcriptional activity, resulting in increased HPA activity and elevated plasma levels of corticotropin and cortisol [374, 375].

SPON1 was co-expressed in both the SCZ GEO datasets and the METH microarray dataset. SPON1 is a protein secreted by ventral plaque cells that facilitates axonal targeting of nerve cells during embryonic development [378, 379]. Due to its critical role in axon nerve junction in embryonic development, it is believed that mutations in SPON1 (particularly the frameshift mutations that lead to complete dysfunction) may be related to SCZ [380]. Indeed, the addition of cytosine in position 602 of the SPON1 gene has been detected in the shared gene pool of SCZ patients. In addition, a GWAS study identified SPON1 variants were in rs2618516 on chromosome 11 (11p15.2). These variants have been shown to cause structural damage in the brains of the elderly and are responsible for various levels of dementia [381]. Further analysis suggested that SPON1 and its surrounding gene networks had a significant association with autism, developmental disturbances, and mental retardation. An analysis of RNA-sequencing data showed SPON1 to be downregulated in astrocytes of patients with SCZ [347, 382]. Furthermore, a comprehensive analysis of microarray data, weighted gene co-expression analysis modules data, and the Database of Genomic Variants in family trios with SCZ identified large rare copy number variations (CNVs) in SPON1 [383]. SPON1 was also identified as a suicide candidate gene associated with SCZ using unbiased genome-wide expression profiling [384]. Collectively, our results and previously published data clearly imply that the downregulation of the SPON1 gene may be responsible for the development of SCZ in METH abusers.

In summary, our study identified higher prevalence of bipolar disorder, dissociative and somatoform disorders, and schizophrenia in METH-abusing population compared to the US population estimates. The prevalence of anxiety, MDD, dysthymic disorders, adjustment disorders, panic disorders, and episodic mood disorders were lower in METH-abusing population. This is the first study to utilize a population level approach to identify the prevalence of psychiatric disorders In METH-abusing individuals. We then performed analysis of microarray datasets to determine co-expressed genes between microarray datasets psychiatric disorders and METH-treated astrocytes. We identified ADSS (for bipolar disorder), STAT5B (for MDD), and SPON1 (for schizophrenia) as the key genes that might be responsible for the development of psychiatric disorders in METH-abusing individuals. Our results can serve as a first step towards the further research to understand the genetic basis of METH-associated psychiatric disorders.

## CHAPTER 5: FUTURE DIRECTIONS

Amphetamines are the world's second most widely used class of illicit drugs. A significant amount of research has been conducted over the last several years, advancing our knowledge about how amphetamines cause neurotoxicity and contribute to the development of psychiatric disorders. However, no effective pharmacotherapy has been approved to treat amphetamine use disorder. Studies performed in this dissertation are among the few that aim to understand the effect of astrocyte transcriptome changes and the role of integrins in the neurotoxicity of amphetamines and associated psychiatric disorders. However, our studies might be the tip of the iceberg. Multiple mechanisms contribute to the development of amphetamine neurotoxicity. The contribution of integrin expression changes to the neurotoxic mechanisms of amphetamines, for example, oxidative stress, needs further research. First, the use co-culture models of astrocytes, neurons, and microglia can give us a better understanding of how the changes in integrin expression affect the overall physiology of these interconnected and interdependent cells in the context of neurotoxicity. Second, the use of integrin knockout models can also prove vital to understand the pathogenesis of amphetamine neurotoxicity. Third, integrin agonists can be tested as potential agents to ameliorate amphetamine neurotoxicity. Therefore, use of co-culture and knockout models to understand the effect of integrins on oxidative stress and cell death can be undertaken to move one step forward in our current understanding.

Our analysis of the data of METH-abusing individuals from the Cerner Health Facts yielded significant insights about the prevalence of psychiatric disorders. Further studies should evaluate the independent effects of age, gender, race, and other demographic characteristics on the prevalence of psychiatric disorders. Likewise, the contribution of ADSS,

STAT5B, and SPON1 in the development of amphetamine-associated psychiatric disorders should be evaluated using various *in vitro* and *in vivo* approaches.

APPENDIX

A. ORIGINAL WESTERN BLOT GEL IMAGES



**Figure A1. Original blot indicating ITGA1 at 24 h from donor 1 for representative western blot used in Figure 39. Experiment date: March 30, 2021**



**Figure A2. Original blot indicating ITGA1 at 36 h from donor 1 for representative western blot used in Figure 39. Experiment date: March 30, 2021**

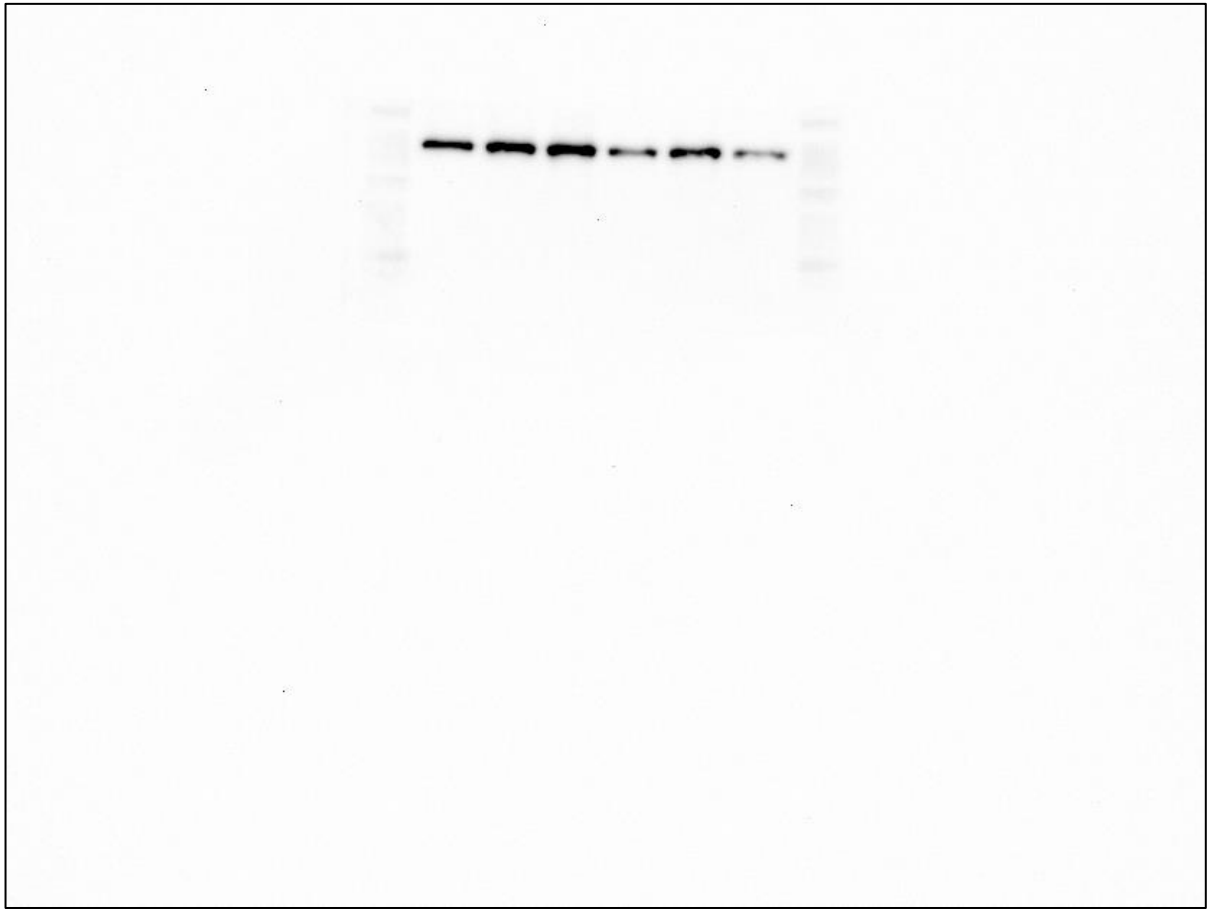


**Figure A3. Original blot indicating ITGA1 at 48 h from donor 1 for representative western blot used in Figure 39. Experiment date: March 30, 2021**

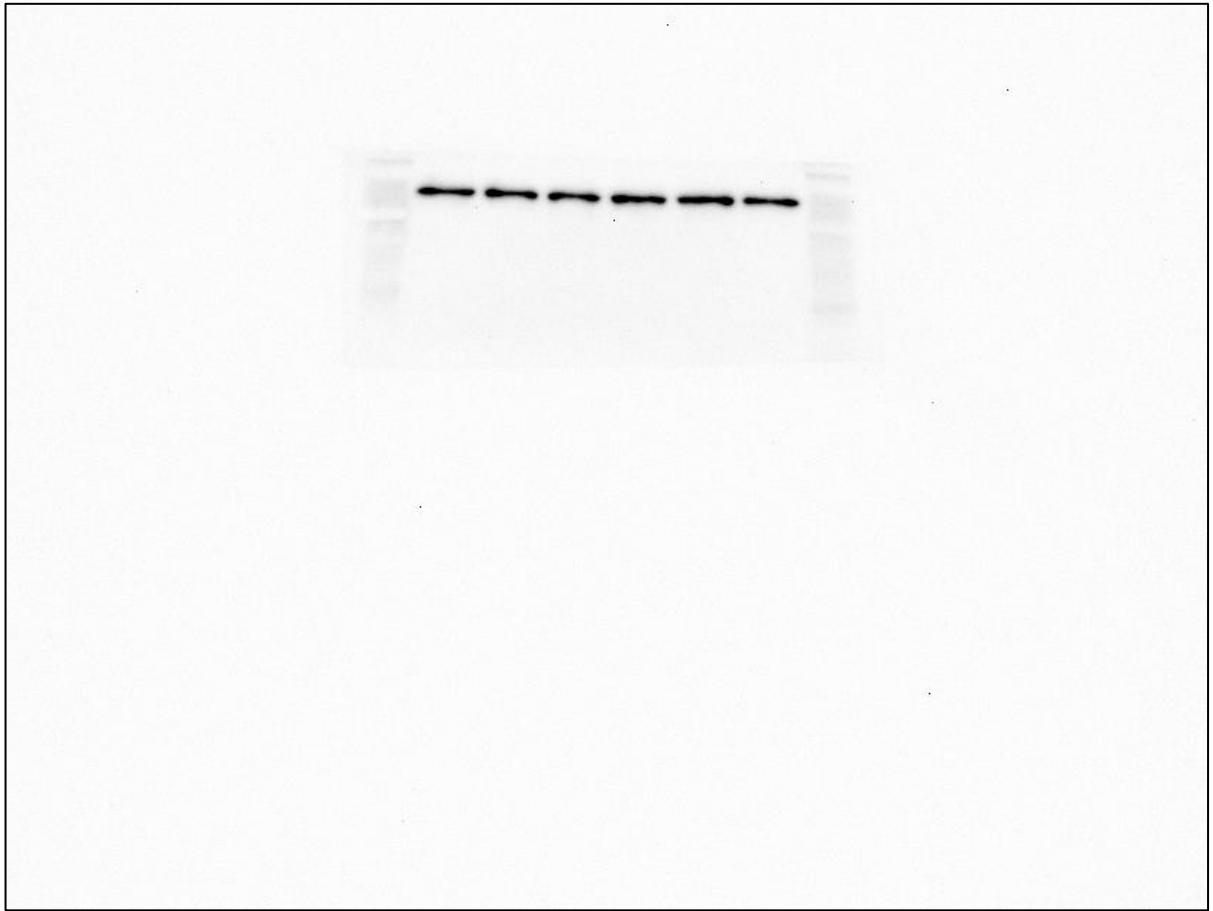


**Figure A4. Original blot indicating ITGA1 at 24 h from donor 2 for representative western blot used in Figure 39. Experiment date: March 30, 2021**

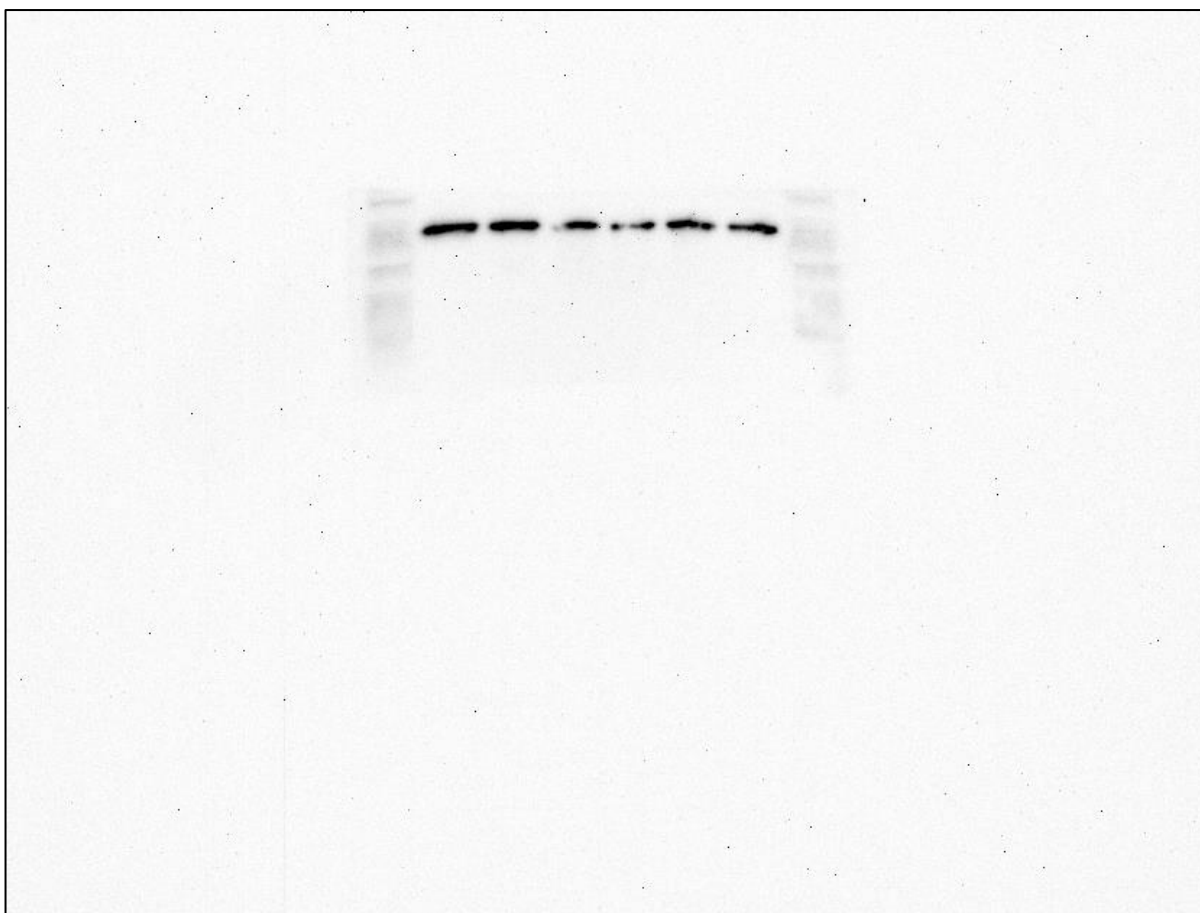


**Figure A5. Original blot indicating ITGA1 at 36 h from donor 2 for representative western blot used in Figure 39. Experiment date: March 30, 2021**

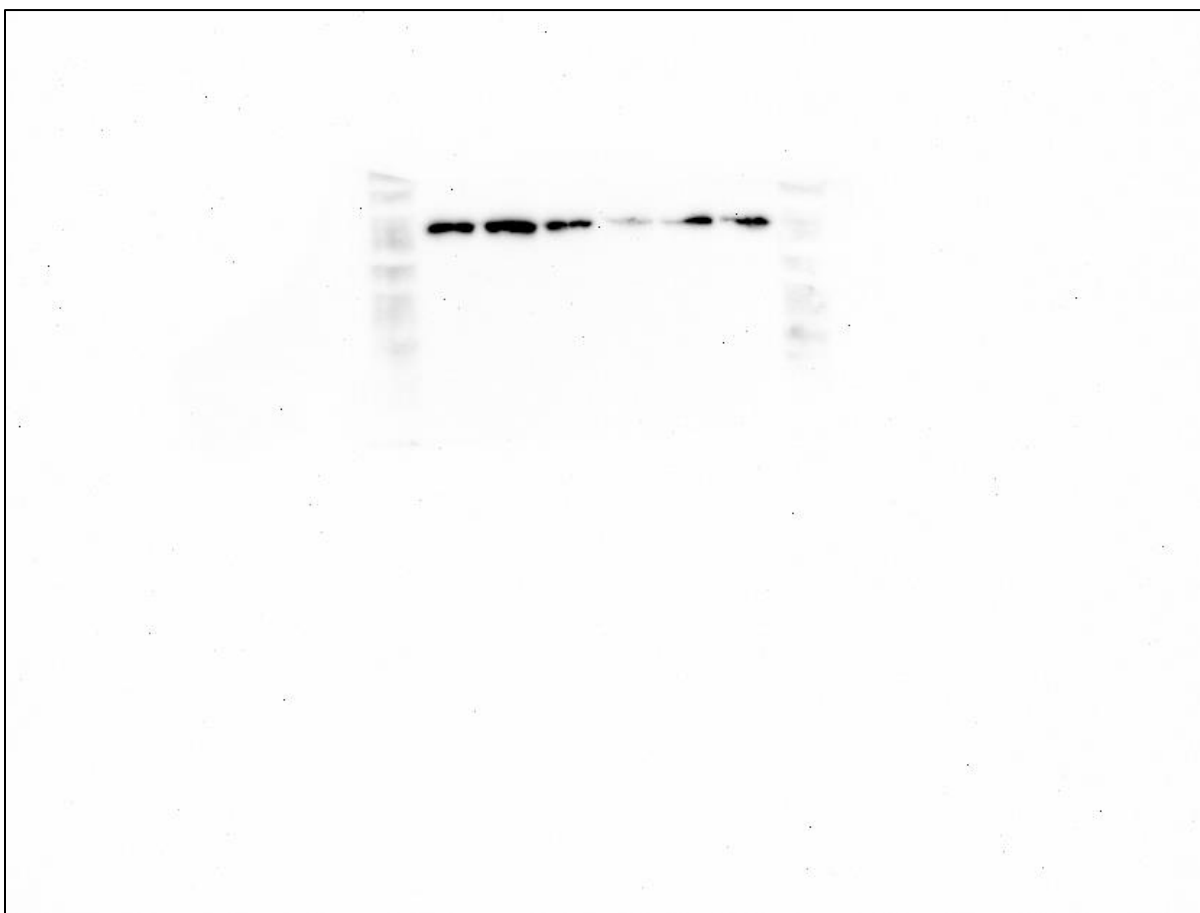


**Figure A6. Original blot indicating ITGA1 at 48 h from donor 2 for representative western blot used in Figure 39. Experiment date: March 30, 2021**

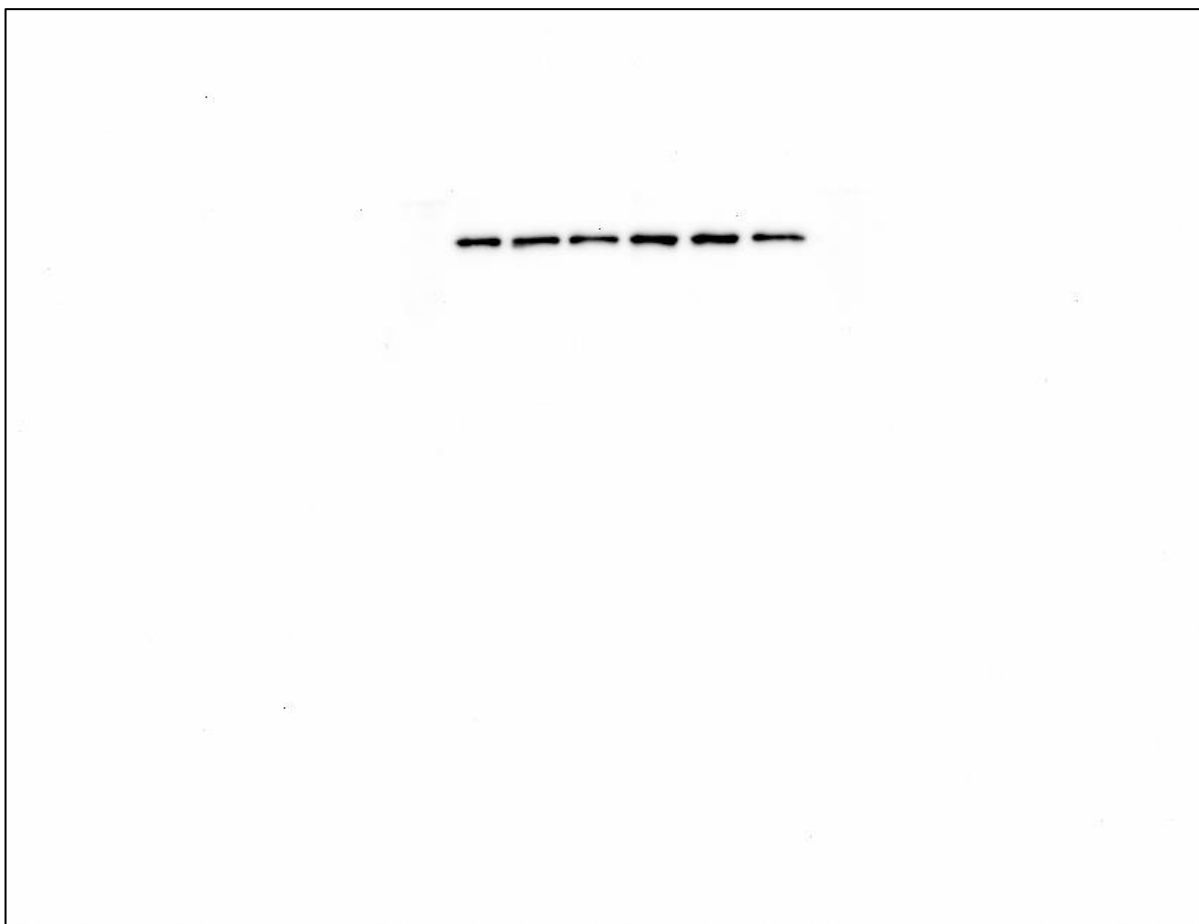


**Figure A7. Original blot indicating ITGA1 at 24 h from donor 3 for representative western blot used in Figure 39. Experiment date: April 6, 2021**

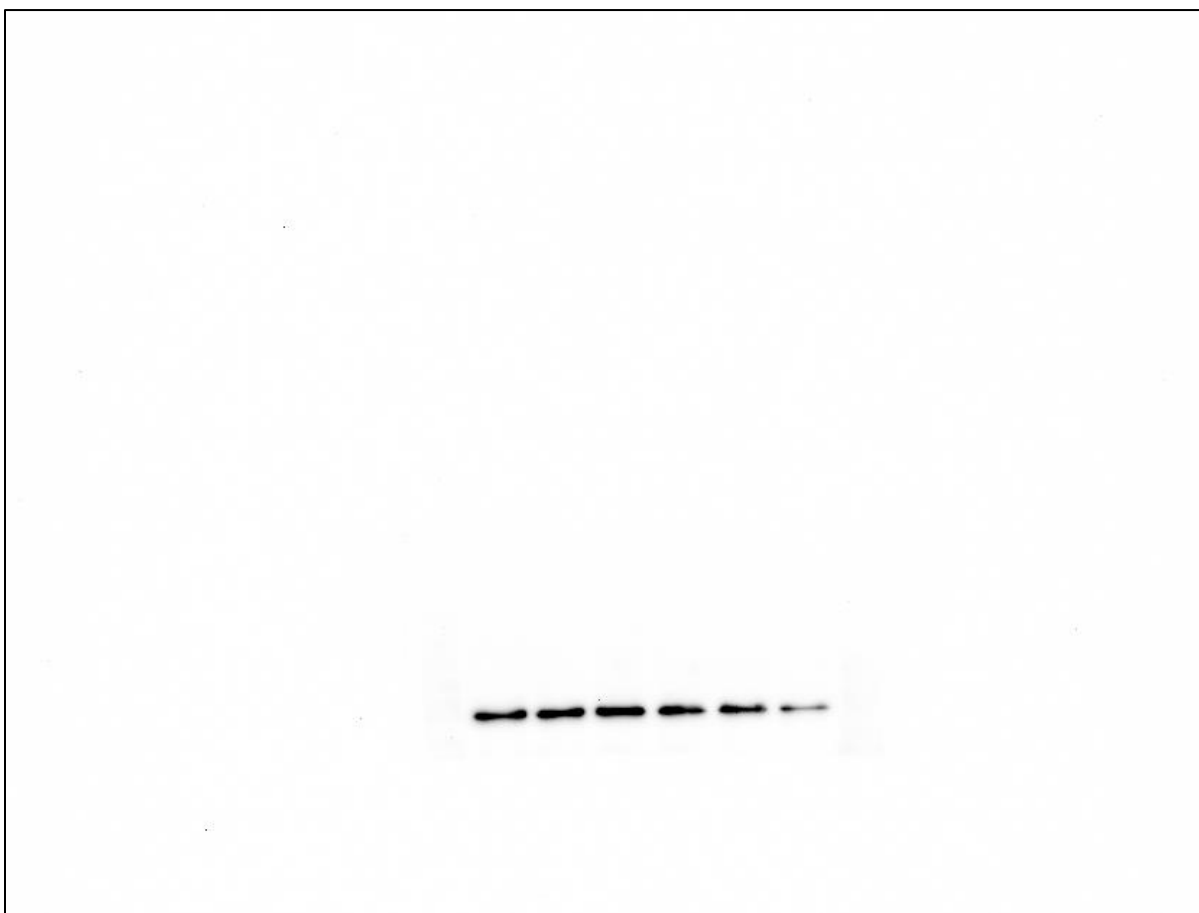


**Figure A8. Original blot indicating ITGA1 at 36 h from donor 3 for representative western blot used in Figure 39. Experiment date: April 6, 2021**



**Figure A9. Original blot indicating ITGA1 at 48 h from donor 3 for representative western blot used in Figure 39. Experiment date: April 6, 2021**

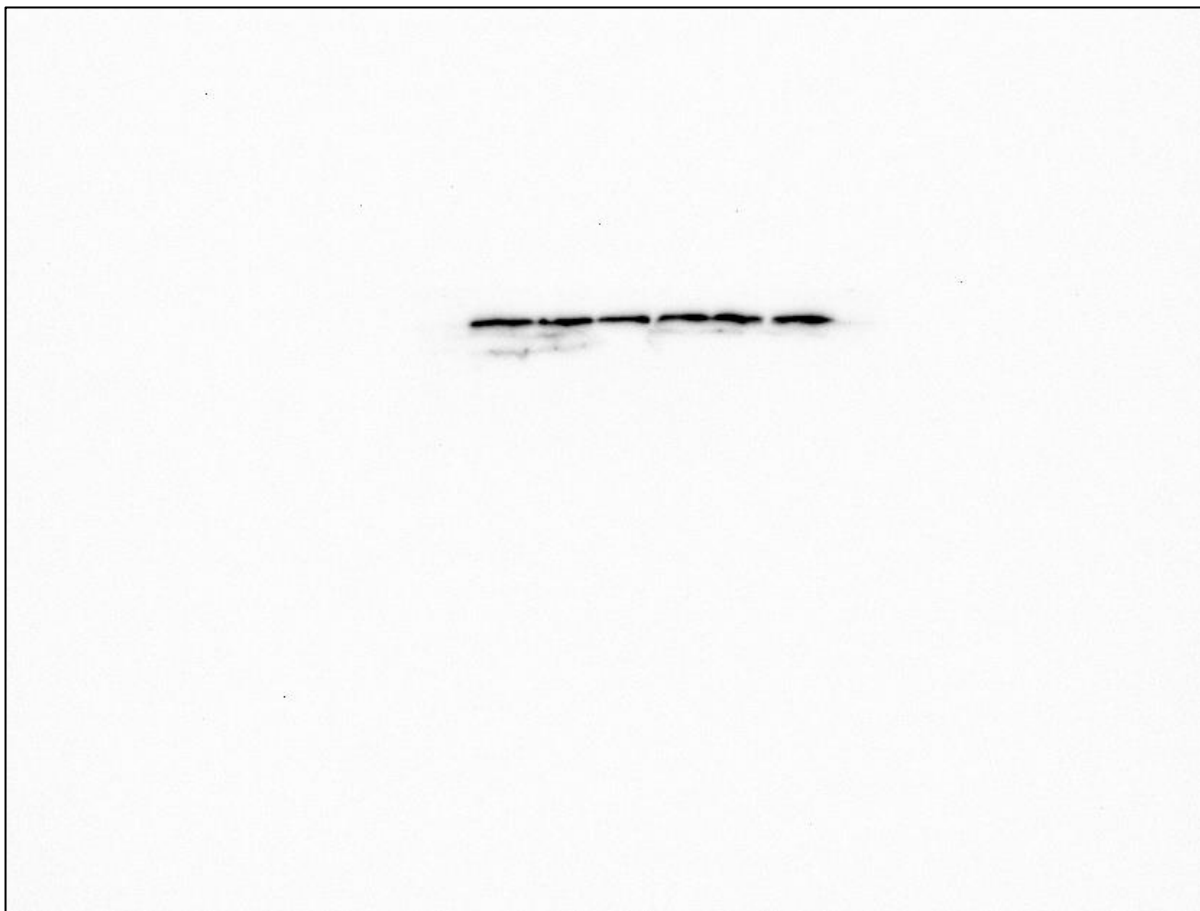


**Figure A10. Original blot indicating ITGA1 at 24 h from donor 4 for representative western blot used in Figure 39. Experiment date: April 6, 2021**



**Figure A11. Original blot indicating ITGA1 at 36 h from donor 4 for representative western blot used in Figure 39. Experiment date: April 6, 2021**



**Figure A12. Original blot indicating ITGA1 at 48 h from donor 4 for representative western blot used in Figure 39. Experiment date: April 6, 2021**

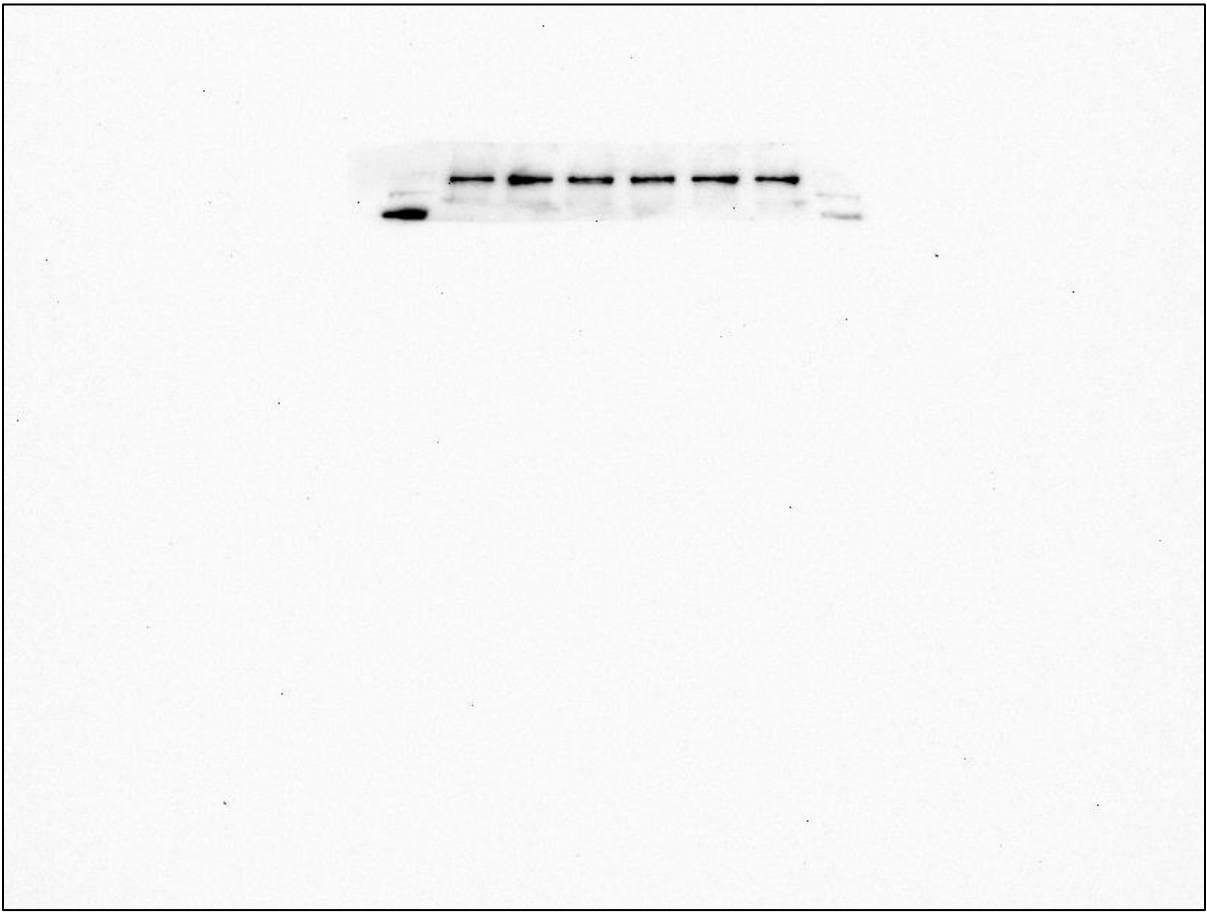


**Figure A13. Original blot indicating ITGA2 at 24 h from donor 1 for representative western blot used in Figure 40. Experiment date: April 14, 2021**

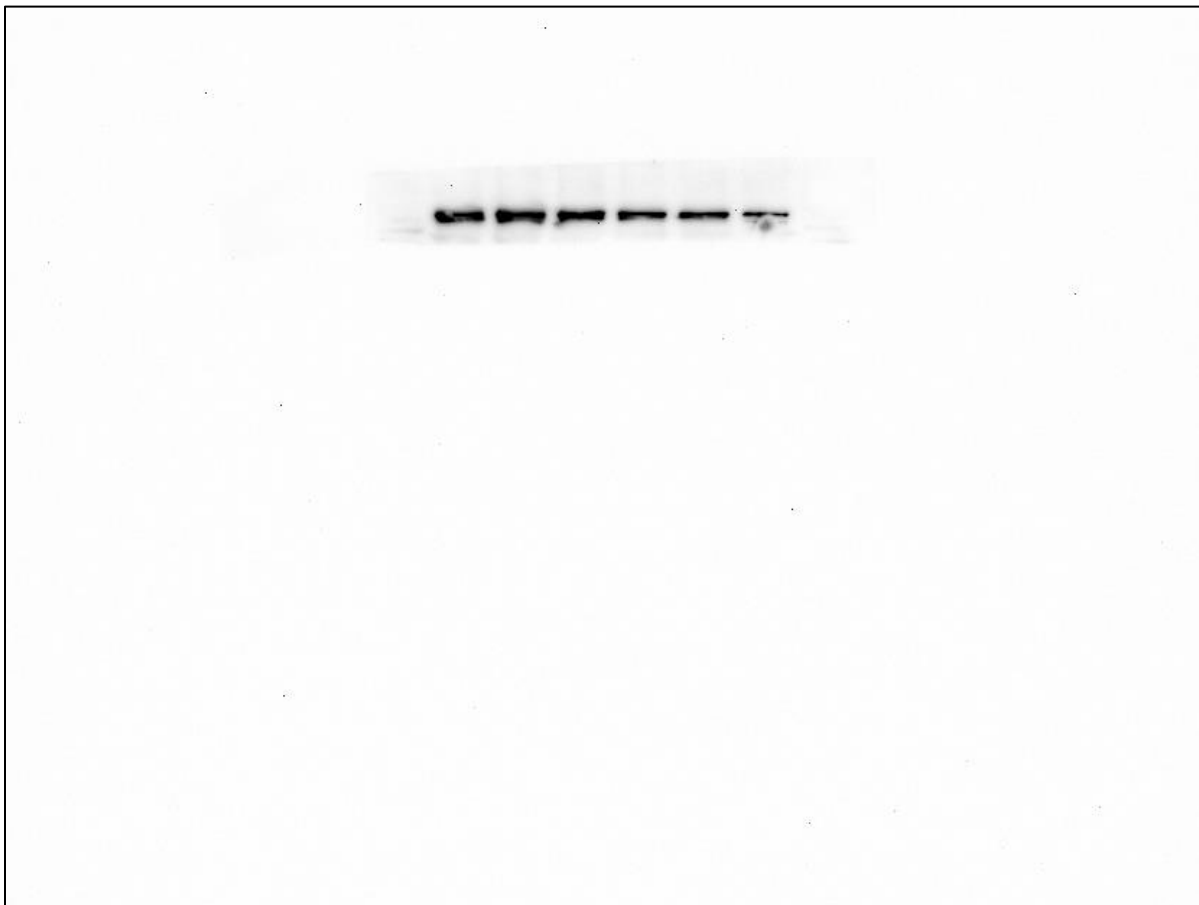


**Figure A14. Original blot indicating ITGA2 at 36 h from donor 1 for representative western blot used in Figure 40. Experiment date: April 14, 2021**



**Figure A15. Original blot indicating ITGA2 at 48 h from donor 1 for representative western blot used in Figure 40. Experiment date: April 14, 2021**

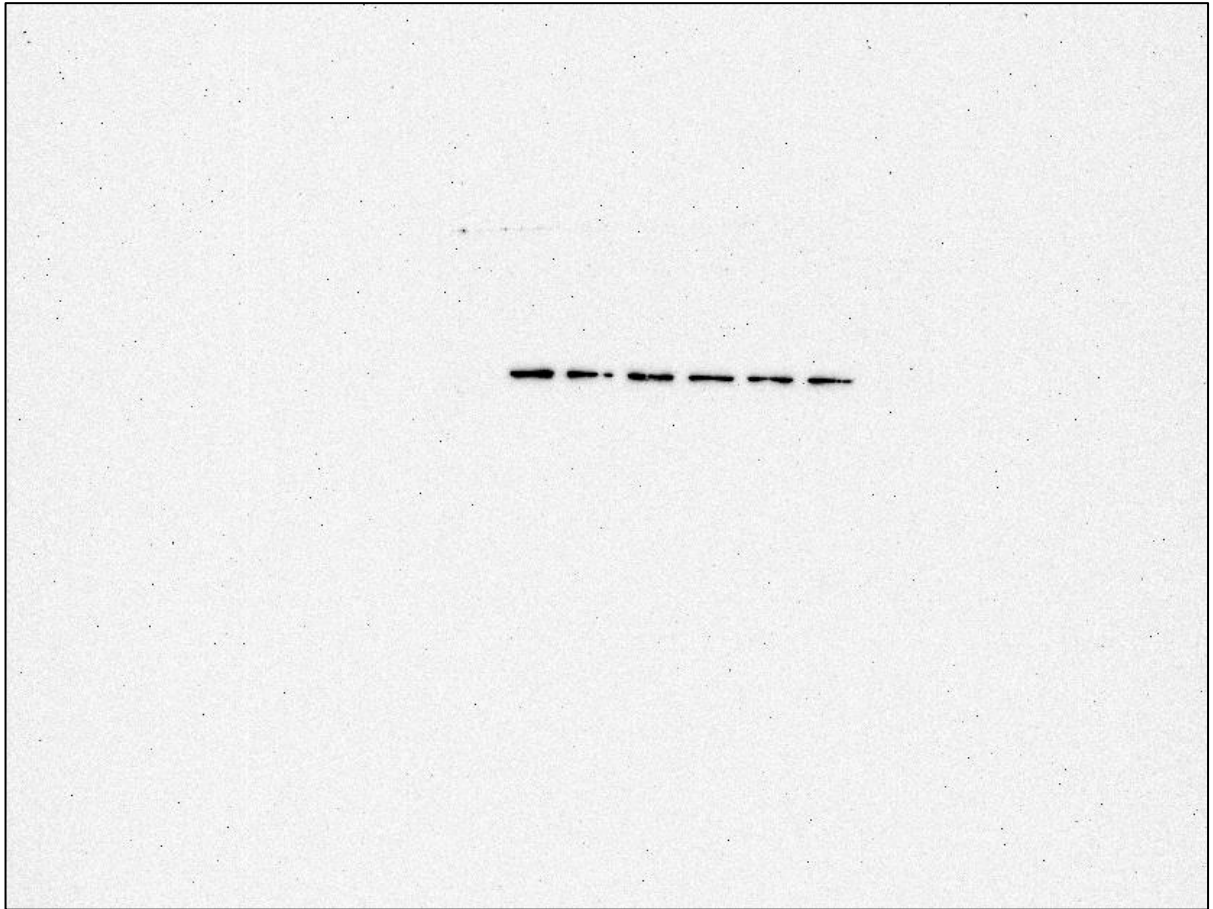


**Figure A16. Original blot indicating ITGA2 at 24 h from donor 2 for representative western blot used in Figure 40. Experiment date: April 14, 2021**

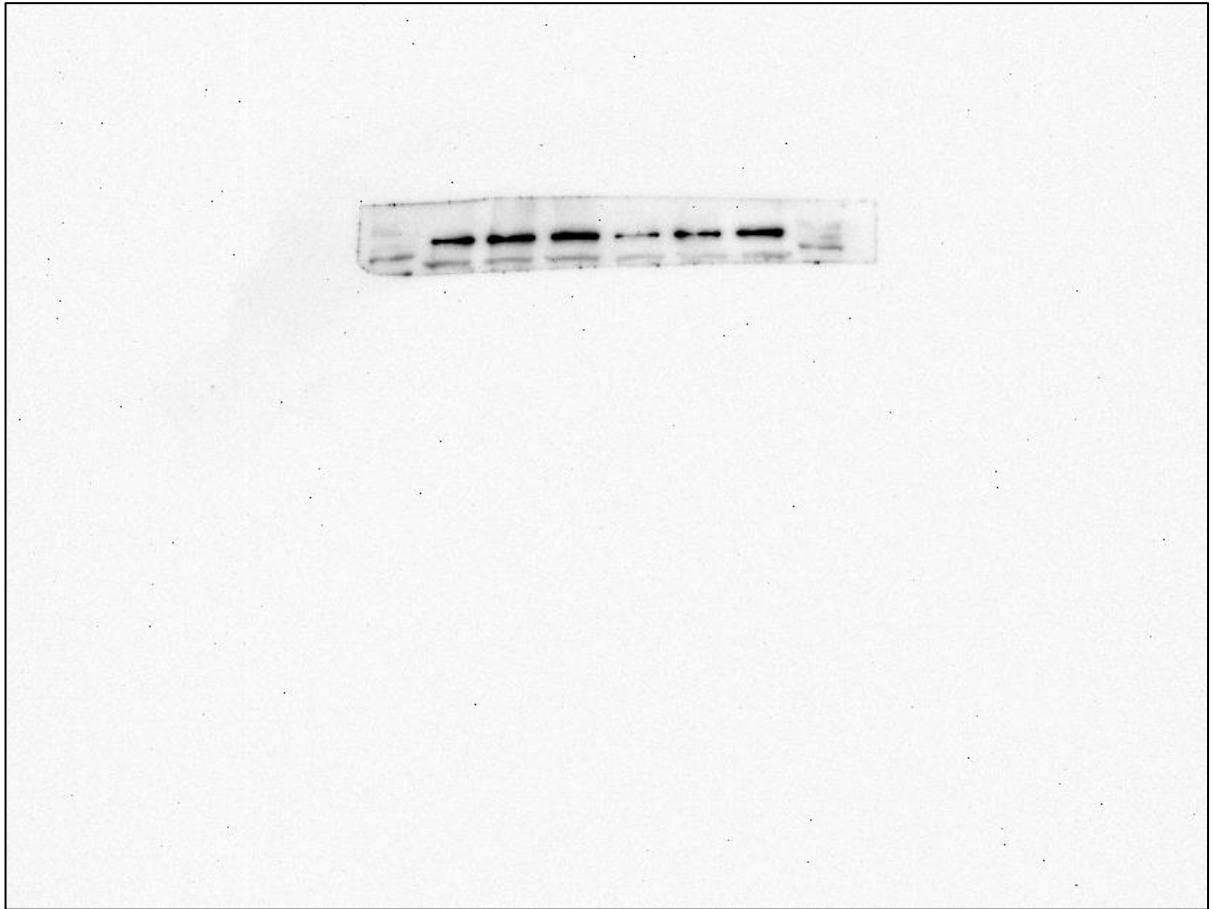


**Figure A17. Original blot indicating ITGA2 at 36 h from donor 2 for representative western blot used in Figure 40. Experiment date: April 14, 2021**



**Figure A18. Original blot indicating ITGA2 at 48 h from donor 2 for representative western blot used in Figure 40. Experiment date: April 14, 2021**

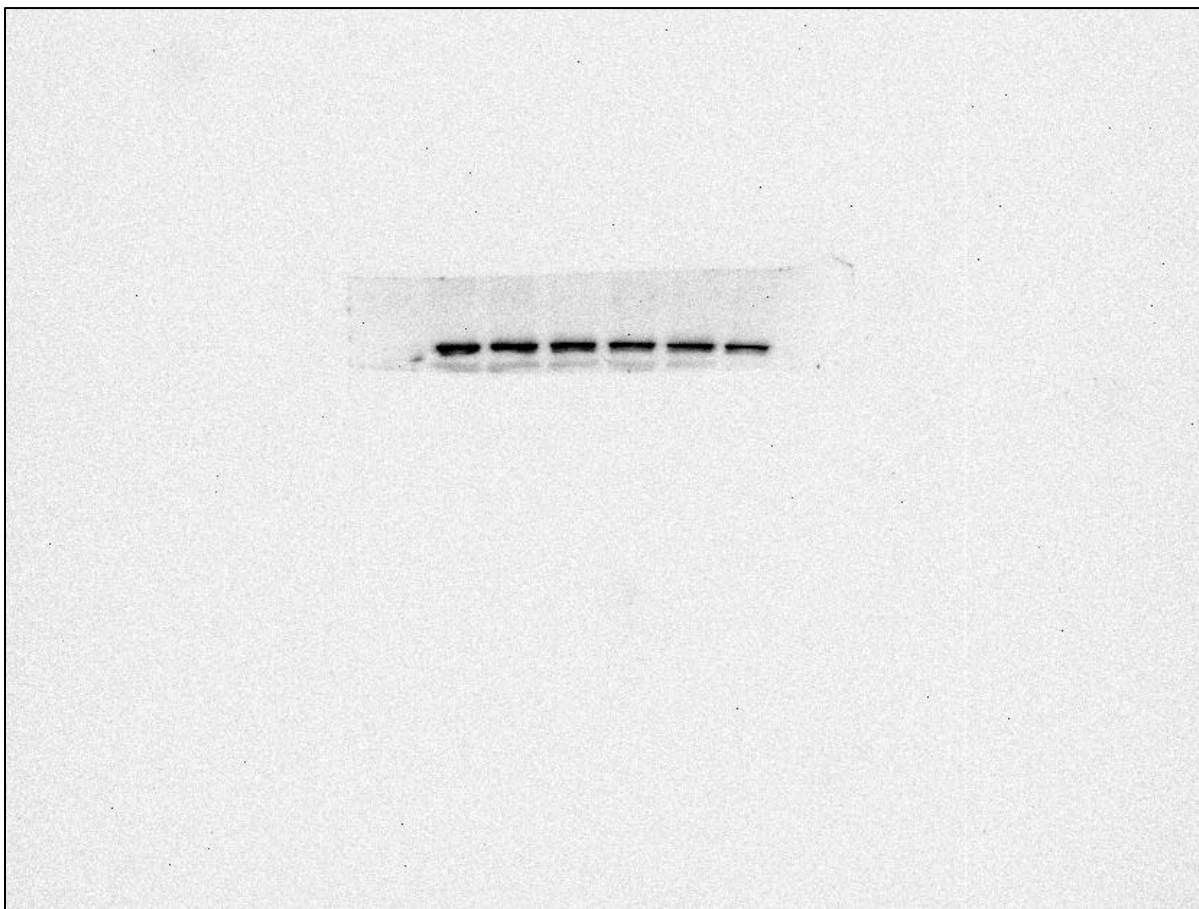


**Figure A19. Original blot indicating ITGA2 at 24 h from donor 3 for representative western blot used in Figure 40. Experiment date: April 20, 2021**

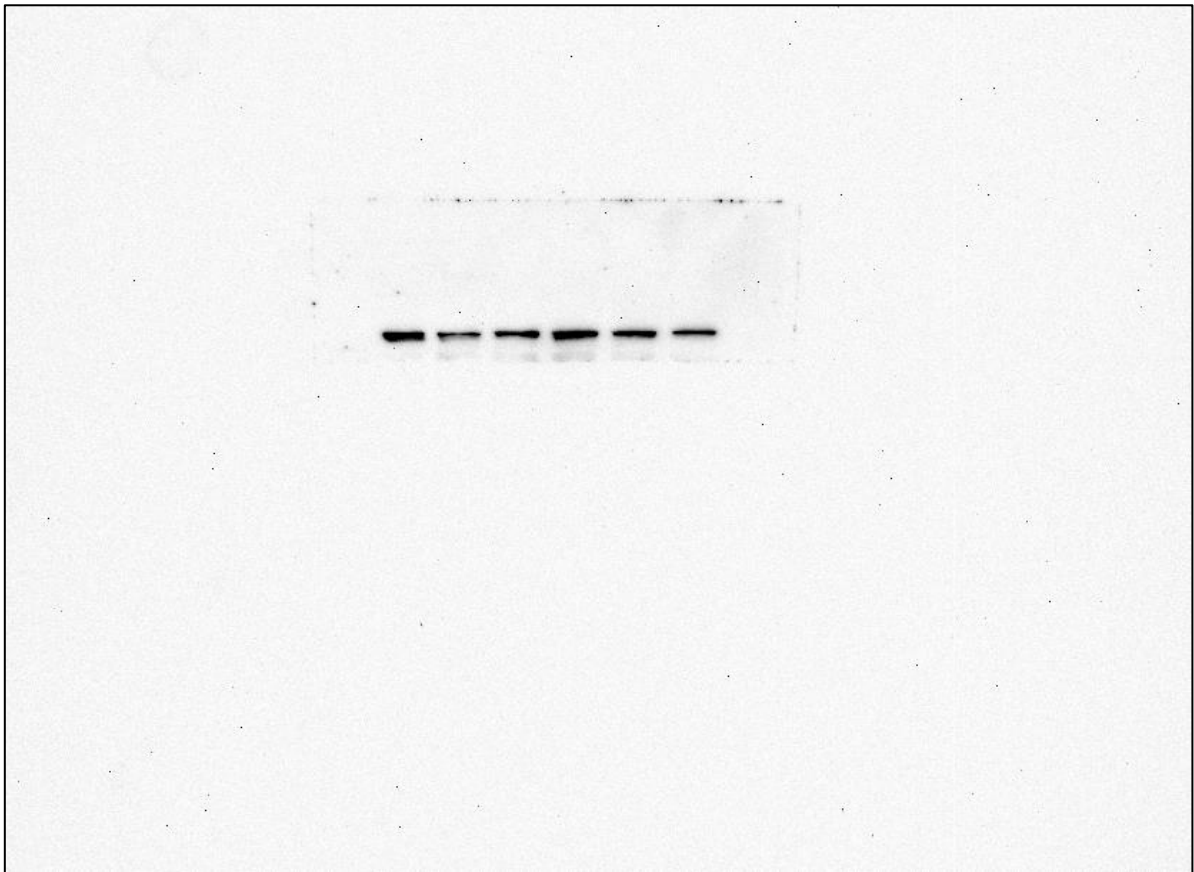


**Figure A20. Original blot indicating ITGA2 at 36 h from donor 3 for representative western blot used in Figure 40. Experiment date: April 20, 2021**

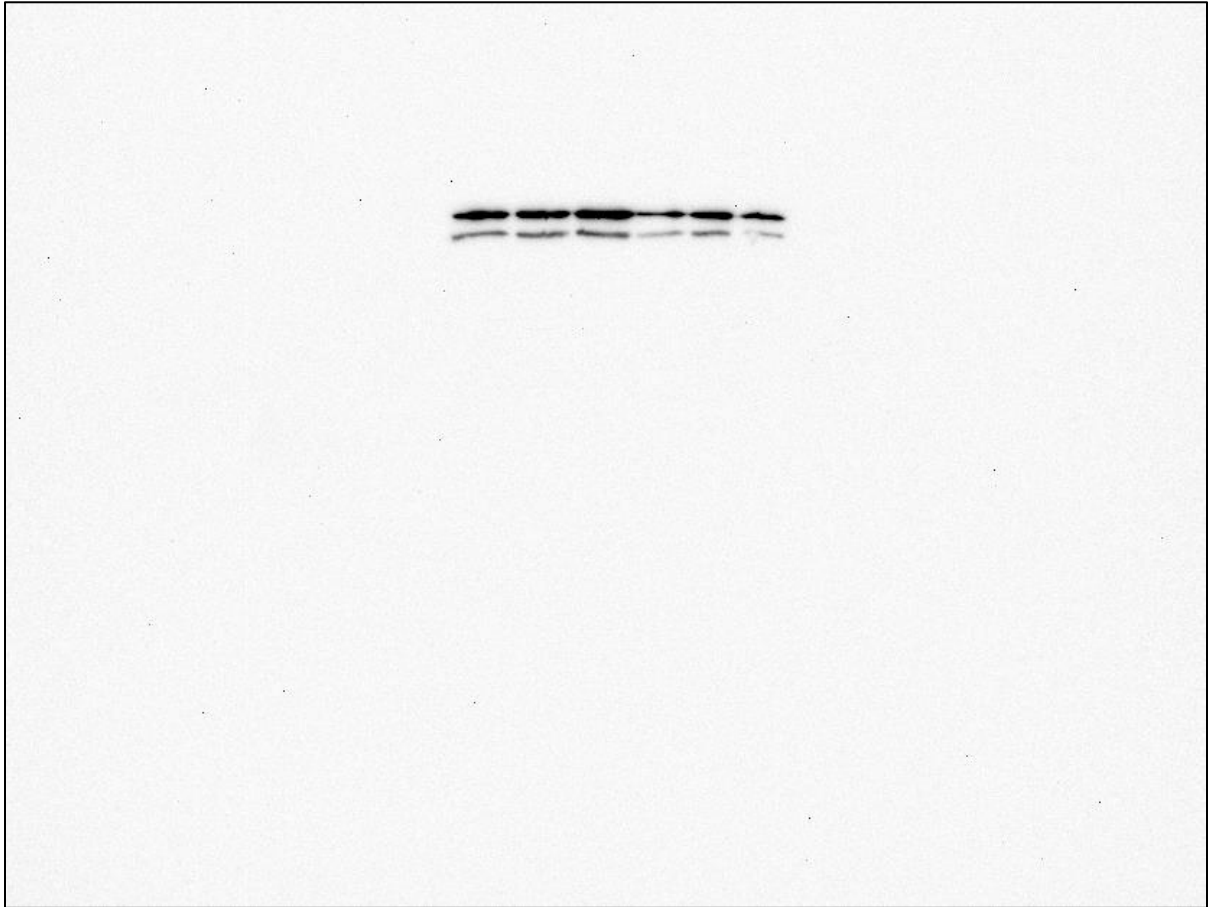


**Figure A21. Original blot indicating ITGA2 at 48 h from donor 3 for representative western blot used in Figure 40. Experiment date: April 20, 2021**

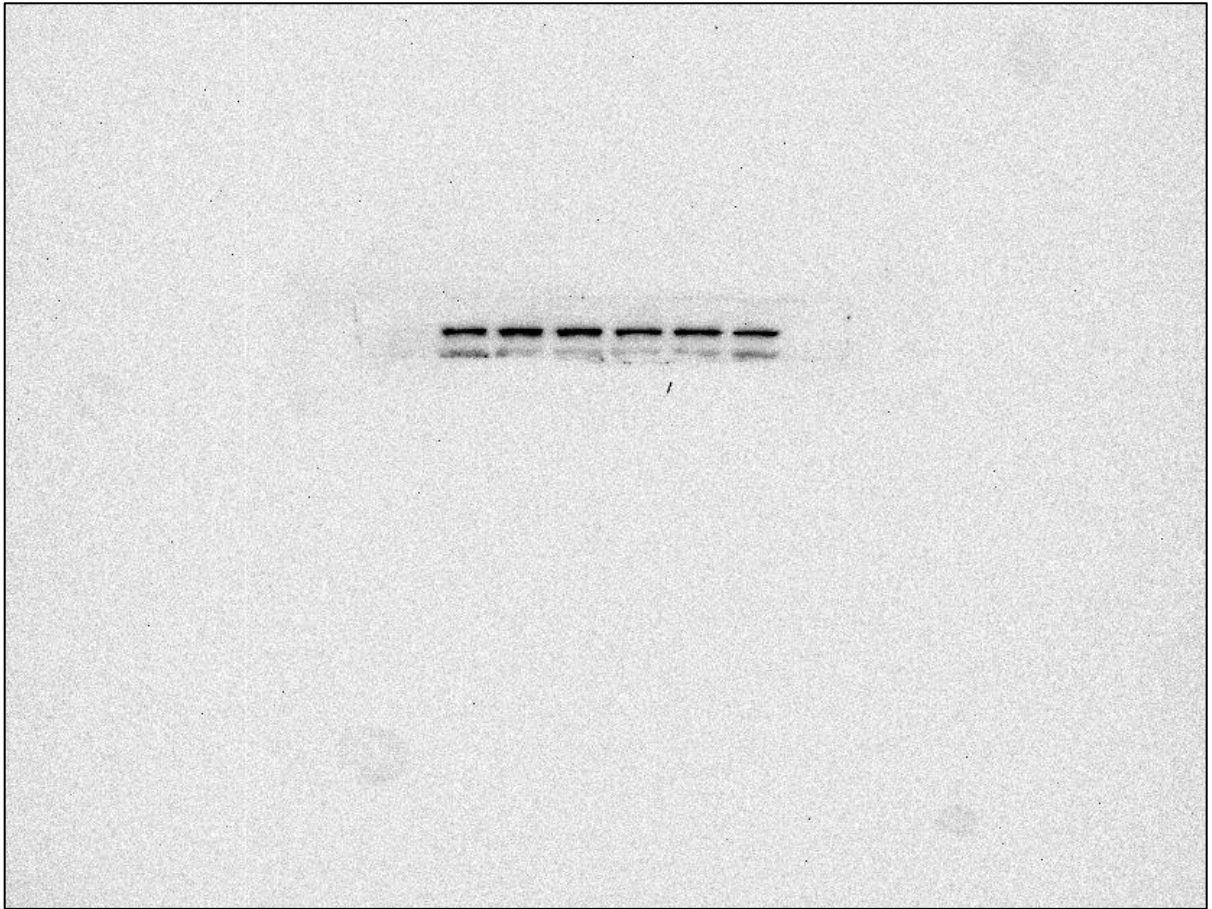


**Figure A22. Original blot indicating ITGA2 at 24 h from donor 4 for representative western blot used in Figure 40. Experiment date: April 20, 2021**

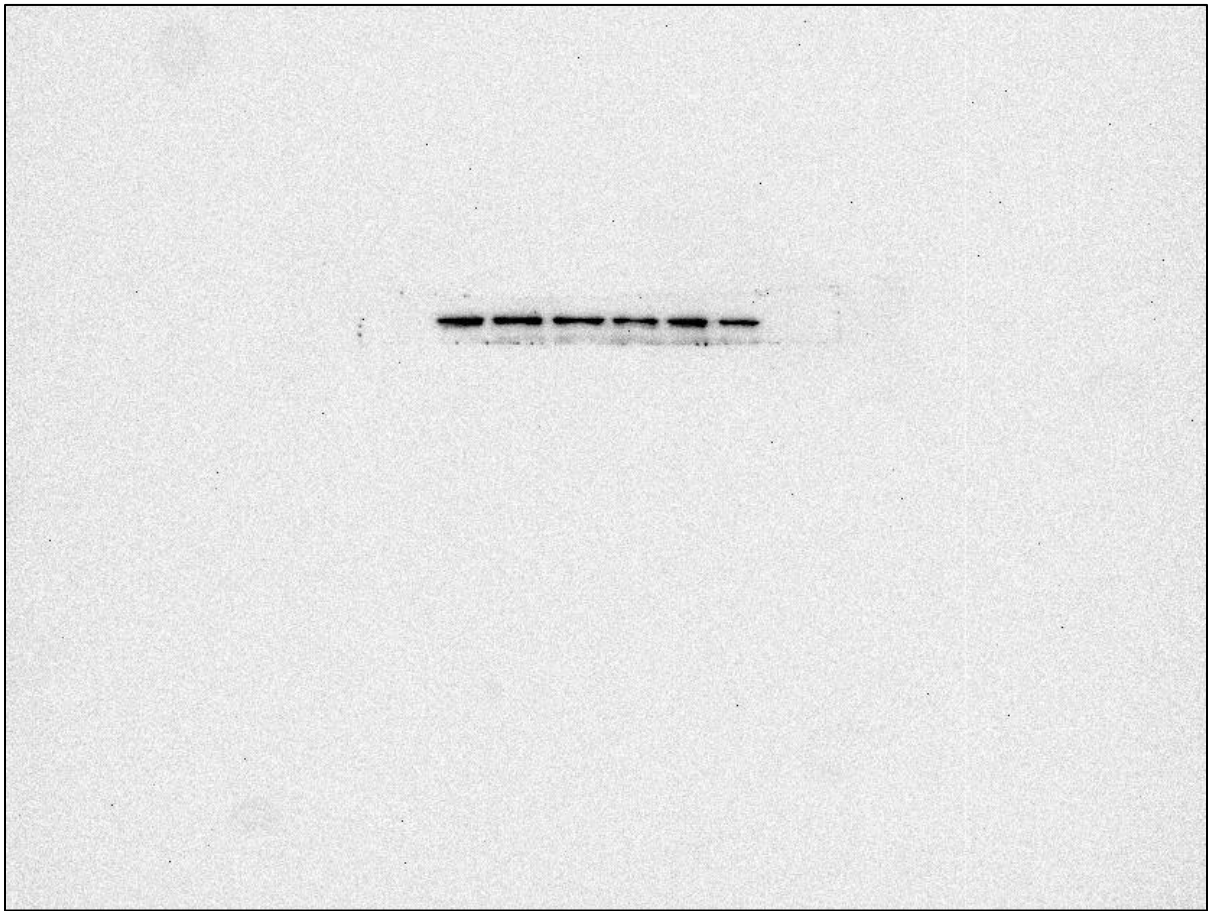


**Figure A23. Original blot indicating ITGA2 at 36 h from donor 4 for representative western blot used in Figure 40. Experiment date: April 20, 2021**

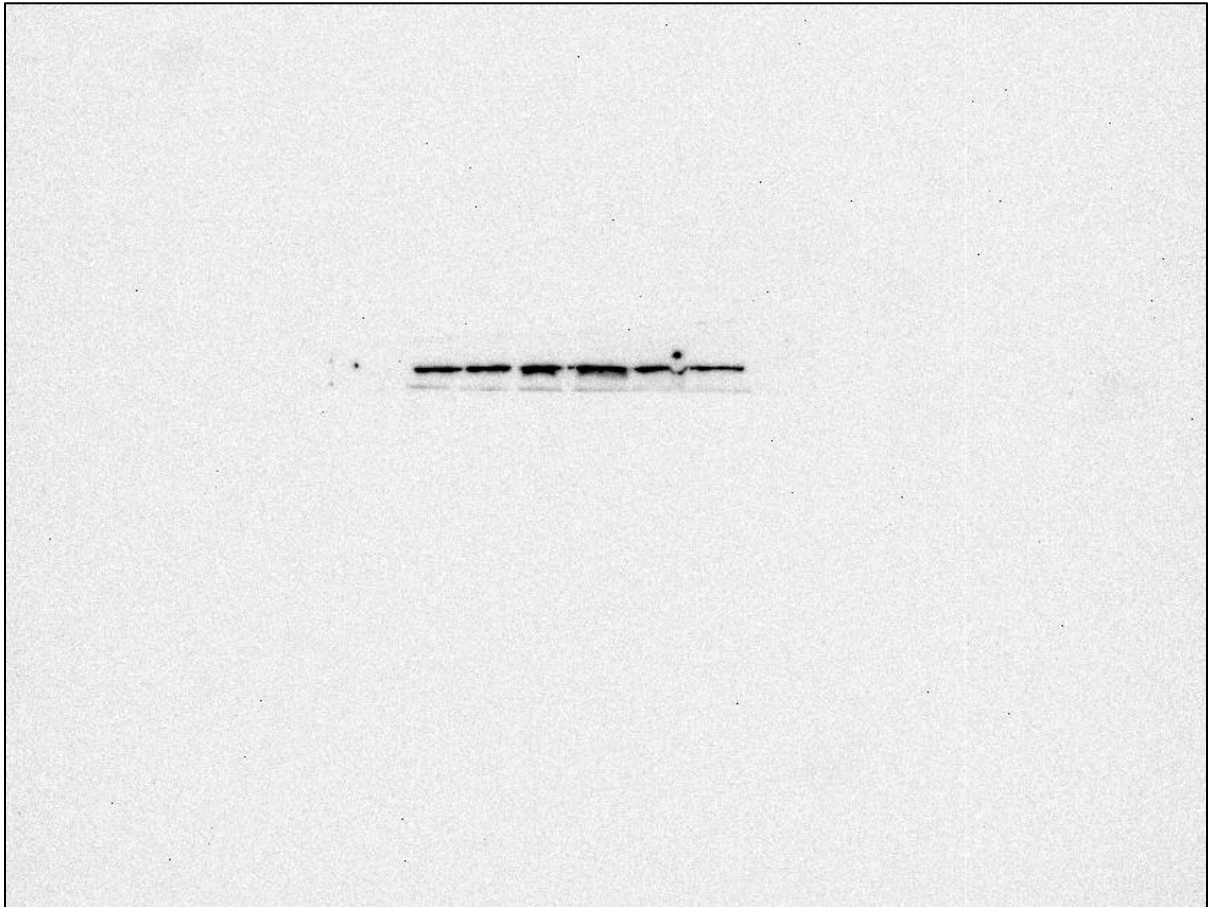


**Figure A24. Original blot indicating ITGA2 at 48 h from donor 4 for representative western blot used in Figure 40. Experiment date: April 20, 2021**

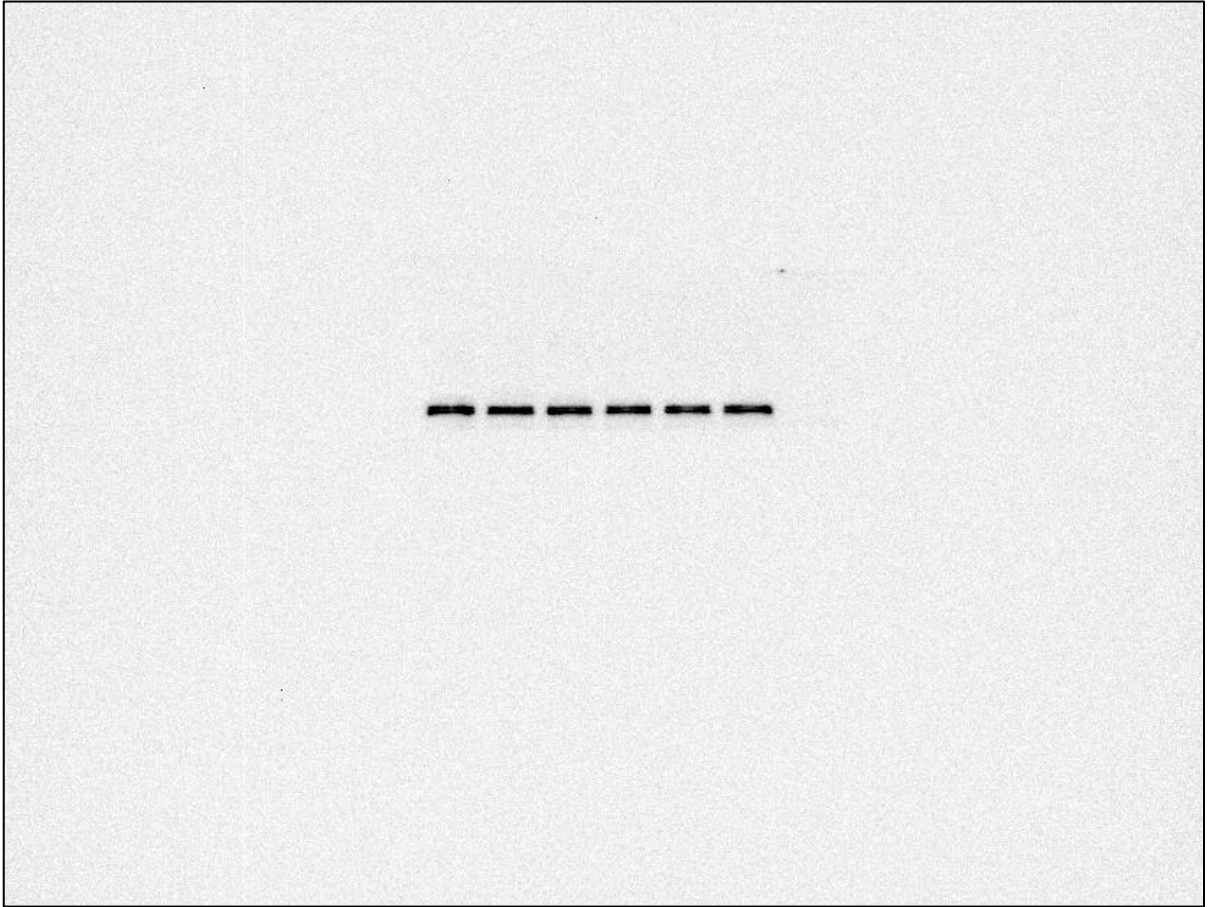


**Figure A25. Original blot indicating ITGB1 at 24 h from donor 1 for representative western blot used in Figure 41. Experiment date: May 5, 2021**

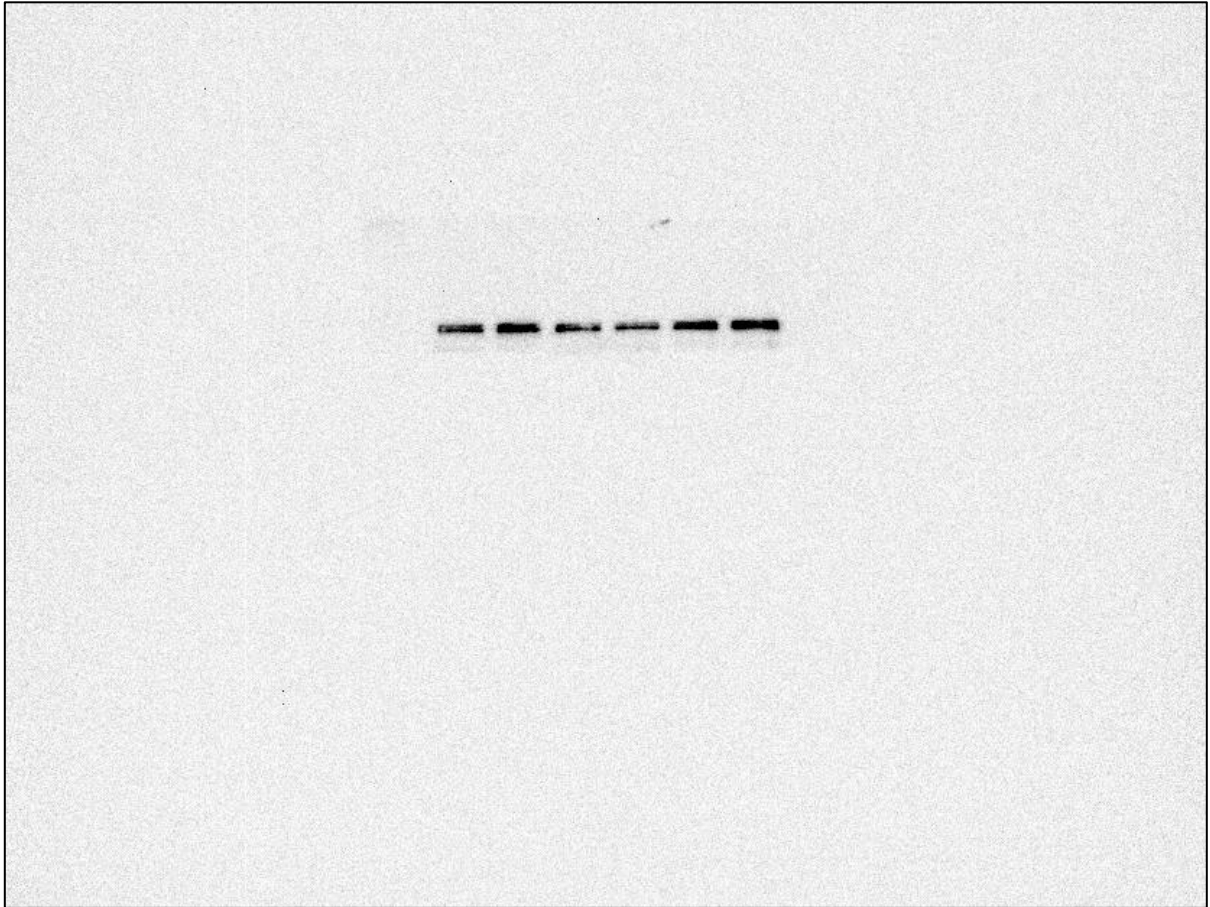


**Figure A26. Original blot indicating ITGB1 at 36 h from donor 1 for representative western blot used in Figure 41. Experiment date: May 5, 2021**



**Figure A27. Original blot indicating ITGB1 at 48 h from donor 1 for representative western blot used in Figure 41. Experiment date: May 5, 2021**

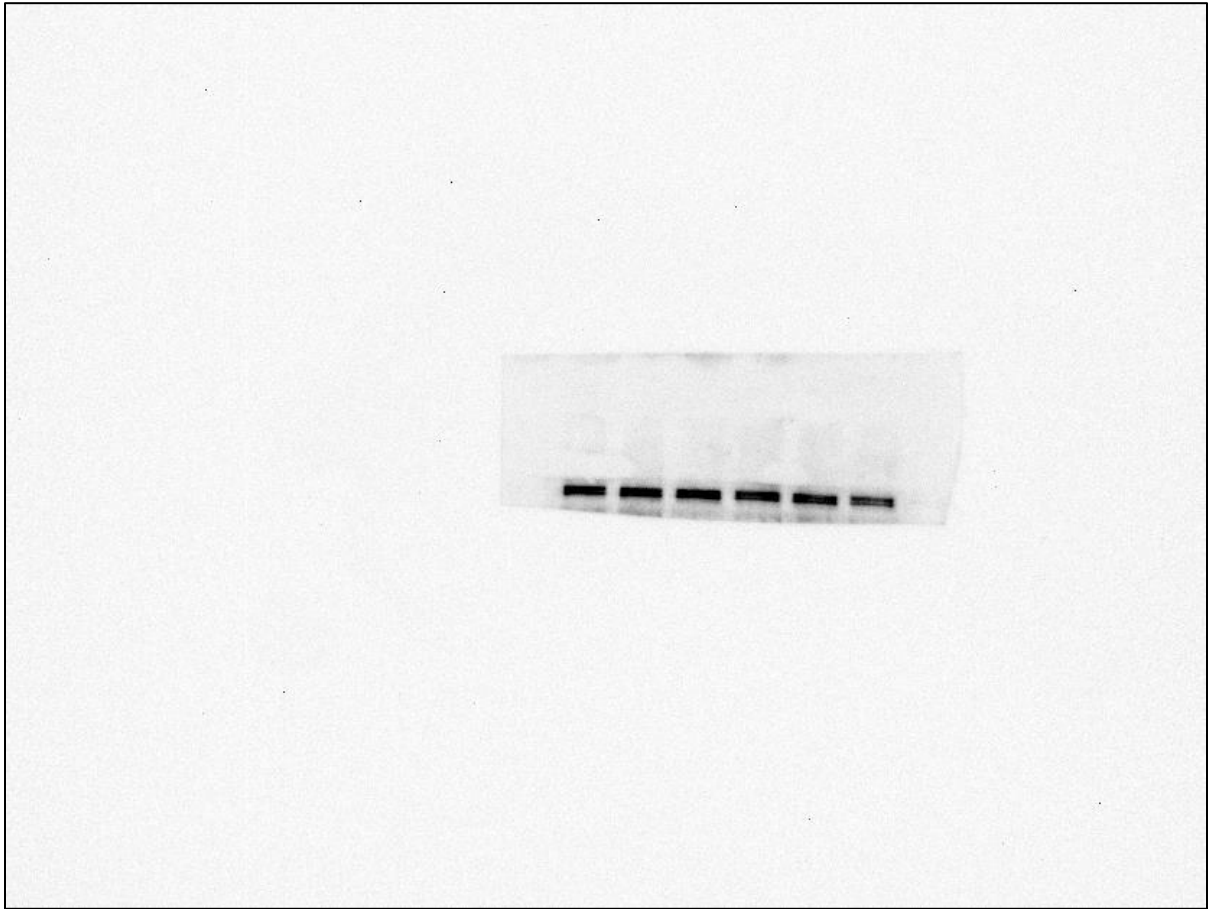


**Figure A28. Original blot indicating ITGB1 at 24 h from donor 2 for representative western blot used in Figure 41. Experiment date: May 5, 2021**

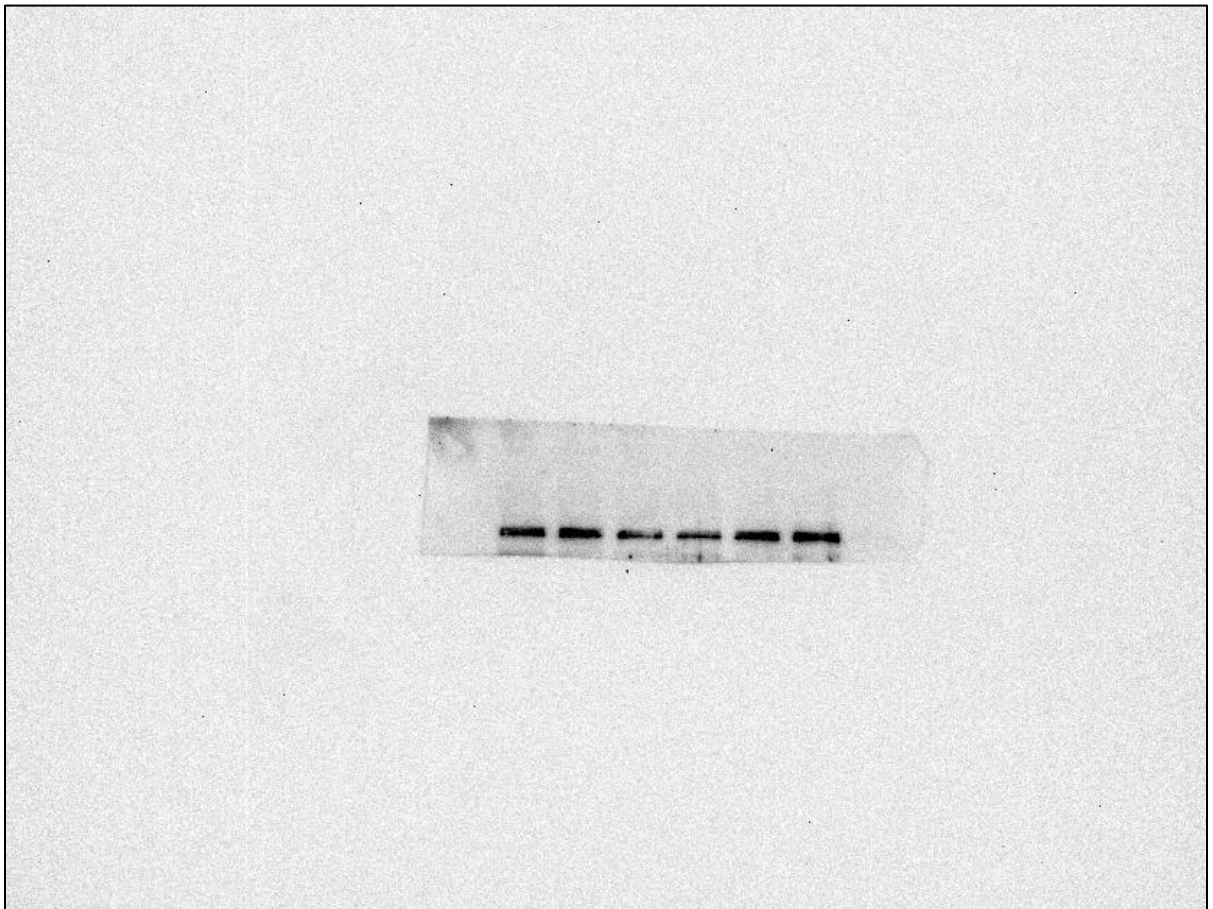


**Figure A29. Original blot indicating ITGB1 at 36 h from donor 2 for representative western blot used in Figure 41. Experiment date: May 5, 2021**



**Figure A30. Original blot indicating ITGB1 at 48 h from donor 2 for representative western blot used in Figure 41. Experiment date: May 5, 2021**

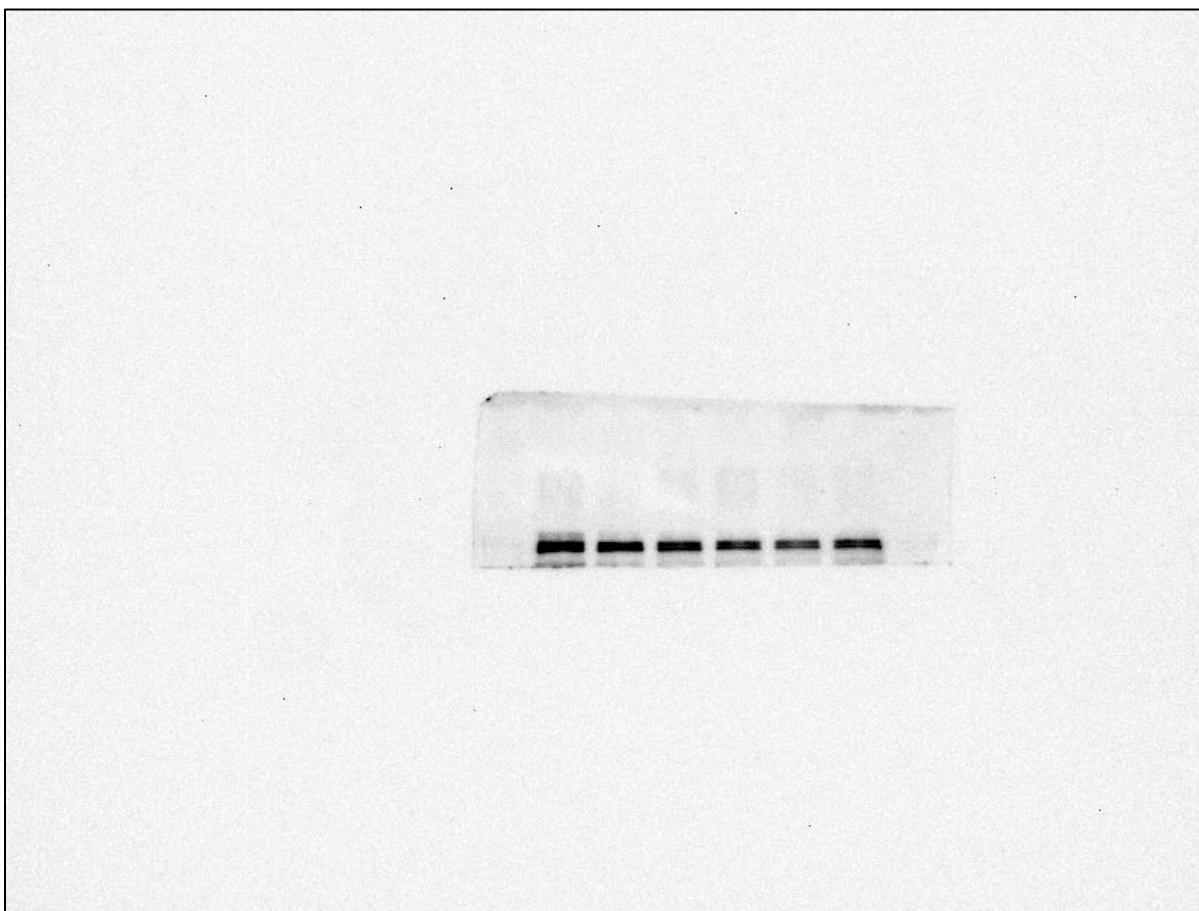


**Figure A31. Original blot indicating ITGB1 at 24 h from donor 3 for representative western blot used in Figure 41. Experiment date: May 10, 2021**

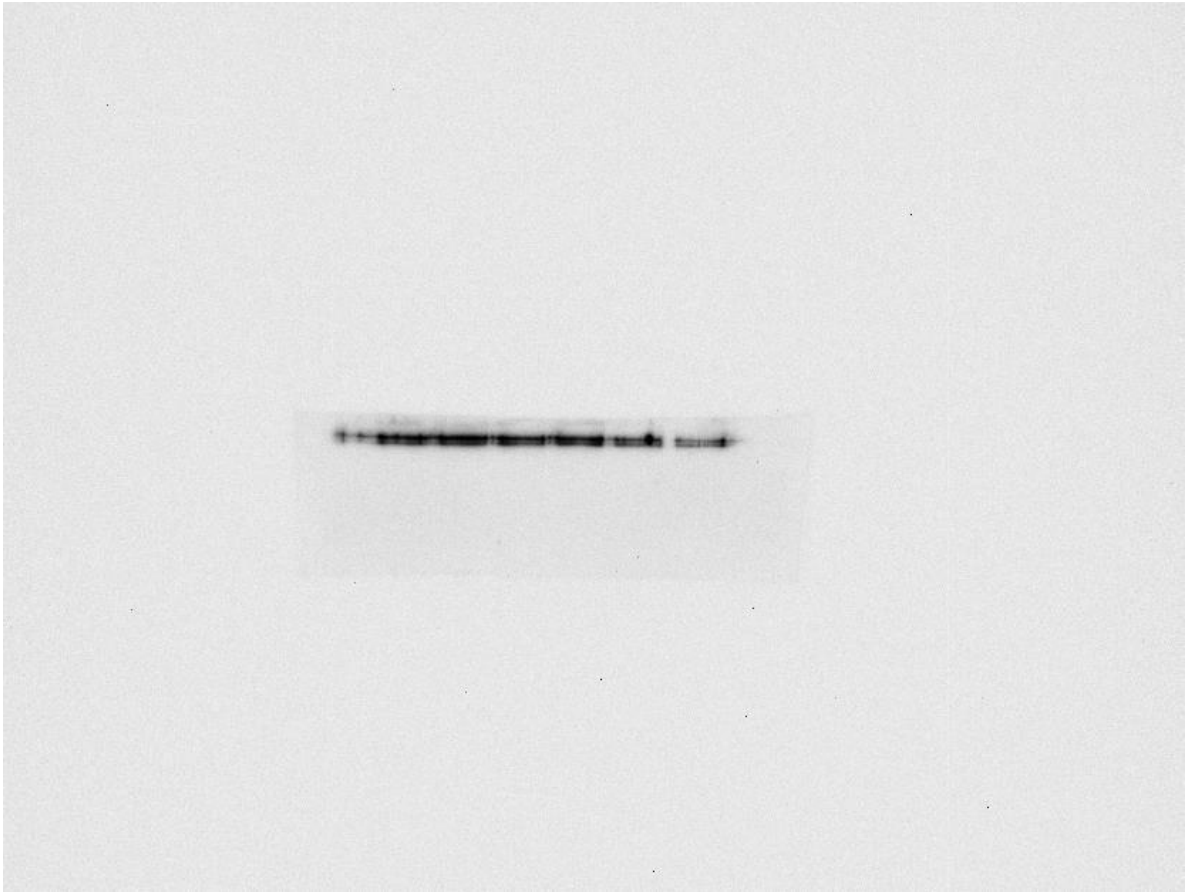


**Figure A32. Original blot indicating ITGB1 at 36 h from donor 3 for representative western blot used in Figure 41. Experiment date: May 10, 2021**

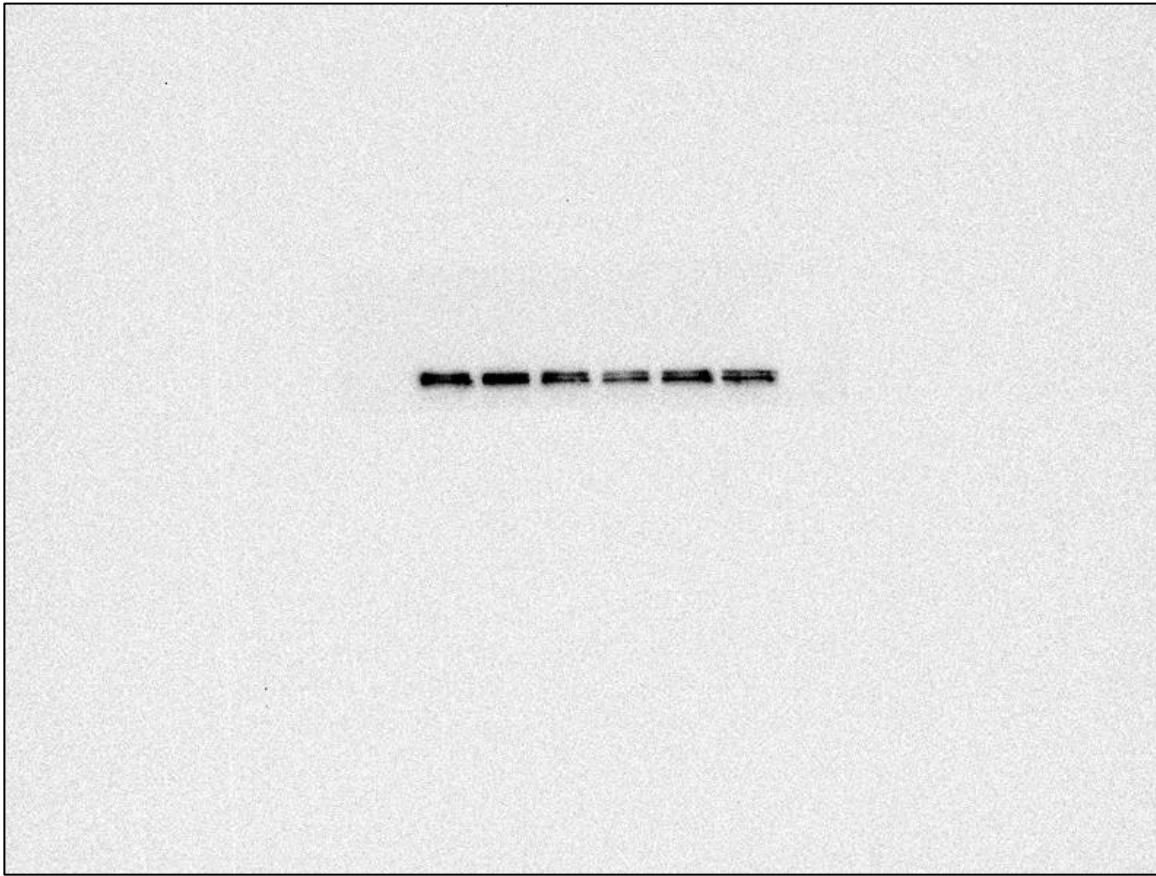


**Figure A33. Original blot indicating ITGB1 at 48 h from donor 3 for representative western blot used in Figure 41. Experiment date: May 10, 2021**



**Figure A34. Original blot indicating ITGB1 at 24 h from donor 4 for representative western blot used in Figure 41. Experiment date: May 10, 2021**

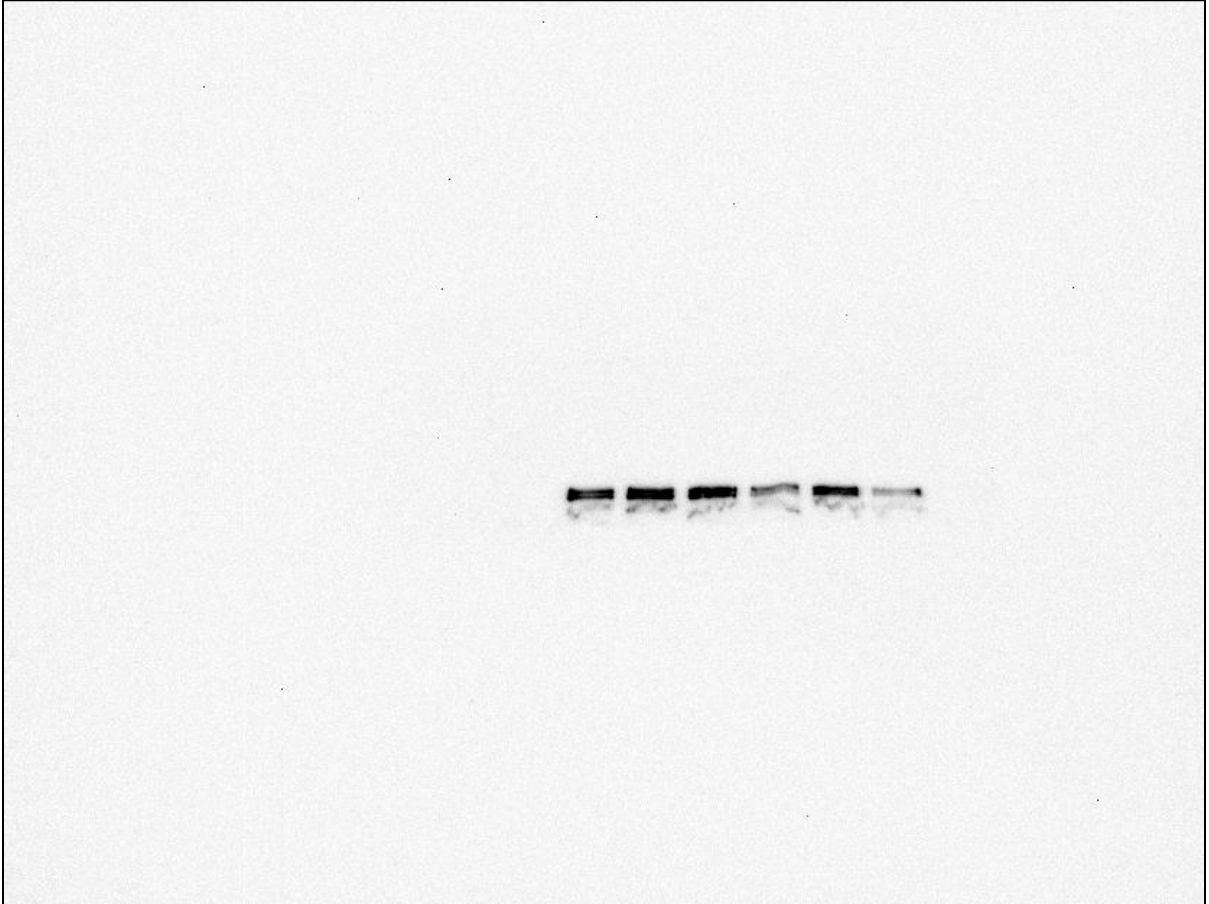


**Figure A35. Original blot indicating ITGB1 at 36 h from donor 4 for representative western blot used in Figure 41. Experiment date: May 10, 2021**



**Figure A36. Original blot indicating ITGB1 at 48 h from donor 4 for representative western blot used in Figure 41. Experiment date: May 10, 2021**

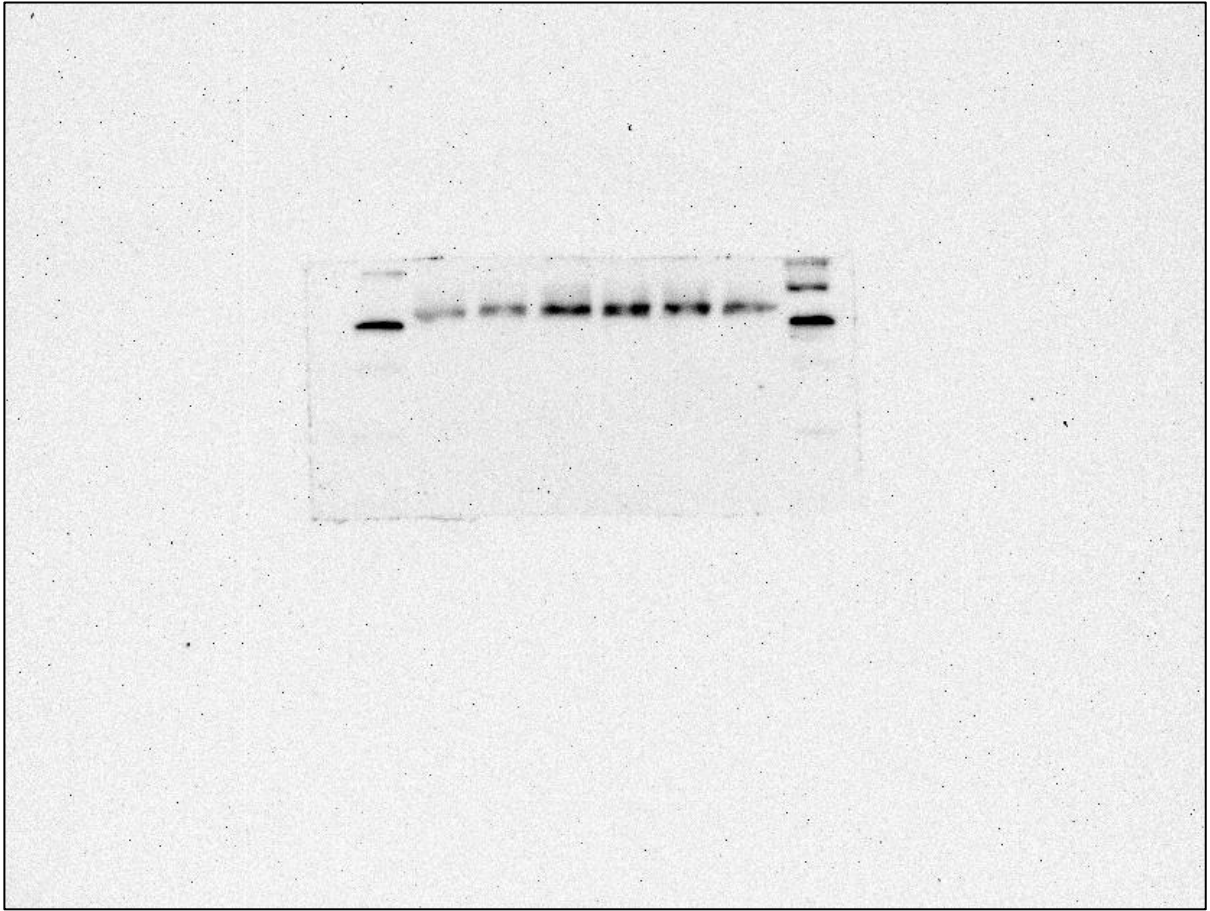


**Figure A37. Original blot indicating caspase-3 at 24 h from donor 1 for representative western blot used in Figure 43. Experiment date: May 17, 2021**



**Figure A38. Original blot indicating caspase-3 at 36 h from donor 1 for representative western blot used in Figure 43. Experiment date: May 17, 2021**

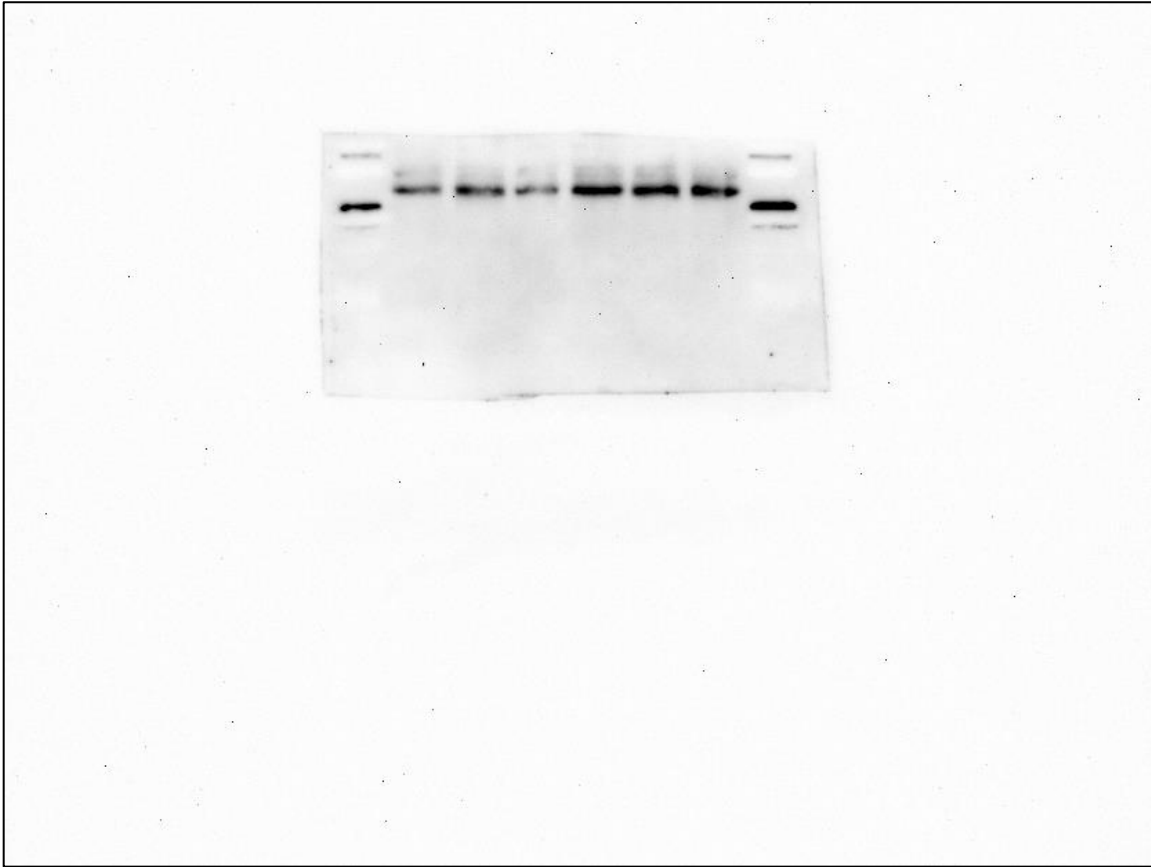


**Figure A39. Original blot indicating caspase-3 at 48 h from donor 1 for representative western blot used in Figure 43. Experiment date: May 17, 2021**

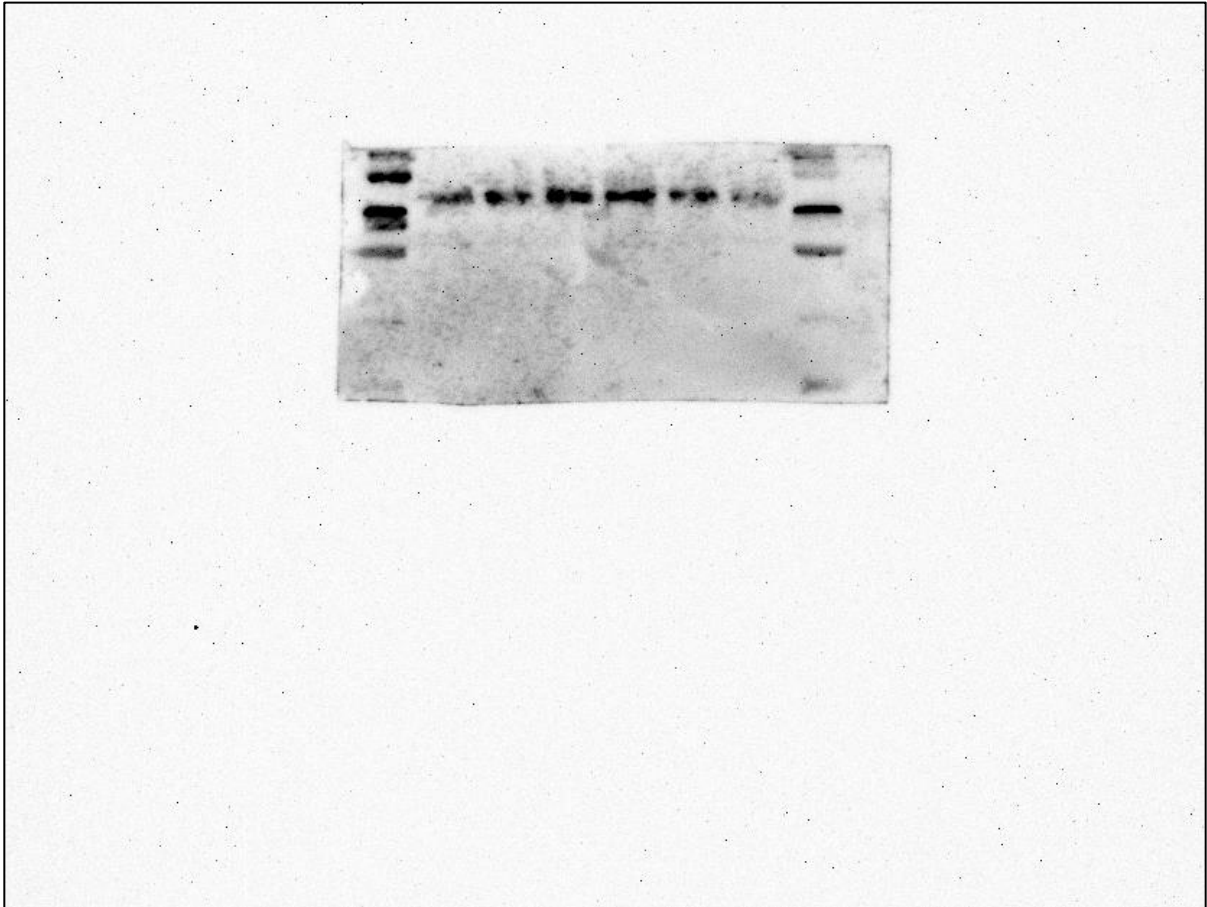


**Figure A40. Original blot indicating caspase-3 at 24 h from donor 2 for representative western blot used in Figure 43. Experiment date: May 17, 2021**

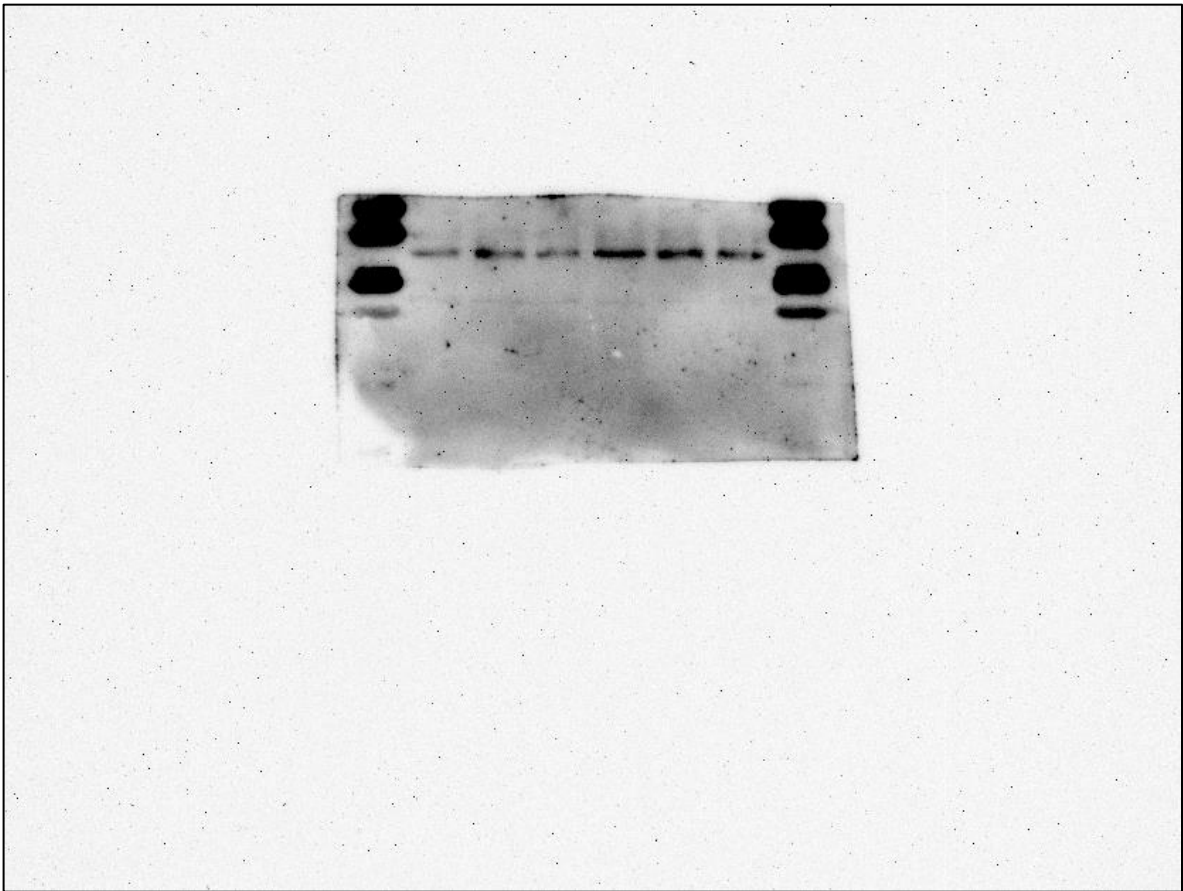


**Figure A41. Original blot indicating caspase-3 at 36 h from donor 2 for representative western blot used in Figure 43. Experiment date: May 17, 2021**

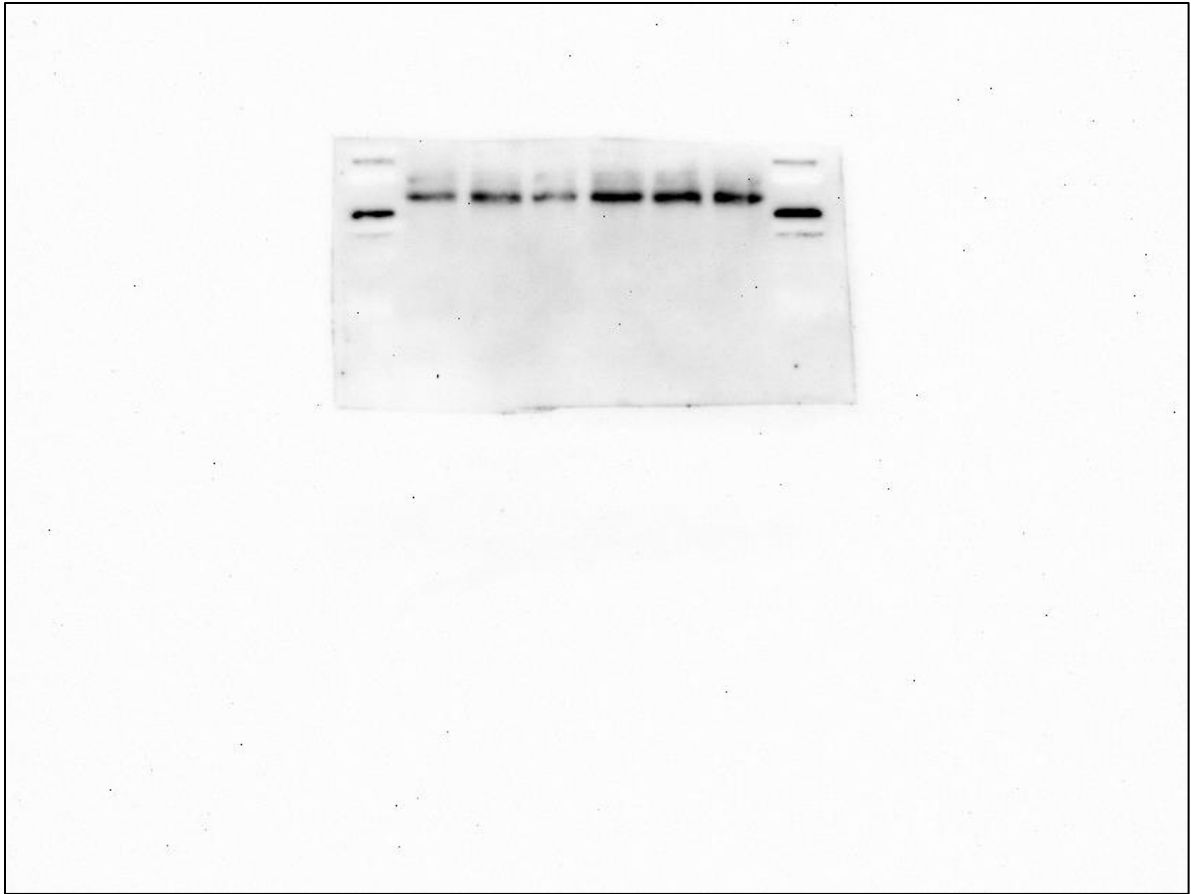


**Figure A42. Original blot indicating caspase-3 at 48 h from donor 2 for representative western blot used in Figure 43. Experiment date: May 17, 2021**

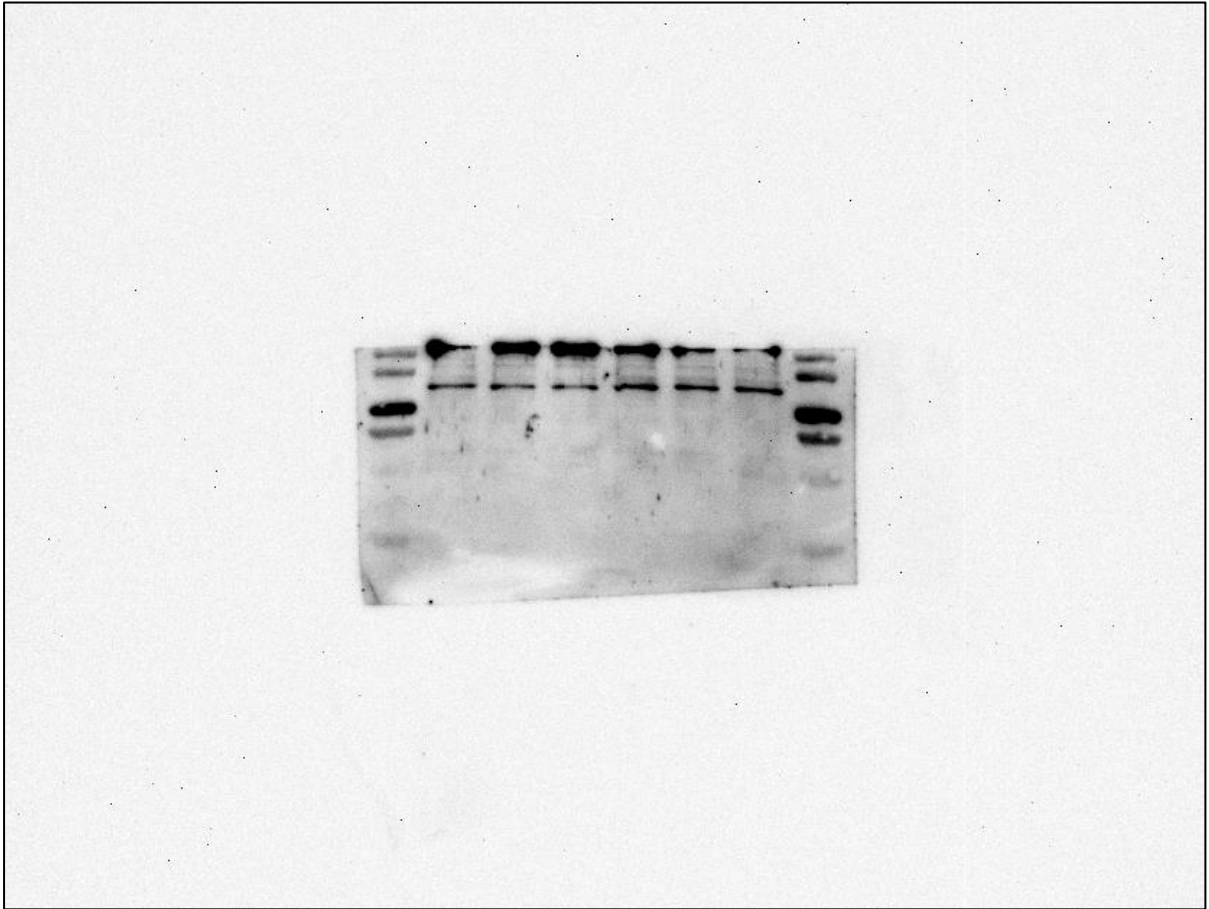


**Figure A43. Original blot indicating caspase-3 at 24 h from donor 3 for representative western blot used in Figure 43. Experiment date: June 23, 2021**

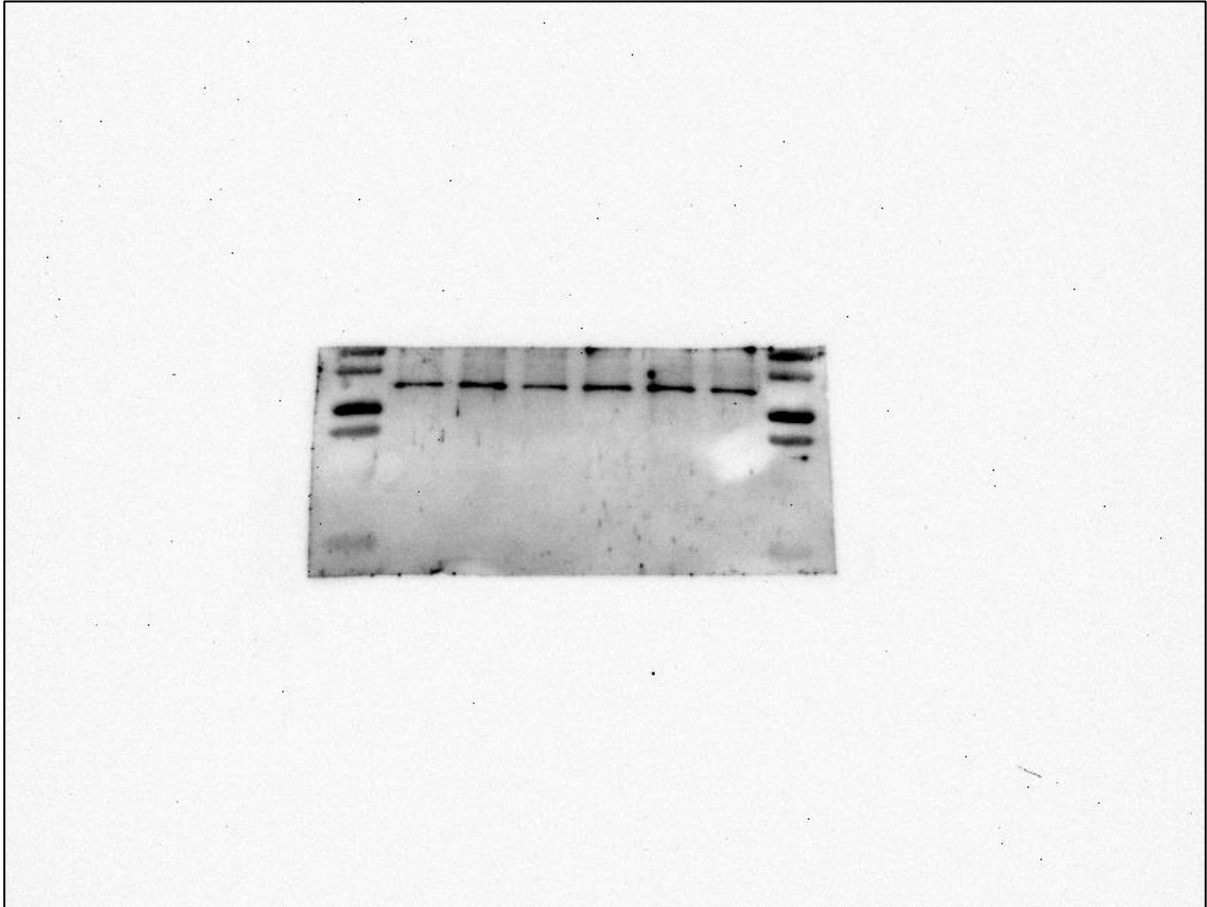


**Figure A44. Original blot indicating caspase-3 at 36 h from donor 3 for representative western blot used in Figure 43. Experiment date: June 23, 2021**



**Figure A45. Original blot indicating caspase-3 at 48 h from donor 3 for representative western blot used in Figure 43. Experiment date: June 23, 2021**



**Figure A46. Original blot indicating cleaved caspase-3 at 24 h from donor 1 for representative western blot used in Figure 43. Experiment date: May 17, 2021**

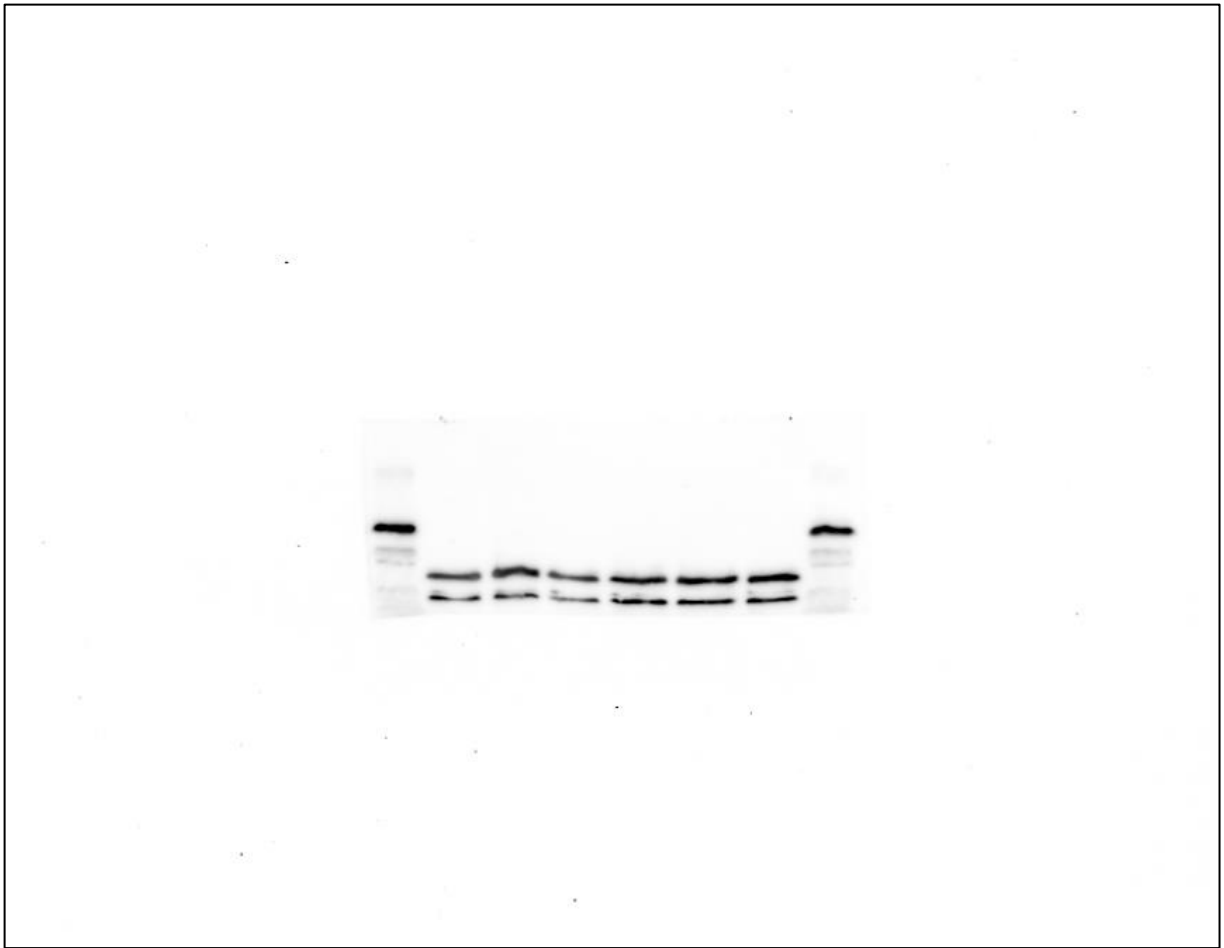


**Figure A47. Original blot indicating cleaved caspase-3 at 36 h from donor 1 for representative western blot used in Figure 43. Experiment date: May 17, 2021**

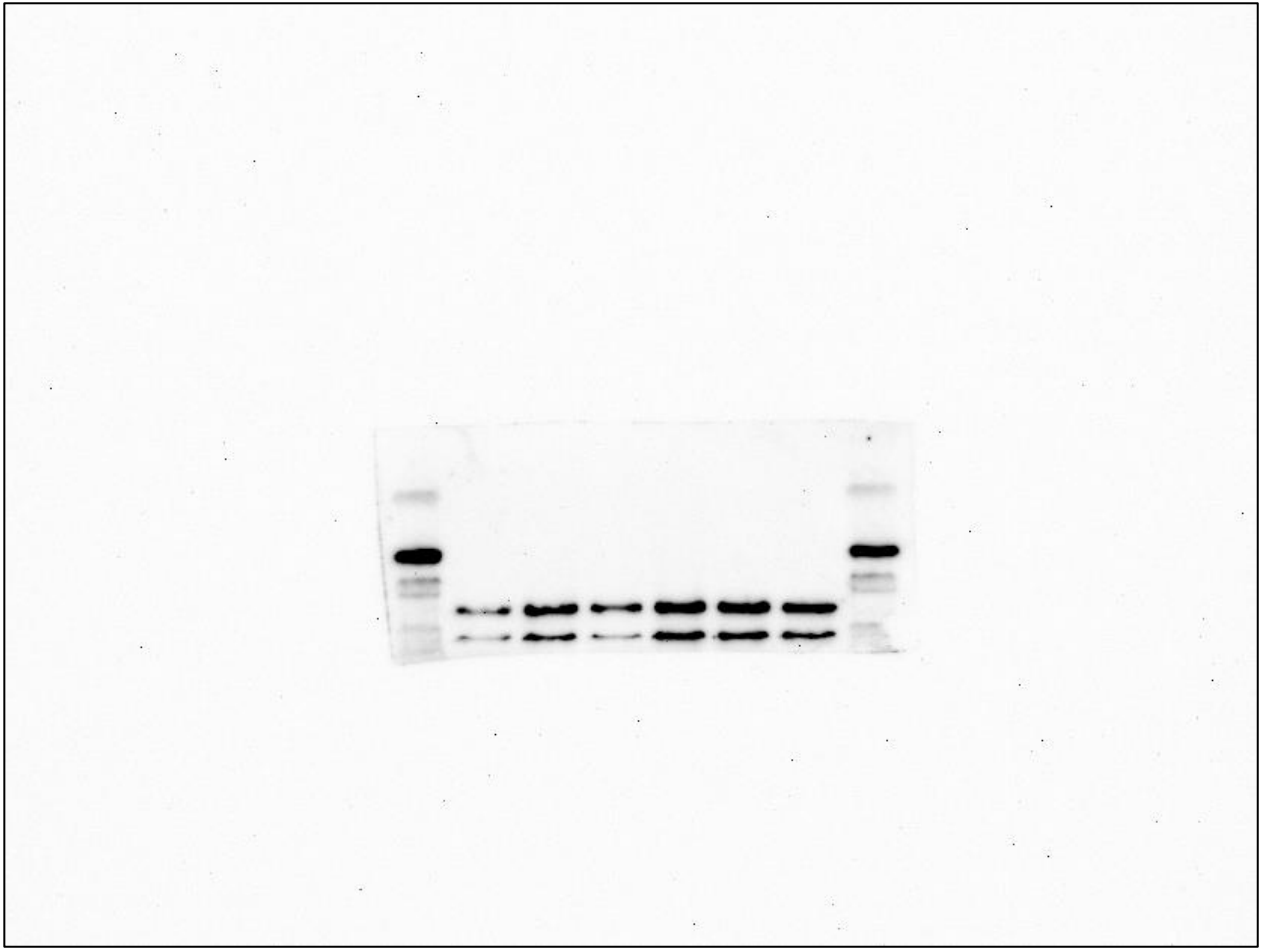


**Figure A48. Original blot indicating cleaved caspase-3 at 48 h from donor 1 for representative western blot used in Figure 43. Experiment date: May 17, 2021**

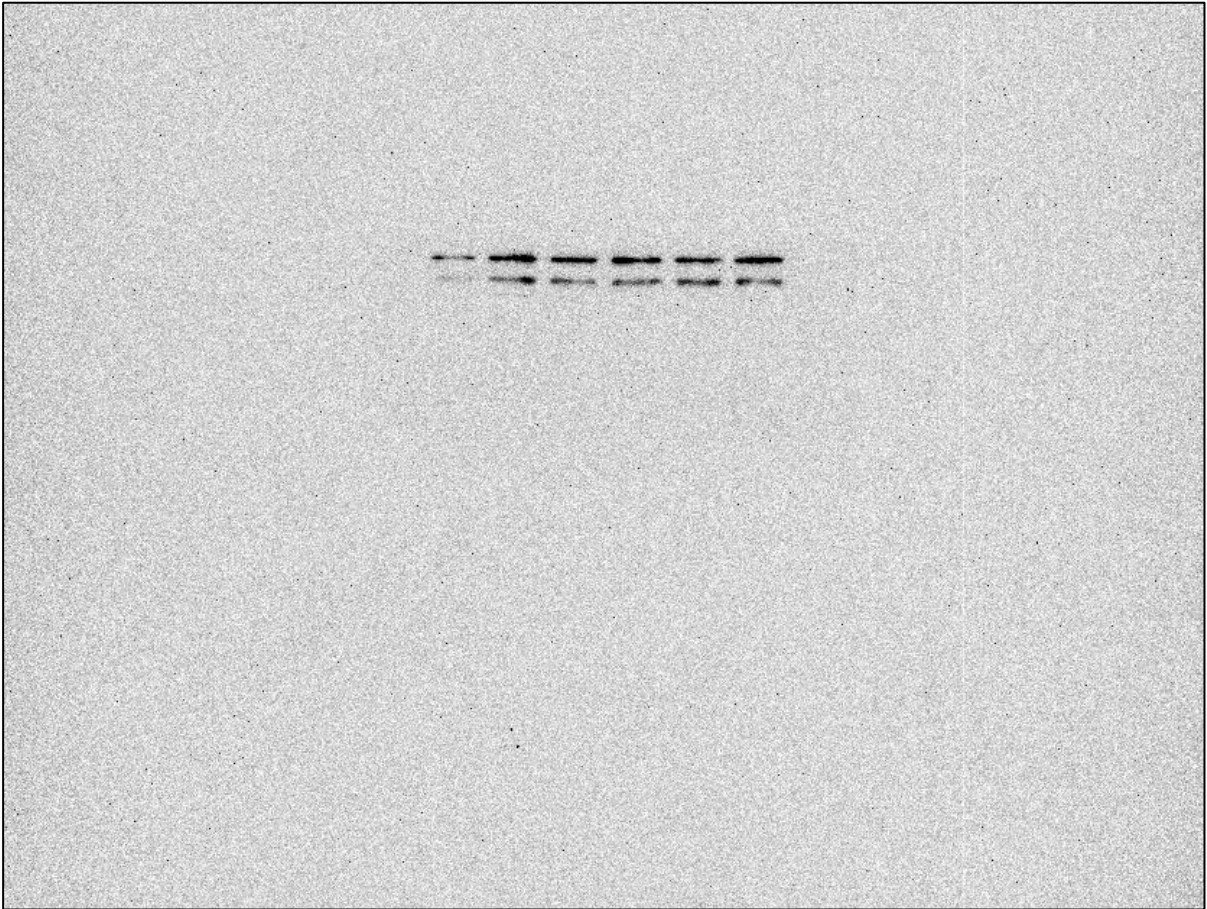


**Figure A49. Original blot indicating cleaved caspase-3 at 24 h from donor 2 for representative western blot used in Figure 43. Experiment date: May 17, 2021**



**Figure A50. Original blot indicating cleaved caspase-3 at 36 h from donor 2 for representative western blot used in Figure 43. Experiment date: May 17, 2021**

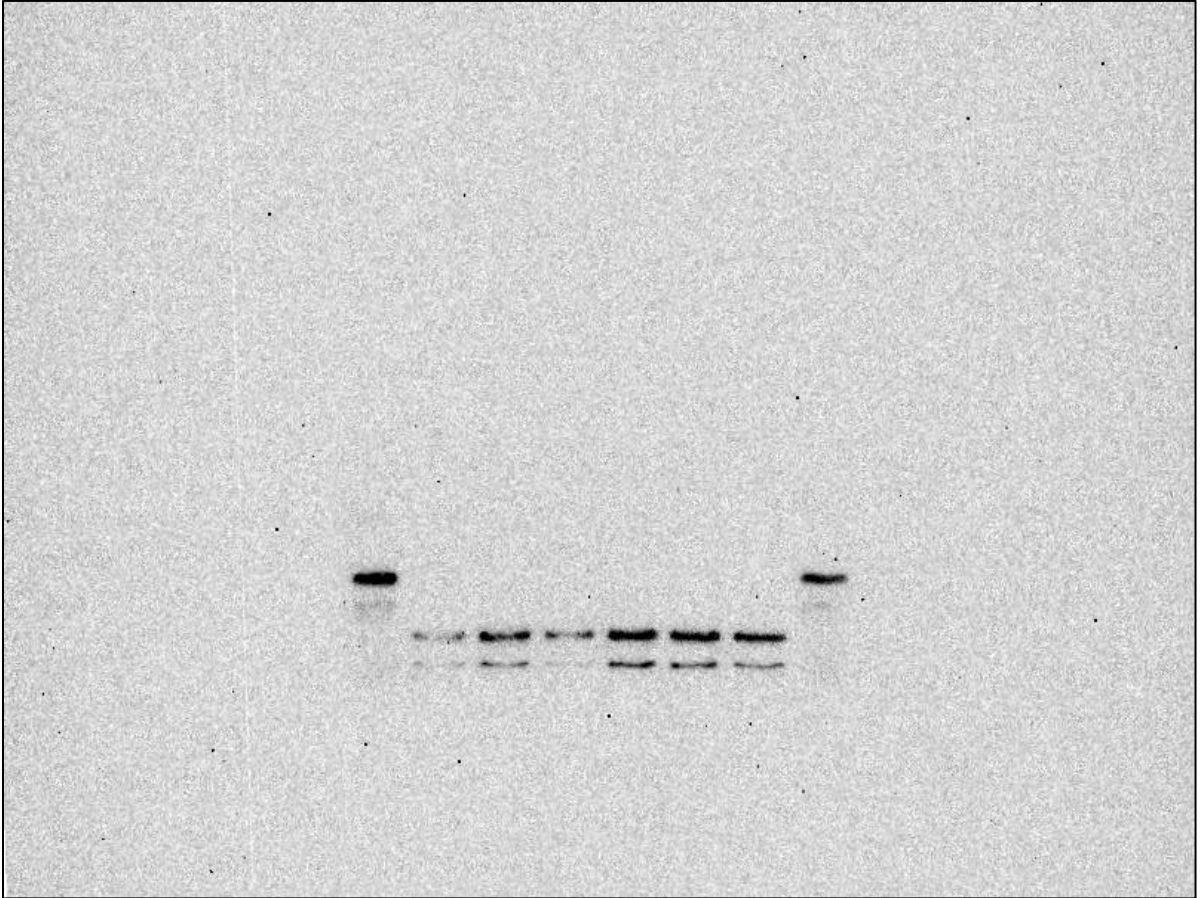


**Figure A51. Original blot indicating cleaved caspase-3 at 48 h from donor 2 for representative western blot used in Figure 43. Experiment date: May 17, 2021**

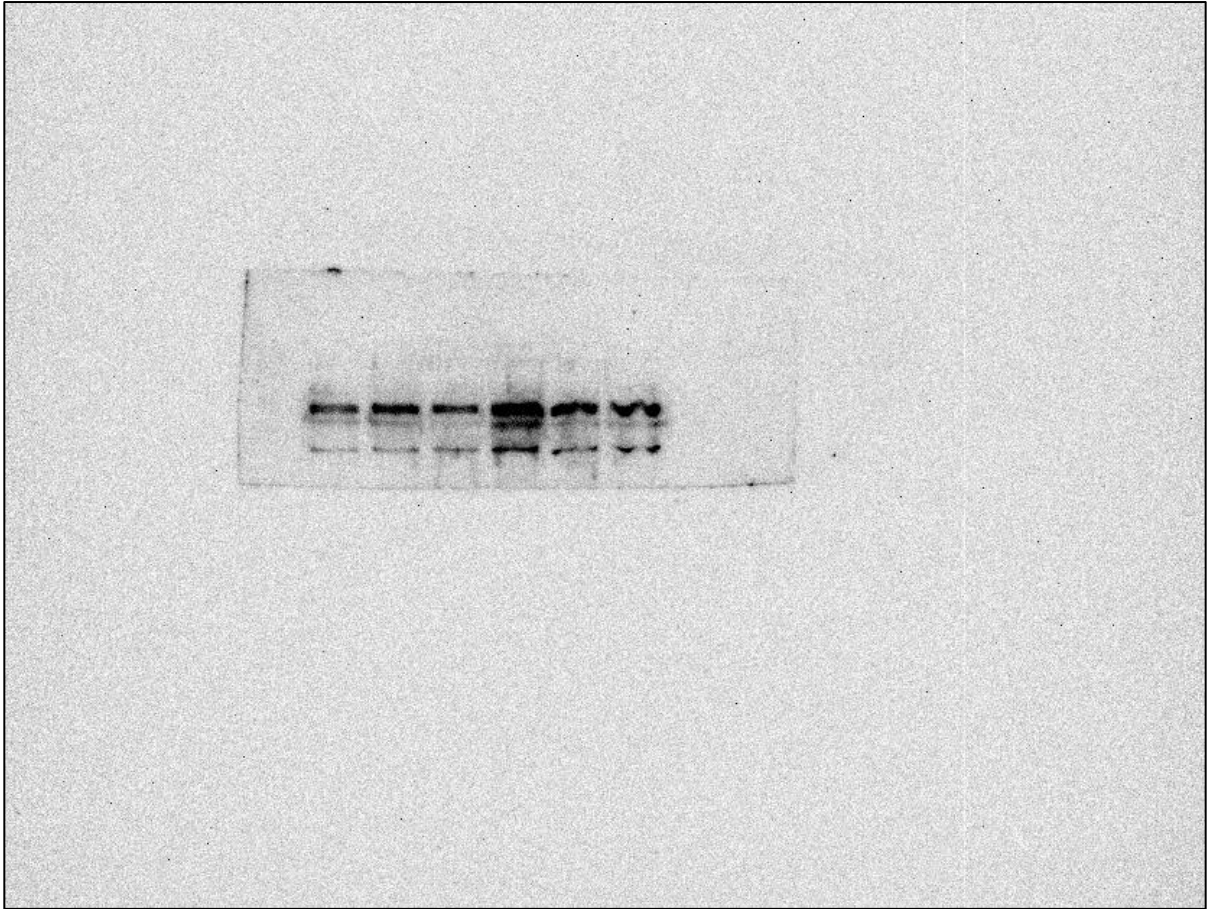


**Figure A52. Original blot indicating cleaved caspase-3 at 24 h from donor 3 for representative western blot used in Figure 43. Experiment date: June 23, 2021**

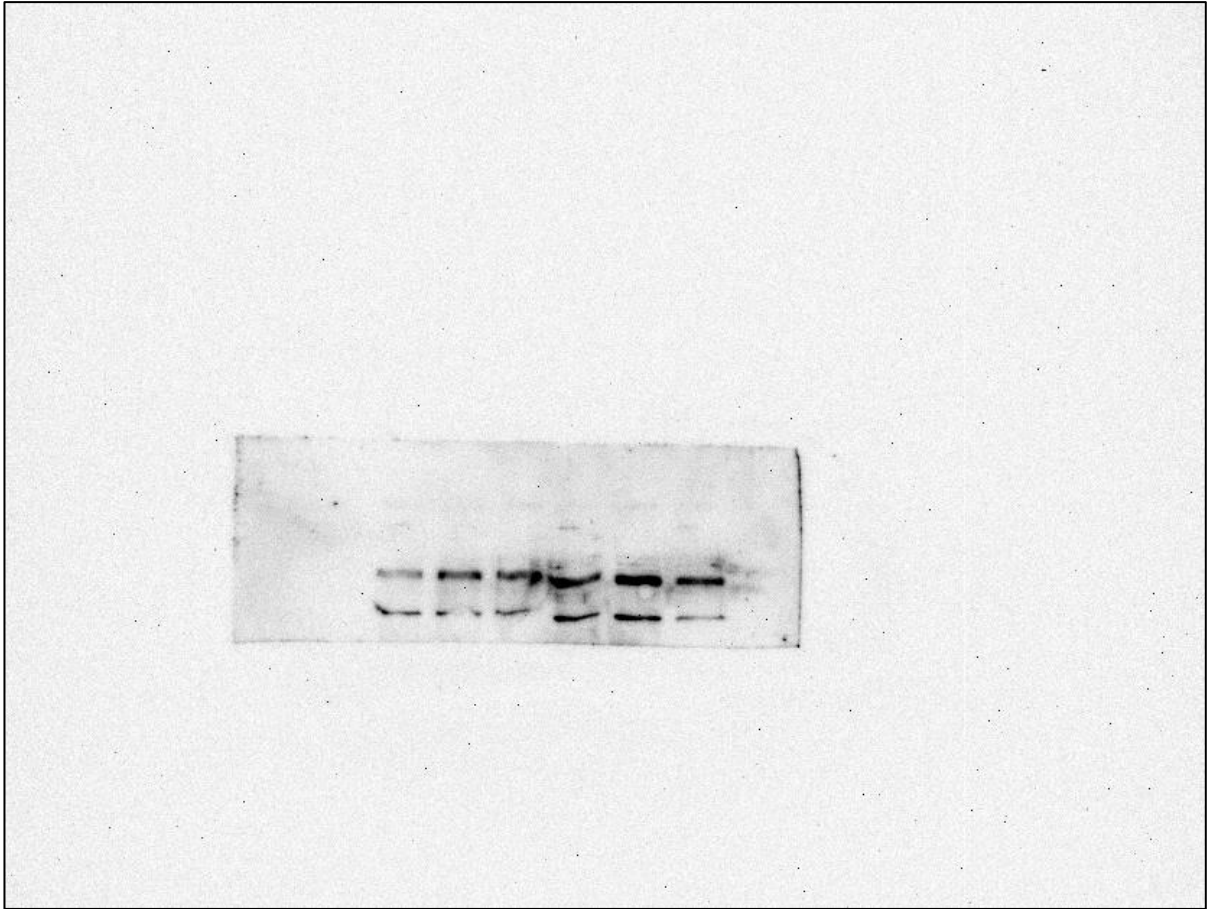


**Figure A53. Original blot indicating cleaved caspase-3 at 36 h from donor 3 for representative western blot used in Figure 43. Experiment date: June 23, 2021**



**Figure A54. Original blot indicating cleaved caspase-3 at 48 h from donor 3 for representative western blot used in Figure 43. Experiment date: June 23, 2021**

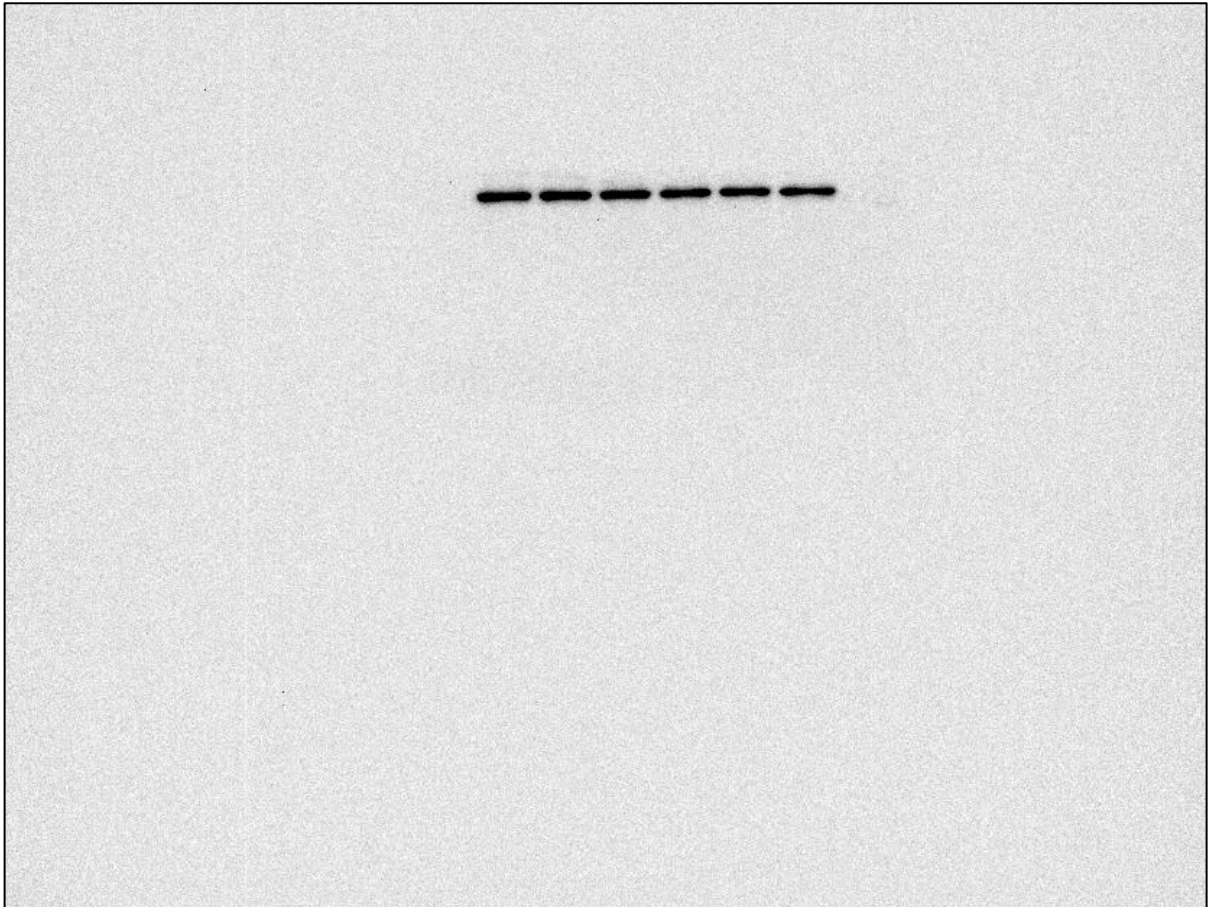


**Figure A55. Original blot indicating GAPDH at 24 h from donor 1 for representative western blot used in Figures 39, 40, 41, and 43. Experiment date: June 1, 2021**

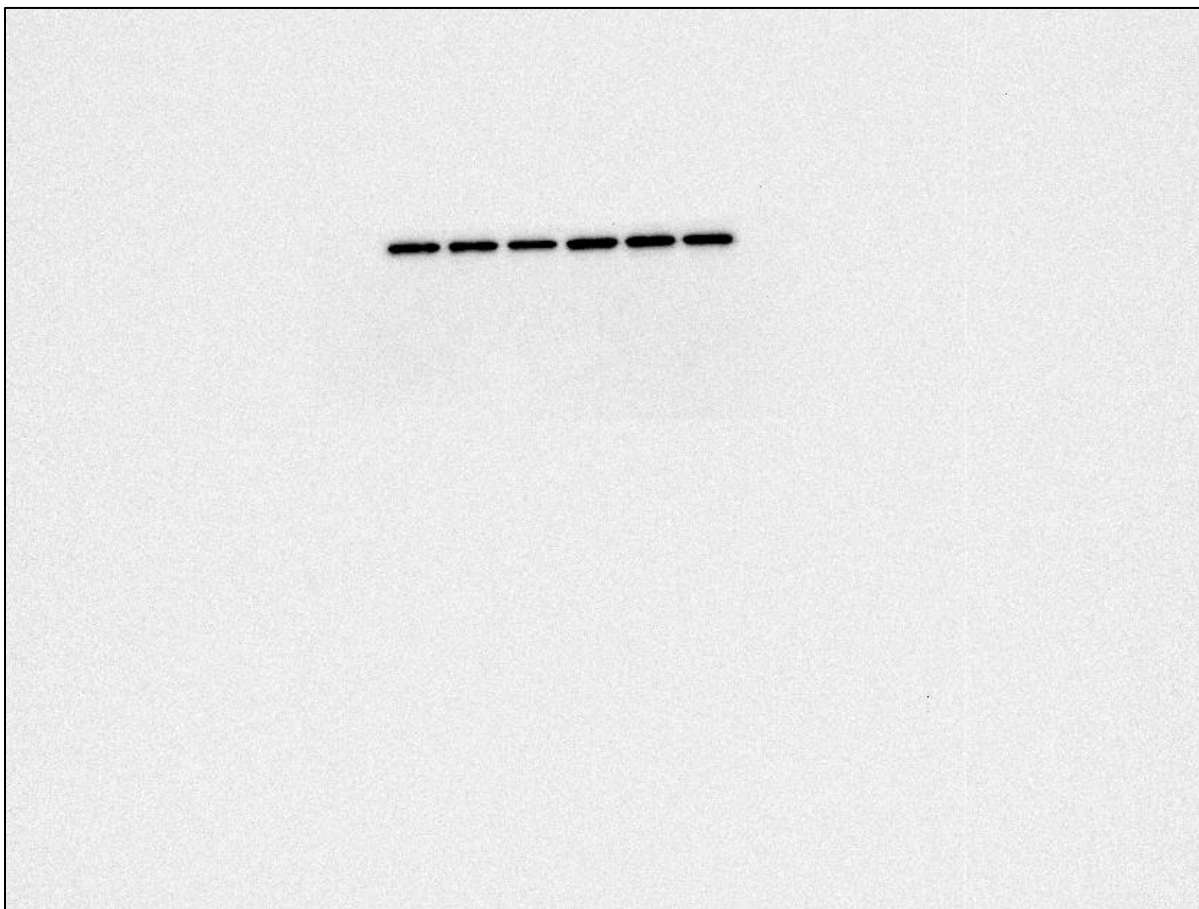


**Figure A56. Original blot indicating GAPDH at 36 h from donor 1 for representative western blot used in Figures 39, 40, 41, and 43. Experiment date: June 1, 2021**

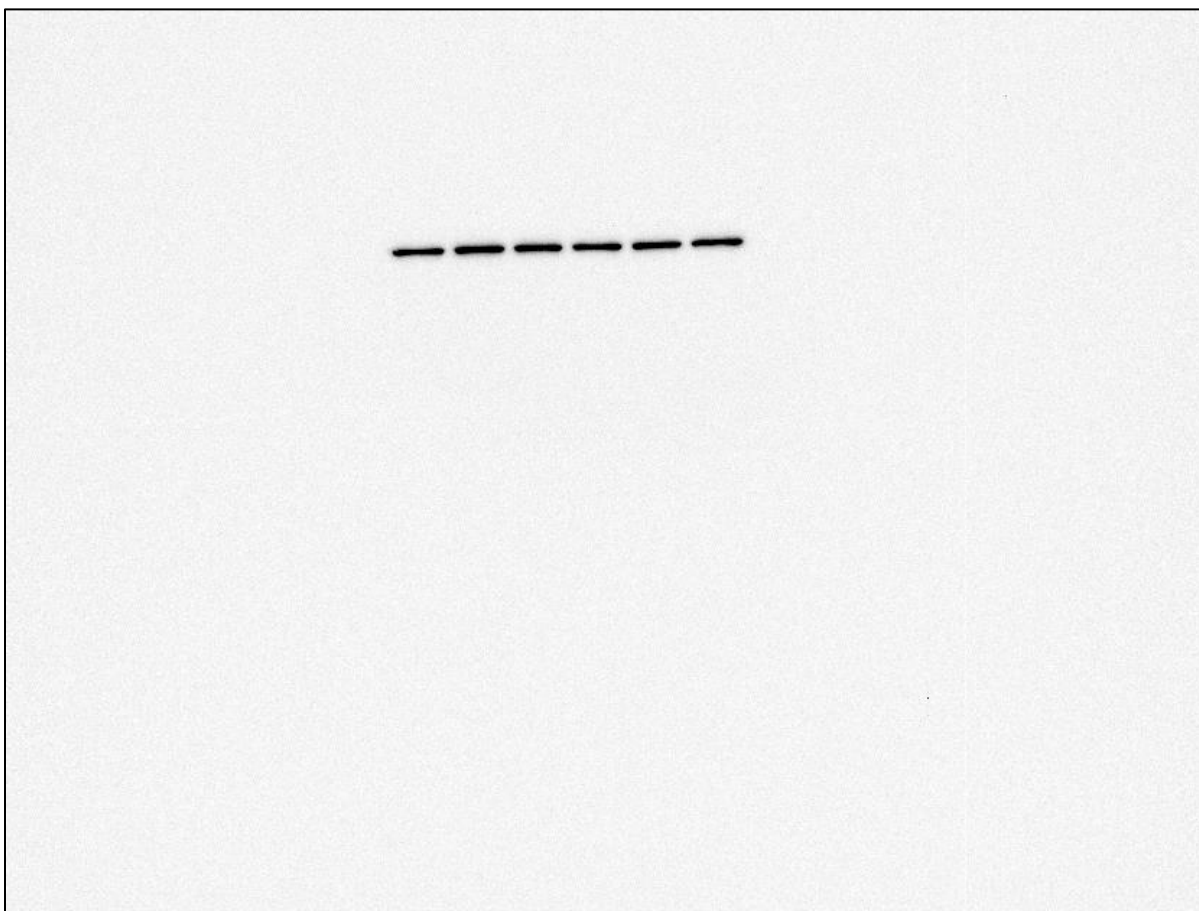


**Figure A57. Original blot indicating GAPDH at 48 h from donor 1 for representative western blot used in Figures 39, 40, 41, and 43. Experiment date: June 1, 2021**

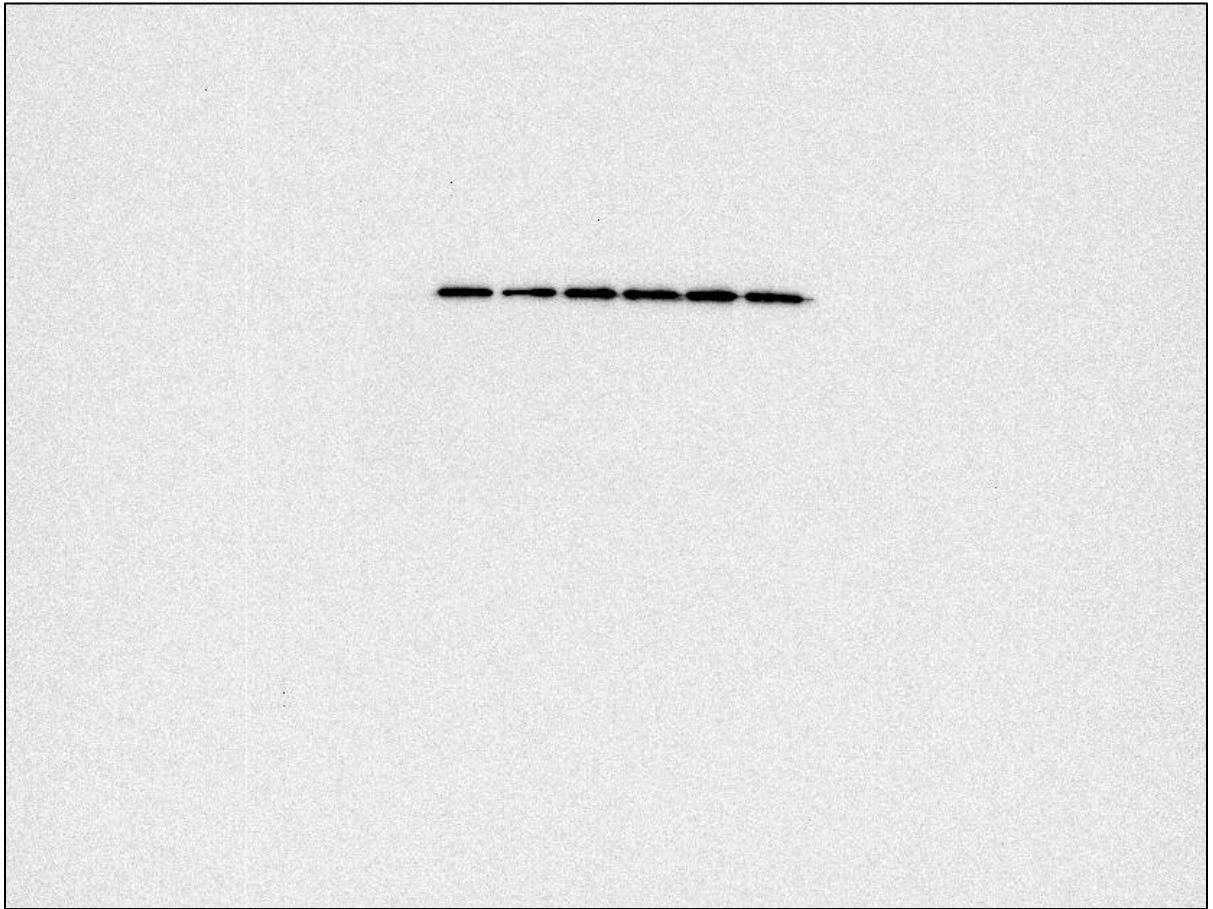


**Figure A58. Original blot indicating GAPDH at 24 h from donor 2 for representative western blot used in Figures 39, 40, 41, and 43. Experiment date: June 1, 2021**

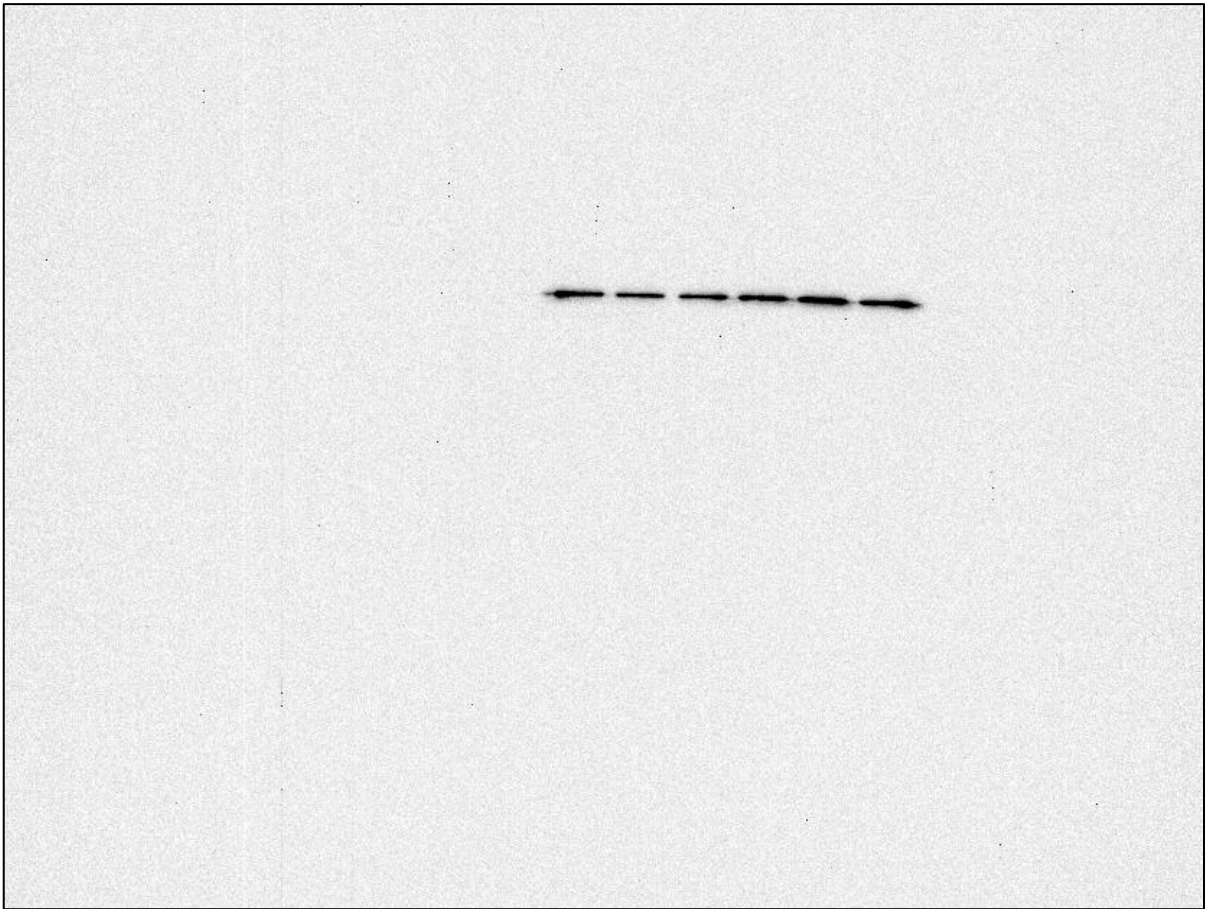


**Figure A59. Original blot indicating GAPDH at 36 h from donor 2 for representative western blot used in Figures 39, 40, 41, and 43. Experiment date: June 1, 2021**



**Figure A60. Original blot indicating GAPDH at 48 h from donor 2 for representative western blot used in Figures 39, 40, 41, and 43. Experiment date: June 1, 2021**

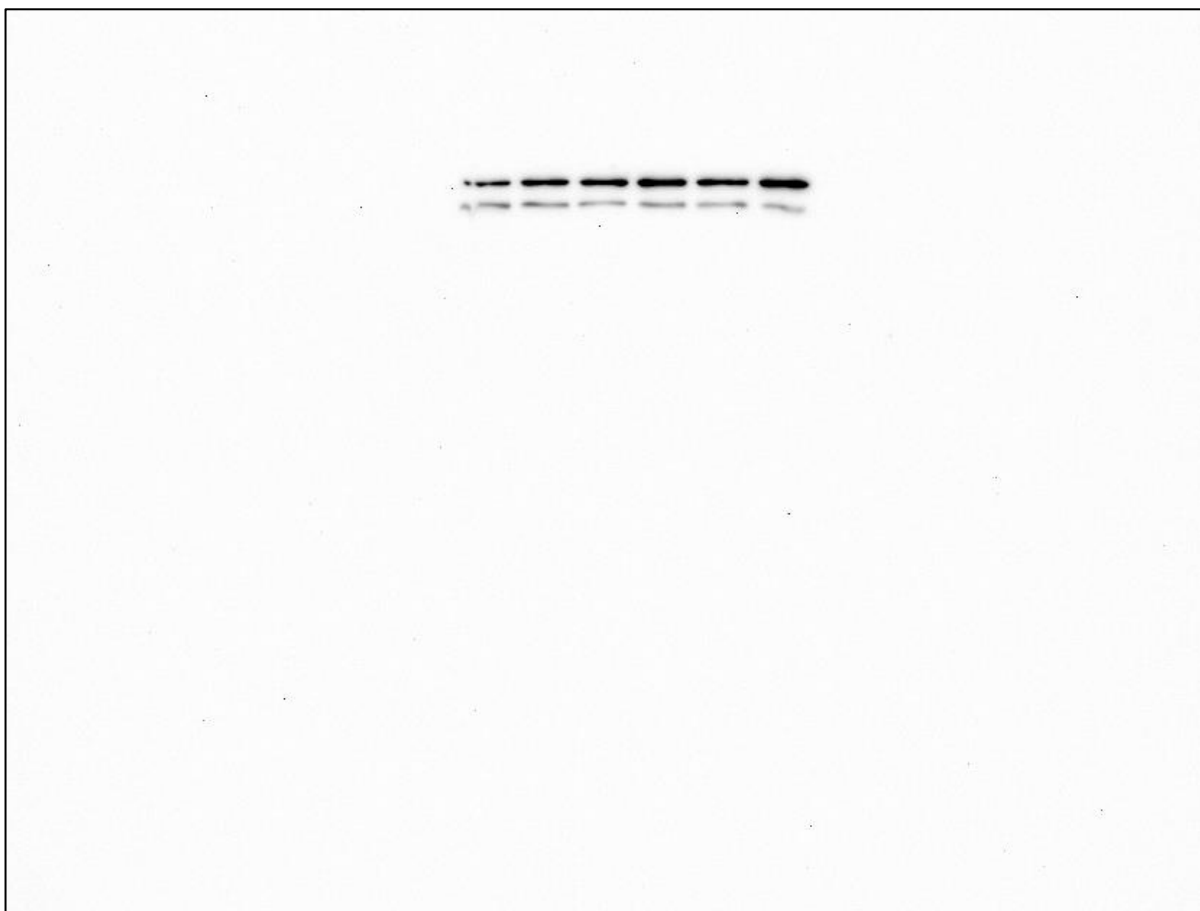


**Figure A61. Original blot indicating GAPDH at 24 h from donor 3 for representative western blot used in Figures 39, 40, and 41. Experiment date: June 4, 2021**

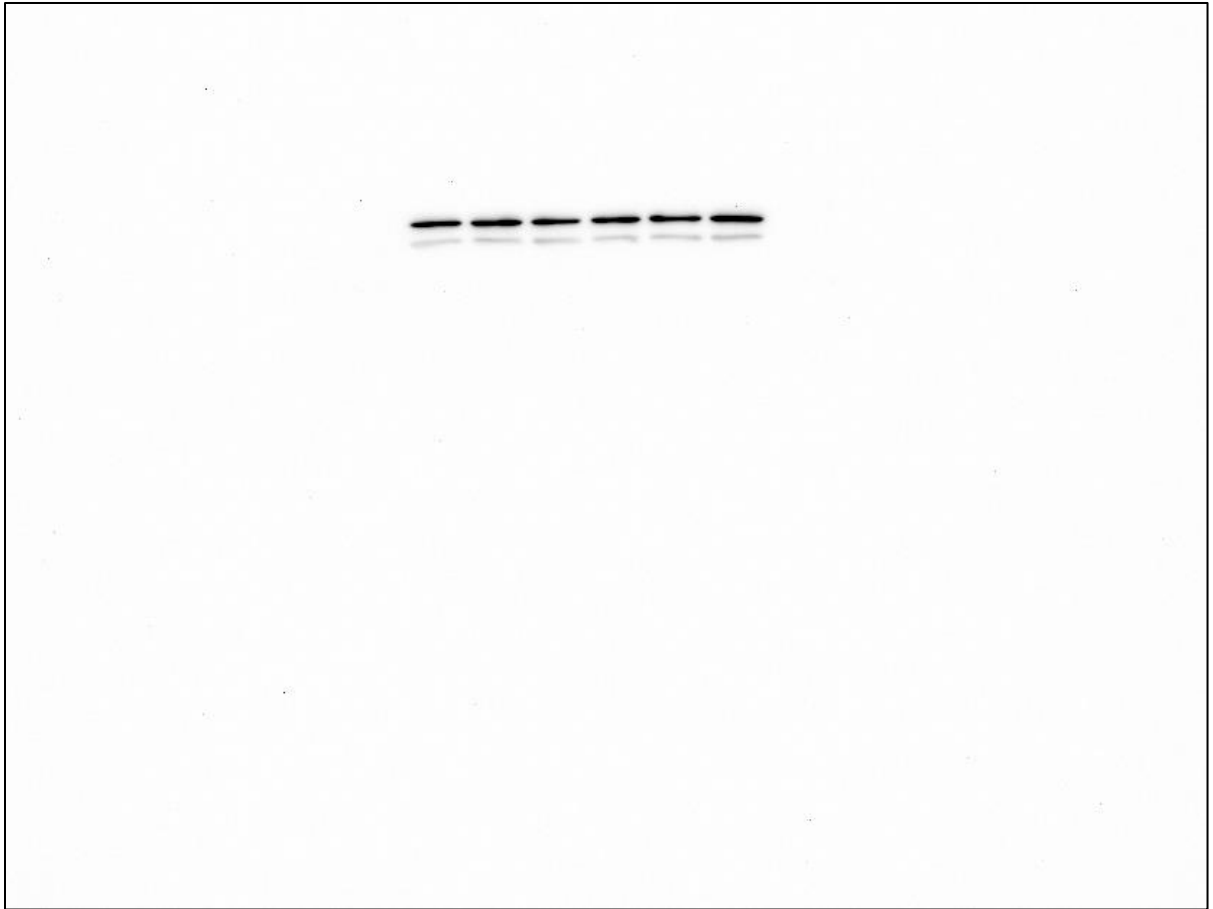


**Figure A62. Original blot indicating GAPDH at 36 h from donor 3 for representative western blot used in Figures 39, 40, and 41. Experiment date: June 4, 2021**



**Figure A63. Original blot indicating GAPDH at 48 h from donor 3 for representative western blot used in Figures 39, 40, and 41. Experiment date: June 4, 2021**

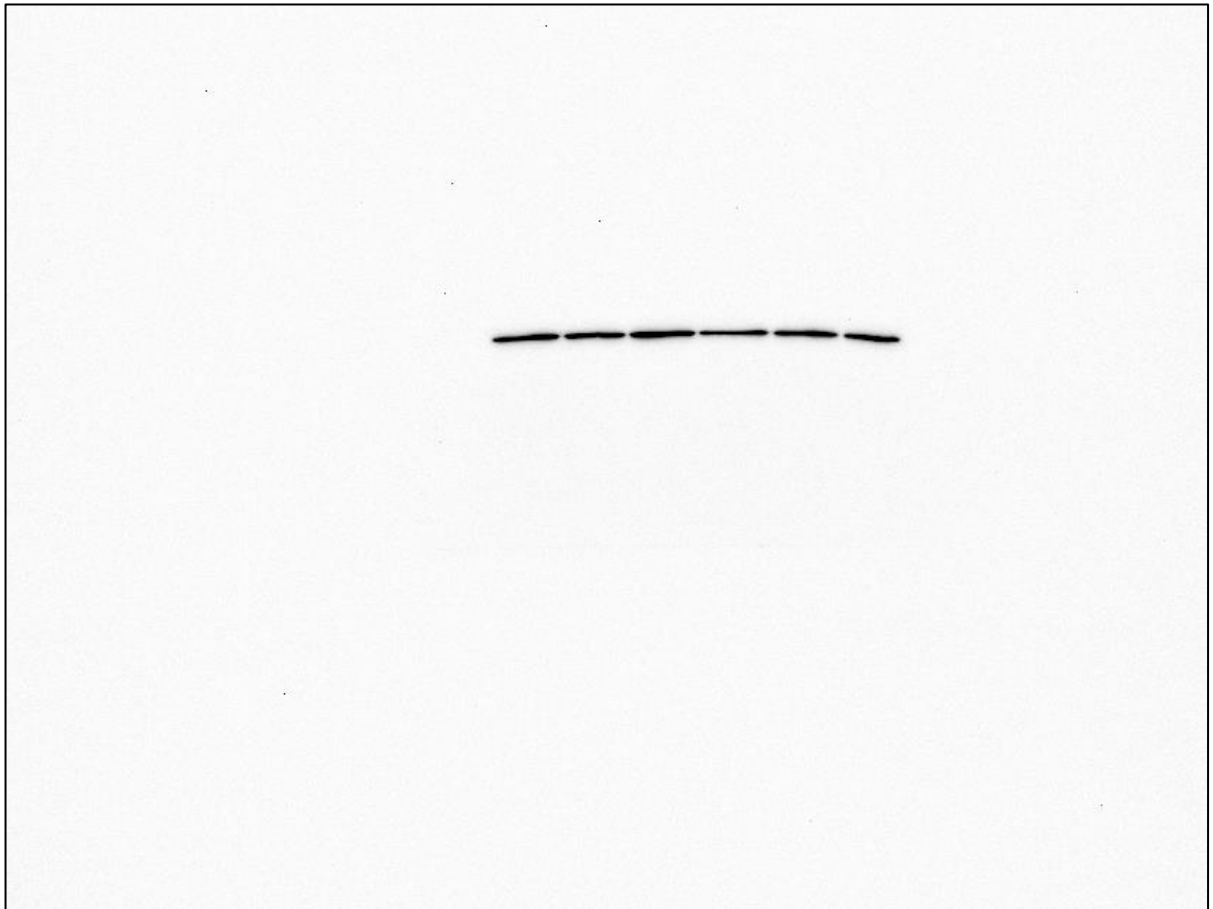


**Figure A64. Original blot indicating GAPDH at 24 h from donor 4 for representative western blot used in Figures 39, 40, and 41. Experiment date: June 4, 2021**



**Figure A65. Original blot indicating GAPDH at 36 h from donor 4 for representative western blot used in Figures 39, 40, and 41. Experiment date: June 4, 2021**

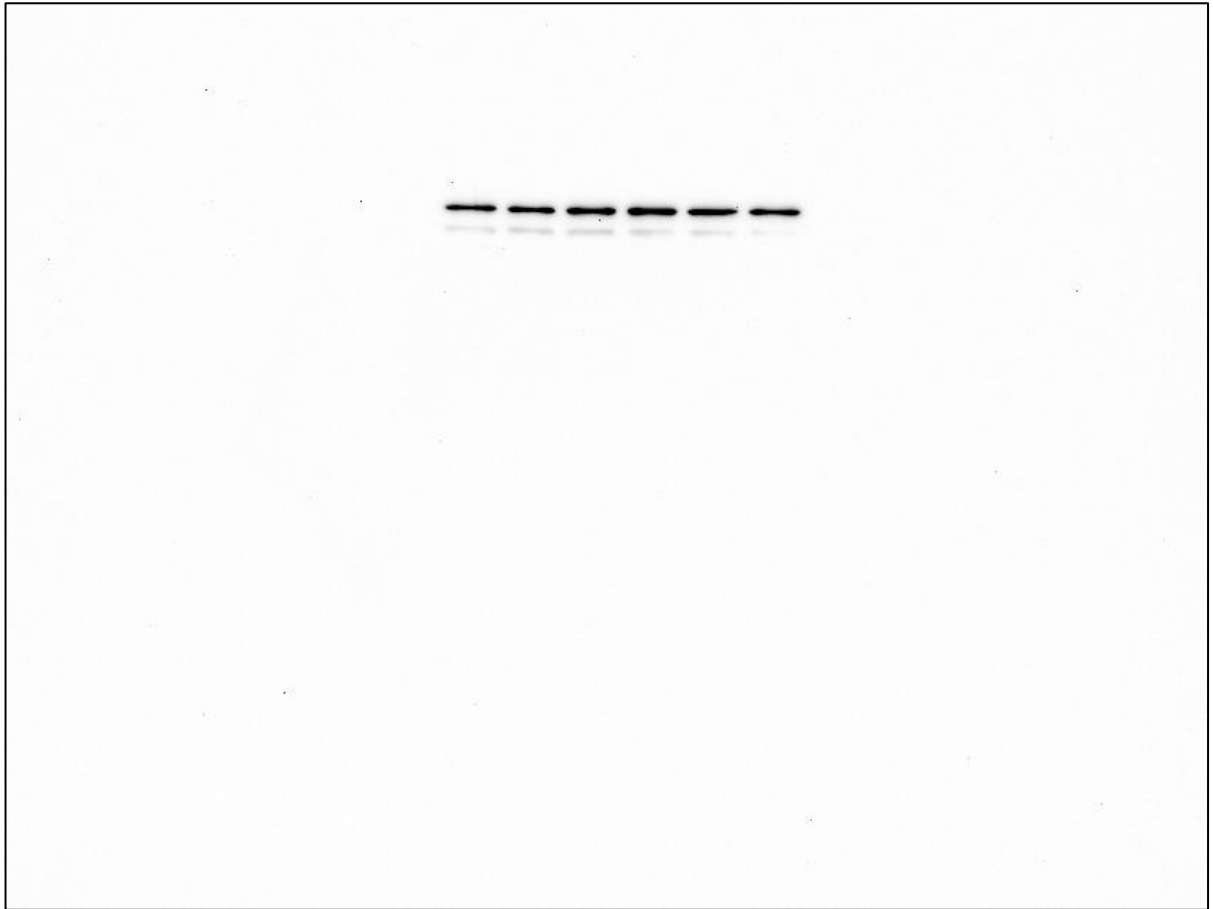


**Figure A66. Original blot indicating GAPDH at 48 h from donor 4 for representative western blot used in Figures 39, 40, and 41. Experiment date: June 4, 2021**

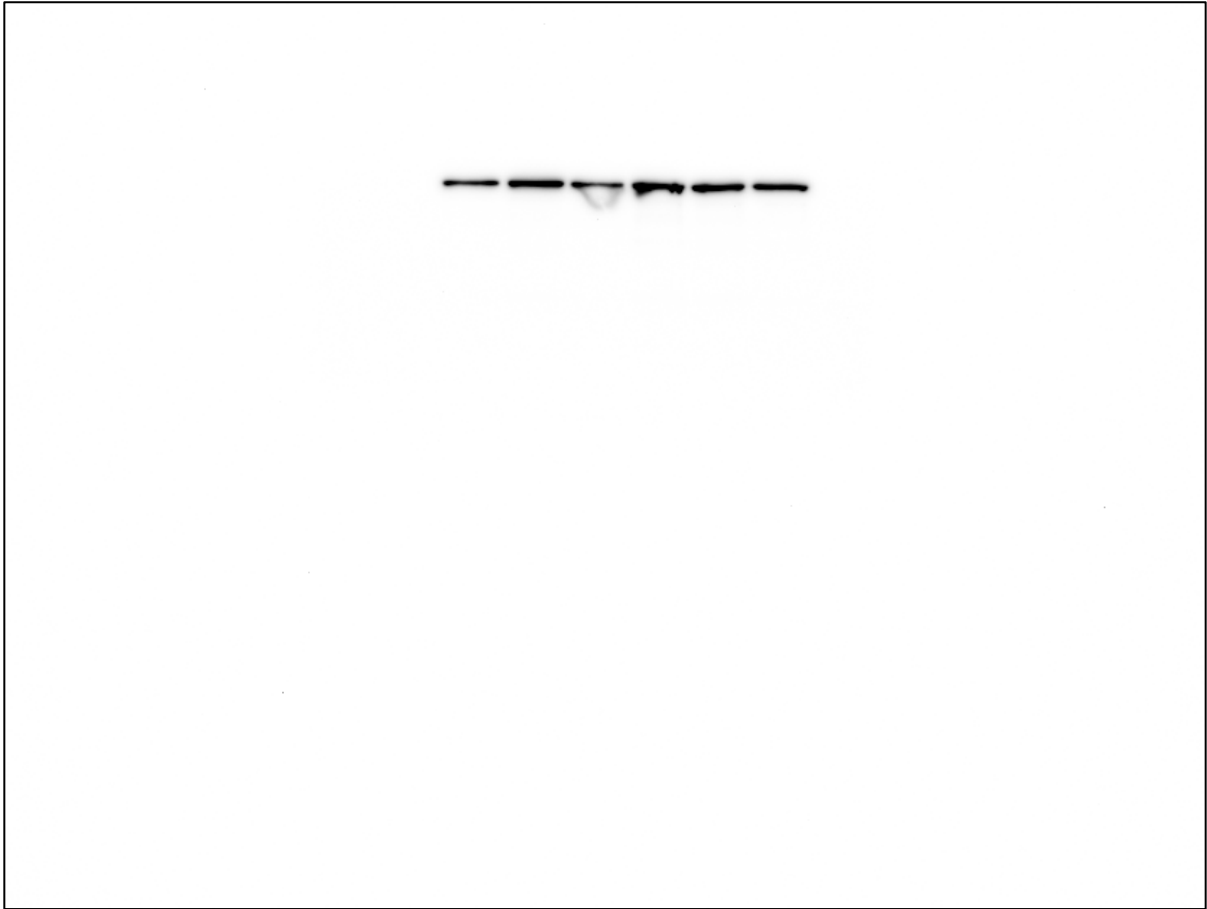


**Figure A67. Original blot indicating GAPDH at 24 h from donor 3 for representative western blot used in Figure 43. Experiment date: June 28, 2021**

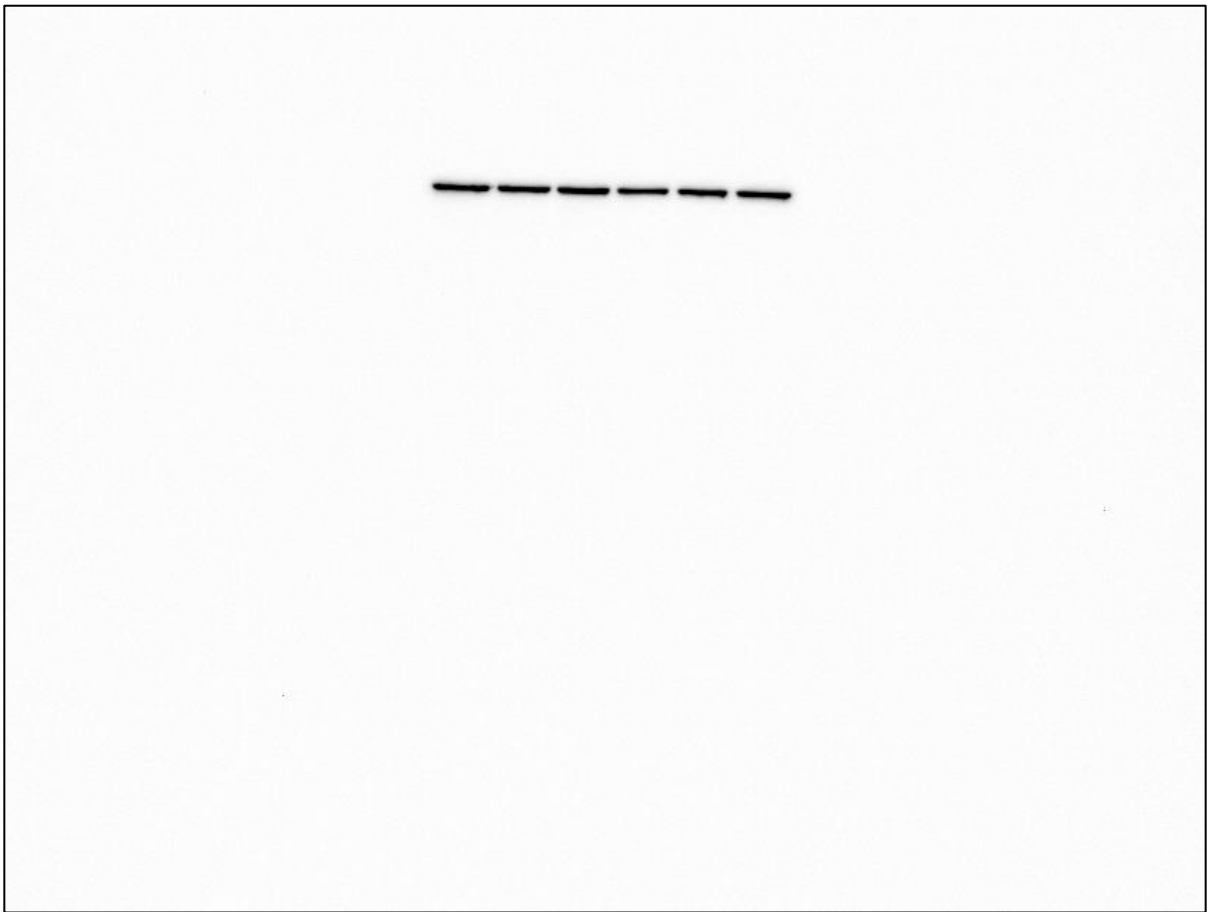


**Figure A68. Original blot indicating GAPDH at 36 h from donor 3 for representative western blot used in Figure 43. Experiment date: June 28, 2021**

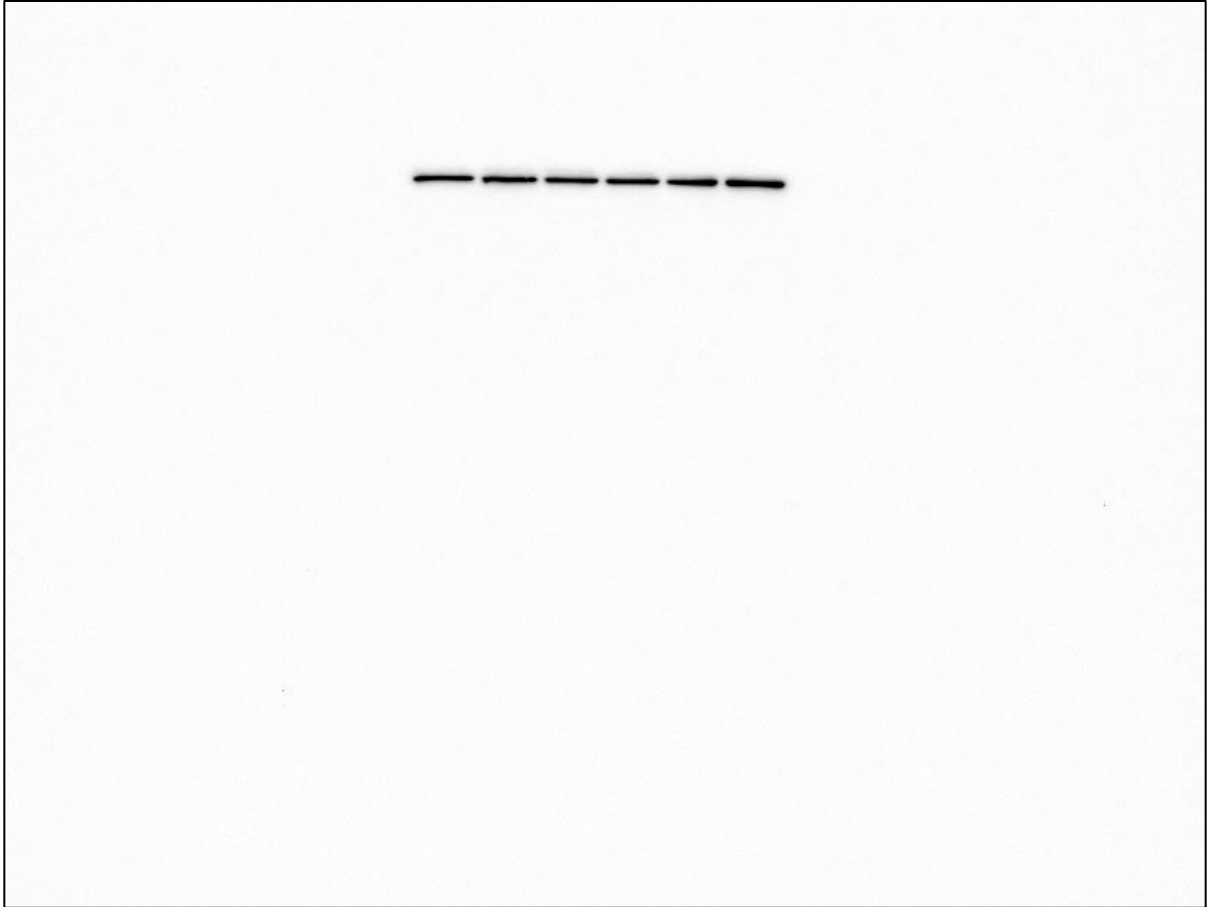


**Figure A69. Original blot indicating GAPDH at 48 h from donor 3 for representative western blot used in Figure 43. Experiment date: June 28, 2021**

B. RAW DENSITOMETRY QUANTIFICATION DATA OF WESTERN BLOT IMAGES

**Table A1: Raw data of densitometric quantification of ITGA1 donor 1 western blots from Fig. 39**

Donor 1	ITGA1						GAPDH		Normalized	Compared to respective controls	
	Sample	Sum	Area	Average	Median	BC Sum	BC Average	Bkgd Average			
ITGA1 24 h	CTRL 1	1,957,531	504	3,883.99	2,768	1,699,130	3,371.29	512.7	579.61	5.82	1.00
	CTRL 2	2,499,679	504	4,959.68	3,840	2,267,889	4,499.78	459.9	514.46	8.75	1.00
	CTRL 3	1,790,653	504	3,552.88	2,390	1,629,625	3,233.38	319.5	478.77	6.75	1.00
	AMPH 1	2,208,696	504	4,382.33	3,190	1,917,182	3,803.93	578.4	432.54	8.79	1.51
	AMPH 2	2,409,457	504	4,780.67	3,540	1,961,149	3,891.17	889.5	413.14	9.42	1.08
	AMPH 3	2,265,499	504	4,495.04	2,701	2,065,007	4,097.24	397.8	390.44	10.49	1.55
ITGA1 36 h	CTRL 1	506492	429	1180.63	695	381438	889.13	291.5	347.51	2.56	1.00
	CTRL 2	695537	429	1621.3	970	552851	1288.7	332.6	223.83	5.76	1.00
	CTRL 3	650844	429	1517.12	998	477141	1112.22	404.9	257.41	4.32	1.00
	AMPH 1	220170	429	513.22	375	128535	299.62	213.6	343.94	0.87	0.34
	AMPH 2	399705	429	931.71	577	296659	691.51	240.2	466.63	1.48	0.26
	AMPH 3	593420	429	1383.26	770	486641	1134.36	248.9	419.22	2.71	0.63
ITGA1 48 h	CTRL 1	1398529	407	3436.19	2156	1134101	2786.49	649.7	410.53	6.79	1.00
	CTRL 2	1901044	407	4670.87	2871	1571170	3860.37	810.5	416.01	9.28	1.00
	CTRL 3	1297053	407	3186.86	2167	1008937	2478.96	707.9	263.53	9.41	1.00
	AMPH 1	680219	407	1671.3	1056	480259	1040	345.2	502.90	2.07	0.30
	AMPH 2	977702	407	2402.22	1643	796505	1252.6	373.4	416.56	3.01	0.32
	AMPH 3	324869	407	798.2	555	197844	486.1	312.1	435.41	1.12	0.12

**Table A2: Raw data of densitometric quantification of ITGA1 donor 2 western blots from Fig. 39**

Donor 2	ITGA1							GAPDH		Normalized	Compared to respective controls
	Sample	Sum	Area	Average	Median	BC Sum	BC Average	Bkgd Average	BC Average		
ITGA1 24 h	CTRL 1	756,064	516	1,465.24	954	607,714	1,177.74	287.5	473.97	2.48	1.00
	CTRL 2	766,935	516	1,486.31	938	649,235	1,258.21	228.1	423.78	2.97	1.00
	CTRL 3	717,205	516	1,389.93	853	592,384	1,148.03	241.9	529.34	2.17	1.00
	AMPH 1	849,739	516	1,646.78	1,022	714,908	1,385.48	261.3	492.64	2.81	1.13
	AMPH 2	911,814	516	1,767.08	1,185	769,449	1,491.18	275.9	565.64	2.64	0.89
	AMPH 3	704,100	516	1,364.53	865	597,339	1,157.63	206.9	472.65	2.45	1.13
ITGA1 36 h	CTRL 1	4994387	559	8934.5	6160	4607503	8242.4	692.1	130.90	62.97	1.00
	CTRL 2	5123236	559	9165	5580	4767153	8528	637	96.40	88.46	1.00
	CTRL 3	2977524	559	5326.52	2492	2742855	4906.72	419.8	106.50	46.07	1.00
	AMPH 1	2282485	559	4083.16	2059	2021543	3616.36	466.8	125.60	28.79	0.46
	AMPH 2	3483658	559	6231.95	3638	3236971	5790.65	441.3	117.30	49.37	0.56
	AMPH 3	3330888	559	5958.65	3385	3081853	5513.15	445.5	121.90	45.23	0.98
ITGA1 48 h	CTRL 1	2352500	468	5026.71	3154	2090045	4465.91	560.8	410.53	10.88	1.00
	CTRL 2	3226600	468	6894.44	5526	2870639	6133.84	760.6	416.01	14.74	1.00
	CTRL 3	1551186	468	3314.5	2030	1376434	2941.1	373.4	263.53	11.16	1.00
	AMPH 1	339889	468	726.26	533	236039	504.36	221.9	502.90	1.00	0.09
	AMPH 2	1053056	468	2250.12	1072	940782	2010.22	239.9	416.56	4.83	0.33
	AMPH 3	1216922	468	2600.26	1508	1087660	2324.06	276.2	435.41	5.34	0.48

**Table A3: Raw data of densitometric quantification of ITGA1 donor 3 western blots from Fig. 39**

Donor 3	ITGA1							GAPDH		Normalized	Compared to respective controls
	Sample	Sum	Area	Average	Median	BC Sum	BC Average	Bkgd Average	BC Average		
ITGA1 24 h	CTRL 1	1,978,703	432	4,580.33	2,506	1,820,720	4,214.63	365.7	854.07	4.93	1.00
	CTRL 2	1,862,604	432	4,311.58	2,752	1,661,205	3,845.38	466.2	1571.42	2.45	1.00
	CTRL 3	1,574,172	432	3,643.92	2,295	1,380,549	3,195.72	448.2	1732.22	1.84	1.00
	AMPH 1	2,494,367	432	5,774.00	3,995	2,234,259	5,171.90	602.1	2364.41	2.19	0.44
	AMPH 2	2,439,192	432	5,646.28	4,027	2,210,361	5,116.58	529.7	1712.77	2.99	1.22
	AMPH 3	1,576,851	432	3,650.12	2,373	1,356,531	3,140.12	510	2804.74	1.12	0.61
ITGA1 36 h	CTRL 1	1090387	546	1997.05	1197	961804	1761.55	235.5	2,652.15	0.66	1.00
	CTRL 2	1293609	546	2369.25	1240	1168356	2139.85	229.4	3,165.53	0.68	1.00
	CTRL 3	1365331	546	2500.61	1386	1235656	2263.11	237.5	2,458.39	0.92	1.00
	AMPH 1	968316	546	1773.47	986	873748	1600.27	173.2	2,778.20	0.58	0.87
	AMPH 2	804880	546	1474.14	801	704197	1289.74	184.4	2,471.62	0.52	0.77
	AMPH 3	371123	546	679.71	403	290042	531.21	148.5	3,525.31	0.15	0.16
ITGA1 48 h	CTRL 1	456950	378	1208.86	996	363697	962.16	246.7	2,834.60	0.34	1.00
	CTRL 2	586120	378	1550.58	1141	476122	1259.58	291	3,121.11	0.40	1.00
	CTRL 3	683427	378	1808.01	1265	590363	1561.81	246.2	2,695.88	0.58	1.00
	AMPH 1	240874	378	637.23	458	181906	481.23	156	5,215.95	0.09	0.27
	AMPH 2	179345	378	474.46	356	123816	327.56	146.9	2,514.41	0.13	0.32
	AMPH 3	711506	378	1882.29	1216	611903	1418.69	263.5	2,092.96	0.68	1.17

**Table A4: Raw data of densitometric quantification of ITGA1 donor 4 western blots from Fig. 39**

Donor 4	ITGA1							GAPDH		Normalized	Compared to respective controls
	Sample	Sum	Area	Average	Median	BC Sum	BC Average	Bkgd Average	BC Average		
ITGA1 24 h	CTRL 1	790,721	490	1,613.72	1,259	670,817	1,369.02	244.7	1242.72	1.10	1.00
	CTRL 2	770,446	490	1,572.34	1,226	617,223	1,259.64	312.7	1208.59	1.04	1.00
	CTRL 3	668,234	490	1,363.74	952	538,482	1,098.94	264.8	1692.34	0.65	1.00
	AMPH 1	819,596	490	1,672.64	1,334	659,856	1,346.64	326	977.26	1.38	1.25
	AMPH 2	865,817	490	1,766.97	1,275	744,248	1,518.87	248.1	1163.93	1.30	1.25
	AMPH 3	882,373	490	1,800.76	1,289	751,788	1,534.26	266.5	1079.43	1.42	2.19
ITGA1 36 h	CTRL 1	785348	480	1636.14	1051	681476	1419.74	216.4	1,490.63	0.95	1.00
	CTRL 2	618112	480	1287.73	863	509296	1061.03	226.7	939.80	1.13	1.00
	CTRL 3	515954	480	1074.9	634	432386	900.8	174.1	984.94	0.91	1.00
	AMPH 1	529317	480	1102.74	795	445941	929.04	173.7	1,064.13	0.87	0.92
	AMPH 2	552850	480	1151.77	822	442066	920.97	230.8	1,430.54	0.64	0.57
	AMPH 3	541221	480	1127.54	867	450741	939.04	188.5	1,559.69	0.60	0.66
ITGA1 48 h	CTRL 1	707162	528	1339.32	829	612069	1159.22	180.1	1,813.51	0.64	1.00
	CTRL 2	700763	528	1327.2	800	598700	1133.9	193.3	1,945.43	0.58	1.00
	CTRL 3	370730	528	702.14	472	285510	540.74	161.4	2,532.36	0.21	1.00
	AMPH 1	438533	528	830.55	438	366883	694.85	135.7	2,933.59	0.24	0.37
	AMPH 2	732649	528	1387.59	827	635549	1203.69	183.9	2,305.93	0.52	0.90
	AMPH 3	270698	528	512.69	304	211033	299.69	113	2,035.43	0.15	0.69

**Table A5: Raw data of densitometric quantification of ITGA2 donor 1 western blots from Fig. 40**

Donor 1	ITGA2							GAPDH		Normalized	Compared to respective controls
	Sample	Sum	Area	Average	Median	BC Sum	BC Average	Bkgd Average	BC Average		
ITGA2 24 h	CTRL 1	436,094	374	1,166.03	821	293,974	786.03	380	579.61	1.36	1.00
	CTRL 2	634,291	374	1,695.97	1,149	504,251	1,348.27	347.7	514.46	2.62	1.00
	CTRL 3	415,465	374	1,110.87	794	307,004	820.87	290	478.77	1.71	1.00
	AMPH 1	422,936	374	1,130.84	774	320,085	855.84	275	432.54	1.98	1.46
	AMPH 2	492,184	374	1,316.00	840	386,566	1,033.60	282.4	413.14	2.50	0.95
	AMPH 3	425,865	374	1,138.68	693	345,754	924.48	214.2	390.44	2.37	1.38
ITGA2 36 h	CTRL 1	1851311	570	3247.91	2605	1499279	2630.31	617.6	758.73	3.47	1.00
	CTRL 2	1986800	570	3485.61	2723	1581017	2773.71	711.9	750.61	3.70	1.00
	CTRL 3	1962576	570	3443.12	2185	1710693	3001.22	441.9	668.12	4.49	1.00
	AMPH 1	1427569	570	2504.51	1603	1138978	1998.21	506.3	870.41	2.30	0.66
	AMPH 2	1349461	570	2367.48	1455	1098490	1927.18	440.3	892.49	2.16	0.58
	AMPH 3	894863	570	1569.94	1109	719303	1261.94	308	837.11	1.51	0.34
ITGA2 48 h	CTRL 1	143310	429	334.06	264	89213	207.96	126.1	646.41	0.32	1.00
	CTRL 2	146318	429	341.07	275	92178	214.87	126.2	831.02	0.26	1.00
	CTRL 3	135020	429	314.73	264	87658	204.33	110.4	746.65	0.27	1.00
	AMPH 1	91695	429	213.74	192	48408	112.84	100.9	693.46	0.16	0.51
	AMPH 2	75698	429	176.45	163	35758	83.35	93.1	727.93	0.11	0.44
	AMPH 3	88260	429	205.73	183	46432	108.23	97.5	701.01	0.15	0.56

**Table A6: Raw data of densitometric quantification of ITGA2 donor 2 western blots from Fig. 40**

Donor 2	ITGA2							GAPDH		Normalized	Compared to respective controls
	Sample	Sum	Area	Average	Median	BC Sum	BC Average	Bkgd Average	BC Average		
ITGA2 24 h	CTRL 1	183,237	429	427.13	311	105,588	246.13	181	473.97	0.52	1.00
	CTRL 2	110,892	429	258.49	209	46,499	108.39	150.1	423.78	0.26	1.00
	CTRL 3	138,180	429	322.10	233	70,569	164.50	157.6	529.34	0.31	1.00
	AMPH 1	114,806	429	267.61	211	55,389	129.11	138.5	492.64	0.26	0.50
	AMPH 2	129,454	429	301.76	231	69,308	161.56	140.2	565.64	0.29	1.12
	AMPH 3	133,456	429	311.09	229	69,835	162.79	148.3	472.65	0.34	1.11
ITGA2 36 h	CTRL 1	506492	429	1180.63	695	381438	889.13	291.5	347.51	2.56	1.00
	CTRL 2	695537	429	1621.3	970	552851	1288.7	332.6	223.83	5.76	1.00
	CTRL 3	650844	429	1517.12	998	477141	1112.22	404.9	257.41	4.32	1.00
	AMPH 1	220170	429	513.22	375	128535	299.62	213.6	343.94	0.87	0.34
	AMPH 2	399705	429	931.71	577	296659	691.51	240.2	466.63	1.48	0.26
	AMPH 3	593420	429	1383.26	770	486641	1134.36	248.9	419.22	2.71	0.63
ITGA2 48 h	CTRL 1	1398529	407	3436.19	2156	1134101	2786.49	649.7	410.53	6.79	1.00
	CTRL 2	1901044	407	4670.87	2871	1571170	3860.37	810.5	416.01	9.28	1.00
	CTRL 3	1297053	407	3186.86	2167	1008937	2478.96	707.9	263.53	9.41	1.00
	AMPH 1	680219	407	1671.3	1056	480259	1040	345.2	502.90	2.07	0.30
	AMPH 2	977702	407	2402.22	1643	796505	1252.6	373.4	416.56	3.01	0.32
	AMPH 3	324869	407	798.2	555	197844	486.1	312.1	435.41	1.12	0.12

**Table A7: Raw data of densitometric quantification of ITGA2 donor 3 western blots from Fig. 40**

Donor 3	ITGA2							GAPDH		Normalized	Compared to respective controls
	Sample	Sum	Area	Average	Median	BC Sum	BC Average	Bkgd Average	BC Average		
ITGA2 24 h	CTRL 1	237,547	352	674.85	588	162,183	460.75	214.1	2428.1	0.19	1.00
	CTRL 2	244,690	352	695.14	555	163,730	465.14	230	2889.74	0.16	1.00
	CTRL 3	214,002	352	607.96	543	139,800	397.16	210.8	2222.62	0.18	1.00
	AMPH 1	197,748	352	561.78	473	125,939	357.78	204	2532.13	0.14	0.74
	AMPH 2	190,365	352	540.81	469	118,064	335.41	205.4	2277.54	0.15	0.91
	AMPH 3	163,371	352	464.12	373	105,431	299.52	164.6	3251.22	0.09	0.52
ITGA2 36 h	CTRL 1	242219	576	420.52	261	167454	290.72	129.8	2,652.15	0.11	1.00
	CTRL 2	156408	576	271.54	204	91089	158.14	113.4	3,165.53	0.05	1.00
	CTRL 3	202378	576	351.35	225	138211	239.95	111.4	2,458.39	0.10	1.00
	AMPH 1	260952	576	453.04	286	185380	321.84	131.2	2,778.20	0.12	1.06
	AMPH 2	190955	576	331.52	225	123447	214.32	117.2	2,471.62	0.09	1.74
	AMPH 3	172908	576	300.19	211	102693	178.29	121.9	3,525.31	0.05	0.52
ITGA2 48 h	CTRL 1	798211	504	1583.75	737	709456	1407.65	176.1	2,834.60	0.50	1.00
	CTRL 2	715902	504	1420.44	736	616614	1223.44	197	3,121.11	0.39	1.00
	CTRL 3	998856	504	1981.86	1091	873460	1733.06	248.8	2,695.88	0.64	1.00
	AMPH 1	362026	504	718.31	418	284611	564.71	153.6	5,215.95	0.11	0.22
	AMPH 2	577767	504	1146.36	556	498739	989.56	156.8	2,514.41	0.39	1.00
	AMPH 3	360759	504	715.79	337	303403	601.99	113.8	2,092.96	0.29	0.45

**Table A8: Raw data of densitometric quantification of ITGA2 donor 4 western blots from Fig. 40**

Donor 4	ITGA2						GAPDH			Normalized	Compared to respective controls
	Sample	Sum	Area	Average	Median	BC Sum	BC Average	Bkgd Average	BC Average		
ITGA2 24 h	CTRL 1	127,173	310	410.24	331	71,838	231.74	178.5	1507.71	0.153703298	1.00
	CTRL 2	140,520	310	453.29	377	81,837	263.99	189.3	1150.37	0.229482688	1.00
	CTRL 3	145,140	310	468.19	366	86,023	277.49	190.7	1565.36	0.177269127	1.00
	AMPH 1	124,292	310	400.94	308	72,119	232.64	168.3	1115.7	0.208514834	1.36
	AMPH 2	130,413	310	420.69	326	75,698	244.19	176.5	1779.33	0.13723705	0.60
	AMPH 3	116,389	310	375.45	303	63,595	205.15	170.3	1105.21	0.185620832	1.05
ITGA2 36 h	CTRL 1	225437	504	447.3	298	157649	312.8	134.5	1,004.46	0.311411106	1.00
	CTRL 2	246227	504	488.55	303	169971	337.25	151.3	847.84	0.397775524	1.00
	CTRL 3	205082	504	406.91	269	134421	266.71	140.2	730.83	0.364941231	1.00
	AMPH 1	173829	504	344.9	269	103017	204.4	140.5	846.60	0.241436334	0.78
	AMPH 2	209521	504	415.72	272	136541	270.92	144.8	724.67	0.373852926	0.94
	AMPH 3	166904	504	331.16	225	99972	198.36	132.8	724.59	0.273754813	0.75
ITGA2 48 h	CTRL 1	190498	385	494.8	297	134750	350	144.8	1,813.51	0.192995903	1.00
	CTRL 2	204043	385	529.98	330	148179	384.88	145.1	1,945.43	0.19783801	1.00
	CTRL 3	234136	385	608.15	387	174884	454.25	153.9	2,532.36	0.179378129	1.00
	AMPH 1	239125	385	621.1	492	160816	417.7	203.4	2,933.59	0.142385269	0.74
	AMPH 2	172334	385	447.62	301	109579	254.62	135.2	2,305.93	0.110419657	0.56
	AMPH 3	143131	385	371.77	256	92465	234.17	125.6	2,035.43	0.115046943	0.64

**Table A9: Raw data of densitometric quantification of ITGB1 donor 1 western blots from Fig. 41**

Donor 1	ITGB1							GAPDH		Normalized	Compared to respective controls
	Sample	Sum	Area	Average	Median	BC Sum	BC Average	Bkgd Average	BC Average		
ITGB1 24 h	CTRL 1	234,715	494	475.13	335	168,519	341.13	134	579.61	0.59	1.00
	CTRL 2	220,619	494	446.60	305	160,746	325.40	121.2	514.46	0.63	1.00
	CTRL 3	214,807	494	434.83	308	153,896	311.53	123.3	478.77	0.65	1.00
	AMPH 1	210,915	494	426.95	285	156,673	317.15	109.8	432.54	0.73	1.25
	AMPH 2	195,089	494	394.92	274	137,044	277.42	117.5	413.14	0.67	1.06
	AMPH 3	212,962	494	431.10	310	148,396	300.40	130.7	390.44	0.77	1.18
ITGB1 36 h	CTRL 1	188624	456	413.65	335	130940	287.15	126.5	758.73	0.38	1.00
	CTRL 2	156846	456	343.96	263	102901	225.66	118.3	750.61	0.30	1.00
	CTRL 3	116653	456	255.82	211	67177	147.32	108.5	668.12	0.22	1.00
	AMPH 1	128240	456	281.23	227	76757	168.33	112.9	870.41	0.19	0.51
	AMPH 2	161673	456	354.55	280	110190	241.65	112.9	892.49	0.27	0.90
	AMPH 3	132625	456	290.84	253	76673	168.14	122.7	837.11	0.20	0.91
ITGB1 48 h	CTRL 1	118177	330	358.11	351	77488	234.81	123.3	646.41	0.36	1.00
	CTRL 2	130280	330	394.79	382	79229	240.09	154.7	831.02	0.29	1.00
	CTRL 3	135449	330	410.45	380	78887	239.05	171.4	746.65	0.32	1.00
	AMPH 1	101774	330	308.41	307	53560	162.31	146.1	693.46	0.23	0.64
	AMPH 2	105638	330	320.12	325	56963	172.62	147.5	727.93	0.24	0.82
	AMPH 3	94537	330	286.48	275	50416	152.78	133.7	701.01	0.22	0.68

**Table A10: Raw data of densitometric quantification of ITGB1 donor 2 western blots from Fig. 41**

Donor 2	ITGB1						GAPDH		Normalized	Compared to respective controls	
	Sample	Sum	Area	Average	Median	BC Sum	BC Average	Bkgd Average			BC Average
ITGB1 24 h	CTRL 1	367,560	352	1,044.20	1,077	241,227	685.30	358.9	473.97	1.45	1.00
	CTRL 2	371,838	352	1,056.36	1,123	255,924	727.06	329.3	423.78	1.72	1.00
	CTRL 3	403,557	352	1,146.47	1,199	236,920	673.07	473.4	529.34	1.27	1.00
	AMPH 1	368,334	352	1,046.40	1,115	217,325	617.40	429	492.64	1.25	0.87
	AMPH 2	367,360	352	1,043.64	1,085	204,524	581.04	462.6	565.64	1.03	0.60
	AMPH 3	294,554	352	836.80	873	159,632	453.50	383.3	472.65	0.96	0.75
ITGB1 36 h	CTRL 1	198435	504	393.72	337	109982	218.22	175.5	347.51	0.63	1.00
	CTRL 2	216426	504	429.42	344	130947	259.82	169.6	223.83	1.16	1.00
	CTRL 3	164268	504	325.93	265	86803	172.23	153.7	257.41	0.67	1.00
	AMPH 1	158471	504	314.43	260	82820	164.33	150.1	343.94	0.48	0.76
	AMPH 2	209781	504	416.23	334	126368	250.73	165.5	466.63	0.54	0.46
	AMPH 3	230682	504	457.7	369	140566	278.9	178.8	419.22	0.67	0.99
ITGB1 48 h	CTRL 1	477542	408	1170.45	1045	348614	854.45	316	410.53	2.08	1.00
	CTRL 2	535571	408	1312.67	1176	391710	960.07	352.6	416.01	2.31	1.00
	CTRL 3	517920	408	1269.41	1114	366470	898.21	371.2	263.53	3.41	1.00
	AMPH 1	342569	408	839.63	677	223841	548.63	291	502.90	1.09	0.52
	AMPH 2	478442	408	1172.65	1070	326502	800.25	372.4	416.56	1.92	0.83
	AMPH 3	300000	408	735.29	572	183719	450.29	285	435.41	1.03	0.30

**Table A11: Raw data of densitometric quantification of ITGB1 donor 3 western blots from Fig. 41**

Donor 3	ITGB1						GAPDH			Normalized	Compared to respective controls
	Sample	Sum	Area	Average	Median	BC Sum	BC Average	Bkgd Average	BC Average		
ITGB1 24 h	CTRL 1	441,954	420	1,052.27	1,000	319,733	761.27	291	427.88	<b>1.78</b>	1.00
	CTRL 2	340,749	420	811.31	754	242,426	577.21	234.1	619.73	<b>0.93</b>	1.00
	CTRL 3	291,190	420	693.31	642	208,156	495.61	197.7	732.68	<b>0.68</b>	1.00
	AMPH 1	254,748	420	606.54	561	176,207	419.54	187	663.88	<b>0.63</b>	0.36
	AMPH 2	230,341	420	548.43	508	147,223	350.53	197.9	698.09	<b>0.50</b>	0.54
	AMPH 3	282,181	420	671.86	668	182,095	433.56	238.3	588.92	<b>0.74</b>	1.09
ITGB1 36 h	CTRL 1	653636	574	1138.74	1068	500492	871.94	266.8	2,652.15	<b>0.33</b>	1.00
	CTRL 2	723430	574	1260.33	1163	545662	950.63	309.7	3,165.53	<b>0.30</b>	1.00
	CTRL 3	616460	574	1073.97	958	448048	780.57	293.4	2,458.39	<b>0.32</b>	1.00
	AMPH 1	629723	574	1097.08	918	471528	821.48	275.6	2,778.20	<b>0.30</b>	0.90
	AMPH 2	510052	574	888.59	711	405756	706.89	181.7	2,471.62	<b>0.29</b>	0.95
	AMPH 3	361596	574	629.96	532	245360	427.46	202.5	3,525.31	<b>0.12</b>	0.38
ITGB1 48 h	CTRL 1	293449	663	442.61	352	208319	314.21	128.4	1,245.04	<b>0.25</b>	1.00
	CTRL 2	289704	663	436.96	311	201989	304.66	132.3	1,838.70	<b>0.17</b>	1.00
	CTRL 3	230612	663	347.83	280	152709	230.33	117.5	2,111.31	<b>0.11</b>	1.00
	AMPH 1	187444	663	282.72	234	113320	170.92	111.8	1,349.30	<b>0.13</b>	0.50
	AMPH 2	245291	663	369.97	306	162813	245.57	124.4	1,302.30	<b>0.19</b>	1.14
	AMPH 3	235214	663	354.77	308	151410	228.37	126.4	1,315.26	<b>0.17</b>	1.59

**Table A12: Raw data of densitometric quantification of ITGB1 donor 4 western blots from Fig. 41**

Donor 4	ITGB1							GAPDH		Normalized	Compared to respective controls
	Sample	Sum	Area	Average	Median	BC Sum	BC Average	Bkgd Average	BC Average		
ITGB1 24 h	CTRL 1	834,688	468	1,783.52	1,430	653,431	1,396.22	387.3	1042.72	1.339017	1.00
	CTRL 2	833,172	468	1,780.28	1,326	665,347	1,421.68	358.6	1008.59	1.409572	1.00
	CTRL 3	695,755	468	1,486.66	1,203	536,588	1,146.56	340.1	1092.34	1.049637	1.00
	AMPH 1	812,135	468	1,735.33	1,386	646,884	1,382.23	353.1	977.56	1.413959	1.06
	AMPH 2	840,161	468	1,795.22	1,264	671,119	1,434.02	361.2	963.93	1.487681	1.06
	AMPH 3	653,531	468	1,396.43	1,035	502,788	1,074.33	322.1	979.43	1.096893	1.05
ITGB1 36 h	CTRL 1	417383	684	610.21	391	335371	490.31	119.9	1,490.63	0.328928	1.00
	CTRL 2	524447	684	766.74	521	430533	629.44	137.3	939.80	0.66976	1.00
	CTRL 3	525388	684	768.11	476	423130	618.61	149.5	984.94	0.628069	1.00
	AMPH 1	260634	684	381.04	299	186967	273.34	107.7	1,064.13	0.256867	0.78
	AMPH 2	394254	684	576.39	397	314841	460.29	116.1	1,430.54	0.32176	0.48
	AMPH 3	199560	684	291.75	223	127124	185.85	105.9	1,559.69	0.119158	0.19
ITGB1 48 h	CTRL 1	1400641	640	2188.5	1386	1278081	1997	191.5	1,813.51	1.101179	1.00
	CTRL 2	1335522	640	2086.75	1192	1203810	1880.95	205.8	1,945.43	0.966856	1.00
	CTRL 3	1185311	640	1852.05	1040	1054175	1647.15	204.9	2,532.36	0.650441	1.00
	AMPH 1	780401	640	1219.38	759	676785	1057.48	161.9	2,933.59	0.360473	0.33
	AMPH 2	588396	640	919.37	581	492203	769.07	150.3	2,305.93	0.333518	0.34
	AMPH 3	777321	640	1214.56	878	644969	1007.76	206.8	2,035.43	0.495109	0.76

**Table A13: Raw data of densitometric quantification of caspase-3 donor 1 western blots from Fig. 43**

Donor 1	Caspase-3								GAPDH	Normalized	Compared to respective controls
	Sample	Sum	Area	Average	Median	BC Sum	BC Average	Bkgd Average	BC Average		
Caspase -3 24 h	CTRL 1	188,818	756	249.76	234	82,222	108.76	141	579.61	0.19	1.00
	CTRL 2	209,152	756	276.66	238	95,147	125.86	150.8	514.46	0.24	1.00
	CTRL 3	299,526	756	396.20	326	184,084	243.50	152.7	478.77	0.51	1.00
	AMPH 1	302,147	756	399.67	319	182,169	240.97	158.7	432.54	0.56	2.97
	AMPH 2	280,505	756	371.04	300	163,703	216.54	154.5	413.14	0.52	2.14
	AMPH 3	229,960	756	304.18	262	115,199	152.38	151.8	390.44	0.39	0.77
Caspase -3 36 h	CTRL 1	111376	588	189.41	172	46049	78.31	111.1	758.73	0.10	1.00
	CTRL 2	143862	588	244.66	194	79711	135.56	109.1	750.61	0.18	1.00
	CTRL 3	108199	588	184.01	174	46047	78.31	105.7	668.12	0.12	1.00
	AMPH 1	115145	588	195.82	172	54816	93.22	102.6	870.41	0.11	1.04
	AMPH 2	180992	588	307.81	235	108432	184.41	123.4	892.49	0.21	1.14
	AMPH 3	179329	588	304.98	248	102830	174.88	130.1	837.11	0.21	1.78
Caspase -3 48 h	CTRL 1	679272	456	1489.63	1363	410596	900.43	589.2	646.41	1.39	1.00
	CTRL 2	851639	456	1867.63	1745	522543	1145.93	721.7	831.02	1.38	1.00
	CTRL 3	565286	456	1239.66	1088	326022	714.96	524.7	746.65	0.96	1.00
	AMPH 1	1162333	456	2548.98	2295	773456	1696.18	852.8	693.46	2.45	1.76
	AMPH 2	1104840	456	2422.89	2221	758234	1662.79	760.1	727.93	2.28	1.66
	AMPH 3	1098150	456	2408.22	2190	743199	1629.82	778.4	701.01	2.32	2.43

**Table A14: Raw data of densitometric quantification of cleaved caspase-3 p19 donor 1 western blots from Fig. 43**

Donor 1	Cleaved caspase-3 p19							GAPDH		Normalized	Compared to respective controls
	Sample	Sum	Area	Average	Median	BC Sum	BC Average	Bkgd Average	BC Average		
Cleaved Caspase -3 p19 24 h	CTRL 1	1,394,502	344	4,053.78	2,766	1,191,060	3,462.38	591.4	2428.1	1.43	1.00
	CTRL 2	1,580,422	344	4,594.25	2,993	1,393,561	4,051.05	543.2	2889.74	1.40	1.00
	CTRL 3	1,527,683	344	4,440.94	3,048	1,354,066	3,936.24	504.7	2222.62	1.77	1.00
	AMPH 1	1,716,566	344	4,990.02	3,482	1,526,196	4,436.62	553.4	2532.13	1.75	1.23
	AMPH 2	1,584,021	344	4,604.71	3,007	1,411,539	4,103.31	501.4	2277.54	1.80	1.29
	AMPH 3	1,260,112	344	3,663.12	2,438	1,083,536	3,149.82	513.3	3251.22	0.97	0.55
Cleaved Caspase -3 p19 36 h	CTRL 1	2516981	451	5580.89	4438	2088305	4630.39	950.5	2,652.15	1.75	1.00
	CTRL 2	2984384	451	6617.26	5802	2652448	5881.26	736	3,165.53	1.86	1.00
	CTRL 3	2140144	451	4745.33	3279	1828412	4054.13	691.2	2,458.39	1.65	1.00
	AMPH 1	3153741	451	6992.77	5323	2727636	6047.97	944.8	2,778.20	2.18	1.25
	AMPH 2	3540812	451	7851.02	6121	2906615	6444.82	1406.2	2,471.62	2.61	1.40
	AMPH 3	3545569	451	7861.57	5887	3120411	6918.87	942.7	3,525.31	1.96	1.19
Cleaved Caspase -3 p19 48 h	CTRL 1	525026	440	1193.24	825	392102	891.14	302.1	2,834.60	0.31	1.00
	CTRL 2	1339741	440	3044.87	2206	1167129	2652.57	392.3	3,121.11	0.85	1.00
	CTRL 3	751594	440	1708.17	1044	623554	1417.17	291	2,695.88	0.53	1.00
	AMPH 1	1593348	440	3621.25	2873	1428875	3247.45	373.8	5,215.95	0.62	1.98
	AMPH 2	1593858	440	3622.4	2932	1438845	3270.1	352.3	2,514.41	1.30	1.53
	AMPH 3	1450206	440	3295.92	2255	1276670	2901.52	394.4	2,092.96	1.39	2.64

**Table A15: Raw data of densitometric quantification of cleaved caspase-3 p17 donor 1 western blots from Fig. 43**

Donor 1	Cleaved caspase-3 p17							GAPDH		Normalized	Compared to respective controls
	Sample	Sum	Area	Average	Median	BC Sum	BC Average	Bkgd Average	BC Average		
Cleaved Caspase -3 p17 24 h	CTRL 1	810,911	344	2,252.53	1,316	656,795	1,824.43	428.1	2428.1	1.43	1.00
	CTRL 2	1,116,532	344	3,101.48	1,708	970,263	2,695.18	406.3	2889.74	1.40	1.00
	CTRL 3	784,736	344	2,179.82	1,326	666,871	1,852.42	327.4	2222.62	1.77	1.00
	AMPH 1	978,679	344	2,718.55	1,712	832,051	2,311.25	407.3	2532.13	1.75	1.21
	AMPH 2	1,084,565	344	3,012.68	1,683	908,273	2,522.98	489.7	2277.54	1.80	1.19
	AMPH 3	759,953	344	2,110.98	1,262	600,652	1,668.48	442.5	3251.22	0.97	0.62
Cleaved Caspase -3 p17 36 h	CTRL 1	1774154	451	4032.17	2342	1495898	3399.77	632.4	2,652.15	1.75	1.00
	CTRL 2	1716045	451	3900.1	2535	1502381	3414.5	485.6	3,165.53	1.86	1.00
	CTRL 3	1315134	451	2988.94	1669	1143534	2598.94	390	2,458.39	1.65	1.00
	AMPH 1	2715894	451	6172.49	3702	2336878	5311.09	861.4	2,778.20	2.18	1.49
	AMPH 2	2561582	451	5821.78	3292	2234750	5078.98	742.8	2,471.62	2.61	1.91
	AMPH 3	2298825	451	5224.6	2902	2013353	4575.8	648.8	3,525.31	1.96	1.23
Cleaved Caspase -3 p17 48 h	CTRL 1	265277	440	602.9	444	160029	363.7	239.2	2,834.60	0.31	1.00
	CTRL 2	742745	440	1688.06	886	622713	1415.26	272.8	3,121.11	0.85	1.00
	CTRL 3	264949	440	602.16	402	171581	389.96	212.2	2,695.88	0.53	1.00
	AMPH 1	1254265	440	2850.6	1482	1118261	2541.5	309.1	5,215.95	0.62	3.80
	AMPH 2	1114816	440	2533.67	1301	978283	2223.37	310.3	2,514.41	1.30	1.95
	AMPH 3	834344	440	1896.24	1059	713564	1621.74	274.5	2,092.96	1.39	5.36

**Table A16: Raw data of densitometric quantification of caspase-3 donor 2 western blots from Fig. 43**

Donor 2	Caspase-3								GAPDH	Normalized	Compared to respective controls
	Sample	Sum	Area	Average	Median	BC Sum	BC Average	Bkgd Average	BC Average		
Caspase-3 24 h	CTRL 1	362,067	576	628.59	590	192,550	334.29	294.3	473.97	0.71	1.00
	CTRL 2	407,093	576	706.76	641	235,272	408.46	298.3	423.78	0.96	1.00
	CTRL 3	496,978	576	862.81	795	296,069	514.01	348.8	529.34	0.97	1.00
	AMPH 1	496,402	576	861.81	745	267,960	465.21	396.6	492.64	0.94	1.34
	AMPH 2	405,599	576	704.16	647	201,522	349.86	354.3	565.64	0.62	0.64
	AMPH 3	340,471	576	591.10	533	143,363	248.90	342.2	472.65	0.53	0.54
Caspase-3 36 h	CTRL 1	278327	370	752.24	747	110347	298.24	454	347.51	0.86	1.00
	CTRL 2	361534	370	977.12	930	120441	325.52	651.6	223.83	1.45	1.00
	CTRL 3	303565	370	820.45	807	91110	246.25	574.2	257.41	0.96	1.00
	AMPH 1	418185	370	1130.23	1109	146159	410.43	729.8	343.94	1.19	1.39
	AMPH 2	398804	370	1077.85	1046	138583	404.16	703.3	366.36	1.10	0.76
	AMPH 3	341660	370	923.41	896	151685	375.91	567.5	319.22	1.18	1.23
Caspase-3 48 h	CTRL 1	74382	442	168.29	156	33055	74.79	93.5	410.53	0.18	1.00
	CTRL 2	80645	442	182.45	162	40334	91.25	91.2	416.01	0.22	1.00
	CTRL 3	69169	442	156.49	150	29256	66.19	90.3	263.53	0.25	1.00
	AMPH 1	104094	442	235.51	179	55164	124.81	110.7	502.90	0.25	1.36
	AMPH 2	120715	442	273.11	196	73200	165.61	107.5	416.56	0.40	1.81
	AMPH 3	116212	442	262.92	194	75282	170.32	92.6	435.41	0.39	1.56

**Table A17: Raw data of densitometric quantification of cleaved caspase-3 p19 donor 2 western blots from Fig. 43**

Donor 2	Cleaved caspase-3 p19						GAPDH		Normalized	Compared to respective controls	
	Sample	Sum	Area	Average	Median	BC Sum	BC Average	Bkgd Average			BC Average
Cleaved Caspase -3 p19 24 h	CTRL 1	63,346	363	174.51	163	30,131	83.01	91.5	1507.71	0.06	1.00
	CTRL 2	102,120	363	281.32	215	61,355	169.02	112.3	1150.37	0.15	1.00
	CTRL 3	90,442	363	249.15	196	52,762	145.35	103.8	1565.36	0.09	1.00
	AMPH 1	101,600	363	279.89	207	60,762	167.39	112.5	1115.7	0.15	2.73
	AMPH 2	84,462	363	232.68	190	46,746	128.78	103.9	1779.33	0.07	0.49
	AMPH 3	100,926	363	278.03	209	63,972	176.23	101.8	1105.21	0.16	1.72
Cleaved Caspase -3 p19 36 h	CTRL 1	109525	492	222.61	190	58307	118.51	104.1	1,004.46	0.12	1.00
	CTRL 2	109095	492	221.74	196	58123	118.14	103.6	847.84	0.14	1.00
	CTRL 3	119660	492	243.21	205	62834	127.71	115.5	730.83	0.17	1.00
	AMPH 1	110593	492	224.78	186	59572	121.08	103.7	846.60	0.14	1.21
	AMPH 2	150378	492	305.65	239	93355	189.75	115.9	724.67	0.26	1.88
	AMPH 3	139909	492	284.37	235	83083	168.87	115.5	724.59	0.23	1.33
Cleaved Caspase -3 p19 48 h	CTRL 1	69052	420	164.41	155	27682	65.91	98.5	1,813.51	0.04	1.00
	CTRL 2	96792	420	230.46	209	51180	121.86	108.6	1,945.43	0.06	1.00
	CTRL 3	74895	420	178.32	165	34995	53.32	95	2,532.36	0.02	1.00
	AMPH 1	107149	420	255.12	243	70445	353.42	111.2	2,933.59	0.12	3.31
	AMPH 2	104723	420	249.34	232	75876	173.04	116.3	2,305.93	0.08	1.20
	AMPH 3	95821	420	228.15	202	56739	136.05	112.1	2,035.43	0.07	3.17

**Table A18: Raw data of densitometric quantification of cleaved caspase-3 p17 donor 2 western blots from Fig. 43**

Donor 2	Cleaved caspase-3 p17							GAPDH		Normalized	Compared to respective controls
	Sample	Sum	Area	Average	Median	BC Sum	BC Average	Bkgd Average	BC Average		
Cleaved Caspase -3 p17 24 h	CTRL 1	810,911	344	2,252.53	1,316	656,795	1,824.43	428.1	2428.1	0.75	1.00
	CTRL 2	1,116,532	344	3,101.48	1,708	970,263	2,695.18	406.3	2889.74	0.93	1.00
	CTRL 3	784,736	344	2,179.82	1,326	666,871	1,852.42	327.4	2222.62	0.83	1.00
	AMPH 1	978,679	344	2,718.55	1,712	832,051	2,311.25	407.3	2532.13	0.91	1.21
	AMPH 2	1,084,565	344	3,012.68	1,683	908,273	2,522.98	489.7	2277.54	1.11	1.19
	AMPH 3	759,953	344	2,110.98	1,262	600,652	1,668.48	442.5	3251.22	0.51	0.62
Cleaved Caspase -3 p17 36 h	CTRL 1	1774154	451	4032.17	2342	1495898	3399.77	632.4	2,652.15	1.28	1.00
	CTRL 2	1716045	451	3900.1	2535	1502381	3414.5	485.6	3,165.53	1.08	1.00
	CTRL 3	1315134	451	2988.94	1669	1143534	2598.94	390	2,458.39	1.06	1.00
	AMPH 1	2715894	451	6172.49	3702	2336878	5311.09	861.4	2,778.20	1.91	1.49
	AMPH 2	2561582	451	5821.78	3292	2234750	5078.98	742.8	2,471.62	2.05	1.91
	AMPH 3	2298825	451	5224.6	2902	2013353	4575.8	648.8	3,525.31	1.30	1.23
Cleaved Caspase -3 p17 48 h	CTRL 1	265277	440	602.9	444	160029	363.7	239.2	2,834.60	0.13	1.00
	CTRL 2	742745	440	1688.06	886	622713	1415.26	272.8	3,121.11	0.45	1.00
	CTRL 3	264949	440	602.16	402	171581	389.96	212.2	2,695.88	0.14	1.00
	AMPH 1	1254265	440	2850.6	1482	1118261	2541.5	309.1	5,215.95	0.49	3.80
	AMPH 2	1114816	440	2533.67	1301	978283	2223.37	310.3	2,514.41	0.88	1.95
	AMPH 3	834344	440	1896.24	1059	713564	1621.74	274.5	2,092.96	0.77	5.36

**Table A19: Raw data of densitometric quantification of caspase-3 donor 3 western blots from Fig. 43**

Donor 3	Caspase-3							GAPDH		Normalized	Compared to respective controls
	Sample	Sum	Area	Average	Median	BC Sum	BC Average	Bkgd Average	BC Average		
Caspase -3 24 h	CTRL 1	259,944	333	780.61	667	125,045	375.51	405.1	7,311.98	0.05	1.00
	CTRL 2	243,919	333	732.49	611	126,503	379.89	352.6	12,538.88	0.03	1.00
	CTRL 3	233,208	333	700.32	602	115,092	345.62	354.7	7,279.69	0.05	1.00
	AMPH 1	344,709	333	1,035.16	866	199,187	598.16	437	13,552.88	0.04	0.86
	AMPH 2	323,254	333	970.73	811	181,562	545.23	425.5	11,804.81	0.05	1.52
	AMPH 3	346,719	333	1,041.20	892	173,359	520.6	520.6	10,143.79	0.05	1.08
Caspase -3 36 h	CTRL 1	398,339	390	1,021.38	862	154,940	397.28	624.1	268.32	1.48	1.00
	CTRL 2	493,718	390	1,265.94	1,056	244,858	627.84	638.1	168.81	3.72	1.00
	CTRL 3	375,213	390	962.08	854	141,759	363.48	598.6	210.42	1.73	1.00
	AMPH 1	462,433	390	1,185.73	977	226,677	581.23	604.5	252.09	2.31	1.56
	AMPH 2	514,790	390	1,319.97	1,024	272,014	697.47	622.5	335.29	2.08	0.56
	AMPH 3	413,156	390	1,059.37	889	203,882	522.77	536.6	309.49	1.69	0.98
Caspase -3 48 h	CTRL 1	435,748	820	531.4	421	203,851	248.6	282.8	1,098.92	0.23	1.00
	CTRL 2	1,073,598	820	1,309.27	795	833,420	1,016.37	292.9	1,095.76	0.93	1.00
	CTRL 3	650,495	820	793.29	606	403,018	491.49	301.8	988.43	0.50	1.00
	AMPH 1	1,149,708	820	1,402.08	1,004	849,752	1,036.28	365.8	1,017.04	1.02	4.50
	AMPH 2	2,032,452	820	2,478.60	1,739	1,722,983	2,101.20	377.4	1,154.37	1.82	1.96
	AMPH 3	2,125,607	820	2,592.20	1,754	1,797,279	2,191.80	400.4	1,463.66	1.50	3.01

**Table A20: Raw data of densitometric quantification of cleaved caspase-3 p19 donor 2 western blots from Fig. 43**

Donor 3	Cleaved caspase-3 p19							GAPDH		Normalized	Compared to respective controls
	Sample	Sum	Area	Average	Median	BC Sum	BC Average	Bkgd Average	BC Average		
Cleaved Caspase -3 p19 24 h	CTRL 1	253,845	989	256.67	236	122,406	123.77	132.9	7,311.98	0.02	1.00
	CTRL 2	284,120	989	287.28	258	141,506	143.08	144.2	12,538.88	0.01	1.00
	CTRL 3	252,622	989	255.43	228	110,799	112.03	143.4	7,279.69	0.02	1.00
	AMPH 1	431,257	989	436.05	389	278,456	281.55	154.5	13,552.88	0.02	1.23
	AMPH 2	326,144	989	329.77	279	176,804	178.77	151	11,804.81	0.02	1.33
	AMPH 3	313,970	989	317.46	256	180,455	182.46	135	10,143.79	0.02	1.17
Cleaved Caspase -3 p19 36 h	CTRL 1	178,561	624	286.16	254	91,388	146.46	139.7	268.32	0.55	1.00
	CTRL 2	265,269	624	425.11	351	156,630	251.01	174.1	168.81	1.49	1.00
	CTRL 3	344,893	624	552.71	502	209,048	335.01	217.7	210.42	1.59	1.00
	AMPH 1	412,964	624	661.8	563	250,100	400.8	261	252.09	1.59	2.91
	AMPH 2	474,177	624	759.9	479	341,202	546.8	213.1	335.29	1.63	1.10
	AMPH 3	343,309	624	550.17	469	165,032	264.47	285.7	309.49	0.85	0.54
Cleaved Caspase -3 p19 48 h	CTRL 1	826,050	800	1,032.56	667	573,890	717.36	315.2	1,098.92	0.65	1.00
	CTRL 2	499,163	800	623.95	446	299,643	374.55	249.4	1,095.76	0.34	1.00
	CTRL 3	597,027	800	746.28	493	404,547	505.68	240.6	988.43	0.51	1.00
	AMPH 1	1,001,677	800	1,252.10	841	774,077	967.6	284.5	1,017.04	0.95	1.46
	AMPH 2	721,284	800	901.61	500	512,324	640.41	261.2	1,154.37	0.55	1.62
	AMPH 3	757,376	800	946.72	532	540,496	675.62	271.1	1,463.66	0.46	0.90

**Table A21: Raw data of densitometric quantification of cleaved caspase-3 p17 donor 3 western blots from Fig. 43**

Donor 3	Cleaved caspase-3 p17							GAPDH		Normalized	Compared to respective controls
	Sample	Sum	Area	Average	Median	BC Sum	BC Average	Bkgd Average	BC Average		
Cleaved Caspase-3 p17 24 h	CTRL 1	171,117	989	173.02	170	70,535	71.32	101.7	693.5594887	0.10	1.00
	CTRL 2	185,972	989	188.04	186	75,995	76.84	111.2	683.4082734	0.11	1.00
	CTRL 3	202,081	989	204.33	198	85,972	86.93	117.4	732.2998296	0.12	1.00
	AMPH 1	263,147	989	266.07	250	138,631	140.17	125.9	1101.119936	0.13	1.24
	AMPH 2	222,455	989	224.93	215	97,346	98.43	126.5	769.5335968	0.13	1.14
	AMPH 3	211,031	989	213.38	190	103,032	104.18	109.2	943.5164835	0.11	0.93
Cleaved Caspase-3 p17 36 h	CTRL 1	183,601	624	294.23	231	95,429	152.93	141.3	675.3644728	0.23	1.00
	CTRL 2	170,928	624	273.92	245	81,196	130.12	143.8	564.6453408	0.23	1.00
	CTRL 3	200,201	624	320.83	288	105,290	168.73	152.1	692.2419461	0.24	1.00
	AMPH 1	291,853	624	467.71	358	168,925	270.71	197	857.4873096	0.32	1.39
	AMPH 2	297,372	624	476.56	333	170,949	273.96	202.6	843.7759131	0.32	1.41
	AMPH 3	168,802	624	270.52	239	71,021	113.82	156.7	453.2291002	0.25	1.03
Cleaved Caspase-3 p17 48 h	CTRL 1	474,687	800	593.36	399	285,807	357.26	236.1	1,098.92	0.33	1.00
	CTRL 2	346,490	800	433.11	333	172,090	215.11	218	1,095.76	0.20	1.00
	CTRL 3	378,372	800	472.97	397	199,891	249.87	223.1	988.43	0.25	1.00
	AMPH 1	526,096	800	657.62	545	323,136	403.92	253.7	1,017.04	0.40	1.22
	AMPH 2	445,651	800	557.06	403	254,291	317.86	239.2	1,154.37	0.28	1.40
	AMPH 3	504,172	800	630.22	453	317,052	396.32	233.9	1,463.66	0.27	1.07



# Creative Commons License De

## Attribution 4.0 International (CC BY 4.0)



This is a human-readable summary of (and not a substitute for) the [license](#).

### You are free to:

**Share** — copy and redistribute the material in any medium or format

**Adapt** — remix, transform, and build upon the material

for any purpose, even commercially.

The licensor cannot revoke these freedoms as long as you follow the license terms.

### Under the following terms:

**Attribution** — You must give appropriate credit, provide a link to the license, and indicate if changes were made. You may do so in any reasonable manner, but not in any way that suggests the licensor endorses you or your use.

**No additional restrictions** — You may not apply legal terms or technological measures that legally restrict others from doing anything the license permits.

### Notices:

You do not have to comply with the license for elements of the material in the public domain or where your use is permitted by an applicable exception or limitation.

No warranties are given. The license may not give you all of the permissions necessary for your intended use. For example, other rights such as publicity, privacy, or moral rights may limit how you use the material.

**SPRINGER NATURE**

**Thank you for your order!**

Dear Mr. Nitish Chaudhari,

Thank you for placing your order through Copyright Clearance Center's RightsLink® service.

**Order Summary**

Licensee: University of Missouri-Kansas City  
Order Date: Jun 21, 2022  
Order Number: 5333650263967  
Publication: Neurochemical Research  
Title: The Crosstalk Between Neurons and Glia in  
Methamphetamine-Induced Neuroinflammation  
Type of Use: Thesis/Dissertation  
Order Total: 0.00 USD

View or print complete [details](#) of your order and the publisher's terms and conditions.

Sincerely,

Copyright Clearance Center

Tel: +1-855-239-3415 / +1-978-646-2777  
[customercare@copyright.com](mailto:customercare@copyright.com)  
<https://myaccount.copyright.com>



**RightsLink**

## REFERENCES

1. Cao, D.N., et al., *Advances and challenges in pharmacotherapeutics for amphetamine-type stimulants addiction*. European Journal of Pharmacology, 2016. **780**: p. 129-135.
2. Rasmussen, N., *Amphetamine-type stimulants: the early history of their medical and non-medical uses*. International Review of Neurobiology, 2015. **120**: p. 9-25.
3. Substance Abuse and Mental Health Services Administration. (2020). *Key substance use and mental health indicators in the United States: Results from the 2019 National Survey on Drug Use and Health (HHS Publication No. PEP20-07-01-001, NSDUH Series H-55)*. Rockville, MD: Center for Behavioral Health Statistics and Quality, Substance Abuse and Mental Health Services Administration. Retrieved from <https://www.samhsa.gov/data/>
4. Han, B., et al., *Methamphetamine use, methamphetamine use disorder, and associated overdose deaths among US adults*. JAMA Psychiatry, 2021. **78**(12): p. 1329-1342.
5. Jones, C.M., W.M. Compton, and D. Mustaquim, *Patterns and characteristics of methamphetamine use among adults—United States, 2015–2018*. Morbidity and Mortality Weekly Report, 2020. **69**(12): p. 317.
6. Blanco, C. and N.D. Volkow, *Management of opioid use disorder in the USA: present status and future directions*. The Lancet, 2019. **393**(10182): p. 1760-1772.
7. Gouzoulis-Mayfrank, E., et al., *Methamphetamine-related disorders*. Deutsches Ärzteblatt International, 2017. **114**(26): p. 455.
8. Hart, C.L., et al., *Acute physiological and behavioral effects of intranasal methamphetamine in humans*. Neuropsychopharmacology, 2008. **33**(8): p. 1847-1855.

9. McKetin, R., et al., *The profile of psychiatric symptoms exacerbated by methamphetamine use*. Drug and Alcohol Dependence, 2016. **161**: p. 104-109.
10. Wang, Z., W.-x. Li, and L. Zhi-Min, *Similarity and difference in drug addiction process between heroin-and methamphetamine-dependent users*. Substance Use & Misuse, 2017. **52**(4): p. 459-467.
11. Grant, K.M., et al., *Methamphetamine-associated psychosis*. Journal of Neuroimmune Pharmacology, 2012. **7**(1): p. 113-139.
12. Lecomte, T., et al., *The prevalence of substance-induced psychotic disorder in methamphetamine misusers: a meta-analysis*. Psychiatry Research, 2018. **268**: p. 189-192.
13. Lappin, J.M., et al., *Increased prevalence of self-reported psychotic illness predicted by crystal methamphetamine use: evidence from a high-risk population*. International Journal of Drug Policy, 2016. **38**: p. 16-20.
14. Salo, R., et al., *Psychiatric comorbidity in methamphetamine dependence*. Psychiatry Research, 2011. **186**(2-3): p. 356-361.
15. Simpson, J.L., et al., *Psychological burden and gender differences in methamphetamine-dependent individuals in treatment*. Journal of Psychoactive Drugs, 2016. **48**(4): p. 261-269.
16. Akindipe, T., D. Wilson, and D.J. Stein, *Psychiatric disorders in individuals with methamphetamine dependence: prevalence and risk factors*. Metabolic Brain Disease, 2014. **29**(2): p. 351-357.

17. Svingen, L., et al., *Associations between family history of substance use, childhood trauma, and age of first drug use in persons with methamphetamine dependence*. *Journal of Addiction Medicine*, 2016. **10**(4): p. 269-273.
18. McKetin, R., et al., *Predicting abstinence from methamphetamine use after residential rehabilitation: Findings from the Methamphetamine Treatment Evaluation Study*. *Drug and Alcohol Review*, 2018. **37**(1): p. 70-78.
19. Huang, M.-C., et al., *Risk of cardiovascular diseases and stroke events in methamphetamine users: a 10-year follow-up study*. *The Journal of Clinical Psychiatry*, 2016. **77**(10): p. 11856.
20. Lappin, J.M., S. Darke, and M. Farrell, *Stroke and methamphetamine use in young adults: a review*. *Journal of Neurology, Neurosurgery & Psychiatry*, 2017. **88**(12): p. 1079-1091.
21. Kevil, C.G., et al., *Methamphetamine use and cardiovascular disease: in search of answers*. *Arteriosclerosis, Thrombosis, and Vascular Biology*, 2019. **39**(9): p. 1739-1746.
22. Reddy, P.K., et al., *Clinical Characteristics and Management of Methamphetamine-Associated Cardiomyopathy: State-of-the-Art Review*. *Journal of the American Heart Association*, 2020. **9**(11): p. e016704.
23. Paratz, E.D., et al., *Is an abnormal ECG just the tip of the ICE-berg? Examining the utility of electrocardiography in detecting methamphetamine-induced cardiac pathology*. *Heart, Lung and Circulation*, 2017. **26**(7): p. 684-689.
24. Darke, S., et al., *Clinical and autopsy characteristics of fatal methamphetamine toxicity in Australia*. *Journal of Forensic Sciences*, 2018. **63**(5): p. 1466-1471.

25. Gladden, R.M., et al., *Changes in opioid-involved overdose deaths by opioid type and presence of benzodiazepines, cocaine, and methamphetamine—25 states, July–December 2017 to January–June 2018*. Morbidity and Mortality Weekly Report, 2019. **68**(34): p. 737.
26. Moszczynska, A. and S.P. Callan, *Molecular, behavioral, and physiological consequences of methamphetamine neurotoxicity: implications for treatment*. Journal of Pharmacology and Experimental Therapeutics, 2017. **362**(3): p. 474-488.
27. Yang, X., et al., *The main molecular mechanisms underlying methamphetamine-induced neurotoxicity and implications for pharmacological treatment*. Frontiers in Molecular Neuroscience, 2018. **11**: p. 186.
28. Yamamoto, B.K. and W. Zhu, *The effects of methamphetamine on the production of free radicals and oxidative stress*. Journal of Pharmacology and Experimental Therapeutics, 1998. **287**(1): p. 107-114.
29. Nordahl, T.E., R. Salo, and M. Leamon, *Neuropsychological effects of chronic methamphetamine use on neurotransmitters and cognition: a review*. The Journal of Neuropsychiatry and Clinical Neurosciences, 2003. **15**(3): p. 317-325.
30. Shin, E.-J., et al., *Role of mitochondria in methamphetamine-induced dopaminergic neurotoxicity: involvement in oxidative stress, neuroinflammation, and pro-apoptosis— a review*. Neurochemical Research, 2018. **43**(1): p. 66-78.
31. Baumann, M.H., et al., *Persistent antagonism of methamphetamine-induced dopamine release in rats pretreated with GBR12909 decanoate*. Journal of Pharmacology and Experimental Therapeutics, 2002. **301**(3): p. 1190-1197.

32. LaVoie, M.J. and T.G. Hastings, *Dopamine quinone formation and protein modification associated with the striatal neurotoxicity of methamphetamine: evidence against a role for extracellular dopamine*. Journal of Neuroscience, 1999. **19**(4): p. 1484-1491.
33. Cadet, J.L. and C. Brannock, *Invited review free radicals and the pathobiology of brain dopamine systems*. Neurochemistry International, 1998. **32**(2): p. 117-131.
34. Dawson, T.M. and V.L. Dawson, *Mitochondrial mechanisms of neuronal cell death: potential therapeutics*. Annual Review of Pharmacology And Toxicology, 2017. **57**: p. 437-454.
35. Burrows, K.B., G. Gudelsky, and B.K. Yamamoto, *Rapid and transient inhibition of mitochondrial function following methamphetamine or 3, 4-methylenedioxymethamphetamine administration*. European Journal of Pharmacology, 2000. **398**(1): p. 11-18.
36. Brown, J.M., M.S. Quinton, and B.K. Yamamoto, *Methamphetamine-induced inhibition of mitochondrial complex II: roles of glutamate and peroxynitrite*. Journal of Neurochemistry, 2005. **95**(2): p. 429-436.
37. Bachmann, R.F., et al., *Common effects of lithium and valproate on mitochondrial functions: protection against methamphetamine-induced mitochondrial damage*. International Journal of Neuropsychopharmacology, 2009. **12**(6): p. 805-822.
38. Thrash-Williams, B., et al., *Methamphetamine-induced dopaminergic toxicity prevented owing to the neuroprotective effects of salicylic acid*. Life Sciences, 2016. **154**: p. 24-29.
39. Nguyen, X.K.T., et al., *Liposomal melatonin rescues methamphetamine-elicited mitochondrial burdens, pro-apoptosis, and dopaminergic degeneration through the inhibition PKC $\delta$  gene*. Journal of Pineal Research, 2015. **58**(1): p. 86-106.

40. Shin, E.-J., et al., *Current understanding of methamphetamine-associated dopaminergic neurodegeneration and psychotoxic behaviors*. Archives of Pharmacal Research, 2017. **40**(4): p. 403-428.
41. JAYANTHI, S., et al., *Methamphetamine causes differential regulation of pro-death and anti-death Bcl-2 genes in the mouse neocortex*. The FASEB Journal, 2001. **15**(10): p. 1745-1752.
42. Beauvais, G., et al., *Involvement of dopamine receptors in binge methamphetamine-induced activation of endoplasmic reticulum and mitochondrial stress pathways*. PloS One, 2011. **6**(12): p. e28946.
43. Raineri, M., et al., *Modafinil abrogates methamphetamine-induced neuroinflammation and apoptotic effects in the mouse striatum*. 2012. **7**(10): e46599
44. Qiao, D., et al., *Insulin-like growth factor binding protein 5 (IGFBP5) mediates methamphetamine-induced dopaminergic neuron apoptosis*. Toxicology Letters, 2014. **230**(3): p. 444-453.
45. Nam, Y., et al., *Ginsenoside Re protects methamphetamine-induced mitochondrial burdens and proapoptosis via genetic inhibition of protein kinase C  $\delta$  in human neuroblastoma dopaminergic SH-SY5Y cell lines*. Journal of Applied Toxicology, 2015. **35**(8): p. 927-944.
46. Lin, M., et al., *Methamphetamine-induced neurotoxicity linked to ubiquitin-proteasome system dysfunction and autophagy-related changes that can be modulated by protein kinase C delta in dopaminergic neuronal cells*. Neuroscience, 2012. **210**: p. 308-332.

47. Shin, E.-J., et al., *PKC $\delta$  knockout mice are protected from para-methoxymethamphetamine-induced mitochondrial stress and associated neurotoxicity in the striatum of mice*. *Neurochemistry International*, 2016. **100**: p. 146-158.
48. Chen, C., et al., *Role of PUMA in methamphetamine-induced neuronal apoptosis*. *Toxicology Letters*, 2016. **240**(1): p. 149-160.
49. Zhang, Y., et al., *Mir143-BBC3 cascade reduces microglial survival via interplay between apoptosis and autophagy: implications for methamphetamine-mediated neurotoxicity*. *Autophagy*, 2016. **12**(9): p. 1538-1559.
50. Chamorro, Á., et al., *Neuroprotection in acute stroke: targeting excitotoxicity, oxidative and nitrosative stress, and inflammation*. *The Lancet Neurology*, 2016. **15**(8): p. 869-881.
51. Tseng, E.E., et al., *Glutamate excitotoxicity mediates neuronal apoptosis after hypothermic circulatory arrest*. *The Annals of Thoracic Surgery*, 2010. **89**(2): p. 440-445.
52. Bahar, E., H. Kim, and H. Yoon, *ER stress-mediated signaling: Action potential and Ca<sup>2+</sup> as key players*. *International Journal of Molecular Sciences*, 2016. **17**(9): p. 1558.
53. Moratalla, R., et al., *Amphetamine-related drugs neurotoxicity in humans and in experimental animals: Main mechanisms*. *Progress in Neurobiology*, 2017. **155**: p. 149-170.
54. Szegezdi, E., et al., *Mediators of endoplasmic reticulum stress-induced apoptosis*. *EMBO Reports*, 2006. **7**(9): p. 880-885.
55. Hetz, C., *The unfolded protein response: controlling cell fate decisions under ER stress and beyond*. *Nature Reviews Molecular Cell Biology*, 2012. **13**(2): p. 89-102.

56. Wongprayoon, P. and P. Govitrapong, *Melatonin protects SH-SY5Y neuronal cells against methamphetamine-induced endoplasmic reticulum stress and apoptotic cell death*. Neurotoxicity Research, 2017. **31**(1): p. 1-10.
57. Sano, R. and J.C. Reed, *ER stress-induced cell death mechanisms*. Biochimica et Biophysica Acta (BBA)-Molecular Cell Research, 2013. **1833**(12): p. 3460-3470.
58. Jayanthi, S., et al., *Methamphetamine induces neuronal apoptosis via cross-talks between endoplasmic reticulum and mitochondria-dependent death cascades*. The FASEB Journal, 2004. **18**(2): p. 238-251.
59. Xu, X., et al., *Nupr1 modulates methamphetamine-induced dopaminergic neuronal apoptosis and autophagy through CHOP-Trib3-mediated endoplasmic reticulum stress signaling pathway*. Frontiers in Molecular Neuroscience, 2017. **10**: p. 203.
60. Xu, E., et al., *Role of microglia in methamphetamine-induced neurotoxicity*. International Journal of Physiology, Pathophysiology and Pharmacology, 2017. **9**(3): p. 84.
61. Thomas, D.M., D.M. Francescutti-Verbeem, and D.M. Kuhn, *The newly synthesized pool of dopamine determines the severity of methamphetamine-induced neurotoxicity*. Journal of Neurochemistry, 2008. **105**(3): p. 605-616.
62. Chao, J., et al., *Molecular mechanisms underlying the involvement of the sigma-1 receptor in methamphetamine-mediated microglial polarization*. Scientific Reports, 2017. **7**(1): p. 1-13.
63. Ojaniemi, M., et al., *Phosphatidylinositol 3-kinase is involved in Toll-like receptor 4-mediated cytokine expression in mouse macrophages*. European Journal of Immunology, 2003. **33**(3): p. 597-605.

64. Tocharus, J., et al., *Melatonin attenuates methamphetamine-induced overexpression of pro-inflammatory cytokines in microglial cell lines*. Journal of Pineal Research, 2010. **48**(4): p. 347-352.
65. Coelho-Santos, V., et al., *Prevention of methamphetamine-induced microglial cell death by TNF- $\alpha$  and IL-6 through activation of the JAK-STAT pathway*. Journal of Neuroinflammation, 2012. **9**(1): p. 1-14.
66. Robson, M.J., et al., *SN79, a sigma receptor ligand, blocks methamphetamine-induced microglial activation and cytokine upregulation*. Experimental Neurology, 2013. **247**: p. 134-142.
67. Shi, S., T. Chen, and M. Zhao, *The Crosstalk Between Neurons and Glia in Methamphetamine-Induced Neuroinflammation*. Neurochemical Research, 2022: p. 1-13.
68. Sofroniew, M.V. and H.V. Vinters, *Astrocytes: biology and pathology*. Acta Neuropathologica, 2010. **119**(1): p. 7-35.
69. Clarke, L.E. and B.A. Barres, *Emerging roles of astrocytes in neural circuit development*. Nature Reviews Neuroscience, 2013. **14**(5): p. 311-321.
70. Bernardinelli, Y., et al., *Activity-dependent structural plasticity of perisynaptic astrocytic domains promotes excitatory synapse stability*. Current Biology, 2014. **24**(15): p. 1679-1688.
71. Haydon, P.G. and G. Carmignoto, *Astrocyte control of synaptic transmission and neurovascular coupling*. Physiological Reviews, 2006. **86**(3): p. 1009-1031.
72. Bezzi, P. and A. Volterra, *A neuron–glia signalling network in the active brain*. Current Opinion in Neurobiology, 2001. **11**(3): p. 387-394.

73. Araque, A., et al., *Gliotransmitters travel in time and space*. *Neuron*, 2014. **81**(4): p. 728-739.
74. Narita, M., et al., *Implication of activated astrocytes in the development of drug dependence: differences between methamphetamine and morphine*. *Annals of the New York Academy of Sciences*, 2008. **1141**(1): p. 96-104.
75. Hess, A., C. Desiderio, and W. McAuliffe, *Acute neuropathological changes in the caudate nucleus caused by MPTP and methamphetamine: immunohistochemical studies*. *Journal of Neurocytology*, 1990. **19**(3): p. 338-342.
76. Broening, H.W., C. Pu, and C.V. Vorhees, *Methamphetamine selectively damages dopaminergic innervation to the nucleus accumbens core while sparing the shell*. *Synapse*, 1997. **27**(2): p. 153-160.
77. De Vito, M.J. and G. Wagner, *Methamphetamine-induced neuronal damage: a possible role for free radicals*. *Neuropharmacology*, 1989. **28**(10): p. 1145-1150.
78. Pu, C. and C.V. Vorhees, *Developmental dissociation of methamphetamine-induced depletion of dopaminergic terminals and astrocyte reaction in rat striatum*. *Developmental Brain Research*, 1993. **72**(2): p. 325-328.
79. Lau, J.W., S. Senok, and A. Stadlin, *Methamphetamine-induced oxidative stress in cultured mouse astrocytes*. *Annals of the New York Academy of Sciences*, 2000. **914**(1): p. 146-156.
80. Bortell, N., et al., *Astrocyte-specific overexpressed gene signatures in response to methamphetamine exposure in vitro*. *Journal of Neuroinflammation*, 2017. **14**(1): p. 1-20.

81. Chen, X., et al., *Astrocyte-derived lipocalin-2 is involved in mitochondrion-related neuronal apoptosis induced by methamphetamine*. ACS Chemical Neuroscience, 2020. **11**(8): p. 1102-1116.
82. Yu, C., et al., *HIV and drug abuse mediate astrocyte senescence in a  $\beta$ -catenin-dependent manner leading to neuronal toxicity*. Aging Cell, 2017. **16**(5): p. 956-965.
83. Eddleston, M. and L. Mucke, *Molecular profile of reactive astrocytes—implications for their role in neurologic disease*. Neuroscience, 1993. **54**(1): p. 15-36.
84. Lin, J.H., et al., *Gap-junction-mediated propagation and amplification of cell injury*. Nature Neuroscience, 1998. **1**(6): p. 494-500.
85. Hynes, R.O., *Integrins: bidirectional, allosteric signaling machines*. Cell, 2002. **110**(6): p. 673-687.
86. Barczyk, M., S. Carracedo, and D. Gullberg, *Integrins*. Cell and Tissue Research, 2010. **339**(1): p. 269-280.
87. Giancotti, F.G., *Integrin signaling: specificity and control of cell survival and cell cycle progression*. Current Opinion in Cell Biology, 1997. **9**(5): p. 691-700.
88. Calderwood, D.A., *Integrin activation*. Journal of Cell Science, 2004. **117**(5): p. 657-666.
89. Stupack, D.G. and D.A. Cheresh, *Get a ligand, get a life: integrins, signaling and cell survival*. Journal of Cell Science, 2002. **115**(19): p. 3729-3738.
90. Rupp, P.A. and C.D. Little, *Integrins in vascular development*. Circulation research, 2001. **89**(7): p. 566-572.
91. Watt, F.M., *Role of integrins in regulating epidermal adhesion, growth and differentiation*. The EMBO Journal, 2002. **21**(15): p. 3919-3926.

92. Tanigami, H., et al., *Astroglial integrins in the development and regulation of neurovascular units*. Pain Research and Treatment, 2012. **2012**.
93. Campbell, I.D. and M.J. Humphries, *Integrin structure, activation, and interactions*. Cold Spring Harbor Perspectives in Biology, 2011. **3**(3): p. a004994.
94. Wegener, K.L., et al., *Structural basis of integrin activation by talin*. Cell, 2007. **128**(1): p. 171-182.
95. Luo, B.-H., C.V. Carman, and T.A. Springer, *Structural basis of integrin regulation and signaling*. Annual Review of Immunology, 2007. **25**: p. 619.
96. Askari, J.A., et al., *Linking integrin conformation to function*. Journal of Cell Science, 2009. **122**(2): p. 165-170.
97. Xiao, T., et al., *Structural basis for allostery in integrins and binding to fibrinogen-mimetic therapeutics*. Nature, 2004. **432**(7013): p. 59-67.
98. Clegg, D.O., et al., *Integrins in the development, function and dysfunction of the nervous system*. Frontiers in Bioscience: A Journal and Virtual Library, 2003. **8**(4): p. d723-d750.
99. Eroglu, C. and B.A. Barres, *Regulation of synaptic connectivity by glia*. Nature, 2010. **468**(7321): p. 223-231.
100. Staubli, U., P. Vanderklish, and G. Lynch, *An inhibitor of integrin receptors blocks long-term potentiation*. Behavioral and Neural Biology, 1990. **53**(1): p. 1-5.
101. Bahr, B.A., et al., *Arg-Gly-Asp-Ser-selective adhesion and the stabilization of long-term potentiation: pharmacological studies and the characterization of a candidate matrix receptor*. Journal of Neuroscience, 1997. **17**(4): p. 1320-1329.
102. Chan, C.-S., et al., *Integrin requirement for hippocampal synaptic plasticity and spatial memory*. Journal of Neuroscience, 2003. **23**(18): p. 7107-7116.

103. Kramar, E., et al., *Alpha3 integrin receptors contribute to the consolidation of long-term potentiation*. Neuroscience, 2002. **110**(1): p. 29-39.
104. Huang, Z., et al., *Distinct roles of the  $\beta 1$ -class integrins at the developing and the mature hippocampal excitatory synapse*. Journal of Neuroscience, 2006. **26**(43): p. 11208-11219.
105. Chan, C.-S., et al.,  *$\beta 1$ -integrins are required for hippocampal AMPA receptor-dependent synaptic transmission, synaptic plasticity, and working memory*. Journal of Neuroscience, 2006. **26**(1): p. 223-232.
106. Chan, C.-S., et al.,  *$\alpha 3$ -integrins are required for hippocampal long-term potentiation and working memory*. Learning & Memory, 2007. **14**(9): p. 606-615.
107. Christopherson, K.S., et al., *Thrombospondins are astrocyte-secreted proteins that promote CNS synaptogenesis*. Cell, 2005. **120**(3): p. 421-433.
108. Barker, A.J., et al., *Developmental control of synaptic receptivity*. Journal of Neuroscience, 2008. **28**(33): p. 8150-8160.
109. Hermosilla, T., et al., *Direct Thy-1/ $\alpha V\beta 3$  integrin interaction mediates neuron to astrocyte communication*. Biochimica et Biophysica Acta (BBA)-Molecular Cell Research, 2008. **1783**(6): p. 1111-1120.
110. Herrera-Molina, R., et al., *Astrocytic  $\alpha V\beta 3$  integrin inhibits neurite outgrowth and promotes retraction of neuronal processes by clustering Thy-1*. PLoS One, 2012. **7**(3): p. e34295.
111. Hama, H., et al., *PKC signaling mediates global enhancement of excitatory synaptogenesis in neurons triggered by local contact with astrocytes*. Neuron, 2004. **41**(3): p. 405-415.

112. Choi, S.S., et al., *Human astrocytes: secretome profiles of cytokines and chemokines*. PloS One, 2014. **9**(4): p. e92325.
113. Siracusa, R., R. Fusco, and S. Cuzzocrea, *Astrocytes: role and functions in brain pathologies*. Frontiers in Pharmacology, 2019: p. 1114.
114. Ogier, C., et al., *Matrix metalloproteinase-2 (MMP-2) regulates astrocyte motility in connection with the actin cytoskeleton and integrins*. Glia, 2006. **54**(4): p. 272-284.
115. Zhang, J. and Y. De Koninck, *Spatial and temporal relationship between monocyte chemoattractant protein-1 expression and spinal glial activation following peripheral nerve injury*. Journal of Neurochemistry, 2006. **97**(3): p. 772-783.
116. Renault-Mihara, F., et al., *Beneficial compaction of spinal cord lesion by migrating astrocytes through glycogen synthase kinase-3 inhibition*. EMBO Molecular Medicine, 2011. **3**(11): p. 682-696.
117. Robel, S., et al., *Conditional deletion of  $\beta$ 1-integrin in astroglia causes partial reactive gliosis*. Glia, 2009. **57**(15): p. 1630-1647.
118. Afshari, F.T., et al., *Schwann cell migration is integrin-dependent and inhibited by astrocyte-produced aggrecan*. Glia, 2010. **58**(7): p. 857-869.
119. Feltri, M.L., et al., *Conditional disruption of  $\beta$ 1 integrin in Schwann cells impedes interactions with axons*. The Journal of Cell Biology, 2002. **156**(1): p. 199-210.
120. Van der Zee, C.E., et al., *Conditional deletion of the *Itgb4* integrin gene in Schwann cells leads to delayed peripheral nerve regeneration*. Journal of Neuroscience, 2008. **28**(44): p. 11292-11303.

121. Johnson, R.L., et al., *Sonic hedgehog: a key mediator of anterior-posterior patterning of the limb and dorso-ventral patterning of axial embryonic structures*. Biochemical Society Transactions, 1994. **22**(3): p. 569-574.
122. Spörle, R. and K. Schughart, *Neural tube morphogenesis*. Current Opinion in Genetics & Development, 1997. **7**(4): p. 507-512.
123. Fournier-Thibault, C., et al., *Sonic hedgehog regulates integrin activity, cadherin contacts, and cell polarity to orchestrate neural tube morphogenesis*. Journal of Neuroscience, 2009. **29**(40): p. 12506-12520.
124. Alvarez, J.I., et al., *The Hedgehog pathway promotes blood-brain barrier integrity and CNS immune quiescence*. Science, 2011. **334**(6063): p. 1727-1731.
125. Singhvi, R., et al., *Engineering cell shape and function*. Science, 1994. **264**(5159): p. 696-698.
126. Frisch, S.M. and E. Ruoslahti, *Integrins and anoikis*. Current Opinion in Cell Biology, 1997. **9**(5): p. 701-706.
127. Frisch, S.M. and H. Francis, *Disruption of epithelial cell-matrix interactions induces apoptosis*. The Journal of Cell Biology, 1994. **124**(4): p. 619-626.
128. Meredith Jr, J., B. Fazeli, and M. Schwartz, *The extracellular matrix as a cell survival factor*. Molecular Biology of the Cell, 1993. **4**(9): p. 953-961.
129. Schlaepfer, D.D., S.K. Mitra, and D. Ilic, *Control of motile and invasive cell phenotypes by focal adhesion kinase*. Biochimica et Biophysica Acta (BBA)-Molecular Cell Research, 2004. **1692**(2-3): p. 77-102.
130. DeMali, K.A., K. Wennerberg, and K. Burridge, *Integrin signaling to the actin cytoskeleton*. Current Opinion in Cell Biology, 2003. **15**(5): p. 572-582.

131. Kornberg, L., et al., *Cell adhesion or integrin clustering increases phosphorylation of a focal adhesion-associated tyrosine kinase*. Journal of Biological Chemistry, 1992. **267**(33): p. 23439-23442.
132. Giancotti, F.G. and E. Ruoslahti, *Integrin signaling*. Science, 1999. **285**(5430): p. 1028-1033.
133. Schlaepfer, D.D., et al., *Integrin-mediated signal transduction linked to Ras pathway by GRB2 binding to focal adhesion kinase*. Nature, 1994. **372**(6508): p. 786-791.
134. Aplin, A.E., et al., *Integrin-mediated adhesion regulates ERK nuclear translocation and phosphorylation of Elk-1*. The Journal of Cell Biology, 2001. **153**(2): p. 273-282.
135. Strömblad, S., et al., *Suppression of p53 activity and p21WAF1/CIP1 expression by vascular cell integrin  $\alpha$ V $\beta$ 3 during angiogenesis*. The Journal of Clinical Investigation, 1996. **98**(2): p. 426-433.
136. Zhang, Z., et al., *The  $\alpha$ 5  $\beta$ 1 integrin supports survival of cells on fibronectin and up-regulates Bcl-2 expression*. Proceedings of the National Academy of Sciences, 1995. **92**(13): p. 6161-6165.
137. Aoudjit, F. and K. Vuori, *Engagement of the  $\alpha$ 2 $\beta$ 1 integrin inhibits Fas ligand expression and activation-induced cell death in T cells in a focal adhesion kinase-dependent manner*. Blood, The Journal of the American Society of Hematology, 2000. **95**(6): p. 2044-2051.
138. Matter, M.L. and E. Ruoslahti, *A signaling pathway from the  $\alpha$ 5 $\beta$ 1 and  $\alpha$ v $\beta$ 3 integrins that elevates bcl-2 transcription*. Journal of Biological Chemistry, 2001. **276**(30): p. 27757-27763.

139. Weintraub, A.S., et al., *Osteopontin deficiency in rat vascular smooth muscle cells is associated with an inability to adhere to collagen and increased apoptosis*. Laboratory Investigation, 2000. **80**(11): p. 1603-1615.
140. Malyankar, U.M., et al., *Osteoprotegerin is an  $\alpha\beta3$ -induced, NF- $\kappa$ B-dependent survival factor for endothelial cells*. Journal of Biological Chemistry, 2000. **275**(28): p. 20959-20962.
141. Buda, A., et al., *Butyrate downregulates  $\alpha2\beta1$  integrin: a possible role in the induction of apoptosis in colorectal cancer cell lines*. Gut, 2003. **52**(5): p. 729-734.
142. Leu, S.T., et al., *Integrin  $\alpha4\beta1$  function is required for cell survival in developing retina*. Developmental Biology, 2004. **276**(2): p. 416-430.
143. Gibson, R.M., et al., *Activation of integrin  $\alpha5\beta1$  delays apoptosis of Ntera2 neuronal cells*. Molecular and Cellular Neuroscience, 2005. **28**(3): p. 588-598.
144. Zahir, N., et al., *Autocrine laminin-5 ligates  $\alpha6\beta4$  integrin and activates RAC and NF $\kappa$ B to mediate anchorage-independent survival of mammary tumors*. The Journal of cell Biology, 2003. **163**(6): p. 1397-1407.
145. Maubant, S., et al., *Blockade of  $\alpha\beta3$  and  $\alpha\beta5$  integrins by RGD mimetics induces anoikis and not integrin-mediated death in human endothelial cells*. Blood, 2006. **108**(9): p. 3035-3044.
146. Bonfoco, E., et al.,  *$\beta1$  integrin antagonism on adherent, differentiated human neuroblastoma cells triggers an apoptotic signaling pathway*. Neuroscience, 2000. **101**(4): p. 1145-1152.

147. Bhattacharya, S., R.M. Ray, and L.R. Johnson, *Integrin  $\beta$ 3-mediated Src activation regulates apoptosis in IEC-6 cells via Akt and STAT3*. *Biochemical Journal*, 2006. **397**(3): p. 437-447.
148. Vachon, P.H., *Integrin signaling, cell survival, and anoikis: distinctions, differences, and differentiation*. *Journal of Signal Transduction*, 2011. **2011**.
149. UNODC, *World drug report*. United Nations New York, NY, 2021.
150. Oberheim, N.A., et al., *Astrocytic complexity distinguishes the human brain*. *Trends in Neurosciences*, 2006. **29**(10): p. 547-553.
151. Vasile, F., E. Dossi, and N. Rouach, *Human astrocytes: structure and functions in the healthy brain*. *Brain Structure and Function*, 2017. **222**(5).
152. Phatnani, H. and T. Maniatis, *Astrocytes in neurodegenerative disease*. *Cold Spring Harbor perspectives in Biology*, 2015. **7**(6): p. a020628.
153. Siracusa, R., R. Fusco, and S. Cuzzocrea, *Astrocytes: role and functions in brain pathologies*. *Frontiers in Pharmacology*, 2019. **10**: p. 1114.
154. Herland, A., et al., *Proteomic and metabolomic characterization of human neurovascular unit cells in response to methamphetamine*. *Advanced Biosystems*, 2020. **4**(9): p. 1900230.
155. Shlens, J., *A tutorial on principal component analysis*. arXiv preprint arXiv:1404.1100, 2014.
156. Lim, W.K., et al., *Comparative analysis of microarray normalization procedures: effects on reverse engineering gene networks*. *Bioinformatics*, 2007. **23**(13): p. i282-i288.
157. Draghici, S., et al., *A systems biology approach for pathway level analysis*. *Genome Research*, 2007. **17**(10): p. 1537-1545.

158. Tarca, A.L., et al., *A Novel Signaling Pathway Impact Analysis (SPIA)*. *Bioinformatics*, 2009. **25**(1): p. 75-82.
159. Khatri, P., et al. *A System Biology Approach for the Steady-State Analysis of Gene Signaling Networks*. In: Rueda, L., Mery, D., Kittler, J. (eds) *Progress in Pattern Recognition, Image Analysis and Applications*. CIARP 2007. Lecture Notes in Computer Science, vol 4756. Springer, Berlin, Heidelberg.
160. Kanehisa, M., et al., *KEGG for integration and interpretation of large-scale molecular data sets*. *Nucleic Acids Research*, 2012. **40**(D1): p. D109-D114.
161. Draghici, S., et al., *Onto-tools, the toolkit of the modern biologist: onto-express, onto-compare, onto-design and onto-translate*. *Nucleic Acids Research*, 2003. **31**(13): p. 3775-3781.
162. Ashburner, M. and S. Lewis. *On ontologies for biologists: The Gene Ontology—Untangling the web*. in *'In Silico' Simulation of Biological Processes: Novartis Foundation Symposium 2002*; **247**:66-80; discussion 80-3, 84-90, 244-52. Wiley Online Library.
163. Albanese, C., et al., *Transforming p21ras Mutants and c-Ets-2 Activate the Cyclin D1 Promoter through Distinguishable Regions (\*)*. *Journal of Biological Chemistry*, 1995. **270**(40): p. 23589-23597.
164. Topacio, B.R., et al., *Cyclin D-Cdk4, 6 drives cell-cycle progression via the retinoblastoma protein's C-terminal helix*. *Molecular Cell*, 2019. **74**(4): p. 758-770. e4.
165. Patil, M., N. Pabla, and Z. Dong, *Checkpoint kinase 1 in DNA damage response and cell cycle regulation*. *Cellular and Molecular Life Sciences*, 2013. **70**(21): p. 4009-4021.

166. Zhang, Y. and T. Hunter, *Roles of Chk1 in cell biology and cancer therapy*. International Journal of Cancer, 2014. **134**(5): p. 1013-1023.
167. Jares, P., A. Donaldson, and J.J. Blow, *The Cdc7/Dbf4 protein kinase: target of the S phase checkpoint?* EMBO Reports, 2000. **1**(4): p. 319-322.
168. Owens, J.C., C.S. Detweiler, and J.J. Li, *CDC45 is required in conjunction with CDC7/DBF4 to trigger the initiation of DNA replication*. Proceedings of the National Academy of Sciences, 1997. **94**(23): p. 12521-12526.
169. Sur, S. and D.K. Agrawal, *Phosphatases and kinases regulating CDC25 activity in the cell cycle: clinical implications of CDC25 overexpression and potential treatment strategies*. Molecular and Cellular Biochemistry, 2016. **416**(1): p. 33-46.
170. Bai, C., et al., *SKP1 connects cell cycle regulators to the ubiquitin proteolysis machinery through a novel motif, the F-box*. Cell, 1996. **86**(2): p. 263-274.
171. Carrano, A.C., et al., *SKP2 is required for ubiquitin-mediated degradation of the CDK inhibitor p27*. Nature Cell Biology, 1999. **1**(4): p. 193-199.
172. Porter, L.A. and D.J. Donoghue, *Cyclin B1 and CDK1: nuclear localization and upstream regulators*. Progress in Cell Cycle Research, 2003. **5**: p. 335-348.
173. Scholey, J.M., I. Brust-Mascher, and A. Mogilner, *Cell division*. Nature, 2003. **422**(6933): p. 746-752.
174. Santaguida, S. and A. Musacchio, *The life and miracles of kinetochores*. The EMBO Journal, 2009. **28**(17): p. 2511-2531.
175. Huang, X., et al., *Securin and separase phosphorylation act redundantly to maintain sister chromatid cohesion in mammalian cells*. Molecular Biology of the Cell, 2005. **16**(10): p. 4725-4732.

176. Zwain, I.H. and S.S. Yen, *Neurosteroidogenesis in astrocytes, oligodendrocytes, and neurons of cerebral cortex of rat brain*. *Endocrinology*, 1999. **140**(8): p. 3843-3852.
177. Tsutsui, K., *Biosynthesis and biological actions of neurosteroids in brain neurons*. *Zoological Science*, 2001. **18**(8): p. 1043-1053.
178. Dluzen, D.E. and J.L. McDermott, *Estrogen, testosterone, and methamphetamine toxicity*. *Annals of the New York Academy of Sciences*, 2006. **1074**(1): p. 282-294.
179. Turchan, J., et al., *Estrogen protects against the synergistic toxicity by HIV proteins, methamphetamine and cocaine*. *BMC Neuroscience*, 2001. **2**(1): p. 1-11.
180. Ghazvini, H., et al., *Effects of treatment with estrogen and progesterone on the methamphetamine-induced cognitive impairment in ovariectomized rats*. *Neuroscience Letters*, 2016. **619**: p. 60-67.
181. Chen, C.-Y., et al., *Amphetamine-Decreased Progesterone and Estradiol Release in Rat Granulosa Cells: The Regulatory Role of cAMP-and Ca<sup>2+</sup>-Mediated Signaling Pathways*. *Biomedicines*, 2021. **9**(5): p. 493.
182. Labib, K., J.A. Tercero, and J.F. Diffley, *Uninterrupted MCM2-7 function required for DNA replication fork progression*. *Science*, 2000. **288**(5471): p. 1643-1647.
183. Chen, R. and M.S. Wold, *Replication protein A: single-stranded DNA's first responder: dynamic DNA-interactions allow replication protein A to direct single-strand DNA intermediates into different pathways for synthesis or repair*. *Bioessays*, 2014. **36**(12): p. 1156-1161.
184. Morrison, A., et al., *A third essential DNA polymerase in S. cerevisiae*. *Cell*, 1990. **62**(6): p. 1143-1151.

185. Waga, S. and B. Stillman, *Anatomy of a DNA replication fork revealed by reconstitution of SV40 DNA replication in vitro*. Nature, 1994. **369**(6477): p. 207-212.
186. Tsurimoto, T. and B. Stillman, *Replication factors required for SV40 DNA replication in vitro. II. Switching of DNA polymerase alpha and delta during initiation of leading and lagging strand synthesis*. Journal of Biological Chemistry, 1991. **266**(3): p. 1961-1968.
187. Bowman, G.D., M. O'Donnell, and J. Kuriyan, *Structural analysis of a eukaryotic sliding DNA clamp-clamp loader complex*. Nature, 2004. **429**(6993): p. 724-730.
188. Zhang, G., et al., *Studies on the interactions between human replication factor C and human proliferating cell nuclear antigen*. Proceedings of the National Academy of Sciences, 1999. **96**(5): p. 1869-1874.
189. Goulian, M., et al., *Discontinuous DNA synthesis by purified mammalian proteins*. Journal of Biological Chemistry, 1990. **265**(30): p. 18461-18471.
190. Mertz, T.M., V. Harcy, and S.A. Roberts, *Risks at the DNA replication fork: effects upon carcinogenesis and tumor heterogeneity*. Genes, 2017. **8**(1): p. 46.
191. Jackson, A.R., A. Shah, and A. Kumar, *Methamphetamine alters the normal progression by inducing cell cycle arrest in astrocytes*. PLoS One, 2014. **9**(10): p. e109603.
192. Baptista, S., et al., *Methamphetamine decreases dentate gyrus stem cell self-renewal and shifts the differentiation towards neuronal fate*. Stem Cell Research, 2014. **13**(2): p. 329-341.
193. Potula, R., et al., *Methamphetamine alters T cell cycle entry and progression: role in immune dysfunction*. Cell Death Discovery, 2018. **4**(1): p. 1-13.
194. Kunkel, T.A. and D.A. Erie, *DNA mismatch repair*. Annual Reviews of Biochemistry, 2005. **74**: p. 681-710.

195. Dao, V. and P. Modrich, *Mismatch-, MutS-, MutL-, and helicase II-dependent unwinding from the single-strand break of an incised heteroduplex*. Journal of Biological Chemistry, 1998. **273**(15): p. 9202-9207.
196. Ramilo, C., et al., *Partial reconstitution of human DNA mismatch repair in vitro: characterization of the role of human replication protein A*. Molecular and cellular Biology, 2002. **22**(7): p. 2037-2046.
197. Modrich, P. and R. Lahue, *Mismatch repair in replication fidelity, genetic recombination, and cancer biology*. Annual Review of Biochemistry, 1996. **65**(1): p. 101-133.
198. Pečina-Šlaus, N., et al., *Mismatch repair pathway, genome stability and cancer*. Frontiers in Molecular Biosciences, 2020: p. 122.
199. Zheng, J., et al., *Expression analyses of 27 DNA repair genes in astrocytoma by TaqMan low-density array*. Neuroscience Letters, 2006. **409**(2): p. 112-117.
200. Kanthasamy, A., et al., *Methamphetamine induces autophagy and apoptosis in a mesencephalic dopaminergic neuronal culture model: role of cathepsin-D in methamphetamine-induced apoptotic cell death*. Annals of the New York Academy of Sciences, 2006. **1074**(1): p. 234-244.
201. Cubells, J.F., et al., *Methamphetamine neurotoxicity involves vacuolation of endocytic organelles and dopamine-dependent intracellular oxidative stress*. Journal of Neuroscience, 1994. **14**(4): p. 2260-2271.
202. Nara, A., et al., *Hyperstimulation of macropinocytosis leads to lysosomal dysfunction during exposure to methamphetamine in SH-SY5Y cells*. Brain Research, 2012. **1466**: p. 1-14.

203. Funakoshi-Hirose, I., et al., *Distinct effects of methamphetamine on autophagy–lysosome and ubiquitin–proteasome systems in HL-1 cultured mouse atrial cardiomyocytes*. *Toxicology*, 2013. **312**: p. 74-82.
204. Li, M.J., et al., *Ibudilast attenuates peripheral inflammatory effects of methamphetamine in patients with methamphetamine use disorder*. *Drug and Alcohol Dependence*, 2020. **206**: p. 107776.
205. Campden, R.I. and Y. Zhang, *The role of lysosomal cysteine cathepsins in NLRP3 inflammasome activation*. *Archives of Biochemistry and Biophysics*, 2019. **670**: p. 32-42.
206. Liu, Q., et al., *Cathepsin C promotes microglia M1 polarization and aggravates neuroinflammation via activation of Ca<sup>2+</sup>-dependent PKC/p38MAPK/NF-κB pathway*. *Journal of Neuroinflammation*, 2019. **16**(1): p. 1-18.
207. Zhao, X., et al., *Cathepsin C aggravates neuroinflammation via promoting production of CCL2 and CXCL2 in glial cells and neurons in a cryogenic brain lesion*. *Neurochemistry International*, 2021: p. 105107.
208. Zhang, Y., et al., *Cathepsin C aggravates neuroinflammation involved in disturbances of behaviour and neurochemistry in acute and chronic stress-induced murine model of depression*. *Neurochemical Research*, 2018. **43**(1): p. 89-100.
209. Droga-Mazovec, G., et al., *Cysteine cathepsins trigger caspase-dependent cell death through cleavage of bid and antiapoptotic Bcl-2 homologues*. *Journal of Biological Chemistry*, 2008. **283**(27): p. 19140-19150.

210. Ueno, N.T., et al., *E1A-mediated paclitaxel sensitization in HER-2/neu-overexpressing ovarian cancer SKOV3. ip1 through apoptosis involving the caspase-3 pathway*. *Clinical Cancer Research*, 2000. **6**(1): p. 250-259.
211. Liang, F., et al., *Monocyte differentiation up-regulates the expression of the lysosomal sialidase, Neu1, and triggers its targeting to the plasma membrane via major histocompatibility complex class II-positive compartments*. *Journal of Biological Chemistry*, 2006. **281**(37): p. 27526-27538.
212. Jiang, K., et al., *Long non-coding RNA TOB1-AS1 modulates cell proliferation, apoptosis, migration and invasion through miR-23a/NEU1 axis via Wnt/b-catenin pathway in gastric cancer*. *European Review for Medical and Pharmacological Sciences*, 2019. **23**(22): p. 9890-9899.
213. Dehay, B., et al., *Pathogenic lysosomal depletion in Parkinson's disease*. *Journal of Neuroscience*, 2010. **30**(37): p. 12535-12544.
214. Hook, V., et al., *Cathepsin B in neurodegeneration of Alzheimer's disease, traumatic brain injury, and related brain disorders*. *Biochimica et Biophysica Acta (BBA)-Proteins and Proteomics*, 2020. **1868**(8): p. 140428.
215. Meng, J., et al., *Nucleus distribution of cathepsin B in senescent microglia promotes brain aging through degradation of sirtuins*. *Neurobiology of Aging*, 2020. **96**: p. 255-266.
216. Cocchiaro, P., et al., *The multifaceted role of the lysosomal protease cathepsins in kidney disease*. *Frontiers in Cell and Developmental Biology*, 2017. **5**: p. 114.
217. Liu, L., et al., *Increased cathepsin D correlates with clinical parameters in newly diagnosed type 2 diabetes*. *Disease Markers*, 2017. **2017**.

218. Lutgens, S.P., et al., *Cathepsin cysteine proteases in cardiovascular disease*. The FASEB Journal, 2007. **21**(12): p. 3029-3041.
219. Kumar, R., P. Herbert, and A. Warrens, *An introduction to death receptors in apoptosis*. International Journal of Surgery, 2005. **3**(4): p. 268-277.
220. Nishitoh, H., et al., *ASK1 is essential for JNK/SAPK activation by TRAF2*. Molecular Cell, 1998. **2**(3): p. 389-395.
221. Dyari, H.R.E., et al., *A novel synthetic analogue of  $\omega$ -3 17, 18-epoxyeicosatetraenoic acid activates TNF receptor-1/ASK1/JNK signaling to promote apoptosis in human breast cancer cells*. The FASEB Journal, 2017. **31**(12): p. 5246-5257.
222. Dewson, G. and R.M. Kluck, *Mechanisms by which Bak and Bax permeabilise mitochondria during apoptosis*. Journal of Cell Science, 2009. **122**(16): p. 2801-2808.
223. Suzuki, Y., et al., *A serine protease, HtrA2, is released from the mitochondria and interacts with XIAP, inducing cell death*. Molecular Cell, 2001. **8**(3): p. 613-621.
224. Bano, D. and J.H. Prehn, *Apoptosis-inducing factor (AIF) in physiology and disease: the tale of a repented natural born killer*. EBioMedicine, 2018. **30**: p. 29-37.
225. Inohara, N., et al., *harakiri, a novel regulator of cell death, encodes a protein that activates apoptosis and interacts selectively with survival-promoting proteins Bcl-2 and Bcl-XL*. The EMBO Journal, 1997. **16**(7): p. 1686-1694.
226. Kasthuber, E.R. and S.W. Lowe, *Putting p53 in context*. Cell, 2017. **170**(6): p. 1062-1078.
227. Bode, A.M. and Z. Dong, *Post-translational modification of p53 in tumorigenesis*. Nature Reviews Cancer, 2004. **4**(10): p. 793-805.

228. Lindahl, T., *Instability and decay of the primary structure of DNA*. Nature, 1993. **362**(6422): p. 709-715.
229. Liu, Y., et al., *Coordination of steps in single-nucleotide base excision repair mediated by apurinic/apyrimidinic endonuclease I and DNA polymerase  $\beta$* . Journal of Biological Chemistry, 2007. **282**(18): p. 13532-13541.
230. Fortini, P. and E. Dogliotti, *Base damage and single-strand break repair: mechanisms and functional significance of short-and long-patch repair subpathways*. DNA Repair, 2007. **6**(4): p. 398-409.
231. Shackelford, D.A., *DNA end joining activity is reduced in Alzheimer's disease*. Neurobiology of Aging, 2006. **27**(4): p. 596-605.
232. Bender, A., et al., *High levels of mitochondrial DNA deletions in substantia nigra neurons in aging and Parkinson disease*. Nature Genetics, 2006. **38**(5): p. 515-517.
233. Kravtsov, Y., et al., *Mitochondrial DNA deletions are abundant and cause functional impairment in aged human substantia nigra neurons*. Nature Genetics, 2006. **38**(5): p. 518-520.
234. Sung, P. and H. Klein, *Mechanism of homologous recombination: mediators and helicases take on regulatory functions*. Nature Reviews Molecular Cell Biology, 2006. **7**(10): p. 739-750.
235. Mimitou, E.P. and L.S. Symington, *Nucleases and helicases take center stage in homologous recombination*. Trends in Biochemical Sciences, 2009. **34**(5): p. 264-272.
236. Wold, M.S., *Replication protein A: a heterotrimeric, single-stranded DNA-binding protein required for eukaryotic DNA metabolism*. Annual Review of Biochemistry, 1997. **66**(1): p. 61-92.

237. Tanaka, K., et al., *A novel human rad54 homologue, Rad54B, associates with Rad51*. Journal of Biological Chemistry, 2000. **275**(34): p. 26316-26321.
238. Xia, B., et al., *Control of BRCA2 cellular and clinical functions by a nuclear partner, PALB2*. Molecular Cell, 2006. **22**(6): p. 719-729.
239. Jensen, R.B., A. Carreira, and S.C. Kowalczykowski, *Purified human BRCA2 stimulates RAD51-mediated recombination*. Nature, 2010. **467**(7316): p. 678-683.
240. Li, M. and X. Yu, *Function of BRCA1 in the DNA damage response is mediated by ADP-ribosylation*. Cancer Cell, 2013. **23**(5): p. 693-704.
241. Nimonkar, A.V., et al., *Human exonuclease 1 and BLM helicase interact to resect DNA and initiate DNA repair*. Proceedings of the National Academy of Sciences, 2008. **105**(44): p. 16906-16911.
242. Morishima, K.-i., et al., *TopBP1 associates with NBS1 and is involved in homologous recombination repair*. Biochemical and Biophysical Research Communications, 2007. **362**(4): p. 872-879.
243. Ropek, N., et al., *Methamphetamine ("crystal meth") causes induction of DNA damage and chromosomal aberrations in human derived cells*. Food and Chemical Toxicology, 2019. **128**: p. 1-7.
244. Tokunaga, I., et al., *The peroxidative DNA damage and apoptosis in methamphetamine-treated rat brain*. The Journal of Medical Investigation, 2008. **55**(3, 4): p. 241-245.
245. Johnson, Z., et al., *Methamphetamine induces DNA damage in specific regions of the female rat brain*. Clinical and Experimental Pharmacology and Physiology, 2015. **42**(6): p. 570-575.

246. Campisi, J. and F. d'Adda di Fagagna, *Cellular senescence: when bad things happen to good cells*. Nature Reviews Molecular Cell Biology, 2007. **8**(9): p. 729-740.
247. Rovillain, E., et al., *An RNA interference screen for identifying downstream effectors of the p53 and pRB tumour suppressor pathways involved in senescence*. BMC Genomics, 2011. **12**(1): p. 1-12.
248. Kumari, R. and P. Jat, *Mechanisms of cellular senescence: cell cycle arrest and senescence associated secretory phenotype*. Frontiers in Cell and Developmental Biology, 2021. **9**: p. 485.
249. Van Deursen, J.M., *The role of senescent cells in ageing*. Nature, 2014. **509**(7501): p. 439-446.
250. Bussian, T.J., et al., *Clearance of senescent glial cells prevents tau-dependent pathology and cognitive decline*. Nature, 2018. **562**(7728): p. 578-582.
251. Mihu, M.R., et al., *Methamphetamine alters the antimicrobial efficacy of phagocytic cells during methicillin-resistant Staphylococcus aureus skin infection*. MBio, 2015. **6**(6): p. e01622-15.
252. Abdullah, C.S., et al., *Methamphetamine induces cardiomyopathy by Sigmar1 inhibition-dependent impairment of mitochondrial dynamics and function*. Communications biology, 2020. **3**(1): p. 1-20.
253. Chavva, H., et al., *Methamphetamine-induced changes in myocardial gene transcription are sex-dependent*. BMC Genomics, 2021. **22**(1): p. 1-16.
254. Yonezawa, T., et al., *Type IV collagen induces expression of thrombospondin-1 that is mediated by integrin  $\alpha 1\beta 1$  in astrocytes*. Glia, 2010. **58**(7): p. 755-767.

255. Lu, Z. and J. Kipnis, *Thrombospondin 1—a key astrocyte-derived neurogenic factor*. The FASEB Journal, 2010. **24**(6): p. 1925-1934.
256. Price, B.R., L.A. Johnson, and C.M. Norris, *Reactive astrocytes: The nexus of pathological and clinical hallmarks of Alzheimer's disease*. Ageing Research Reviews, 2021. **68**: p. 101335.
257. Son, S.M., et al., *Thrombospondin-1 prevents amyloid beta-mediated synaptic pathology in Alzheimer's disease*. Neurobiology of Aging, 2015. **36**(12): p. 3214-3227.
258. Betts, E.S., et al., *Analysis of methamphetamine-induced changes in the expression of integrin family members in the cortex of wild-type and c-fos knockout mice*. Neurotoxicity Research, 2002. **4**(7-8): p. 617-623.
259. Killisch, I., et al., *Characterization of early and late endocytic compartments of the transferrin cycle. Transferrin receptor antibody blocks erythroid differentiation by trapping the receptor in the early endosome*. Journal of Cell Science, 1992. **103**(1): p. 211-232.
260. Bohdanowicz, M. and S. Grinstein, *Vesicular traffic: a Rab SANDwich*. Current biology, 2010. **20**(7): p. R311-R314.
261. Via, L.E., et al., *Arrest of mycobacterial phagosome maturation is caused by a block in vesicle fusion between stages controlled by rab5 and rab7*. Journal of Biological Chemistry, 1997. **272**(20): p. 13326-13331.
262. Mottola, G., *The complexity of Rab5 to Rab7 transition guarantees specificity of pathogen subversion mechanisms*. Frontiers in Cellular and Infection Microbiology, 2014. **4**: p. 180.

263. Rogers, L.D. and L.J. Foster, *The dynamic phagosomal proteome and the contribution of the endoplasmic reticulum*. Proceedings of the National Academy of Sciences, 2007. **104**(47): p. 18520-18525.
264. Forgac, M., *Vacuolar ATPases: rotary proton pumps in physiology and pathophysiology*. Nature Reviews Molecular Cell Biology, 2007. **8**(11): p. 917-929.
265. Pomilio, C., et al., *Glial alterations from early to late stages in a model of Alzheimer's disease: Evidence of autophagy involvement in A $\beta$  internalization*. Hippocampus, 2016. **26**(2): p. 194-210.
266. Wang, Y., et al., *TREM2 lipid sensing sustains the microglial response in an Alzheimer's disease model*. Cell, 2015. **160**(6): p. 1061-1071.
267. Chung, W.-S., et al., *Astrocytes mediate synapse elimination through MEGF10 and MERTK pathways*. Nature, 2013. **504**(7480): p. 394-400.
268. Konishi, H., S. Koizumi, and H. Kiyama, *Phagocytic astrocytes: Emerging from the shadows of microglia*. Glia, 2022.
269. Koistinaho, M., et al., *Apolipoprotein E promotes astrocyte colocalization and degradation of deposited amyloid- $\beta$  peptides*. Nature Medicine, 2004. **10**(7): p. 719-726.
270. Morizawa, Y.M., et al., *Reactive astrocytes function as phagocytes after brain ischemia via ABCA1-mediated pathway*. Nature Communications, 2017. **8**(1): p. 1-15.
271. Baker, D.J., et al., *Lysosomal and phagocytic activity is increased in astrocytes during disease progression in the SOD1 G93A mouse model of amyotrophic lateral sclerosis*. Frontiers in Cellular Neuroscience, 2015: p. 410.

272. Savage, J.C., et al., *Nuclear receptors license phagocytosis by trem2+ myeloid cells in mouse models of Alzheimer's disease*. Journal of Neuroscience, 2015. **35**(16): p. 6532-6543.
273. Neher, J.J., et al., *Phagocytosis executes delayed neuronal death after focal brain ischemia*. Proceedings of the National Academy of Sciences, 2013. **110**(43): p. E4098-E4107.
274. Kim, Y., J. Park, and Y.K. Choi, *The role of astrocytes in the central nervous system focused on BK channel and heme oxygenase metabolites: A review*. Antioxidants, 2019. **8**(5): p. 121.
275. Tallóczy, Z., et al., *Methamphetamine inhibits antigen processing, presentation, and phagocytosis*. PLoS Pathogens, 2008. **4**(2): p. e28.
276. Melega, W.P., et al., *Methamphetamine blood concentrations in human abusers: application to pharmacokinetic modeling*. Synapse, 2007. **61**(4): p. 216-220.
277. Rivière, G.J., W.B. Gentry, and S.M. Owens, *Disposition of methamphetamine and its metabolite amphetamine in brain and other tissues in rats after intravenous administration*. Journal of Pharmacology and Experimental Therapeutics, 2000. **292**(3): p. 1042-1047.
278. Chatterjee, N. and G.C. Walker, *Mechanisms of DNA damage, repair, and mutagenesis*. Environmental and Molecular Mutagenesis, 2017. **58**(5): p. 235-263.
279. Wang, J.Y., *Focus: Death: Cell Death Response to DNA Damage*. The Yale Journal of Biology and Medicine, 2019. **92**(4): p. 771.
280. Pekny, M., et al., *Astrocytes: a central element in neurological diseases*. Acta Neuropathologica, 2016. **131**(3): p. 323-345.

281. Rossi, D. and A. Volterra, *Astrocytic dysfunction: insights on the role in neurodegeneration*. Brain Research Bulletin, 2009. **80**(4-5): p. 224-232.
282. Linker, K., S. Cross, and F. Leslie, *Glial mechanisms underlying substance use disorders*. European Journal of Neuroscience, 2019. **50**(3): p. 2574-2589.
283. Villoslada, P., *Neuroprotective therapies for multiple sclerosis and other demyelinating diseases*. Multiple Sclerosis and Demyelinating Disorders, 2016. **1**(1): p. 1-11.
284. Chou, S.-C., et al., *Recent advances in preventing neurodegenerative diseases*. Faculty Reviews, 2021. **10**.
285. Bradshaw, A.D., et al., *Integrin alpha 2 beta 1 mediates interactions between developing embryonic retinal cells and collagen*. Development, 1995. **121**(11): p. 3593-3602.
286. DeFreitas, M.F., et al., *Identification of integrin  $\alpha 3\beta 1$  as a neuronal thrombospondin receptor mediating neurite outgrowth*. Neuron, 1995. **15**(2): p. 333-343.
287. Galileo, D.S., et al., *Retrovirally introduced antisense integrin RNA inhibits neuroblast migration in vivo*. Neuron, 1992. **9**(6): p. 1117-1131.
288. Anton, E., J.A. Kreidberg, and P. Rakic, *Distinct functions of  $\alpha 3$  and  $\alpha v$  integrin receptors in neuronal migration and laminar organization of the cerebral cortex*. Neuron, 1999. **22**(2): p. 277-289.
289. Jones, E.V., et al., *Astrocytes control glutamate receptor levels at developing synapses through SPARC- $\beta$ -integrin interactions*. Journal of Neuroscience, 2011. **31**(11): p. 4154-4165.
290. Baldwin, K.T. and C. Eroglu, *Molecular mechanisms of astrocyte-induced synaptogenesis*. Current Opinion in Neurobiology, 2017. **45**: p. 113-120.

291. Ikeshima-Kataoka, H., C. Sugimoto, and T. Tsubokawa, *Integrin Signaling in the Central Nervous System in Animals and Human Brain Diseases*. International Journal of Molecular Sciences, 2022. **23**(3): p. 1435.
292. Wu, X. and D.S. Reddy, *Integrins as receptor targets for neurological disorders*. Pharmacology & Therapeutics, 2012. **134**(1): p. 68-81.
293. Carneiro, A.M., *The emerging role of integrins in neuropsychiatric disorders*. Neuropsychopharmacology, 2010. **35**(1): p. 338.
294. Peng, H., et al., *Integrins and dystroglycan regulate astrocyte wound healing: the integrin  $\beta 1$  subunit is necessary for process extension and orienting the microtubular network*. Developmental Neurobiology, 2008. **68**(5): p. 559-574.
295. Kumar, P., A. Nagarajan, and P.D. Uchil, *Analysis of cell viability by the lactate dehydrogenase assay*. Cold Spring Harbor Protocols, 2018. **2018**(6): p. pdb. prot095497.
296. Li, M.D., et al., *Transcriptome profiling and pathway analysis of genes expressed differentially in participants with or without a positive response to topiramate treatment for methamphetamine addiction*. BMC Medical Genomics, 2014. **7**(1): p. 1-15.
297. Milner, R., et al., *Responses of endothelial cell and astrocyte matrix-integrin receptors to ischemia mimic those observed in the neurovascular unit*. Stroke, 2008. **39**(1): p. 191-197.
298. Hu, Q., et al., *Proteolytic processing of the caspase-9 zymogen is required for apoptosome-mediated activation of caspase-9*. Journal of Biological Chemistry, 2013. **288**(21): p. 15142-15147.

299. Hauck, C.R., T. Hunter, and D.D. Schlaepfer, *The v-Src SH3 domain facilitates a cell adhesion-independent association with focal adhesion kinase*. Journal of Biological Chemistry, 2001. **276**(21): p. 17653-17662.
300. Cho, S.Y. and R.L. Klemke, *Extracellular-regulated kinase activation and CAS/Crk coupling regulate cell migration and suppress apoptosis during invasion of the extracellular matrix*. The Journal of Cell Biology, 2000. **149**(1): p. 223-236.
301. Scatena, M., et al., *NF- $\kappa$ B mediates  $\alpha$ v $\beta$ 3 integrin-induced endothelial cell survival*. The Journal of Cell Biology, 1998. **141**(4): p. 1083-1093.
302. Conant, K., et al., *Methamphetamine-associated cleavage of the synaptic adhesion molecule intercellular adhesion molecule-5*. Journal of Neurochemistry, 2011. **118**(4): p. 521-532.
303. Heino, J., et al., *Regulation of cell adhesion receptors by transforming growth factor- $\beta$ : concomitant regulation of integrins that share a common  $\beta$ 1 subunit*. Journal of Biological Chemistry, 1989. **264**(1): p. 380-388.
304. Stadlin, A., J.W. Lau, and Y. Szeto, *A Selective Regional Response of Cultured Astrocytes to Methamphetamine*. Annals of the New York Academy of Sciences, 1998. **844**(1): p. 108-121.
305. Dang, J., et al., *Glial cell diversity and methamphetamine-induced neuroinflammation in human cerebral organoids*. Molecular Psychiatry, 2021. **26**(4): p. 1194-1207.
306. Bélanger, M. and P.J. Magistretti, *The role of astroglia in neuroprotection*. Dialogues in Clinical Neuroscience, 2022. **11**(3):281-295

307. Oksanen, M., et al., *Astrocyte alterations in neurodegenerative pathologies and their modeling in human induced pluripotent stem cell platforms*. Cellular and Molecular Life Sciences, 2019. **76**(14): p. 2739-2760.
308. Lange, J., et al., *Compromised astrocyte function and survival negatively impact neurons in infantile neuronal ceroid lipofuscinosis*. Acta Neuropathologica Communications, 2018. **6**(1): p. 1-21.
309. del Zoppo, G.J. and R. Milner, *Integrin–matrix interactions in the cerebral microvasculature*. Arteriosclerosis, Thrombosis, and Vascular Biology, 2006. **26**(9): p. 1966-1975.
310. Stumm, G., et al., *Amphetamines induce apoptosis and regulation of bcl-x splice variants in neocortical neurons*. The FASEB Journal, 1999. **13**(9): p. 1065-1072.
311. Krasnova, I.N., B. Ladenheim, and J.L. Cadet, *Amphetamine induces apoptosis of medium spiny striatal projection neurons via the mitochondria-dependent pathway*. The FASEB Journal, 2005. **19**(7): p. 1-22.
312. Capela, J.P., et al., *The neurotoxicity of hallucinogenic amphetamines in primary cultures of hippocampal neurons*. Neurotoxicology, 2013. **34**: p. 254-263.
313. Shah, A., et al., *HIV gp120-and methamphetamine-mediated oxidative stress induces astrocyte apoptosis via cytochrome P450 2E1*. Cell Death & Disease, 2013. **4**(10): p. e850-e850.
314. Shah, A. and A. Kumar, *Methamphetamine-mediated endoplasmic reticulum (ER) stress induces type-1 programmed cell death in astrocytes via ATF6, IRE1 $\alpha$  and PERK pathways*. Oncotarget, 2016. **7**(29): p. 46100.

315. Strater, J., et al., *Rapid onset of apoptosis in vitro follows disruption of beta 1-integrin/matrix interactions in human colonic crypt cells*. *Gastroenterology*, 1996. **110**(6): p. 1776-1784.
316. Aplin, A.E., A.K. Howe, and R. Juliano, *Cell adhesion molecules, signal transduction and cell growth*. *Current Opinion in Cell Biology*, 1999. **11**(6): p. 737-744.
317. Dedhar, S., B. Williams, and G. Hannigan, *Integrin-linked kinase (ILK): a regulator of integrin and growth-factor signalling*. *Trends in Cell Biology*, 1999. **9**(8): p. 319-323.
318. Pozzi, A., et al., *Integrin  $\alpha1\beta1$  mediates a unique collagen-dependent proliferation pathway in vivo*. *The Journal of Cell Biology*, 1998. **142**(2): p. 587-594.
319. Tagaya, M., et al., *Rapid loss of microvascular integrin expression during focal brain ischemia reflects neuron injury*. *Journal of Cerebral Blood Flow & Metabolism*, 2001. **21**(7): p. 835-846.
320. McKetin, R., et al., *Major depression among methamphetamine users entering drug treatment programs*. *Medical Journal of Australia*, 2011. **195**: p. S51-S55.
321. Darke, S., et al., *Major physical and psychological harms of methamphetamine use*. *Drug and Alcohol Review*, 2008. **27**(3): p. 253-262.
322. Glasner-Edwards, S., et al., *Clinical course and outcomes of methamphetamine-dependent adults with psychosis*. *Journal of Substance Abuse Treatment*, 2008. **35**(4): p. 445-450.
323. Cloutier, R.L., R.G. Hendrickson, and B. Blake, *Methamphetamine-related psychiatric visits to an urban academic emergency department: an observational study*. *The Journal of Emergency Medicine*, 2013. **45**(1): p. 136-142.

324. KAY-LAMBKIN, F.J., et al., *Stepping through treatment: reflections on an adaptive treatment strategy among methamphetamine users with depression*. Drug and Alcohol Review, 2010. **29**(5): p. 475-482.
325. Newton, T.F., et al., *Theories of addiction: methamphetamine users' explanations for continuing drug use and relapse*. American Journal on Addictions, 2009. **18**(4): p. 294-300.
326. Vos, P., et al., *A retrospective review of trends and clinical characteristics of methamphetamine-related acute psychiatric admissions in a South African context*. African Journal of Psychiatry, 2010. **13**(5).
327. Moos, R.H., A.C. Nichol, and B.S. Moos, *Risk factors for symptom exacerbation among treated patients with substance use disorders*. Addiction, 2002. **97**(1): p. 75-85.
328. Lee, N.K., et al., *Pharmacotherapy for amphetamine dependence: A systematic review*. Drug and Alcohol Dependence, 2018. **191**: p. 309-337.
329. Anderson, A.L., et al., *Bupropion for the treatment of methamphetamine dependence in non-daily users: a randomized, double-blind, placebo-controlled trial*. Drug and Alcohol Dependence, 2015. **150**: p. 170-174.
330. Brensilver, M., K.G. Heinzerling, and S. Shoptaw, *Pharmacotherapy of amphetamine-type stimulant dependence: an update*. Drug and Alcohol Review, 2013. **32**(5): p. 449-460.
331. Lile, J.A., et al., *Physiological and subjective effects of acute intranasal methamphetamine during extended-release alprazolam maintenance*. Drug and Alcohol Dependence, 2011. **119**(3): p. 187-193.

332. Hellem, T.L., K.J. Lundberg, and P.F. Renshaw, *A review of treatment options for co-occurring methamphetamine use disorders and depression*. *Journal of Addictions Nursing*, 2015. **26**(1): p. 14.
333. Barrowclough, C., et al., *Evaluating integrated MI and CBT for people with psychosis and substance misuse: recruitment, retention and sample characteristics of the MIDAS trial*. *Addictive Behaviors*, 2009. **34**(10): p. 859-866.
334. Rawson, R.A., et al., *A multi-site comparison of psychosocial approaches for the treatment of methamphetamine dependence*. *Addiction*, 2004. **99**(6): p. 708-717.
335. Ryan, M., et al., *Gene expression analysis of bipolar disorder reveals downregulation of the ubiquitin cycle and alterations in synaptic genes*. *Molecular Psychiatry*, 2006. **11**(10): p. 965-978.
336. Iwamoto, K., et al., *Molecular characterization of bipolar disorder by comparing gene expression profiles of postmortem brains of major mental disorders*. *Molecular Psychiatry*, 2004. **9**(4): p. 406-416.
337. Chen, C., et al., *The transcription factor POU3F2 regulates a gene coexpression network in brain tissue from patients with psychiatric disorders*. *Science Translational Medicine*, 2018. **10**(472): p. eaat8178.
338. Lanz, T.A., et al., *Postmortem transcriptional profiling reveals widespread increase in inflammation in schizophrenia: a comparison of prefrontal cortex, striatum, and hippocampus among matched tetrads of controls with subjects diagnosed with schizophrenia, bipolar or major depressive disorder*. *Translational Psychiatry*, 2019. **9**(1): p. 1-13.

339. Iwamoto, K., M. Bundo, and T. Kato, *Altered expression of mitochondria-related genes in postmortem brains of patients with bipolar disorder or schizophrenia, as revealed by large-scale DNA microarray analysis*. Human Molecular Genetics, 2005. **14**(2): p. 241-253.
340. Tsuang, M.T., et al., *Assessing the validity of blood-based gene expression profiles for the classification of schizophrenia and bipolar disorder: A preliminary report*. American Journal of Medical Genetics Part B: Neuropsychiatric Genetics, 2005. **133**(1): p. 1-5.
341. Chang, L.-C., et al., *A conserved BDNF, glutamate-and GABA-enriched gene module related to human depression identified by coexpression meta-analysis and DNA variant genome-wide association studies*. PloS One, 2014. **9**(3): p. e90980.
342. Teixeira, P.D., et al., *Brain STAT5 modulates long-term metabolic and epigenetic changes induced by pregnancy and lactation in female mice*. Endocrinology, 2019. **160**(12): p. 2903-2917.
343. Narayan, S., et al., *Molecular profiles of schizophrenia in the CNS at different stages of illness*. Brain Research, 2008. **1239**: p. 235-248.
344. Feinstein, Y., et al., *F-spondin and mindin: two structurally and functionally related genes expressed in the hippocampus that promote outgrowth of embryonic hippocampal neurons*. Development, 1999. **126**(16): p. 3637-3648.
345. Schubert, D., et al., *F-spondin promotes nerve precursor differentiation*. Journal of Neurochemistry, 2006. **96**(2): p. 444-453.
346. Burstyn-Cohen, T., et al., *Accumulation of F-spondin in injured peripheral nerve promotes the outgrowth of sensory axons*. Journal of Neuroscience, 1998. **18**(21): p. 8875-8885.

347. Gandal, M.J., et al., *Shared molecular neuropathology across major psychiatric disorders parallels polygenic overlap*. *Science*, 2018. **359**(6376): p. 693-697.
348. Narvaez, J.C., et al., *Psychiatric and substance-use comorbidities associated with lifetime crack cocaine use in young adults in the general population*. *Comprehensive Psychiatry*, 2014. **55**(6): p. 1369-1376.
349. Herrero, M.J., et al., *Psychiatric comorbidity in young cocaine users: induced versus independent disorders*. *Addiction*, 2008. **103**(2): p. 284-293.
350. Ford, J.D., et al., *Association of psychiatric and substance use disorder comorbidity with cocaine dependence severity and treatment utilization in cocaine-dependent individuals*. *Drug and Alcohol Dependence*, 2009. **99**(1-3): p. 193-203.
351. Franke, A.G., et al., *Psychiatric Comorbidity and Psychopathology of Methamphetamine Users—Are There Gender Differences?* *International Journal of Mental Health and Addiction*, 2022: p. 1-18.
352. Ries, R.K., S.C. Miller, and D.A. Fiellin, *Principles of addiction medicine*. 2009: Lippincott Williams & Wilkins.
353. Penninx, B.W.J.H., et al., *Anxiety disorders*. *The Lancet*, 2021. **397**(10277): p. 914-927.
354. Patel, R.K. and G.M. Rose, *Persistent Depressive Disorder*, in *StatPearls [Internet]*. 2021, StatPearls Publishing.
355. Strain, J.J., et al., *Adjustment disorder: a multisite study of its utilization and interventions in the consultation-liaison psychiatry setting*. *General Hospital Psychiatry*, 1998. **20**(3): p. 139-149.

356. Kessler, R.C., et al., *The epidemiology of panic attacks, panic disorder, and agoraphobia in the National Comorbidity Survey Replication*. Archives of General Psychiatry, 2006. **63**(4): p. 415-424.
357. Brand, B.L., et al., *Separating fact from fiction: An empirical examination of six myths about dissociative identity disorder*. Harvard Review of Psychiatry, 2016. **24**(4): p. 257-70
358. Badner, J. and E. Gershon, *Meta-analysis of whole-genome linkage scans of bipolar disorder and schizophrenia*. Molecular psychiatry, 2002. **7**(4): p. 405-411.
359. Lewis, C.M., et al., *Genome scan meta-analysis of schizophrenia and bipolar disorder, part II: Schizophrenia*. The American Journal of Human Genetics, 2003. **73**(1): p. 34-48.
360. Zhang, F., et al., *An association study of ADSS gene polymorphisms with schizophrenia*. Behavioral and Brain Functions, 2008. **4**(1): p. 1-6.
361. Smeland, O.B., et al., *Genome-wide analysis reveals extensive genetic overlap between schizophrenia, bipolar disorder, and intelligence*. Molecular psychiatry, 2020. **25**(4): p. 844-853.
362. Cardno, A.G. and M.J. Owen, *Genetic relationships between schizophrenia, bipolar disorder, and schizoaffective disorder*. Schizophrenia Bulletin, 2014. **40**(3): p. 504-515.
363. Able, A.A., J.A. Burrell, and J.M. Stephens, *STAT5-interacting proteins: a synopsis of proteins that regulate STAT5 activity*. Biology, 2017. **6**(1): p. 20.
364. Furigo, I.C., et al., *Brain STAT5 signaling modulates learning and memory formation*. Brain Structure and Function, 2018. **223**(5): p. 2229-2241.

365. Yi, Z., et al., *Blood-based gene expression profiles models for classification of subsyndromal symptomatic depression and major depressive disorder*. PloS One, 2012. **7**(2): p. e31283.
366. Tanaka, M., et al., *Region-and time-dependent gene regulation in the amygdala and anterior cingulate cortex of a PTSD-like mouse model*. Molecular Brain, 2019. **12**(1): p. 1-16.
367. Yehuda, R., et al., *Gene expression patterns associated with posttraumatic stress disorder following exposure to the World Trade Center attacks*. Biological Psychiatry, 2009. **66**(7): p. 708-711.
368. Sarapas, C., et al., *Genetic markers for PTSD risk and resilience among survivors of the World Trade Center attacks*. Disease markers, 2011. **30**(2-3): p. 101-110.
369. Sartor, C.E., et al., *Common heritable contributions to low-risk trauma, high-risk trauma, posttraumatic stress disorder, and major depression*. Archives of General Psychiatry, 2012. **69**(3): p. 293-299.
370. Duncan, L.E., et al., *Largest GWAS of PTSD (N= 20 070) yields genetic overlap with schizophrenia and sex differences in heritability*. Molecular Psychiatry, 2018. **23**(3): p. 666-673.
371. Weissman, M.M., et al., *A Mega-analysis Of Genome-wide Association Studies For Major Depressive Disorder*. 2013. **18**(4): p. 497-511
372. Garrett, M.E., et al., *Gene expression analysis in three posttraumatic stress disorder cohorts implicates inflammation and innate immunity pathways and uncovers shared genetic risk with major depressive disorder*. Frontiers in Neuroscience, 2021: p. 938.

373. Borsini, A., et al., *Interferon-alpha reduces human hippocampal neurogenesis and increases apoptosis via activation of distinct STAT1-dependent mechanisms*. International Journal of Neuropsychopharmacology, 2018. **21**(2): p. 187-200.
374. Holsboer, F. and N. Barden, *Antidepressants and hypothalamic-pituitary-adrenocortical regulation*. Endocrine Reviews, 1996. **17**(2): p. 187-205.
375. Stetler, C. and G.E. Miller, *Depression and hypothalamic-pituitary-adrenal activation: a quantitative summary of four decades of research*. Psychosomatic Medicine, 2011. **73**(2): p. 114-126.
376. Solomon, M.B., et al., *Deletion of forebrain glucocorticoid receptors impairs neuroendocrine stress responses and induces depression-like behavior in males but not females*. Neuroscience, 2012. **203**: p. 135-143.
377. Baes, C.V.W., et al., *Assessment of the hypothalamic–pituitary–adrenal axis activity: glucocorticoid receptor and mineralocorticoid receptor function in depression with early life stress—a systematic review*. Acta Neuropsychiatrica, 2012. **24**(1): p. 4-15.
378. Burstyn-Cohen, T., et al., *F-Spondin is required for accurate pathfinding of commissural axons at the floor plate*. Neuron, 1999. **23**(2): p. 233-246.
379. Debby-Brafman, A., et al., *F-Spondin, expressed in somite regions avoided by neural crest cells, mediates inhibition of distinct somite domains to neural crest migration*. Neuron, 1999. **22**(3): p. 475-488.
380. Nagae, M., et al., *Structure of the F-spondin reeler domain reveals a unique  $\beta$ -sandwich fold with a deformable disulfide-bonded loop*. Acta Crystallographica Section D: Biological Crystallography, 2008. **64**(11): p. 1138-1145.

381. Jahanshad, N., et al., *Genome-wide scan of healthy human connectome discovers SPON1 gene variant influencing dementia severity*. Proceedings of the National Academy of Sciences, 2013. **110**(12): p. 4768-4773.
382. Gandal, M.J., et al., *Transcriptome-wide isoform-level dysregulation in ASD, schizophrenia, and bipolar disorder*. Science, 2018. **362**(6420): p. eaat8127.
383. Wu, X., et al., *Genome-wide study of copy number variation implicates multiple novel loci for schizophrenia risk in Han Chinese family trios*. Iscience, 2021. **24**(8): p. 102894.
384. Kim, S., et al., *Suicide candidate genes associated with bipolar disorder and schizophrenia: an exploratory gene expression profiling analysis of post-mortem prefrontal cortex*. BMC Genomics, 2007. **8**(1): p. 1-10.

## VITA

Nitish Chaudhari was born on July 15, 1989, in Bhusawal, India. He was educated in public schools in Bhusawal and Nashik, where he was brought up. After his high school, he completed his Bachelor of Pharmacy from University of Pune, India. After bachelor's degree, he completed a Post Graduate Diploma in Patents law from National Academy of Legal Studies and Research University of Law, India, and a Master of Pharmacy degree specializing in Pharmacology and Toxicology from University of Mumbai, India, both in 2013. During the Summer of 2013, he was selected to participate in World Intellectual Property Organization's special summer program in Intellectual Property Law in Singapore.

After completing post-graduation from India, Mr. Chaudhari came to United States in Fall 2014 to join the interdisciplinary Ph.D. program at UMKC to pursue doctoral degree. During his graduate study, Mr. Chaudhari was awarded with several scholarships, including the Robert C. Lanman Graduate Pharmacology Scholarship and Thomas D. Ross Graduate Memorial Scholarship. Mr. Chaudhari has published 3 papers in peer-reviewed journals and currently have 3 first-author manuscripts in preparation and submission phases.